TECHNISCHE UNIVERSITÄT MÜNCHEN
Lehrstuhl für Informationstechnische Regelung

Design of Interactive Motor Behaviors for Close Joint Action of Humans and Robots

Alexander Imanuel Mörtl

Vollständiger Abdruck der von der Fakultät für Elektrotechnik und Informationstechnik der Technischen Universität München zur Erlangung des akademischen Grades eines

Doktor-Ingenieurs (Dr.-Ing.)

genehmigten Dissertation.

Vorsitzender:	Univ.-Prof. Gordon Cheng, Ph.D.

Prüfer der Dissertation:

1. Univ.-Prof. Dr.-Ing. Sandra Hirche
2. Univ.-Prof. Dr.-Ing./Univ. Tokio Martin Buss

Die Dissertation wurde am 29.04.2014 bei der Technischen Universität München eingereicht und durch die Fakultät für Elektrotechnik und Informationstechnik am 28.10.2014 angenommen.

Foreword

This thesis summarizes research carried out during my five years of work at the Institute of Automatic Control Engineering (LSR) and later, at the newly founded Institute for Information-Oriented Control (ITR) of the Technische Universität München. During this time, a number of people gave me support and advice in different ways. As the thesis at hand would not have been possible without their efforts, I would like to express my gratitude to all these people.

First and foremost, I would like to thank my advisor Prof. Sandra Hirche for giving me the opportunity to conduct research in her renowned robotics and control group, for the stimulating discussions broadening my mind and scientific way of thinking, and for providing me with enough freedom and an excellent research environment to realize my ideas. Sincere thanks also go to Prof. Martin Buss for leading the LSR as an institute that fosters a collaborative and interdisciplinary spirit. I thank the administrative team of the institutes for their kind and professional support in all nonscientific matters.

My collaborators within the excellence initiative research cluster CoTeSys considerably contributed to the successful conclusion of this thesis. Special thanks go to my long-time office mate Martin Lawitzky; thank you for the fruitful collaborations and discussions we had in the field of physical human-robot interaction, for your kind advice in all coding and computing issues, and the funny moments we shared. In related pHRI projects, I was working with Philine Donner and José Ramón Medina Hernández; thank you for your enthusiasm and inspiration during our joyful collaborations. The interdisciplinary collaboration with Prof. Cagatay Basdogan, Dr. Metin Sezgin and Dr. Ayşe Küçükyılmaz from Koç University, Istanbul, was an exciting experience during my PhD times. I especially thank Ayşe for her scientific input and commitment during her stay at the lab in Munich, which enabled the profound study on role allocation. In the field of movement coordination, I was working with Tamara Lorenz among other researchers at the Ludwigs-Maximilians-Universität München; thank you for the pleasant collaborations we had for all these years. I thank Dr. Azwirman Gusrialdi for the inspiring discussions on synchronization theory. My gratitude also goes to the former MuRoLa team and all my colleagues at the LSR and the ITR for the helpfulness and the pleasant atmosphere in the lab.

Also, I would like to thank all the students who worked closely with me, especially Huan Lu for her contribution to the manipulator control scheme, as well as Marco Karmann, Lars Kreutz and Lu Zeng for their valuable support in conducting the numerous experiments.

Finally, I would like to express my gratitude to my parents and my girlfriend Julia for accompanying me with their enduring encouragement, their understanding and love during this challenging period of my live.

Munich, April 2014 Alexander Mörtl

Abstract

Advanced behavioral capabilities are key to the successful application of robotic assistants and companions in human environments. Possible scenarios range from activities of daily living, such as household chores, over assembly in highly flexible manufacturing settings, physical training for rehabilitation to cooperation in search and rescue teams. Since many of those applications involve close joint action with humans and shared workspaces, robots need to be capable of human-oriented and socially compatible motor behaviors. The ultimate goal shall be seamless interaction; if a human partner in a joint action task is replaced by a robot, the interaction shall not deteriorate, neither in terms of human sensation nor in terms of task performance. Close couplings of the partners make the design of interactive motor behavior a challenging endeavor. In particular, joint action mediated through the visual and the haptic modality induces instantaneous negotiation processes between the partners: Fluent and collision-free interaction in shared workspaces requires intuitive strategies for movement coordination; the energy exchange through physical cooperation poses the additional challenge of efficient effort distribution. Only a deep understanding of the human interactive behavior can lead to seamless interaction with robots. Experimental studies of human joint action and system-theoretic models need to be co-designed to obtain valuable models of human behavior. Prototyping and systematic evaluations by means of immersive scenarios and realistic embodiments of robotic partners are technically challenging, yet essential steps towards successful human-robot joint action.

This thesis presents a novel interdisciplinary methodology, in order to achieve a holistic design of interactive motor behaviors for robots. Two design perspectives are identified and pursued. The analytical perspective aims at the model-directed exploration of human behavior through the experimental study of how humans interact. In the context of visual coordination, this perspective is shown to provide a superior entry into the design process. A quantitative description of inter-human movement coordination in the form of a fully parameterized, dynamical synchronization model is developed. The synthetical perspective aims at a system-theoretic and function-oriented design of interactive behavior, while existing principles and models of human behavior are integrated as well. Utilizing the identified model of human coordination behavior and dynamical system theory, synchronization behavior for goal-directed joint action is synthesized. Simultaneous phase and event synchronization allows to dynamically form a variety of interaction patterns, which enable a robot to smoothly coordinate its movements with those of a human partner. In the context of visual-haptic cooperation, role behavior is designed, in order to dynamically distribute the physical effort during joint object manipulation. Based on the geometrical decomposition of the task, effort sharing policies are developed and efficient strategies for dynamic role allocation are synthesized. As the methodology emphasizes a tight interrelation of theory and experimentation, prototyping of interactive behavior and extensive experimental studies by means of an anthropomorphic robot and a virtual reality system are conducted throughout this work.

Zusammenfassung

Hochentwickelte Verhaltensweisen sind entscheidend für den erfolgreichen Einsatz von Robotern als Helfer und Begleiter im Umfeld des Menschen. Mögliche Szenarien reichen von Alltagstätigkeiten wie Hausarbeiten, über Montage in der hochflexiblen Fertigung, physischem Training in der Rehabilitation bis hin zu Kooperation in Such- und Rettungsteams. Da viele dieser Anwendungen enge Zusammenarbeit mit Menschen und gemeinsame Arbeitsräume bedingen, müssen Roboter motorisches Verhalten beherrschen, das am Menschen orientiert und sozial kompatibel ist. Oberstes Ziel soll eine reibungslose Interaktion sein; wenn ein menschlicher Partner in einer gemeinsamen Tätigkeit durch einen Roboter ersetzt wird, darf sich die Interaktion bezogen auf die menschliche Wahrnehmung und die Arbeitsleistung nicht verschlechtern. Enge Verkopplungen der Partner machen die Entwicklung von motorischem Interaktionsverhalten zu einer Herausforderung. Visuell und haptisch vermitteltes, gemeinsames Handeln bedingt insbesondere Prozesse des unmittelbaren Verhandelns zwischen den Partnern: Flüssige und kollisionsfreie Interaktion in gemeinsamen Arbeitsräumen erfordert intuitive Strategien zur Bewegungskoordination; der Energieaustausch durch physische Kooperation bildet die zusätzliche Herausforderung, den Arbeitsaufwand effizient zu verteilen. Einzig ein tiefgreifendes Verständnis des menschlichen Interaktionsverhaltens kann zu einer reibungslosen Interaktion mit Robotern führen. Experimentalstudien der menschlichen Zusammenarbeit und systemtheoretische Modelle sind gemeinsam zu entwickeln, um hochwertige Verhaltensmodelle des Menschen zu gewinnen. Prototypenentwicklung und methodische Evaluierung mittels immersiver Szenarien und realistischer Verkörperungen von Robotern sind technisch herausfordernde, jedoch unerlässliche Schritte in Richtung erfolgreicher Mensch-Roboter Zusammenarbeit.

Diese Dissertation stellt eine neue interdisziplinäre Methodik vor, um motorisches Interaktionsverhalten für Roboter ganzheitlich zu entwickeln. Zwei Entwurfsperspektiven werden identifiziert und verfolgt. Die analytische Perspektive strebt eine modellorientierte Erforschung menschlichen Verhaltens an, indem die Interaktion von Menschen experimentell untersucht wird. Im Rahmen der visuellen Koordination wird gezeigt, dass diese Perspektive einen ausgezeichneten Einstieg in den Entwurfsprozess darstellt. Es wird eine quantitative Beschreibung der zwischenmenschlichen Bewegungskoordination in Form eines parametrierten, dynamischen Synchronisierungsmodells entwickelt. Die synthetische Perspektive strebt ein systemtheoretisches und funktionsorientiertes Design an, während bestehende Grundsätze und Modelle menschlichen Verhaltens einbezogen werden. Das Modell des menschlichen Koordinationsverhaltens und dynamische Systemtheorie wird angewendet, um Synchronisierungsverhalten für zielgerichtetes, gemeinsames Handeln zu synthetisieren. Durch gleichzeitige Phasen- und Ereignissynchronisierung kann dynamisch eine Vielzahl von Interaktionsmustern gebildet werden, welche es einem Roboter ermöglichen, seine Bewegungen reibungslos mit denen eines Menschen abzustimmen. Im Rahmen der visuell-haptischen Kooperation werden Rollenverhalten entwickelt, um den physischen Aufwand während der gemeinsamen Objekthandhabung dynamisch zu verteilen. Anhand einer geometrischen Aufgabenzerlegung werden Methoden zur Aufwandsaufteilung entwickelt und effiziente Strategien zur dynamischen Rollenverteilung synthetisiert. Da die Methodik eine enge Beziehung von Theorie und Experiment betont, werden in der gesamten Arbeit prototypische Interaktionsverhalten entwickelt und umfassende Experimentalstudien mit einem anthropomorphen Roboter und einem System für virtuelle Realität durchgeführt.

Contents

1 Introduction **1**
- 1.1 Applications . . . 2
- 1.2 Problem Definition . . . 3
- 1.3 Challenges . . . 4
- 1.4 Main Contributions and Outline . . . 5

2 Conceptual Foundations **9**
- 2.1 Design Methodology . . . 9
  - 2.1.1 Requirements on Interactive Motor Behavior . . . 10
  - 2.1.2 Two Design Perspectives . . . 11
- 2.2 System-Theoretic Foundations . . . 14
  - 2.2.1 Dynamical Systems . . . 14
  - 2.2.2 Behavioral Dynamics . . . 15
  - 2.2.3 System Identification . . . 17
- 2.3 Studying Human Interactive Behavior . . . 18
  - 2.3.1 Aspects of Psychological Experiments . . . 19
  - 2.3.2 Experimental Measures . . . 21
- 2.4 Technical Foundations . . . 24
  - 2.4.1 Manipulator Control . . . 24
  - 2.4.2 Control of Mobile Manipulators . . . 26
- 2.5 Summary . . . 28

3 Modeling of Human Movement Coordination **29**
- 3.1 Background . . . 30
  - 3.1.1 Experimental Studies and Key Results . . . 30
  - 3.1.2 Modeling and Identification Approaches . . . 31
- 3.2 Model-Directed Experimental Design . . . 34
  - 3.2.1 Concept and Paradigm . . . 34
  - 3.2.2 Human-Human Experiment . . . 37
  - 3.2.3 Phase Reconstruction Techniques . . . 40
- 3.3 Analytical Results . . . 42
  - 3.3.1 Synchronization Patterns . . . 42
  - 3.3.2 Observing the Response to Initial Excitation . . . 44
  - 3.3.3 Attractor Regimes . . . 45
  - 3.3.4 Synchronization Index . . . 47
- 3.4 Human-Human Synchronization Model . . . 48
  - 3.4.1 Model Structure . . . 48
  - 3.4.2 Stability Analysis . . . 50

3.4.3 Identification and Results . . . 52
3.5 Discussion . . . 55
3.5.1 Interpretation of Results . . . 55
3.5.2 Implications for the Design of Interactive Behavior . . . 57
3.6 Conclusion and Open Issues . . . 58

4 Synchronization Behavior for Action Coordination 61
4.1 Background . . . 62
4.1.1 Human Sensorimotor Synchronization . . . 62
4.1.2 Limit Cycle Systems in Robotics . . . 63
4.1.3 Human-Machine Movement Synchronization . . . 63
4.2 Design of Synchronization Behavior . . . 64
4.2.1 Representation of Repetitive Joint Action . . . 64
4.2.2 Synchronization Modes . . . 68
4.2.3 Dynamical Entrainment Process . . . 70
4.2.4 From Movement to Phase . . . 74
4.2.5 From Phase to Movement . . . 77
4.3 Human-Robot Movement Synchronization . . . 80
4.3.1 The Joint Action Task . . . 80
4.3.2 Implementation . . . 81
4.3.3 Human-Robot Experiment . . . 85
4.3.4 Evaluation Criteria . . . 87
4.4 Experimental Results . . . 88
4.4.1 External Assessment of Synchronization . . . 89
4.4.2 Internal Assessment of the Behavioral Dynamics . . . 90
4.5 Discussion . . . 92
4.5.1 Implications on Human-Robot Joint Action . . . 92
4.5.2 Issues in the Design of Synchronization Behavior . . . 93
4.6 Conclusion and Open Issues . . . 94

5 Role Behavior for Physical Cooperation 99
5.1 Background . . . 100
5.1.1 Physical Robotic Assistance . . . 100
5.1.2 Relation to Haptic Shared Control . . . 103
5.2 Physical Effort Sharing in Cooperative Manipulation . . . 104
5.2.1 Problem Formulation and Concept . . . 104
5.2.2 Task Representation . . . 106
5.2.3 Input Wrench Decomposition . . . 108
5.2.4 Effort Sharing Policies . . . 110
5.3 Static Role Behavior . . . 114
5.3.1 Interaction Control Scheme . . . 114
5.3.2 Analysis of the Interactive Behavior . . . 116
5.3.3 Experimental Evaluation . . . 119
5.4 Design of Dynamic Role Behavior . . . 122
5.4.1 Role Allocation Strategies . . . 122

5.4.2 Synthesis of Role Allocations . . . 127
5.4.3 Interaction Control Scheme . . . 130
5.5 Evaluation of Dynamic Role Behavior . . . 131
5.5.1 Human-Robot Experiment . . . 132
5.5.2 Evaluation Criteria . . . 135
5.5.3 Experimental Results . . . 137
5.5.4 Discussion . . . 140
5.6 Conclusion and Open Issues . . . 142

6 Conclusions and Future Directions **145**
6.1 Concluding Remarks . . . 145
6.2 Outlook . . . 147

A Experimental Setups **149**
A.1 VR-System for Visual-Haptic Rendering . . . 149
A.2 Environment for Full-Scale Interaction . . . 150
A.2.1 Six DoF Mobile Manipulator . . . 150
A.2.2 Motion Capture Systems . . . 151

B Haptic Rendering of VR Scenes **152**
B.1 Haptic Interfaces . . . 152
B.2 Haptic Rendering with Admittance-Type Devices . . . 152
B.3 Visual Rendering of Virtual Environments . . . 154

C Questionnaire **155**
C.1 Task Load . . . 155
C.2 Task Experience . . . 155

Bibliography **157**

List of Figures

1.1 Exemplary scenario of close joint action: Cooperative assembly during car restoration. 2
1.2 Investigated classes of joint motor action: Visual coordination with individual goals *(left)* and visual-haptic cooperation towards a shared goal *(right)*. 3
1.3 The thesis aims to realize seamless HRI in close joint action tasks. 5

2.1 Dynamical formulation of the perception-action cycle between an agent and the environment, and the concept of behavioral dynamics. Adapted from Warren [185]. 15
2.2 Inertial admittance-type control scheme including manipulator-base coordination. 26
2.3 (a) Desired and (b) actual configuration of the base with respect to the rigidly grasped object, described by the preferred and actual configuration of the end effector, $\boldsymbol{x}_{\mathrm{d}}^{*R}$ and $\boldsymbol{x}^{R}$ respectively. 27

3.1 Overview scheme depicting the two-layered concept of movement coordination. Agent a and b jointly engage in repetitive actions. The observed movements are transformed to phases in the lower layer. In the upper layer, the coordination behavior is assumed to be governed by the individual and joint behavioral dynamics, which are represented by coupled phase oscillators. Dark arrows represent the analytical perspective on HHI pursued in this chapter. Light arrows outline the envisaged stage of action generation when the behavioral model is deployed to HRI, see Chapter 4. 35
3.2 Experimental task designed to study HHI behavior. Participants are performing goal-directed arm movements while sitting face to face. 36
3.3 Experimental setup with dimensions. Person a and person b sit in chairs opposite to each other. The task was to alternately tap on two assigned dots (start and target, diameter 8 mm) with a pen in hand. The dots were marked on a round table and each one was surrounded by a white area (diameter 60 mm). 38
3.4 Motion trajectory $\boldsymbol{x}(t) \in \mathbb{R}^3$ and projected trajectory $x(t) \in \mathbb{R}$ between the agent's start and target point. The origin O of the task space is set such, that $x(t)$ is zero-mean. 40
3.5 State-space trajectory of quasi-harmonic human hand movements. Normalized velocity is plotted against the normalized position. The counterclockwise evolving trajectories form approximately a closed curve of circular shape. The position x_{n} is reversed to obtain a phase θ increasing over time. 41

3.6 How did synchrony evolve? Visualization of synchronization as Lissajous plots of the hand position of person b relative to that of person a, accumulated in a heat map. Data are plotted separately for the conditions zero-cycle (ZC), quarter-cycle (QC) and half-cycle (HC) as well as for the first, third, sixth and ninth cycle. The dyads tend to synchronize already early in the trial. 43

3.7 Actual initial phase differences $\Phi_0 = \Phi(t = 0)$ over all trials for the conditions zero-cycle (ZC), quarter-cycle (QC) and half-cycle (HC), calculated with the spectral technique. Time $t = 0$ denotes the movement onset of the delayed person. Dashed lines indicate the phase relations triggered by the start off conditions. 44

3.8 Histograms of the relative phase difference Φ_r (a)-(c), and heat maps depicting the transients of Φ_r towards the respective attractor $\overline{\Phi_\mathrm{r}}$ (ordinate) (d)-(f), accumulating all trials in the three conditions. Brightness codes frequency. The plot is indexed by the phase θ_i of the delayed person (abscissa). Phases are obtained from the spectral technique. 45

3.9 Synchronization index SI for the conditions zero-cycle (ZC), quarter-cycle (QC) and half-cycle (HC), averaged over all trials. For comparison, the SI is calculated separately for the state-space, spectral and hybrid technique. The bars represent standard errors of the means. 47

3.10 Stability of the equilibrium points of the extended Kuramoto model. The phase difference between the two oscillators converges close to 0 (in-phase) or π (anti-phase) depending on the strength of coupling K and the frequency detuning $\Delta\omega$. 51

3.11 Phase difference $\Phi(t)$ derived from experimental data via the spectral technique and simulated by means of the parameterized model. The parameters [rad·s^{-1}] are $\Delta\omega$=-0.49 and K=0.41 at an RMSE$_\Phi$=0.23. 53

4.1 Limit cycle γ of an exemplary cyclic state trajectory $\boldsymbol{\xi}(t)$ in its state space with $n = 3$. If γ is cyclic, yet not closed exactly, the period T is determined by the return time of $\boldsymbol{\xi}$ to the Poincaré secant surface S. 65

4.2 (a) Exemplary limit cycle γ with the state $\boldsymbol{\xi} = [\, x \;\; \dot{x}\,]^\mathrm{T}$ and $L = 3$ primitives. The segmentation points $\boldsymbol{\xi}_i$ are given by the intersection of γ with the abscissa. (b) The corresponding events $t_{l,1}$, primitive durations $T_{l,1}$ and the uniformly growing phase θ depicted for period $i = 1$. 66

4.3 Modes between harmonic oscillations: Phase synchronization resulting in in-phase or anti-phase relations comes about with event synchronization with respect to the segmentation points $\boldsymbol{\xi}_1^{\mathrm{a/b}}$ and $\boldsymbol{\xi}_2^{\mathrm{a/b}}$. (a) Motion trajectories $x^{\mathrm{a/b}}(t)$ illustrating the temporal relation. (b) Their limit cycle representations $\gamma^{\mathrm{a/b}}$ in a position-velocity state space, illustrating the phase difference. 69

4.4 (a) Exemplary limit cycles $\gamma^{a/b}$ with $L^a = 2$ and $L^b = 3$ primitives in position-velocity state spaces. The evolution of the events in $\gamma^{a/b}$, (b) without synchronization, (c) for synchronization of the events (t_0^a, t_0^b) as achieved by phase synchronization, (d) for additional synchronization of (t_1^a, t_2^b). The shaded areas indicate the time span Δt defining event synchronization. . . 70

4.5 R.h.s. terms of an exemplary phase difference dynamics (4.12) over $\Phi \in [0, 2\pi]$. The intersection points of the graphs of $\Delta\omega$ and $-H(\Phi)$ denote the equilibria with $\dot{\Phi} = 0$. The vector field is illustrated on the abscissa. 72

4.6 Circular illustration of the synchronization problem between the exemplary limit cycles γ^a (inner circle) and γ^b (outer circle) introduced in Figure 4.4. (a) The DoF available for synchronization: The periods $T^{a/b}$ and the phase difference Φ are both governed by the process (3.11). Additionally, the relative primitive durations $\boldsymbol{d}^{a/b}$ are governed by the process (4.14). (b) Perfect synchronization of the event pairs (t_0^a, t_0^b) and (t_1^a, t_2^b), leading to coincident circles and events. 73

4.7 (a) Exemplary evolution of the predicted event $\hat{t}_{0,i+1}$ over time t. (b) Corresponding evolution of the phase $\hat{\theta}$ obtained from (4.24). The slope of $\hat{\theta}$ instantaneously relates the left over phase $2\pi i - \hat{\theta} \geq 0$ in period i to the left over time span $\hat{t}_{0,i+1} - t > 0$. Black dots denote boundary conditions. Gray graphs depict perfect prediction and the corresponding harmonic phase respectively. 76

4.8 (a) Family of $R = 4$ limit cycles γ^r with differing periods T^r. In the position-velocity state space, shapes differ due to $\dot{x}$ scaling with T^r. (b) Close-up illustrating distance-based classification *(top)*. Events are predicted based on the previously acquired evolution of events in γ^{r*} *(bottom)*. 77

4.9 Transformation of the process variables $\theta, \boldsymbol{d}$ into a limit cycle with $L = 3$ primitives μ_l, employing the minimum-jerk movement model. (a) Piecewise-continuous substitutions h_l illustrated for the unperturbed phase with $\dot{\theta} = const.$ (gray graph) and $\boldsymbol{d} = const.$ (b) Continuous, cyclic movement trajectory composed by polynomials f_l. For the corresponding limit cycle representation, cf. γ^b in Figure 4.4a. 79

4.10 The joint action task designed for the human-robot synchronization experiment. In a symmetric setup, both human and robot perform slightly different action tasks while facing each other. Odd-indexed primitives μ_l consider dwell times, even-indexed ones denote movements. Target points are marked by circles of 115 mm in diameter. 81

4.11 (a) The evolution of events for the experimental task, with the relative durations d_l corresponding to the primitives μ_l in Figure 4.10. Again, odd-indexed durations are due to expected dwell times in the segmentation points. (b) The cycle γ^R synchronized to γ^H in three different modes, denoted mode 1-3. Vertical dashed lines indicate synchronized events. Intuitively speaking, the human precedes the robot in mode 2 and vice versa in mode 3. 82

4.12 The vector field function H designed by continuous concatenation of sine periods between the stable equilibrium points according to Table 4.1. Vertical dashed lines separate the regions of attraction for the case of equal frequencies $\Delta\omega = 0$ and define the active mode $m = 1, 2, 3$. The plot is parameterized by unit amplitude and $\boldsymbol{d}^{\mathrm{R}} = [0.05\ 0.25\ 0.05\ 0.4\ 0.05\ 0.2]^{\mathrm{T}}$. . 83
4.13 Phase plot of the family of reference limit cycles with equally distributed phase velocities $\dot{\theta} \in [1, 2]$ rads^{-1}. Positions are expressed in the table-centered frame, which is aligned to the frame in Figure 4.10. The relative primitive durations are set $\boldsymbol{d}_0 = [0.05\ 0.2\ 0.05\ 0.16\ 0.05\ 0.22\ 0.05\ 0.22]^{\mathrm{T}}$. Those and the segmentation points denoted by filled dots are mean values, which resemble the observations made from pilot trials with a human experimenter. 84
4.14 Cyclic effector path of the robot obtained from the minimum-jerk model and expressed in robot coordinates. Filled dots denote segmentation points, open dots denote via points with relative elevation of 0.05 m above the xy-plane. 84
4.15 The experimental setup and scenario of a prototypical joint pick and place task *(left)*. Hand movements are made available to the robot in real time by tracking the glove the human interaction partner is wearing *(right)*. . . 85
4.16 The mode-related asynchrony MASYN averaged separately over all trials for the three start-off modes under the conditions NOS and PES. The bars represent standard errors of the means. 90
4.17 Evolution of selected process variables in a sample trial under condition PES and start-off mode 3. Vertical solid lines denote mode switches. 96
4.18 Relative amount of time spent in each mode and relative amount of mode switches, both averaged separately over all trials for the three start-off modes under the conditions NOS and PES. 97
4.19 Relative frequencies of occurrence of the relative phase difference Φ_{r} under the conditions NOS and PES *(left panel)*, and relative frequency of occurrence of the attracted equilibrium phase differences $\Phi_{\mathrm{r,e}}$ under PES *(right panel)*. 97
4.20 Entrainment measures averaged separately over all trials for the three start-off modes under the conditions NOS and PES. The bars represent standard errors of the mean. 98
4.21 The evolution of the instantaneous phase estimation for the first half of the sample trial. 98

5.1 Conceptual overview: Two agents cooperatively manipulates a common object according to a shared plan. Both agents employ an inverse object model and impedance control loop (a) generating desired object-centered wrenches (b). The effort-role behavior determines the control inputs applied at the agents' grasp points (c), which compose the object-centered wrench (d) required for configuration tracking of the object. Later, a scheme to allocate the agents' roles based on mutual feedback of the control inputs will be developed. 104

5.2 Cooperative manipulation of a rigid object by multiple agents acting at different grasp points. 107
5.3 Illustration of the input decomposition in a one-dimensional redundant task. (a) Minimum-norm solution for $\tilde{\boldsymbol{u}} = [\tilde{u}_1 \;\; \tilde{u}_2]^{\mathrm{T}}$. (b) Possible, but inefficient solution causing an internal wrench. 109
5.4 Illustrative scenario of planar cooperative manipulation: One human *(left)* and one robot *(right)* jointly move a bulky object in the x-y-plane. 110
5.5 Given exemplary external wrench realized by three different effort sharing policies. 113
5.6 The interaction control scheme deployed to investigate static role behavior. The human partner is supposed to track the common desired trajectory $\boldsymbol{x}_{c,\mathrm{d}}$. 114
5.7 Exemplary reference trajectory $\boldsymbol{x}_{c,\mathrm{d}}(\tau)$ and actual configuration $\boldsymbol{x}_c$, with (a) the desired configuration $\boldsymbol{x}_{c,\mathrm{d}}(\tau^*)$ obtained from reference adaptation, and (b) possible desired configuration $\boldsymbol{x}_{c,\mathrm{d}}(\tau = t)$ resulting from replay over time t. 115
5.8 Case study within the planar dyadic scenario, considering the task of purely translational object transfer in the redundant direction y^C. Any deviations in path direction $\Delta x_{c,y}$ vanish due to reference adaptation. 117
5.9 Case study from Figure 5.8 for deviations in the non-redundant DoF $\Delta x_{c,\phi}$ and $\Delta x_{c,x}$ from the desired configuration $\boldsymbol{x}_{c,\mathrm{d}}(\tau^*)$ (gray silhouette). The deviations remain for cooperative compensation by object-centered impedance control. 119
5.10 Screen shot of the virtual environment used for the planar transport task. . 119
5.11 Mean and standard deviation of the root-mean-square error of the wrenches applied by the human partner. Components x, y are expressed in the object frame C. 121
5.12 Mean and standard deviation of the root-mean-square error of the configuration. Components x, y are expressed in the object frame C. 122
5.13 Evolutions of the policy parameter $\alpha(t)$ simulated for an artificial profile of the human wrench component $\hat{u}^C_{1,y}(t)$. In the example, the robot expects a wrench component $\tilde{u}^C_{1,y} > 0$ from the human, hence $\hat{u}^C_{1,y} \geq 0$ denotes agreement and lets α gradually rise. 129
5.14 Overall interaction control scheme embedding the dynamic effort-role behavior. 131
5.15 Prototypical scenario of cooperative object manipulation and experimental setup: A human-robot dyad jointly transporting a bulky table. 132
5.16 Cooperatively manipulated table equipped with a handle and wrench sensor for the human *(left side)* and a grasp flange for the robot *(right side)*. The grasp points were at a height of 0.92 m over ground. 133
5.17 Bird's eye view of the lab area used in the experiment with four designated parking configurations of the table $\boldsymbol{x}_{c,i}$. The outer box represents the boundaries of the environment spanning a square of approximately $8\,\mathrm{m} \times 8\,\mathrm{m}$. Gray regions are occupied by obstacles. The dotted curves represent the paths $\boldsymbol{x}_{c,i}(\tau)$ connecting the parking configurations. 134

5.18 Average task completion times. The bars represent standard errors of the means. 137
5.19 The averaged measures of physical effort under each condition. The bars represent standard errors of the means. 138
5.20 The amount of disagreement averaged over all trials under each condition. The bars represent standard errors of the means. 138
5.21 Sample trials under the condition WPRA *(top panel)* and DPRA *(bottom panel)*: Evolution of the policy parameter $\alpha(t)$ depending on the human wrench component $\hat{u}^C_{1,y}(t)$. Vertical bold lines separate the four task segments. 139
5.22 Frequency distribution of the policy parameter α over all trials under the condition WPRA *(top panel)* and DPRA *(bottom panel)*. 140
5.23 Means of the subjective measures in each condition. The bars represent standard errors of the means. 141

A.1 The two DoF VR system used in the experiment described in Section 5.3.3. 149
A.2 The human-sized mobile robot used in the experiments described in Section 4.3 and Section 5.5. 150

B.1 Haptic rendering of a virtual environment by an admittance-type control scheme. In addition to the object dynamics, the integration of an artificial partner and environmental constraints is illustrated as well. 153

List of Tables

3.1 Means of estimated model parameters [rad·s^{-1}], mean RMSE$_\Phi$ assessing model fit and number of trials N_s with stable parameter sets. Means are taken over 294 valid trials, standard deviations are taken over dyads. . . . 53
3.2 Results of the trial-wise regression: R^2 represents the percentage of the variance explained by the model, N_v is the number of valid trials included into analysis for the respective condition, and $N_{p<.001}$ lists the number of significant model fits. 54

4.1 Stable equilibrium relations of the implemented synchronization process. . 82

Notations

Abbreviations

ANOVA	analysis of variance
CPG	central pattern generator
DoF	degree(s) of freedom
HHI	human-human interaction
HRI	human-robot interaction
LED	light emitting diode
PD	proportional-derivative
PEM	prediction-error method
pHRI	physical human-robot interaction
SMS	sensorimotor synchronization
TLX	task load index
VR	virtual reality

Experimental Conditions

ZC	partners triggered with zero-cycle difference
QC	partners triggered with quarter-cycle difference
HC	partners triggered with half-cycle difference
NOS	no synchronization behavior of the robot
PES	phase and event synchronization behavior of the robot
MIN	minimum robot effort
BAL	balanced effort of the partners
MAX	maximum robot effort
CRA	constant role allocation of the robot
WPRA	weighted proactive role allocation of the robot
DPRA	discrete proactive role allocation of the robot

Conventions

Scalars are denoted by upper and lower case letters in italic type. *Vectors* are denoted by bold lower case letters in italic type. *Matrices* are denoted by bold upper case letters in italic type.

x or X	scalar
$\boldsymbol{x}$	vector
$\boldsymbol{X}$	matrix
$\boldsymbol{X}^{\mathrm{T}}$	transposed of $\boldsymbol{X}$
$\boldsymbol{X}^{-1}$	inverse of $\boldsymbol{X}$
$\boldsymbol{X}^{+}$	pseudoinverse of $\boldsymbol{X}$
$\mathrm{Ker}(\boldsymbol{X})$	kernel of $\boldsymbol{X}$
$\dim(\boldsymbol{x})$	dimension of $\boldsymbol{x}$
$\boldsymbol{I}$	identity
$f(\cdot)$	scalar function
$\boldsymbol{f}(\cdot)$	vector function
$\hat{x}$	estimated or predicted value of x
$\overline{x}$	average value of x
x^{*}	optimal value of x
x'	specific value of x
$\Delta(\cdot)$	difference value
$\dot{x}, \ddot{x}$	first, second time derivative of x
$\|\cdot\|$	Euclidean norm

Subscripts and Superscripts

$(\cdot)_0$	initial value at time $t = 0$
$(\cdot)_{\mathrm{d}}$	desired value
$(\cdot)_{\mathrm{e}}$	equilibrium value
$(\cdot)_{\mathrm{l}}$	lower bound value
$(\cdot)_{\mathrm{m}}$	measured value
$(\cdot)_{\mathrm{n}}$	normalized value
$(\cdot)_{\mathrm{u}}$	upper bound value
$(\cdot)_{\mathrm{r}}$	relative value
$(\cdot)_{\mathrm{th}}$	threshold value
$(\cdot)_{x,y}$	translational component in x, y-direction
$(\cdot)_{\phi}$	rotational component
$(\cdot)^{\mathrm{a}}$	associated with agent a
$(\cdot)^{\mathrm{b}}$	associated with agent b
$(\cdot)^{\mathrm{H}}$	associated with human agent
$(\cdot)^{\mathrm{R}}$	associated with robotic agent
$(\cdot)^{C}$	expressed in object frame C
$(\cdot)^{R}$	expressed in robot frame R

Symbols

Unless otherwise denoted:

$\boldsymbol{A}$	decomposition matrix
$\boldsymbol{B}_i$	wrench basis of ith agent
c	blending function
c_f	force scaling function
$\boldsymbol{C}^{(\cdot)}$	coupling function
$\mathbb{C}$	complex numbers
d_l	relative duration of lth primitive
$\boldsymbol{d}$	vector of relative primitive durations
$\boldsymbol{D}_r$	robot damping matrix
$e_{(\cdot)}$	error component
$\boldsymbol{f}$	movement model
$\boldsymbol{f}(\cdot)$	friction and gravitation
$\boldsymbol{f}_c(\cdot)$	object friction and gravitation
$F(a, b)$	value of F-statistic. a, b: DoF of variance
$\boldsymbol{F}^{(\cdot)}$	autonomous dynamics
g	polynomial function
$\boldsymbol{G}_i$	partial grasp matrix of ith agent
$\boldsymbol{G}$	complete grasp matrix
h_l	lth substitution function
H	vector field function
i	period index
$\boldsymbol{J}$	manipulator Jacobian
K	Kuramoto coupling strength
$\boldsymbol{K}$	feedback matrix
$K_{(\cdot)}$	control gain
$\boldsymbol{K}_d$	damping matrix, derivative gain
$\boldsymbol{K}_p$	stiffness matrix, proportional gain
L	number of primitives
m	synchronization mode
$\boldsymbol{M}$	lumped mass matrix
$\boldsymbol{M}_c$	object mass matrix
$\boldsymbol{M}_r$	robot mass matrix
$\mathbb{N}$	natural numbers
N_s	number of trials with stable attractors
N_v	number of valid trials
p	probability of test statistic if null-hypothesis is assumed
$\boldsymbol{q}$	manipulator joint configuration
$\boldsymbol{Q}$	weighing matrix
$\boldsymbol{r}_{(\cdot)}$	grasp constraint vector
$\boldsymbol{R}$	rotation matrix
$\mathbb{R}$	real numbers

s_l	lth scaling function
t	time
t_j	discrete time index
$t_{l,i}$	lth event in ith period
$t(a)$	value of t-statistic. a: DoF
T	period
$T_{l,i}$	duration of lth primitive in ith period
${}^I\boldsymbol{T}_R$	homogeneous transform from frame R to I
u_I	interactive force
$\boldsymbol{u}$	input wrench
$\boldsymbol{u}_c$	external object wrench
$\boldsymbol{u}_i$	input wrench of ith agent
$\tilde{\boldsymbol{u}}$	applied wrench
$\tilde{\boldsymbol{u}}_i$	applied wrench of ith agent
$\tilde{\boldsymbol{u}}_{\text{bal}}$	min-norm applied wrench
$\boldsymbol{u}_{c,\text{dyn}}$	dynamics-generated external object wrench
$\boldsymbol{u}_{c,\text{imp}}$	impedance-generated external object wrench
$\boldsymbol{u}_{y,\text{agr}}$	agreement wrench threshold
V	potential function
w	manipulability
x	position
$\dot{x}$	velocity
$\boldsymbol{x}$	effector configuration
$\boldsymbol{x}_\text{b}$	base configuration
$\boldsymbol{x}_c$	object configuration
$\boldsymbol{x}_{c,i}$	ith object goal configuration
$\boldsymbol{x}_i$	grasp point of ith agent
y	Cartesian position component
α	policy parameter
α_dis	discrete policy parameter
γ	limit cycle
Δt_p	processing delay
$\Delta\omega$	frequency detuning
ζ	analytic signal
η	perturbation
θ	phase
λ_j	jth kernel vector parameter
μ_l	lth primitive
ξ	agreement function
$\boldsymbol{\xi}$	state vector
$\boldsymbol{\xi}_l$	lth segmentation point
$\boldsymbol{\Xi}$	set of segmentation points
$\pi_{(\cdot)}$	effort sharing policy

τ	temporal parameter
$\tau_{(\cdot)}$	time constant
ϕ	rotation angle
$\boldsymbol{\phi}_i$	kinematic grasp constraint of ith agent
Φ	phase difference
χl	lth normalized parameter
ω	natural frequency

Measures

AD	amount of disagreement
ASYN	asynchrony
AW_i	accumulated work of ith agent
$\mathrm{AW}_{\mathrm{table}}$	accumulated work conducted on table
CT	completion time
CV	circular variance
MASYN	mode-related asynchrony
MSI	mode-related synchronization index
R^2	coefficient of determination
$\mathrm{RMSE}_{(\cdot)}$	root-mean-square error
$\mathrm{SD}_{(\cdot)}$	standard deviation
SI	synchronization index

1 Introduction

Nowadays, robots are no longer confined to classical manufacturing settings, where they execute pre-planned tasks in highly structured environments. Abolishing the strict separation of the human and the robotic workspaces, novel application scenarios envisage robots as capable assistants and partners, that unburden humans in real-world settings. Robotic assistants could contribute to various activities of daily living, cooperate shoulder to shoulder with human workers in flexible manufacturing settings or perform physical training with rehabilitation patients. These examples—we will detail the application scenarios further in the following section—involve motor actions, that could be beneficially performed by robots jointly with humans in shared workspaces. Performing action tasks in typically unstructured surroundings requires adaptive and flexible motor capabilities. In general, the interactive motor behavior of a robot describes the functional relationship, how actions are taken in response to environmental stimuli, e.g. the behavior resulting from a motor skill that allows to visually track and dynamically catch a ball. This thesis focuses on the specific demands on the interactive motor behavior that are related to human-robot interaction (HRI), i.e. action taking in response to and in coordination with human partners. Designing robots as capable partners is fundamentally different from considering them merely as tools. An active contribution towards the task goals requires robots to generate their own action plans by means of autonomous capabilities. Interactive motor behaviors need to allow efficient and intuitive negotiation of the partners' individual intentions, in order to impose a commonly shared action plan. Furthermore, close and enduring contact between humans and robots requires the interactive behavior of robots to be socially compatible, in order to be accepted as companions [13, 21]. Besides the communication through speech, facial expressions and gestures, humans are known to employ efficient coordination mechanisms to successfully perform motor tasks in joint action [158]. Those mechanisms include mutual task representations, performance monitoring and action prediction based on the common coding of perception and action. Capturing the behavioral features of human-human interaction (HHI) into mathematical models in a first step, and employing these models to develop robotic partners in a second step, is considered a promising approach to successfully enable HRI in the novel field of joint motor action.

Currently, both explicit models of the interactive motor behavior between humans and human-oriented behavioral models enabling natural and bidirectional motor interaction of robots with humans are missing. Therefore, this dissertation proposes a holistic and interdisciplinary methodology to systematically analyze and synthesize interactive motor behaviors for close human-robot joint action. The ultimate goal is *seamless interaction* in human-robot teams, i.e. replacing one partner in a human team by a robotic partner does not degrade the interaction, both in terms of human sensation and task performance.

Fig. 1.1: Exemplary scenario of close joint action: Cooperative assembly during car restoration.

1.1 Applications

This work is motivated by the variety of real-world applications, in which robot assistants and companions are engaging in close joint action with humans. Remarkably, those target scenarios differ substantially from classical industrial applications of robots, where the workspaces of humans and robots are strictly separated. Representatives scenarios of joint motor action in different domains shall be reviewed and outlined in the following:

- *Service domain.* The activities of daily living provide many applications for service robots to unburden humans, e.g. during household chores, care taking and shopping. Physical assistants that help humans moving furniture and fixtures, such as tables and boxes, are developed [59, 80, 82]. Closely related, personal robots are designed to enable elderly or disabled people an independent life, by assisting in various tasks such as cooking, serving drinks, setting tables, or providing walking aids [11, 55]. In search and rescue scenarios, physical cooperation of mixed human-robot teams is essential, where robots are contributing through their complementary capabilities [110].

- *Manufacturing domain.* Assembly tasks in highly flexible manufacturing settings may benefit from human-robot joint action. The collaborative mounting of a windshield is investigated in [189]. In a similar scenario, an autonomous mobile robot actively assists a human worker mounting a bulky steel bumper onto a car [199], see Figure 1.1. The application of robotic helpers on construction sites is investigated as well, in order to cooperatively and flexibly handle heavy construction material [92].

- *Medical domain.* Applications of robotic devices for the therapy of motor diseases, e.g. originated from a stroke, are experiencing attention [58]. Various supporting behaviors for physical rehabilitation training are investigated, with the therapy being adapted to the patients' individual needs [83]. There, haptic interaction is often performed through virtual environments.

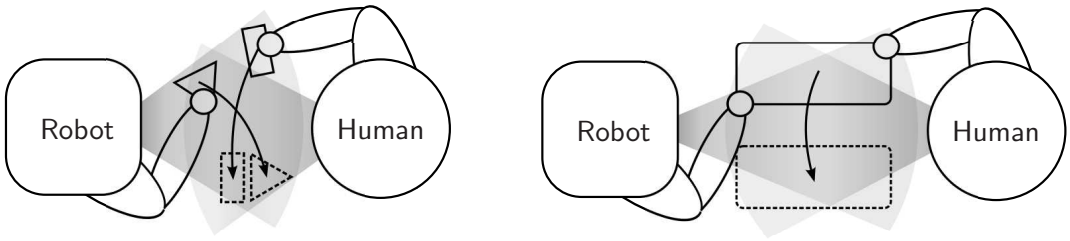

Fig. 1.2: Investigated classes of joint motor action: Visual coordination with individual goals *(left)* and visual-haptic cooperation towards a shared goal *(right)*.

- *Entertainment domain.* Human-robot dancing is a popular paradigm of pHRI that has been studied repeatedly [62, 80]. Rhythmic behavior in response to music or partners is believed to be an essential component of natural social interaction [106]. Similarly, natural interaction through hand-shaking [184] serves as further example of rhythmic joint action. Finally, the development of interactive robotic toys gains attraction [140].

All of the examples—which are by no means complete—involve close joint action between humans and robots in social settings. The successful and seamless integration of robots in such scenarios demands for a human-oriented design of their interactive behavior.

1.2 Problem Definition

From the above applications, we extract the key features that close joint action shall be confined to within this work. Whereas the coordination and organization of heterogeneous teams composed by multiple robots and humans raises further challenges [159, 190], we investigate close joint action of *human-robot dyads* as the elementary problem. The typical setting is commonly characterized by neighboring or overlapping workspaces of the partners, and potentially by a physical coupling between the partners. The physical coupling is established either directly or through a jointly manipulated object. This problem setting is covered well by two selected joint action paradigms, that will be deployed to analyze, model and design interactive motor behaviors, see Figure 1.2. In the following, joint motor action is structured in three major dimensions. Those are the negotiation level of interaction, the form of interaction and the involved sensory modalities.

In her framework on human-human haptic collaboration, Groten [47] proposes to distinguish two levels of collaboration under the assumption of a dyadic movement task. This two-level structure shall be adopted to confine the addressed problem setting. The higher or *decisive* level is referred to as the negotiation process on *where* to move. Here, the partners integrate e.g. differing individual movement paths, action sequences, or task goals into a commonly shared intention. On the lower or *executive* level, the partners are assumed to negotiate on *how* to move. Here, the partners agree e.g. on the timing and effort put into their actions to jointly accomplish the task. Though we are aware that negotiation may take place on both levels of interaction simultaneously, the task goals are assumed to be already negotiated successfully on the decisive level. Hence, we investigate and design interactive motor behavior on the executive level.

Parker [120] distinguishes four common forms of interaction, which are collective, cooperative, collaborative and coordinative. From those, *coordinative* and *cooperative* interaction are of particular interest, as both imply the partners being aware of each other. While the former refers to agents that work towards individual goals without interfering each other, the latter assumes the agents to work towards a shared goal such, that they benefit from each other.

Though the interactive motor behavior of humans is usually mediated by a wealth of combinations among the available sensory modalities, we confine the targeted scenarios to interaction through the *visual* and the *haptic* modality, more precisely its kinesthetic part. As those are considered as the essential enablers of close joint action, they are investigated first before another modality, such as verbal communication, is added. The informational coupling of the partners is established through visual feedback in non-contact tasks, and through visual-haptic feedback in contact tasks.

1.3 Challenges

Integrating knowledge from different disciplines, namely human behavioral science, experimental psychology, system theory and robotics poses the overall challenge of this work. As research tends to be conducted separately in these disciplines, holistic methodological concepts on the design of interactive behavior are missing. From the problem setting sketched above, we derive the concrete challenges towards the ultimate goal of seamless HRI.

Joint motor action is characterized by *instantaneous negotiation and reaction*. Scenarios of visual coordination, as the one in Figure 1.2 left, require the agents to instantaneously adjust their actions in response to each other, in order to avoid collisions and to support a smooth work flow. Scenarios of physical cooperation, as illustrated in Figure 1.2 right, additionally involve the simultaneous exchange of physical energy and information. This bidirectional exchange is unique to the haptic modality. The distribution of the physical effort arising from contact tasks needs to be negotiated instantaneously and continuously among the agents.

Consequently, robots cannot be successfully deployed in joint action by following a purely task-oriented design rationale. Instead, human factors and habits have to be incorporated early in the design process. However, only fragments of principal knowledge exist so far, while models of human behavior with applicability to technical systems are rare. Therefore, the first step to acquire such models is to *scientifically investigate the interactive behavior between humans*, which implies the design of psychological experiments. In a next step, *mathematical descriptions* have to be developed to model the purposeful regularities and variabilities of the human interactive behavior. Importantly, identification techniques and experiments need to be co-designed to obtain valuable and quantitative modeling results.

Inspired by system-theoretic considerations, human behavioral principles and models, interactive behavior for robotic agents can then be synthesized. Since we are lacking comprehensive and validated human models, the developed concepts can neither be proved to be optimal solely on a theoretic basis, nor reliably evaluated through pure simulation. Instead, the *prototyping of robotic agents* and the *implementation of interactive behavior*

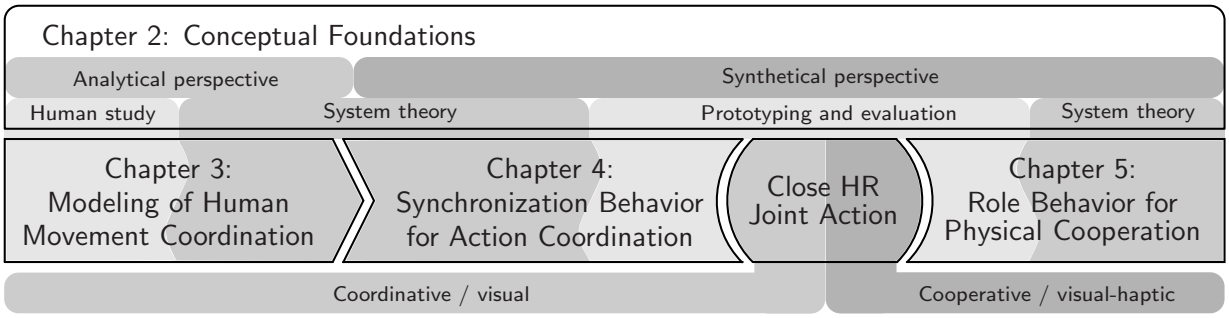

Fig. 1.3: The thesis aims to realize seamless HRI in close joint action tasks.

initially serves the proof of concept. The realistic embodiment of interactive behavior by means of humanoid or anthropomorphic robots poses a challenge by itself, which is due to the limitations of state-of-the-art technical systems.

Finally, the resulting *interactive behavior of the human and the robotic prototype* has to be systematically evaluated. Again, psychological experiments with human participants need to be designed, in order to rate the quality of the developed concepts and to draw conclusions on future re-designs.

1.4 Main Contributions and Outline

This thesis proposes an interdisciplinary methodology to design the interactive motor behavior of robots, that are capable of joint action in coordination and cooperation with human partners. In brief, the following main contributions are distinguished:

- Co-design of system-theoretic modeling concepts, robotic prototypes and psychological experiments for a profound analysis and evaluation of HHI and HRI throughout this work
- Novel modeling and identification concept of natural human-human coordinative behavior based on the synchronization dynamics of coupled oscillators. This work is published in [196, 198, 201].
- Synthesis of advanced motor coordination capabilities within the synchronization concept and experimental evidence of their efficacy in human-robot joint action. This work is published in [197, 202].
- Effort sharing concept derived from system-theoretic modeling of non-point-mass cooperative manipulation and interactive strategies for dynamic role allocation. This work is published in [194, 195, 199, 200].

These contributions address the above key challenges towards close human-robot joint action. The methodological concept builds on two fundamental approaches, which are the analytical and the synthetical design perspective. These perspectives guide the structure of the thesis, which is illustrated in Figure 1.3. The application in two representative scenarios of coordinative, visual interaction and cooperative, visual-haptic interaction illustrates the

efficacy and potentials of the proposed design methodology. In the following, a more detailed summary of the contributions is given in the form of an outline of the thesis.

The *conceptual foundations* of this thesis are introduced in Chapter 2. After a definition of the requirements on seamless interaction, the design methodology is introduced, which comprises the analytical and the synthetical perspective. The reader is then familiarized with the system-theoretic foundations required for modeling and identification. After a discussion of important aspects regarding the design and the evaluation of human-human and human-robot experiments, the technical foundations required for prototyping of robotic partners are laid.

Movement coordination plays an important role in the interactive behavior of humans, especially when performing actions together in shared workspaces. During repetitive action, a frequently observed phenomenon is movement synchronization, which refers to a bounded temporal relationship between the moving entities. In Chapter 3, spontaneous synchronization is experimentally evidenced to emerge even during a goal-directed movement task in a novel paradigm of rhythmic HHI. *Modeling of human movement coordination* in co-design with the experimental study reveals the coordination dynamics among human dyads to be replicated successfully by the synchronization of coupled oscillators. The identification technique is based on the natural response dynamics to an initial excitation; it is innovative in the context of HHI, since it allows to quantitatively describe the unbiased interactive behavior. The developed behavioral model is ready for the implementation of interactive robotic behavior.

The behavioral model derived from the analytical perspective on human movement coordination bootstraps the design of *synchronization behavior for action coordination* with artificial partners in Chapter 4. Since action coordination through synchronization is found to be key to the social interaction between humans, its potentials to enhance the interaction repertoire of robots is investigated. Starting from limit cycle representations of mixed continuous and discrete repetitive actions, a synchronization concept is developed, which synchronizes arbitrary limit cycle pairs in a variety of enhanced synchronization modes. The novelty of this concept stems from the unified entrainment dynamics, which achieves both continuous phase and discrete event synchronization simultaneously. The experimental study of human-robot action coordination serves the proof of concept and highlights the strong potentials to foster seamless HRI.

Many joint action tasks require the physical cooperation of two or more partners to be successfully accomplished, e.g. the transport of a heavy and bulky object to a desired goal configuration. Humans manage to intuitively negotiate their contributions in such situations through self-organized and temporarily consistent patterns of haptic interaction. The design of interactive *role behavior for physical cooperation* of robotic assistants with human partners is addressed in Chapter 5. In an approach that is novel in the context of pHRI, the cooperative manipulation problem is geometrically decomposed to reveal the input redundancies. In a first step, meaningful policies for physical effort sharing among cooperating dyads are derived, that exploit these redundancies and render static role behavior. Based on those policies, a set of strategies for dynamic role allocation by means of haptic feedback from the human is synthesized. The static and the dynamic role behavior of artificial partners is extensively evaluated in both a VR and an immersive

full-scale pHRI scenario.

Chapter 6 provides the *overall conclusions and future directions* derived from the proposed design methodology and the presented applications. The insights gained from passing the design process for the two different scenarios and interaction types are put together, and the impact on the field of human-robot joint action is outlined. The thesis finishes with an identification of promising directions for future research, which may further advance the interactive motor behavior of robotic partners.

2 Conceptual Foundations

The methodological concept and the fundamental knowledge required in each step of the design process shall be introduced in this chapter, before interactive behavior is analyzed and synthesized in the selected scenarios of coordination and cooperation in the Chapters 3-5. Aiming at the ultimate goal of seamless HRI in close joint action tasks, a holistic methodology on the design of interactive behavior for robotic agents is proposed in Section 2.1. Based on the requirements on joint motor action with human partners, two paths in the design process are separated. Depending on how well the targeted application domain is covered by existing knowledge on human interactive behavior, either the analytical or the synthetical perspective is pursued. Via the analysis of HHI, human behavioral models are developed first in the former. In the latter, those and other existing models of human behavior are integrated in the synthesis process. The system theoretic foundations that both perspectives rely on are introduced in Section 2.2. Those encompass dynamical systems and their specific application to model the perception-action behavior of agents, which is called behavioral dynamics. A basic background on system identification is provided along with a particular technique on the parameter identification of dynamical system models, that is of practical relevance for the identification of a human behavioral model later in this work. The design methodology involves both HHI and HRI experimental studies, in which the interactive behavior of humans is observed and evaluated. In Section 2.3, the basics of psychological experiments are treated, which include design aspects specific to joint motor action and considerations on the selection of the interaction scenario. Both behavioral and subjective measures suitable for analysis and evaluation in the context of joint motor action are discussed as well. The synthesis of interactive behavior inevitably involves the implementation of robotic prototypes. Those are either physically embodied agents in real interaction scenarios, or virtual agents in computerized environments.[1] For a mobile manipulator representing an anthropomorphic interaction partner, the relevant control schemes for compliant motion tracking, force control and manipulator-base coordination are presented in Section 2.4. The chapter is finalized by a short summary of the introduced concepts and prerequisites in Section 2.5, such that the reader is prepared to their application in the concrete problem settings this work is tackling.

2.1 Design Methodology

First of all, a number of essential properties of seamless joint action are identified, and posed as general requirements for the design of interactive behavior. These requirements, together with the challenges derived in Section 1.3, give rise to two complementing perspectives in

[1] The technical foundations required for visual-haptic rendering of virtual interaction scenarios are found in Appendix B.

the design methodology, which we detail thereafter along with related work on interactive motor behavior.

2.1.1 Requirements on Interactive Motor Behavior

Goal-Directedness

Robots actively contributing to joint action tasks need to be able to impose their own intentions or plans, as the human partner does. Since both partners naturally may have different intentions, they usually have to negotiate a common plan, which allows coordination or cooperation towards the task goals. The negotiation of intentions is crucial to accomplish joint action tasks. In favor of a clear focus of this work, it is assumed that the partners already share a common plan on the decisive level of interaction. However, on the executive level, the *compliance with an active, goal-directed contribution* of the robot needs to be ensured explicitly. Goal-directedness needs to be part of the design of interactive behavior, that is applicable beyond purely passive following and reacting.

Efficiency

Robots can only be deployed beneficially in joint action tasks, if they are able to utilize the available capabilities and resources of both the human and themselves reasonably regarding the task goals. Therefore, the interactive behavior needs to optimize *efficiency*, which means in many cases to keep the human effort in terms of motor actions or applied force, and also the time required for task completion as low as possible. For instance, during physical cooperation, the effort required for cooperative manipulation needs to be shared such, that unnecessary counteracting forces are avoided.

Intuitiveness

The interactive behavior of robots should meet human experiences and expectations. Through *intuitiveness*, cumbersome learning phases to accommodate to the robot are avoided or shortened. At the same time, the extra mental demand allocated due to interaction with the robotic partner is kept as low as possible. Instead, it is saved for joint task accomplishment, which relates to efficiency as well. The construct of intuitiveness is expected to be indirectly reflected in smooth and fluent interaction, where e.g. no hesitation and abrupt movements are observed. Here, predictability is considered to be strongly related, since reasoning on the partner's future behavior should be eased, if common knowledge applies and experiences are met.

Pleasure

Joint action tasks are affected by the social setting the partners are performing in. The interactive behavior of robots should convey the feeling of comfort and *pleasure* to the human partner. Positive emotions are expected to motivate and encourage the human to engage in the task, and thus, to foster efficiency as well. For instance, behavior may

appear threatening due to excessively fast or jerky movements. Intuitiveness is considered as a prerequisite of pleasure.

Safety

Safety is mandatory in the domain of close HR joint action and particularly in pHRI, yet it is not the main focus of this work. Advances in the mechanical design and the motor control of robots contribute to safety, see e.g. the work of Albu-Schäffer et al. [4] and Haddadin et al. [51]. Intuitiveness and predictability may significantly add to safe HRI as well. An overview on safety and dependability with a focus on pHRI is given in [23].

2.1.2 Two Design Perspectives

The methodological concept of this work builds on two design perspectives, which are denoted the *analytical* and the *synthetical perspective*. The analytical perspective aims at the analysis and the modeling of natural human behavior through the observation of how humans interact. This precursory step is shown to provide a profound entry point into the design process of interactive behavior for robots, if little is known about the corresponding human behavior [47]. The synthetical perspective directly aims at the design stage from a system-theoretic and engineering point of view, while existing principal knowledge and models of human behavior are integrated. Both perspectives rely on psychological experiments involving human participants. Notably, the design process may be run through iteratively, in order to converge to the desired quality of interactive behavior.

Analytical Perspective

Taking the human behavior as the optimal reference represents one possible path of the design process. The idea of this approach is based on the fundamental assumption that if the behavior of a robot is similar to that of a human partner in joint action, HRI should achieve evaluation results similar to HHI. Therefore, all the requirements defined in the previous section are derived from human joint action. However, it is not sufficient to purely replay recorded trajectories of e.g. motion and force. Instead, a deeper understanding of the functional relationship of behavioral variables and feedback mechanisms is required [62, 100, 183]. Investigating physical collaboration between humans and robots, this observation is also made by Reed et al. [134]. While a sample trajectory of human behavior replayed by the robot is not recognized by the participants to be artificial, the human interactive behavior specific to the collaboration with human partners is not observed for the artificial, static behavior. Capturing the human interactive behavior including its essential aspects of flexibility and adaptability is the key idea of the analytical perspective.

Human motor behavior is frequently modeled on an individual level, i.e. in settings where individuals interact through motor action with their environment, such as arm movements to reach objects or walking. From a behavioral viewpoint, a basic aspect of human movements is smoothness, an observation which is mathematically modeled by Flash and Hogan [36]. The principle of minimizing the jerk—the third derivative of the movement with respect to time—holds true for point-to-point hand movements. Indeed, this handy model

is employed frequently in HRI [20, 32]. A variety of further formulations of human motor behavior based on cost functions is investigated in the framework of optimal control, which may also include the feedback of environmental information in closed-loop optimization, see [170] for an excellent review. These optimization approaches highlight the property of human motor behavior to minimize both effort and error. The adaptation capability of human motor behavior reveals e.g. an optimal selection of impedance parameters with respect to the task demands [16]. Models comprising impedance control and inverse dynamics of the task are found to account for the observed adaptation processes of human motor behavior [38]. The inter-limb coordination of movements plays another important role in human motor behavior. Regarding its temporal aspect, Haken et al. [53] inspire a whole research community with their synchronization model, which explains the coordination of bi-manual finger tapping. Regardless of intra- or interpersonal coordination, the modeling approaches found in literature mainly focus on purely rhythmic behavior. More details on the topic are given in Section 3.1.

Some works investigate human-human motor behavior in joint action tasks. Yet, the results are mainly of principal nature, which is only of limited use in the design of interactive behavior. In a one DoF positioning task that is jointly performed by human dyads, Reed et al. [134] discover via time-series analysis temporarily consistent patterns in the force trajectories. Their results evidence in the form of principal knowledge, that the partners specialize to different aspect of the task, i.e. one partner takes over the acceleration, while the other takes over the deceleration. However, the underlying negotiation process leading to this phenomenon remains still unclear. Explicit behavioral modeling of HHI is conducted by Feth et al. [33]. The authors investigate a collaborative pursuit tracking task, in which the continuous reference trajectory of a jointly manipulated object is to be tracked. It is hypothesized that the dyadic tracking behavior can be represented by the same control-theoretic model structure, which is proposed for single person piloting [103]. Based on the time series of the tracking error and the sum of the applied forces recorded in their experiment, the controller parameters are identified and the behavioral model is successfully validated to extend to HHI.

Due to the manifold characteristics of human-human interactive behavior and their strong dependence on the joint action task, further studies are required to derive and identify human behavioral descriptions. The challenge is to represent these descriptions in the form of models, which are implementable to both predict and render human behavior when substituting a human partner by a robot. In contrast to sequential actions and turn taking, close joint action demands for bidirectional interaction models on fast and continuous time scales. An appropriate theoretical language for modeling provide dynamical systems, which are introduced in Section 2.2. The so-derived models provide a good starting point for the synthesis of advanced artificial behavior for HRI.

Synthetical Perspective

The second part of the design process is referred to as the synthesis of interactive behavior by utilizing knowledge from both system theory and human behavioral study. It has to be noted that the analytical perspective is a precursory step, which also leads to the synthesis stage later. After missing models of human behavior have been developed, those

are integrated into the design, cf. Figure 1.3. In the synthetical perspective, we consider as the starting point the development of a goal-directed model of the joint action task, which relates the task state of the contributing partners to their goals. Such an internal representation is congruent with the architecture of human joint action proposed by Vesper et al. [181]. Building a representation of the partner's task allows to assess the overall performance with respect to the task goals, and also the contribution of the partner. Such on-line performance or error assessment is referred to as a monitoring process in human joint action [181]. Specifically, the mutual dependencies of both partners' parts of the task are modeled. Those dependencies are introduced through the spatio-temporal constraints of e.g. joint object manipulation, object hand-overs, or intersections of the movement paths. As we demand from robotic partners to actively contribute towards the task goals, models of human interactive behavior have a twofold purpose: First, short-term predictions on future actions of the human partner are gained. Second, action taking of the robot is made predictable for the human partner. The simulation of others' actions by means of one's own motor system is considered an essential prediction mechanism in human joint action, which relies on the common coding of perceived and performed actions [157]. Another purposeful aspect of the interactive behavior observed during HHI is what is called coordination smoothers in [181]. For instance, movement variabilities lowered in joint action or the formation of stable movement patterns support coordination by introducing a common structure or pace to interaction. Adopting these aspects of human interactive behavior is considered key to successful human-robot joint action.

Many works in the field of HRI realize tool-like behaviors, which render the robot only to react to human commands. For instance, Takubo et al. [165] exploit for joint object manipulation the idea to render the behavior of a commonly known mechanism, i.e. that of a wheelbarrow. Other behaviors implement guiding rulers [141], ball casters [59], or helping hands for object positioning [189] or reaching [29]. Since modeling and predicting human behavior is a sophisticated endeavor, only recently research works begin to investigate both goal-directed and human-oriented interactive behaviors of robots. For instance, robotic assistance for physical joint action making use of human task knowledge is proposed in [199]. In a proof-of-concept implementation, an initially reactive robot is shown to build a combined model of both the human task-related behavior and the task through the observation of behavioral variables, which are the effector motion and the interaction force. Theoretical frameworks that render a variety of interactive role behaviors are developed in [31, 70, 104], ranging from passive follower to active leader behaviors. Though their applicability in realistic joint action scenarios is not fully proven yet, these approaches open up the perspective of capable robot partners. At the same time, they motivate the synthesis of interactive behaviors, that provide advanced coordination and cooperation skills for robots working with human partners towards shared task goals.

After the conceptual formulation of interaction models, the next step within the design process is the development and implementation of robotic prototypes. Similar to the early stage in the analytical perspective, the HRI behavior is assessed by means of psychological experiments in the final stage of the synthetical perspective. On the one hand, these HRI studies serve the proof of concept, as they aim to evidence the efficacy of the synthesized behavior in joint action. On the other hand, the tuning of the behavioral model in its

parameter space can be explored systematically, and the resulting HRI behavior can be evaluated regarding the set of experimental measures. As introduced later in Section 2.3.2, those may comprise e.g. task performance and physical effort measures.

2.2 System-Theoretic Foundations

2.2.1 Dynamical Systems

In this work, the agents' interactive behavior is phenomenologically described by systems relating the inputs, i.e. the perceived stimuli, to the observed outputs, i.e. the action responses. Dynamical systems are introduced to capture the dynamic relations of both the behavior of humans in the analytical perspective, and the behavior of artificial agents in the synthetical perspective.

State-Space Formulation

Among the existing formulations of dynamical systems, only the generic state-space formulation based on ordinary differential equations is considered here. We assume that the system behavior is modeled by the set of *first-order differential equations*

$$\begin{aligned}
\dot{\xi}_1(t) &= F_1\left(\xi_1(t), \xi_2(t), \ldots, \xi_n(t),\, u_1(t), u_2(t), \ldots, u_m(t),\, t\right) \\
\dot{\xi}_2(t) &= F_2\left(\xi_1(t), \xi_2(t), \ldots, \xi_n(t),\, u_1(t), u_2(t), \ldots, u_m(t),\, t\right) \\
&\vdots \\
\dot{\xi}_n(t) &= F_n\left(\xi_1(t), \xi_2(t), \ldots, \xi_n(t),\, u_1(t), u_2(t), \ldots, u_m(t),\, t\right),
\end{aligned} \tag{2.1}$$

which are also called the equations of motion. The minimal set of variables ξ_i required to describe the dynamical evolution of the system $\boldsymbol{\xi}(t)$, with the vector $\boldsymbol{\xi} = [\ \xi_1 \ \ldots \ \xi_n\ ]^{\mathrm{T}}$, is denoted the set of states of the system. The number of states n is also called the order of the system. The variables u_j denote the inputs to the system, which are gathered in the vector $\boldsymbol{u} = [\ u_1 \ \ldots \ u_m\ ]^{\mathrm{T}}$. Given some initial state $\boldsymbol{\xi}(t_0) = \boldsymbol{\xi}_0$ and the input $\boldsymbol{u}(t)$ for $t \geq t_0$, the evolution of $\boldsymbol{\xi}(t)$ is determined by the—generally nonlinear—vector field function $\boldsymbol{F} = [\ F_1 \ \ldots \ F_n\ ]^{\mathrm{T}}$, which describes for each state its rate of change.

Remark 2.1 In addition to (2.1), a set of differential equations for the outputs of the system may be defined, if the outputs differ from the states.

If in contrast to the representation (2.1), the right hand sides do not explicitly depend on time t, the system is time-invariant. It is also called *autonomous*, as long as time is the independent variable. The evolution $\boldsymbol{\xi}(t)$ can then be represented by a trajectory in the state space, where time is implicit, see e.g. the limit cycle representations in Section 4.2.1.

Example 2.1 (Mechanical Impedance) An elementary mass-spring-damper system relating the response in terms of the position x and velocity $\dot{x}$ to the force input u represents a dynamical system, which is denoted a mechanical impedance. Its model is described by

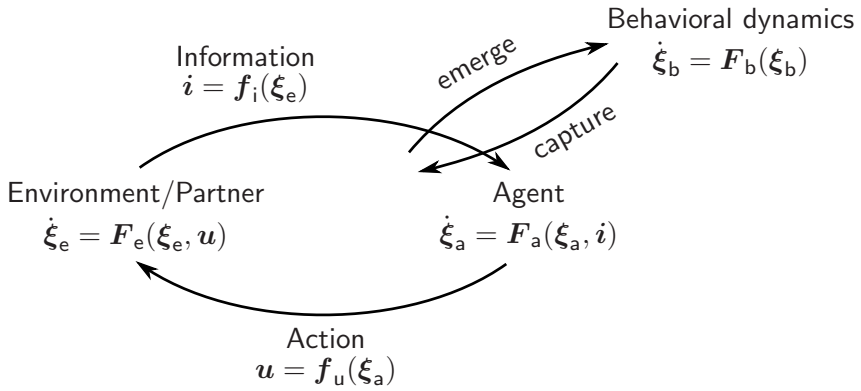

Fig. 2.1: Dynamical formulation of the perception-action cycle between an agent and the environment, and the concept of behavioral dynamics. Adapted from Warren [185].

the second-order differential equation

$$m\ddot{x} + b\dot{x} + kx = u, \tag{2.2}$$

where m denotes the mass, b the viscous damping coefficient, and k the spring stiffness. By defining the states $\xi_1 = x$ and $\xi_2 = \dot{x}$, the state-space formulation of (2.2) reads

$$\begin{aligned} \dot{\xi}_1 &= \xi_2 \\ \dot{\xi}_2 &= \frac{1}{m}\left(-k\xi_1 - b\xi_2 + u\right). \end{aligned}$$

In closed-form descriptions of cross-coupled dynamical systems, such as the systems of coupled oscillators investigated in Chapter 3 and 4, the inputs may be substituted by mutual output or state components respectively.

2.2.2 Behavioral Dynamics

Some features of the theoretical framework called *behavioral dynamics* by Warren [185] are presented in the following. It describes the organization of the interactive behavior between an agent and the environment, which encompasses the task and in this work, a further agent coupled by perceptual information. Dynamical systems are utilized to render action behavior and model behavioral patterns that are both stable and flexible. Those patterns are assumed not to be imposed and regulated soley by the individual agents, but only to emerge as the result of a self-organization among the agent and the environment. Furthermore, the concept of behavioral dynamics does not rely on detailed internal representations—which is beneficial as those are still rare for human agents. Instead, the apparent interactive behavior of complex systems is captured by simple, low-order descriptions, that are directly driven by sensory information. As a consequence, such descriptions usually have to remain rather task specific. The dynamical systems approach is outlined in Figure 2.1.

- On a first level, both the agent and the environment—which comprises the interaction partner in our case—are modeled by differential equations. The law of physics $\boldsymbol{F}_\mathrm{e}$

governs the environmental state $\boldsymbol{\xi}_\mathrm{e}$. An information function $\boldsymbol{f}_\mathrm{i}$ accounts for the perceptual processing of certain environmental properties through vision, haptics, and other modalities into informational variables $\boldsymbol{i}$. Those are input to the agent's law of control $\boldsymbol{F}_\mathrm{a}$, which determines the evolution of the state $\boldsymbol{\xi}_\mathrm{a}$ as a description of the agent's action behavior. The perception-action cycle is closed by the effector function $\boldsymbol{f}_\mathrm{u}$, which transforms the action state into external forces $\boldsymbol{u}$ applied to the environment.

- On the second level of description, the concept of behavioral dynamics now seeks to capture the emergent behavior of the perception-action cycle by a high-level dynamical system $\boldsymbol{F}_\mathrm{b}$, which is expressed in behavioral state variables $\boldsymbol{\xi}_\mathrm{b}$. Thus, both levels of description are linked bidirectionally.

Dynamical systems theory provides an elegant language to characterize motor behavior. Stable solutions, to which the state of the dynamical system converges are called *attractors*, and unstable ones, from which the state diverges are called *repellers*. Among the variety of attractors, two types are of particular interest in this work, as they are the building blocks for modeling stable interactive behavior by means of the dynamical systems approach:

- *Stable fixed points (point attractors)* model behavior tending towards stable equilibrium values, which may represent individual or collective goals of the agents with respect to the task. In contrast, *unstable fixed points (repellers)* allows to model avoidance behavior of undesired states. Later, we will make use of fixed points in the phase difference dynamics to replicate preferred phase relations of interacting human dyads in Chapter 3, and to model enhanced entrainment modes among human-robot dyads in Chapter 4.

- *Closed periodic orbits (stable limit cycle attractors)* model behavior tending towards stable, self-sustained oscillations, such as the execution of repetitive action tasks under spatial task constraints. Limit cycles exhibit one neutral DoF that may be subject to adaptation, while the remaining DoF are stable and resist perturbations. Limit cycle systems are characterized further in Section 4.2.1.

The stability of these attractors is modulated by their attractor strength or their corresponding relaxation time respectively, which determines how fast perturbations away from equilibrium decay.

Remark 2.2 Continuous re-parameterization of the dynamical system by so-called control parameters may lead to *bifurcations*, which denote topological or structural changes of the attractors through a changing morphology of the vector field. Besides the aforementioned attractors, bifurcations represent another powerful tool in the framework of behavioral dynamics. For instance, the bifurcation property of dynamical systems is exploited in the Haken-Kelso-Bunz model to replicate behavioral transitions, which are induced by the suddenly changing number of attractors depending on a continuous change of the control parameter [53].

2.2.3 System Identification

The goal of system identification is to build mathematical models, e.g. dynamical systems, by recording and analyzing accessible observations, i.e. the input and the output data from the system under consideration [93]. The procedure involves the following three points:

- The *data set*, which consists of recorded input and output data, usually by means of discrete sampling. Notably, the design of the identification experiment needs to aim at maximizing the informational content in the data set.
- The *set of candidate models* providing the model structure. Their choice usually depends on physical considerations, or a-priori principal knowledge. Model sets without parameters of explicit physical meaning are called non-parametric models or *black-box models*. For their identification, e.g. the impulse or frequency response is analyzed. In contrast, *gray-box models* are parametric models, that feature parameters with a physical meaning associated.[2] Due to their relevance in this work, we will focus on the identification of gray-box models.
- The *identification method*, which includes the criterion to assess the set of candidate models based on the data set, and the algorithm to numerically compute the estimates.

Often, alterations to those three points have to be made, in order to iteratively converge to a satisfactory model quality. A comprehensive background on the wide field of system identification is given in [93, 94].

Prediction-Error Method (PEM) for Gray-Box Identification

For a single-input-single-output system, we assume that pairs of input samples $u(t) \in \mathbb{R}$ and output samples $y(t) \in \mathbb{R}$ are measured at discrete times $t = 1, 2, \ldots, N$, such that we obtain the data set

$$Z^N = \{u(1), y(1), u(2), y(2), \ldots, u(N), y(N)\}\,. \tag{2.3}$$

Remark 2.3 For systems without any measured input u, the problem of system identification reduces to the identification of time-series models, also called signal models. A typical example is to estimate through gray-box identification the coefficients of ordinary differential equations to fit a given response trajectory $y(t)$.

Assuming further, that we decided for a particular model structure, a corresponding one-step ahead predictor needs to be found, taking the general form

$$\hat{y}(t|\theta) = g(t, Z^{t-1}, \boldsymbol{\theta}), \tag{2.4}$$

with $\hat{y}(t|\theta)$ being the predicted output at time t and $\boldsymbol{\theta} \in D_\theta \subset \mathbb{R}^d$ gathering the d parameters of the model.

[2] For completeness, so-called white-box models seek to describe the system internals on a physical basis as detailed as possible.

Remark 2.4 For the special case of a noise-free model, the model structure itself, e.g. of the form (2.1), represents a predictor, which is then called a simulation model.

The prediction error sequence for $t = 1, \ldots, N$ is then constructed by

$$e(t, \boldsymbol{\theta}) = y(t) - \hat{y}(t|\boldsymbol{\theta}). \tag{2.5}$$

The idea of PEM is to select the parameter estimate $\hat{\boldsymbol{\theta}}_N$ based on Z^N such, that the prediction errors $e(t, \hat{\boldsymbol{\theta}}_N)$ become as small as possible. Hence, the norm or validity measure $V_N(\boldsymbol{\theta}, Z^N) : \mathbb{R}^d \times \mathbb{R}^N \to \mathbb{R}$ defined as

$$V_N(\boldsymbol{\theta}, Z^N) = \frac{1}{N} \sum_{t=1}^{N} l(e(t, \boldsymbol{\theta})) \tag{2.6}$$

is calculated. Different types of the scalar function l in (2.6) exist, with the quadratic form $l(e) = e^2$ being a standard choice. Furthermore, linear filters may be deployed to $e(t, \boldsymbol{\theta})$ prior to the calculation of (2.6), in order to suppress eventual high-frequency disturbances or low-frequency drifts. Finally, the parameter estimate $\hat{\boldsymbol{\theta}}_N$ is obtained as the solution of the minimization problem

$$\hat{\boldsymbol{\theta}}_N = \arg \min_{\boldsymbol{\theta} \in D_\theta} V_N(\boldsymbol{\theta}, Z^N). \tag{2.7}$$

In general, (2.7) cannot be solved analytically. Iterative search methods need to be deployed to compute numerical solutions. Software tools such as the *MATLAB System Identification Toolbox* provide efficient gradient estimation techniques and search methods.

Remark 2.5 Unknown initial states of the model may be co-estimated with the parameters, which renders especially useful for systems with rather slow dynamics compared to the length N of the data set.

2.3 Studying Human Interactive Behavior

The proposed design methodology relies on profound experimental studies. At the very beginning of the design process, well-posed experimental designs are required for a systematic analysis, modeling and identification of the interactive behavior in HHI settings. Similarly, after the development of behavioral models and prototyping of interactive behavior for robots, the evaluation is again based on human studies, which are at this stage conducted in HRI settings. Both the aspects of experimental design and the evaluation techniques presented in the following focus on the field of joint motor action, which is central to this work.

2.3.1 Aspects of Psychological Experiments

Factors, Conditions and Disturbances

The scientific investigation of interactive behavior through psychological experiments involves the intentional and systematic manipulation and observation of multiple variables. Two types of variables are of fundamental importance: The independent variables, also called *factors* or treatments, are actively manipulated, and the effects on the behavior are observed by means of the dependent variables, also called measures. Specifically, the initial condition of interaction and the type of interactive behavior rendered by the robot are introduced as factors in this work. While the former serves the identification of human interactive behavior at an early stage of the design process, the latter enables the evaluation of the developed robotic behavior at the final stage.

The levels of the factors are denoted the experimental *conditions*, which are systematically varied by the experimenter according to the experimental design. At least two different levels of each factor must be chosen. Referring to the factors relevant in this work, a number of different initial conditions are applied to human dyads, in order to observe their corresponding response dynamics, and a number of different behavioral models are applied to the artificial interaction partner. Those may differ only regarding the model parameters or the whole model structure.

Remark 2.6 For comparative evaluation of advanced behavioral models, one model may be designated a *baseline condition* implementing a "standard" behavior, which is reproducible by common state-of-the-art methods.

Additionally, a number of unsystematic influences or *disturbances* effect the dependent variables, and thus, may confound the experiment. Relevant disturbances in human behavior studies include the expectation and motivation of the participants, visual or auditive distraction of the participants, or unintended ambiguities in the task instruction and execution. Ideally, all relevant influences are either eliminated or controlled, e.g. kept constant by following a standardized experimental procedure.

Experimental Design

The variability of human behavior poses particular challenges for the design of experimental studies. Both person-specific differences and changes of the behavior over time due to adaptation processes may act as disturbances. One of the goals of a thorough experimental design is to counteract such influences. In a *within-subject design*, each participant is presented multiple conditions of the factors, in contrast to a between-subject design, where each participant experiments with only one condition. The former is adopted in this work, since it allows to compare the behavioral changes of different conditions immediately within one individual, which eliminates person-specific disturbances. Within-subject designs, also called repeated measures designs, often present the same combination of experimental conditions multiple times to account for the variabilities of human motor behavior. However, counter-balancing or randomization of the conditions has to be applied, to compensate for practice effects due to sequential testing.

Remark 2.7 Many studies on human-human motor behavior introduce control conditions to investigate the effect of the partner, i.e. the task is also performed by a single participant and compared to the dyadic condition. Other control conditions investigate the effect of certain sensory modalities, e.g. the availability of haptic feedback from the object and/or the partner during task execution is manipulated.

The studies reported in this work aim to explore human behavior in natural and interactive settings, thus, the experimental tasks are performed only in joint action—indeed, all except one inevitably require joint action. Visual and haptic feedback is left unconstrained.

The quality of an experimental study is assessed by its validity. The *internal validity* refers to the unique interpretability and consistency of the results, whereas the *external validity* refers to the generalizability of the results beyond the experimental setting. Strong influence has the chosen sample size, i.e. the number of units of analysis. In this work, the unit of analysis is a dyad of participants in the HHI experiment, with each participant being part of one dyad only, and an individual participant in the HRI experiments. Sophisticated methods exist to choose the sample size depending e.g. on the desired effect sizes. As a rule of thumb, at least ten units of analysis are recommended to allow for statistical inference. Statistical analysis is required to distinguish if measures are affected by the experimental conditions or simply by noise, and to infer on a larger population than the sample population. Seeking to maximize both internal validity and external validity usually leads to a trade-off, which is illustrated by means of the experimental setting: In *laboratory experiments*, disturbance variables can be effectively eliminated, which in general leads to a high internal validity of the experiment. At the same time, the generalizability is constrained due to the artificial environment, which might lead to low external validity. In contrast, *field experiments* allow for realistic surroundings, and therefore yield high external validity, while uncontrolled disturbances often shrink their internal validity.

Remark 2.8 Some works that employ field experiments in the domain of HRI are found in the literature, see e.g. [186]. Mostly, communication aspects of social interaction are investigated, without robotic manipulation being involved. Field studies on joint action behavior, however, carried out e.g. in natural domestic environments, would induce severe concerns regarding the safety and the dependability of state-of-the-art robotic prototypes in shared workspaces.

This work employs solely laboratory experiments. Notably, the validity of those is additionally influenced by the type of the interaction scenarios, as discussed in the following.

Virtual vs. Real Interaction Scenarios

In research studies on haptic HHI and HRI, particularly pHRI, interaction tasks are often simulated in VR environments due to some benefits compared to real world environments: VR studies with humans can be conducted in an ultimately controlled environment, i.e. the interaction situations are standardized and well reproducible with high internal validity. The feedback modalities available to the user are fully controllable, e.g. the goal points or the instructed configuration trajectory may be hidden or blurred. High-fidelity haptic

interaction with a virtual partner is usually realized at low expenses regarding the hardware setup and software development, in particular when focusing on interaction in one or only few task-related DoF. The task characteristics, such as the workspace requirements can be matched to the technical specifications of the available haptic device. Furthermore, many haptic devices provide force and position measurements of high quality at the human interaction point. Any other physical variables can be derived from the physical simulation of the virtual environment. Consequently, complex data acquisition systems become unnecessary in many cases. In short, experiments conducted in VR interaction scenarios achieve high internal validity due to their precise measurements and effectively controlled or eliminated disturbance variables. This makes them well suited for fundamental research on human interactive behavior.

However, the external validity of VR experiments is often limited. Joint action scenarios have to be complemented by visual feedback to render natural interaction. High degrees of user immersion into the VR environment requires realistic visual rendering and advanced visual displays, such as head-mounted displays with a high resolution and a large field of view at low weight. Particularly in joint motor action which physically changes the environment, it is believed that an ultimate feeling of presence is hard to create in human participants. For instance, physical embodiment positively affects social interaction when compared to a virtual partner [182]. The interaction and co-location with a physically embodied robot is considered essential to conclude on the generalizability of evaluations. Besides the proof of concept provided by the implementation of real interaction scenarios, the evaluation of embodied HRI gives valuable feedback on the progress of both research and development towards the actual goal, which is to build embodied robotic partners sharing their workspace with humans in real world applications. Thus, HRI experiments are indispensable for evaluations with high external validity.

2.3.2 Experimental Measures

Both for modeling and evaluation of interactive behavior, relevant dependent variables have to be selected for experimental observation from the large amount of potential information. Such a variable is defined to assume one concrete value from a set of at least two possible values at each instant of time. Due to the continuous nature of motor behavior, many variables in this context are defined on a continuous scale over time, such as position and force information in visual-haptic interaction. The corresponding trajectories are then acquired through sampling at discrete time steps, such that time-series data of that variables are available for each trial of the experimental task. For their interpretation, specific parameters, behavioral patterns and pattern formation processes need to be identified through trajectory analysis, statistical analysis or control-theoretic modeling [50], where characteristic parameters are extracted based on the underlying model assumption.

In the following, two important classes of behavioral measures with relevance to joint motor action are discussed by means of popular examples, which are *performance measures* and *effort measures*. Furthermore, *subjective measures* acquired by means of questioning the participants are distinguished.

Performance Measures

Many performance measures are *accuracy* related, which makes them dependent on the goals of the specific task. For instance, in so-called tracking tasks, where a moving target or a given path has to be pursued as exactly as possible, the tracking performance of the participant is measured by means of the deviation of his/her interaction point or cursor from the instructed reference [34]. Scalar measures of the tracking quality are obtained e.g. from the root-mean-square (RMS) deviation accumulated over the position trajectory of each trial. Remarkably, this performance measure is applicable mainly in VR experiments, since predefined paths rarely exist in real world tasks. Also, the desired path of human participants is practically not assessable, unless indirectly by instructing it. In goal-hitting or positioning tasks, the deviations from a number of known, predefined goal points may be measured alternatively [194]. Depending on the task, more specific failure measures include the number or the duration of collisions with obstacles and forbidden regions, or missed goal configurations.

Generic speed assessment provides the *task completion time*. However, similar to accuracy-related measures, the completion time strongly depends on how the participants are instructed to perform the task, since the human performance is subject to the speed-accuracy trade-off found by Fitts [35]. Depending on the task goals, typical instructions encourage the participants to perform e.g. as fast as possible, as precise as possible, or at comfortable speed.

Remark 2.9 The motor capabilities of robotic prototypes designed for HRI, such as anthropomorphic and humanoid robots, are limited regarding movement velocity, acceleration and output force due to their technical specifications and safety reasons. Those capabilities are below that of humans for many state-of-the-art robots. Both the experimental task and the task instruction have to be designed such, that the required task effort and the human performance meet the robotic motor capabilities, in order to allow for an undistorted evaluation of human-robot joint action.

The behavioral measures described above can be calculated both for individual and joint performance of motor tasks. Due to relevance within this work, the *degree of synchronization* between two agents is introduced to quantitatively assess emerging patterns in a pair of simultaneously recorded movement trajectories. This behavioral measure focuses on the behavioral relationship of the partners, rather than on criteria straightforwardly derived from the objective goals of a motor task. Nevertheless, the group of synchronization measures introduced later in this work is regarded to be related to the task performance, since synchronization is expected to support mutual coordination and predictability of actions.

Effort Measures

The physical effort arising from haptic interaction is quantified by measures that are derived from physical variables and based on force components. First of all, the magnitude of the *interaction force* represents a basic measure by itself. It is taken at the interface between the agent and the manipulated object, the partner or the haptic device. Since environmental changes during physical cooperation are effected through both motion and

forces, *power* and *energy* variables are further representative measures. Their calculation requires motion and force referred to the same location of the considered interface. Again, taking the magnitude accumulates both flow directions in the effort measure, because at least the human partner is unable to recoup energy, e.g. through deceleration.

Remark 2.10 In pHRI experimental setups, grasp points are often realized by designated handles, each with a force sensor attached to directly acquire the interaction forces. Since usually separate data acquisition systems are employed for force and motion measurement, their time series data have to be synchronized thoroughly to avoid artifacts in the calculation of power and energy measures.

More specific measures are derived by decomposing the interaction force into the external (motion-causing) force component and the internal (squeezing or stretching) force component. The latter, also called interactive forces [48], provide a measure of the disagreement among the partners, or the negotiation effort respectively. Higher-level measures found in literature include efficiency measures relating performance to effort [49] and dominance measures analyzing each partner's contribution to the motion-causing effort [48, 130]. Scalar measures that represent whole trials are obtained from integration or averaging over the time series data. Integral versions should be preferred to the corresponding mean versions, if the trial durations vary within the experiment.

Those force-based effort measures are biased by the passive dynamics of the human body, first and foremost the inertial and damping properties, which cause non-zero interaction forces even for passive body movements. In order to take into account the true, metabolic effort of the human due to muscle contraction, additional measurements are required. Physiological measures, such as surface electromyography (EMG) directly determine the activation level of the contributing muscles.

Subjective Measures

As an additional source of information on the sensation of interaction and the experiences of the participants, subjective measures acquired by means of questionnaires may complement the behavioral measures. In particular, this holds true for the evaluation of HRI, since explicit user feedback may provide valuable hints going beyond pure observation on how to improve the interactive behavior of robot prototypes in future design iterations. In contrast to behavioral variables that are continuously available, questionnaires permit an information acquisition only at discrete instances of time, e.g. before and after the experiment, or between the experimental trials. This fact emphasizes the qualitative nature of subjective measures. The latent constructs operationalized by questionnaires, such as the feeling of presence or the feeling of togetherness, are prone to noise and biases. As a consequence, the reliability and validity of questionnaires is rather sensitive. Indeed, their construction can be regarded as an entire discipline, which involves the formulation and wording of questions, their organization as well as the selection of scales and answering options. The interested reader finds guidelines on the topic in [124]. If existing in the target domain, it is advisable to administer standardized questionnaires, that are successfully validated. For instance, in the experimental study on physical cooperation presented in

Chapter 5, the well established questions of the NASA task load index (TLX) are asked, which assess the construct of perceived workload [56].

2.4 Technical Foundations

The realization of prototypical interaction partners requires fundamental knowledge on how to control the involved technical systems. Although a variety of control schemes for mobile manipulators exists, only those schemes with practical relevance to the experiments conducted within this work are presented. These schemes are tailored to the experimental setup described in Appendix A.2.1, yet they apply to similar mechanisms as well.

2.4.1 Manipulator Control

Motion Tracking of the Effector Configuration

The control scheme is developed under the assumption of a serial-link anthropomorphic manipulator, with seven rotational joints and the vector $\boldsymbol{q} \in \mathbb{R}^7$ denoting the joint coordinates. Stiff independent PD-joint controllers supported by gravity compensation of the manipulator mass provide sufficiently accurate tracking of the desired joint configuration $\boldsymbol{q}_\mathrm{d}$. First, the goal is to realize tracking of the end effector configuration $\boldsymbol{x} \in SE(3)$ of the manipulator, which describes its Cartesian position and orientation. The single redundant DoF of the manipulator is used to construct an augmented task space with the configuration

$$\tilde{\boldsymbol{x}} = \begin{bmatrix} \boldsymbol{x} & \psi \end{bmatrix}^\mathrm{T}, \tag{2.8}$$

where additionally the elbow angle $\psi \in \mathbb{R}$ according to [163] is defined. The corresponding velocity is denoted by $\dot{\tilde{\boldsymbol{x}}} \in \mathbb{R}^7$. The mapping between the augmented configuration $\tilde{\boldsymbol{x}}$ and the joint configuration $\boldsymbol{q}$ reads

$$\tilde{\boldsymbol{x}} = \boldsymbol{\phi}(\boldsymbol{q}), \tag{2.9}$$

where the function $\boldsymbol{\phi} : \mathbb{R}^7 \to \mathbb{R}^7$ describes the forward kinematics. Then, the Jacobian representing the differential forward kinematics of the manipulator[3] can be derived, which is denoted by the square matrix $\boldsymbol{J}(\boldsymbol{q}) \in \mathbb{R}^{7\times7}$. The inverse mapping of the desired velocity trajectory $\dot{\tilde{\boldsymbol{x}}}_\mathrm{d}(t)$ to the desired joint trajectory

$$\boldsymbol{q}_\mathrm{d}(t) = \boldsymbol{q}_\mathrm{d}(0) + \int_0^t \boldsymbol{J}^{-1}(\boldsymbol{q}(\tau))\dot{\tilde{\boldsymbol{x}}}_\mathrm{d}(\tau)\mathrm{d}\tau \tag{2.10}$$

is denoted the differential inverse kinematics. Notably, the inverse of the manipulator Jacobian $\boldsymbol{J}^{-1}(\boldsymbol{q})$ exists only for nonsingular joint configurations

$$\boldsymbol{q} \in \{\boldsymbol{q} \,|\, \det(\boldsymbol{J}(\boldsymbol{q})) \neq 0\}.$$

[3] Depending on the representation of the orientational part of $\boldsymbol{x}$, the analytical and the geometrical Jacobian is distinguished.

To avoid excessively high joint velocities $\dot{\boldsymbol{q}}$ in the vicinity of singular joint configurations, the singular values of the inverse Jacobian are bounded—at the cost of tracking errors—by a weighted damped solution according to [162].

Remark 2.11 The DoF defined by ψ may be utilized to maximize e.g. some manipulability measure or the distance to the joint limits. In this work, the elbow angle is set $\psi_\mathrm{d} = const.$ during physical interaction. During movement tasks, a desired trajectory $\psi_\mathrm{d}(t)$ is tracked, such that $\tilde{\boldsymbol{x}}(t)$ resembles the configurations of a human arm performing the task.

Due to the required numerical integration, the differential inverse kinematics is prone to drift phenomena, i.e. the computed joint configuration deviates from $\boldsymbol{q}_\mathrm{d}$. As a remedy, a corrective velocity term in the task space

$$\Delta\dot{\tilde{\boldsymbol{x}}}_\mathrm{cl} = \boldsymbol{K}_\mathrm{cl}\left(\tilde{\boldsymbol{x}}_\mathrm{d} - \tilde{\boldsymbol{x}}\right) \tag{2.11}$$

is calculated, where $\boldsymbol{K}_\mathrm{cl} \in \mathbb{R}^{7\times7}$ is a positive definitive, diagonal gain matrix. The actual configuration $\tilde{\boldsymbol{x}}$ is obtained from (2.9). Adding (2.11) to (2.10) yields the closed-loop inverse kinematics

$$\boldsymbol{q}_\mathrm{d}(t) = \boldsymbol{q}_\mathrm{d}(0) + \int_0^t \boldsymbol{J}^{-1}(\boldsymbol{q}(\tau))\left(\dot{\tilde{\boldsymbol{x}}}_\mathrm{d}(\tau) + \Delta\dot{\tilde{\boldsymbol{x}}}_\mathrm{cl}(\tau)\right)\mathrm{d}\tau, \tag{2.12}$$

which controls the configuration error to zero in the task space.

Position-Based Impedance Control

Pure position control as described above would result in excessively large interaction forces, if the task involves physical contact of the stiff manipulator with the environment. Therefore, a compliant behavior of the end effector is required. The concept of impedance control introduced by Hogan [60] provides active compliance through dynamical regulation of the interaction between the manipulator and the environment. The relation between the contact wrench $\Delta\boldsymbol{u} \in \mathbb{R}^6$ and the corresponding motion $\Delta\boldsymbol{x} \in \mathbb{R}^6$ of the end effector is defined by the second-order mechanical impedance

$$\Delta\boldsymbol{u} = \boldsymbol{M}_r\Delta\ddot{\boldsymbol{x}} + \boldsymbol{D}_r\Delta\dot{\boldsymbol{x}} + \boldsymbol{K}_r\Delta\boldsymbol{x}, \tag{2.13}$$

with virtual mass $\boldsymbol{M}_r \in \mathbb{R}^{6\times6}$, damping $\boldsymbol{D}_r \in \mathbb{R}^{6\times6}$ and stiffness $\boldsymbol{K}_r \in \mathbb{R}^{6\times6}$. For diagonal and positive-definite matrices, the dynamics (2.13) represents the mechanical impedance of an elementary mass-spring-damper system, which is decoupled in the directions of $\Delta\boldsymbol{x}$. Considering an admittance causality, (2.13) is solved for the motion variables $\Delta\boldsymbol{x}$, given the contact wrench $\Delta\boldsymbol{u}$. A new configuration $\boldsymbol{x}'_\mathrm{d}$ is introduced, such that

$$\boldsymbol{x}_\mathrm{d} = \boldsymbol{x}'_\mathrm{d} + \Delta\boldsymbol{x} \tag{2.14}$$

modifies the desired configuration in (2.12) in case of contact wrenches. This type of compliant tracking of the end effector configuration is called admittance control or position-

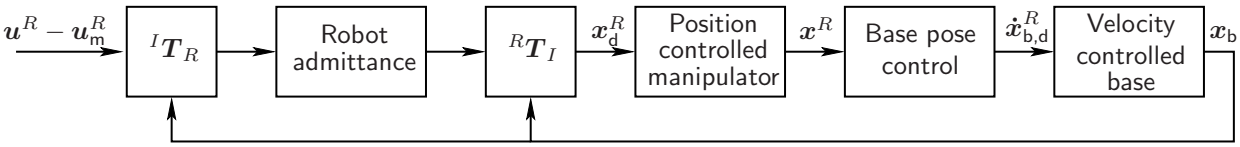

Fig. 2.2: Inertial admittance-type control scheme including manipulator-base coordination.

based impedance control in the task space [162]. The control scheme is utilized in the experiment described in Section 4.3.

Remark 2.12 The impedance (2.13) renders a compliant behavior of the end effector configuration $\boldsymbol{x}$, while the elbow angle ψ remains under position control. Special attention needs to be paid to the rotational part of $\Delta\boldsymbol{x}$. While the rotational acceleration and velocity are calculated straightforward from torques, a suitable representation of the angular deviation is required. Here, quaternions and the quaternion propagation rule provide an elegant solution.

Admittance-Type Force Control

Utilizing the control scheme for end effector configuration tracking from above, a desired wrench of the robot $\boldsymbol{u}_{\mathrm{d}}$ shall be tracked. Therefore, the impedance relation (2.13) is parameterized by $\boldsymbol{K}_r = \boldsymbol{0}$, and the new desired configuration in (2.14) is set to $\boldsymbol{x}'_{\mathrm{d}} = const.$. Further, the contact wrench is re-defined,

$$\Delta\boldsymbol{u} = \boldsymbol{u}_{\mathrm{d}} - \boldsymbol{u}_{\mathrm{m}}, \tag{2.15}$$

where $\boldsymbol{u}_{\mathrm{m}}$ denotes the wrench measured at the end effector. Then, the resulting second-order control law reads

$$\boldsymbol{u}_{\mathrm{d}} - \boldsymbol{u}_{\mathrm{m}} = \boldsymbol{M}_r\ddot{\boldsymbol{x}}_{\mathrm{d}} + \boldsymbol{D}_r\dot{\boldsymbol{x}}_{\mathrm{d}}, \tag{2.16}$$

which realizes position-based force control in the task space. The control dynamics is interpreted as an admittance with the matrices $\boldsymbol{M}_r$ and $\boldsymbol{D}_r$ rendering the virtual mass and damping.

2.4.2 Control of Mobile Manipulators

Manipulator-Base Decomposition

In order to make use of the extended workspace of a mobile robot composed by a manipulator-base system, the control law (2.16) is calculated in the inertial frame similar to [176]. The overall control scheme depicted in Figure 2.2 compensates for repositioning of the mobile base via the transformations between the local robot frame R and the inertial frame I, which are denoted by ${}^I\boldsymbol{T}_R$ and ${}^R\boldsymbol{T}_I$. Mobile manipulators usually resemble a macro-mini structure [75]. The heavy base (macro mechanism) is characterized by a rather slow and coarse dynamics in contrast to the lightweight manipulator (mini mechanism), which is characterized by a fast and accurate dynamics. The presented control scheme effectively decouples the end effector pose of the manipulator $\boldsymbol{x}$ from the base configuration $\boldsymbol{x}_{\mathrm{b}}$. Ideally, the overall dynamics are locally governed by the high mechanical

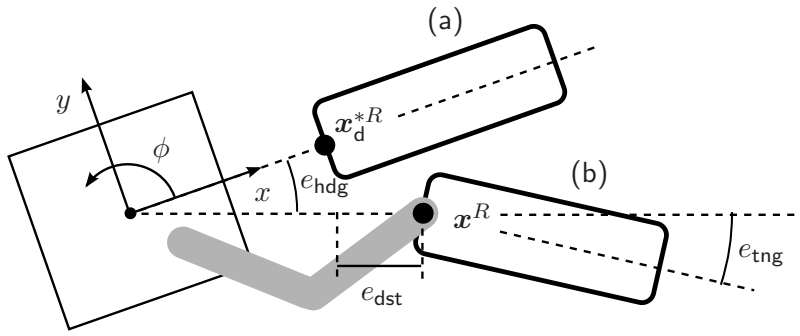

Fig. 2.3: (a) Desired and (b) actual configuration of the base with respect to the rigidly grasped object, described by the preferred and actual configuration of the end effector, $\boldsymbol{x}_{\text{d}}^{*R}$ and $\boldsymbol{x}^R$ respectively.

bandwidth of the manipulator. This scheme is deployed in the experiment on physical cooperation described in Section 5.5.

Remark 2.13 Manipulator-base decomposition through compensation of the base motion is well suited for mobile bases, that provide precise configuration measurements, but only limited actuation and tracking capabilities.

Remark 2.14 If the dynamics of a torque-controlled mobile base is given, which is true for many holonomic bases, the redundant manipulator-base system can be alternatively treated as a unified system, see e.g. [75, 166]. The decomposition into the task-space and the nullspace by means of the dynamically consistent inverse of the Jacobian of the overall redundant system results in a manipulator-base coordination, that minimizes the kinetic energy of the system [75].

Control of the Mobile Base

The desired following behavior of an omni-directional mobile base with the planar configuration

$$\boldsymbol{x}_{\text{b}} = \begin{bmatrix} x_{\text{b},\phi} & x_{\text{b},x} & x_{\text{b},y} \end{bmatrix}^{\text{T}}$$

is ensured by a control law generating the desired velocity

$$\dot{\boldsymbol{x}}_{\text{b,d}}^{R} = \text{diag}\left(K_{\text{hdg}}, K_{\text{dst}}, K_{\text{tng}}\right) \begin{bmatrix} e_{\text{hdg}} & e_{\text{dst}} & e_{\text{tng}} \end{bmatrix}^{\text{T}}. \tag{2.17}$$

Three independent proportional controllers with the gains K_{hdg}, K_{dst} and K_{tng} move the mobile base to control the heading error e_{hdg}, the distance error e_{dst} and the tangential error e_{tng} to zero. Those errors are defined with respect to a desired relative configuration of the manipulated object and the robot base, as illustrated in Figure 2.3. Given a six DoF manipulator, the $\dim(\boldsymbol{x}_{\text{b}}) = 3$ redundant DoF of the manipulator-base system are used to impose a preferred, task-specific configuration of the end effector $\boldsymbol{x}_{\text{d}}^{*R}$ with respect to the robot base frame R. For a rigid grasp of the manipulator on the object, the errors e_{hdg}, e_{dst} and e_{tng} are functions of the configuration error between $\boldsymbol{x}_{\text{d}}^{*R}$ and $\boldsymbol{x}^R$. The control gains in (2.17) are tuned to achieve a smoothly-damped, spring-like following behavior of the platform, that keeps the manipulator within its workspace bounds during

mobile manipulation. The velocity command $\dot{\boldsymbol{x}}^R_{\mathrm{b,d}}$ is then executed by an omni-directional velocity control law as proposed in [112].

Remark 2.15 The preferred configuration of the end effector $\boldsymbol{x}^{*R}_{\mathrm{d}}$ can be chosen to meet e.g. some lower bound $w_{\mathrm{l}} \in \mathbb{R}^+$ of the velocity manipulability measure

$$w(\boldsymbol{q}) = \sqrt{\det\left(\boldsymbol{J}\left(\boldsymbol{q}\right)\boldsymbol{J}\left(\boldsymbol{q}\right)^{\mathrm{T}}\right)} > w_{\mathrm{l}} \quad \forall\, \boldsymbol{q} \in D_w.$$

The domain

$$D_w = \{\boldsymbol{q} \,|\, \|\boldsymbol{x}^{*R}_{\mathrm{d}} - \boldsymbol{\phi}(\boldsymbol{q})\| < \Delta\boldsymbol{x}^R_w\}$$

considers joint configurations within the workspace centered around $\boldsymbol{x}^{*R}_{\mathrm{d}}$ and bounded by $\Delta\boldsymbol{x}^R_w$.

2.5 Summary

In this chapter, the design methodology is introduced, which guides the development of interactive behavior in this work. The analytical perspective on joint action is suggested to start with, if the behavioral features of humans are not yet understood completely in the target domain. The idea is to analyze, model and identify the dynamics of the human interactive behavior based on HHI experiments. The synthetical perspective is beneficially applied, if profound knowledge of human behavior already exists in the target domain. Here, the key components are a representational model of the joint action task and the corresponding model of human behavior, in order to both predict the partner's actions and be predictable for the partner. Each iteration of the design process is completed by prototyping robotic behavior and evaluating it in HRI experiments. Dynamical systems, their specific application called behavioral dynamics and gray-box system identification are introduced as the common modeling tools to capture the dynamic interrelations between perception and action. Due to their importance in the methodology, we introduce basic aspects of psychological experiments regarding their design and the deployed measures in the context of interactive motor behavior. In particular, the validity trade-off between virtual and real scenarios is discussed. Finally, we present the relevant control techniques that render the motor actions of a robotic prototype composed by an anthropomorphic manipulator and a mobile base.

3 Modeling of Human Movement Coordination

Humans manage to successfully coordinate their movements in many situations of daily life. Movement coordination can be intrapersonal (interlimb), e.g. coordination of one's left with one's right arm on a neural basis, or interpersonal, i.e. coordination with another person through information exchange. There is a wide range of actions that people perform together in shared workspaces, requiring individual movements to be coordinated. Examples range from handing over objects, manipulating a common workpiece to setting up a table. In order to prevent collisions and injuries in the worst case, the agents are required to keep certain spatial and temporal relations of their actions. People often seem to take on such coordinative behavior without much effort in a smooth manner. Coordination often comes about as movement synchronization during repetitive action. Synchronization refers to the establishment of a bounded temporal relationship between the interacting entities. It is assumed to be originated and sustained by a convergent dynamical process spanning across the interacting agents.

The contribution of this chapter is a systematic modeling approach to describe human-human interactive behavior in a quantitative way. Following the analytical perspective introduced as part of the methodological concept in Chapter 2, our goal is to provide a comprehensive description that can be transfered to robots and evaluated in HRI. Three research questions are addressed in this chapter: First, is movement synchronization observed in rhythmic HHI a phenomenon that also holds in goal-directed tasks? Second, if yes, when does synchronization between humans emerge during such a task and which patterns emerge? Third, how can we capture the observed effects in a mathematical model which is implementable to render corresponding robotic behavior? The presented experimental study evidences that people also synchronize their arm movements in a goal-directed task, which is characterized by the need for precise movements. These findings are in line with previous studies on interpersonal movement coordination in purely rhythmic tasks [138, 139, 151]. Movement synchronization is found to be guided by a dynamical process, which leads to stable coordination patterns in natural HHI. From an analytical and model-directed point of view, we characterize the emerging patterns and the quality of coordination by the extent of phase synchronization. Through system identification based on the experimental data, a parameterized model is derived which is ready for implementation and evaluation in HRI and, thus, lays the foundations for the behavior synthesis presented in Chapter 4.

This chapter is organized as follows: Section 3.1 provides the reader with an overview on existing works researching interpersonal movement coordination in the fields of experimental psychology as well as dynamical system theory. The proposed modeling concept along with the novel task paradigm and the experimental method is described in Section 3.2. In Section 3.3, key patterns of human-human synchronization are discovered and characterized in detail for the sake of modeling. The appropriate model structure is de-

rived and investigated for its parameter and stability properties in Section 3.4. Parameter identification is presented jointly with an evaluation of the results here as well. The quantitative results obtained from the modeling concept are discussed thoroughly with respect to their generalizability, explanatory power and methodological issues in Section 3.5. The chapter finishes in Section 3.6 with the conclusion on the analytical perspective to human behavioral modeling and open vistas for future research.

3.1 Background

Since modeling of HHI behavior in repetitive movement tasks is the central contribution of this chapter, we review related work on the exploration and modeling of human movement coordination in the following. Note that the focus is put on movement synchronization, as it is considered as key feature of rhythmic movement coordination.

3.1.1 Experimental Studies and Key Results

Numerous studies conducted in the domain of experimental psychology provide evidence for human movement synchronization. Without stating completeness, we review in the following some of the most interesting works that discover features of interpersonal entrainment in human interactive behavior observed in a variety of action tasks. Mostly, purely rhythmic task paradigms are applied, in which synchronization to in-phase (symmetric) and anti-phase (alternating) relations is either instructed or observed to spontaneously emerge.

Intentional Entrainment

For dyads sitting side-by-side and moving their lower legs in accordance with a metronome, coordination breakdown resulting in a transition from the anti-phase to the in-phase mode is observed with increased frequency [151]. Another popular experimental paradigm is the swinging of hand-held pendulums while the participants are sitting side-by-side. In addition to the coupled frequency of oscillations, it allows to manipulate the difference of the preferred physical frequency of the pendulums as control parameter by changing their lengths or weights [148]. Shifts of the frequency difference are found to induce corresponding shifts of the stable phase relations during visually coordinated pendulum swinging.

Unintentional Entrainment

The emergence of unintended coordination in the laboratory task of pendulum swinging is shown as well [150]. It is argued that the same mechanisms of dynamical self-organization as observed in intrapersonal coordination apply. Similar behavior is observed in [138]. In [139], a paradigm is introduced in which two people are moving forth and back next to each other in rocking chairs. Dyads unintentionally rock in synchrony, although different weights attached to the chairs manipulate the frequencies at which they would naturally oscillate without extra effort. Dyads facing each other and performing oscillatory index finger movements are also found to unintentionally synchronize by deviating from their individually preferred frequency [117]. Persistence of entrainment after preventing visual

feedback is attributed to a social memory effect. Similarly, during side-by-side walking on a treadmill, pairs of participants tend to synchronize their gait to intermittently stable patterns, even when no instruction to synchronize is given [178]. In addition to extensively investigated couplings provided through the visual and auditive modality, unintentional entrainment through haptics is spontaneously emerging as well. Strongest in-phase synchronization during side-by-side walking is found for couples with mutual haptic feedback through holding hands [193]. Light fingertip contact during rhythmic postural sway seemingly stabilizes spontaneous in-phase coordination within dyads [161].

Social Effects

Besides the above behavioral observations, synchronization affects social relationships. During observing or listening to simulated dyads walking in different patterns of synchrony, interpersonal rapport between the walkers is judged highest for the most stable forms of in-phase and anti-phase coordination [107]. Metronome-paced finger movements that are synchronous to that of an experimenter leads to higher interpersonal affiliation ratings than asynchronous tapping [63]. Furthermore, rocking in synchrony enhances perceptual sensitivity towards each other, and fosters the cooperative abilities in a subsequent joint action task [177]. Conversely, the individual degree of sociality of interaction partners influences the extent of synchronization. Regardless if sociality is manipulated through priming instructions, or resulting from person-specific characteristics, social-oriented participants achieve a higher degree of synchronization than self-oriented ones during rhythmic arm movements in [96].

3.1.2 Modeling and Identification Approaches

Movement synchronization—as a basic principle of human interactive behavior—is investigated repeatedly by means of dynamical systems that model interconnected perception-action loops and generate dynamical patterns [9, 155]. In this context, the reader is referred to the comprehensive review on behavioral dynamics provided by Warren [185]. In contrast to the dynamical systems approach, the research domain of sensorimotor synchronization (SMS) usually focuses on discrete linear modeling from an information-processing point of view. Insights to be gained from relevant works on SMS will be reviewed in Chapter 4.

Intrapersonal Movement Coordination – the Haken-Kelso-Bunz Model

Pioneering work on modeling intrapersonal coordination of limbs is conducted by Haken et al. [53]. The authors propose a minimal dynamical model of coupled nonlinear oscillators—known as the Haken-Kelso-Bunz (HKB) model—which successfully reproduces the transition between stable coordination patterns during bimanual finger-tapping. It is originated from the theoretical framework of synergetics [52], which describes the self-organized interplay of many DoF in the (human motor control) system by one or few order parameters or collective variables respectively. Those are slowly changing in time and represent stable coordinative states at a macroscopic level, which are the in-phase and anti-phase relation in the finger tapping task. The system may be driven through its co-

ordinative states by the control parameter, such as an external pacing frequency provided through a metronome. For the task of bi-manual finger tapping, the phase difference Φ taken from the phases of the oscillatory finger trajectories turns out to be the appropriate order parameter. For the design of the attractor dynamics $\dot{\Phi} = \frac{\partial V}{\partial \Phi}$, Haken et al. [53] postulate 2π-periodicity, i.e. for the corresponding potential function, $V(\Phi) = V(\Phi + 2\pi)$ holds, and left-to-right symmetry between both hands, i.e. $V(-\Phi) = V(\Phi)$ holds. The simplest potential well mapping the observed behavior to the collective dynamics reads

$$V = -a\cos\Phi - b\cos(2\Phi). \tag{3.1}$$

If the ratio of the parameters $\frac{b}{a}$ is changed depending on the control parameter, the change of the attractor basins in the attractor landscape (3.1) well describes the coordination phenomena: The dynamics bifurcate from bistability between in-phase and anti-phase to monostability of the in-phase relation, if $\frac{b}{a}$ is decreased and the frequency is increased respectively beyond the critical value $\frac{b}{a} = 0.25$.

Remark 3.1 Besides the dynamics at the collective level, a lower-level description is part of the HKB model, which includes both the phase and the amplitudes of the hand movements. It also accounts for the decreasing amplitudes when increasing the driving frequency.

Several modifications of the HKB model are proposed. Two additional oscillators are introduced in [10] to represent the level of movement generation through the end effectors while explicitly accounting for the mechanical properties of a human limb. This neuro-mechanical model should foster the fundamental analysis of the interplay between the neural and the effector level during simple, purely rhythmic movements. In order to gain deeper insights into the dynamics of human coordination, experimental paradigms which utilize a human's periodical input to drive oscillatory mechanical systems with different eigenfrequencies are applied repeatedly. The task paradigm of swinging pendulums originally introduced by Turvey et al. [173] is also employed by Schmidt et al. [152]. An extension of the HKB coupling function by a frequency detuning term similar to the coupling function proposed in [18] is found to account for both the effects of different eigenfrequencies and external forcing frequencies.

Interpersonal Movement Coordination

Originally developed to model intrapersonal coordination of movements, dynamical models of coupled oscillators are found to qualitatively explain interpersonal coordination as well. While participants had to swing hand-held pendulums, coordination phenomenons are matched the predicted features of the HKB model [148]. In a subsequent study, Schmidt et al. [153] compare the characteristics of intended intra- and interpersonal coordination by applying the same pendulum paradigm. Frequency detuning imposed through different eigenfrequencies and frequency levels are introduced as control parameters. Depending on the frequency level and the intended phase relation, the authors obtain the coupling strength of a local dynamical model similar to [18]. The number of coordination breakdowns, the phase fluctuation and the coupling strength reveal interpersonal coordination to

be weaker than intrapersonal coordination. The regression method to identify the coupling strength relies on a-priori knowledge of the pendulum-wrist system's frequency detuning, which limits the approach to oscillatory effector systems.

Fundamental research work on fitting nonlinear dynamic models to trajectories of human rhythmic movements is conducted in [73]. Observed functional relationships between the external driving frequency and the amplitudes and peak velocities of the movements are found to be reproduced well by a mixture of van der Pol and Rayleigh oscillators with stable parameter fits. The model is fitted to the limit cycle data in the position-velocity state space. In a more general approach, Eisenhammer et al. [30] propose a reconstruction method of time series data based on polynomial dynamical models, which are fitted to the vector field of an appropriate state-space representation of the data. While also transients of a pair of coupled oscillators can be reconstructed from simulated data, the method is rather sensitive to noise and requires an extensive observation of transient regimes to yield stable results, since the whole state-space region is reconstructed. Inspired by the numerous variations of coupled oscillators models of rhythmic limb movements, Beek et al. [8] systematically analyze how different components such as linear and nonlinear elastic and friction terms contribute to the composition of rhythmic movement. Jirsa and Kelso [71] show in their work on dynamical movement models how the attractor landscape in its state space can be formed to reproduce a variety of both discrete and rhythmic movement behaviors, using their so-called excitators. Elementary human movement trajectories in response to different stimuli are replicated qualitatively by stimulating the respective excitator model. The authors show that their approach extends to coupled dynamical systems as well, yet given a certain action task it may require sophisticated design to obtain the desired features of coordinated movement behavior. The aforementioned approaches accurately model basic human motor behavior in rhythmic tasks, yet the movement reproduction and coordination is tightly encoded by the functional state-space representation of the oscillator dynamics, making them less flexible in their application to constrained, goal-directed tasks.

Similar to [10], in [22] a neuro-mechanical unit per agent is proposed, which is driven by a cross-coupled pair of self-sustained oscillators. The intended modes of coordination during pendulum swinging are replicated, as well as the effect of resonance tuning when the pendulums were manipulated individually. The coordination patterns observed by Richardson et al. [139] during chair rocking are also related qualitatively to the predictions of the HKB model, yet explicit modeling is not conducted.

Common to the fundamental research work on rhythmic movement coordination between humans is that the exploration and modeling is mostly approached by means of combined oscillatory task-effector systems, such as hand-held pendulums. However, little is known about the coordination behavior of humans in goal-directed action tasks, to what extent the fundamental findings and modeling approaches on movement coordination apply, and how the observed effects can be described in a quantitative way.

3.2 Model-Directed Experimental Design

3.2.1 Concept and Paradigm

The modeling concept relying on dynamical systems theory of coupled oscillators and the experimental study of human behavior is presented. Its novelty stems from:

- The modularity and transferability of the modeling scheme to ease the design of corresponding robotic behavior from the very beginning on.
- The task paradigm introducing the highly relevant class of goal-directed movements and, thus, going beyond purely rhythmic tasks.
- The system-theoretic idea to observe the human behavioral dynamics naturally emerging in response to an initial excitation, instead of continuously controlling it.

Phase Synchronization of Coupled Oscillators

The general dynamical equations of two limit cycle oscillators that are mutually coupled are given by

$$\begin{aligned} \dot{\boldsymbol{\xi}}^{\mathrm{a}} &= \boldsymbol{F}^{\mathrm{a}}(\boldsymbol{\xi}^{\mathrm{a}}) + \boldsymbol{C}^{\mathrm{a}}(\boldsymbol{\xi}^{\mathrm{a}}, \boldsymbol{\xi}^{\mathrm{b}}) \\ \dot{\boldsymbol{\xi}}^{\mathrm{b}} &= \boldsymbol{F}^{\mathrm{b}}(\boldsymbol{\xi}^{\mathrm{b}}) + \boldsymbol{C}^{\mathrm{b}}(\boldsymbol{\xi}^{\mathrm{b}}, \boldsymbol{\xi}^{\mathrm{a}}), \end{aligned} \tag{3.2}$$

where $\boldsymbol{\xi}^{\mathrm{a}} \in \mathbb{R}^{n^{\mathrm{a}}}$ is the n^{a}-dimensional state vector for oscillator a, $\boldsymbol{F}^{\mathrm{a}} : \mathbb{R}^{n^{\mathrm{a}}} \to \mathbb{R}^{n^{\mathrm{a}}}$ represents the autonomous dynamics, and $\boldsymbol{C}^{\mathrm{a}} : \mathbb{R}^{n^{\mathrm{a}}} \times \mathbb{R}^{n^{\mathrm{b}}} \to \mathbb{R}^{n^{\mathrm{a}}}$ is the coupling function, that bidirectionally links the oscillators and enables interaction. The dynamics for oscillator b are defined analogously.

Remark 3.2 The formulation (3.2) implies in a physical interpretation, that the modeled system can be decomposed into two independent oscillating systems, that interact through weak coupling. Else, the system could be modeled in an atomic fashion.

If the oscillators are harmonic and weakly coupled, $n^{\mathrm{a/b}} = 1$ and we may write $\boldsymbol{F}^{\mathrm{a/b}} = \omega^{\mathrm{a/b}}$ and $\boldsymbol{\xi}^{\mathrm{a/b}} = \theta^{\mathrm{a/b}}$, with the natural frequency $\omega^{\mathrm{a/b}} \in \mathbb{R}$ and the phase $\theta^{\mathrm{a/b}} \in \mathbb{R}$.

Definition 3.1 (Phase Synchronization) Two phase oscillators interacting such, that

$$|\Phi_{i,j}(t)| < \epsilon, \text{ with } \Phi_{i,j}(t) = i\theta^{\mathrm{a}}(t) - j\theta^{\mathrm{b}}(t) \tag{3.3}$$

holds, with the generalized phase difference $\Phi_{i,j}(t)$ and a positive constant $\epsilon \in \mathbb{R}^{+}$, are called to show phase synchronization or phase locking [126]. Positive constants $i, j \in \mathbb{N}$ allow to detect phase synchronization of order $i : j$.

Remark 3.3 Since $\Phi_{i,j}(t)$ quantifies the interaction in a single variable, it is also called *collective* in dynamical systems theory. The dynamics of phase synchronization are then sufficiently described by the trajectory $\Phi_{i,j}(t)$, with its attractors determining the collective behavior of the coupled dynamical system.

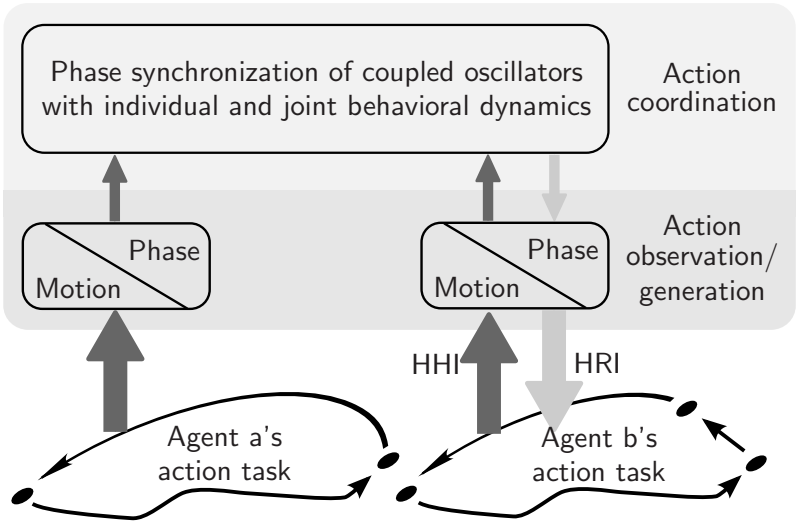

Fig. 3.1: Overview scheme depicting the two-layered concept of movement coordination. Agent a and b jointly engage in repetitive actions. The observed movements are transformed to phases in the lower layer. In the upper layer, the coordination behavior is assumed to be governed by the individual and joint behavioral dynamics, which are represented by coupled phase oscillators. Dark arrows represent the analytical perspective on HHI pursued in this chapter. Light arrows outline the envisaged stage of action generation when the behavioral model is deployed to HRI, see Chapter 4.

From Coupled Oscillators to Human Interactive Behavior

Following the definition of phase synchronization, the conceptual approach to model HHI behavior is outlined in Figure 3.1. Each of the action tasks a and b is represented by the agent's end effector positions over time, which we call the motion trajectory in the following. Since the interaction of the coupled oscillators is described by the evolution of their phases, the transformation between motion trajectories and phases is required. It provides the phase of an action task, which models an agent's observation of the other's action. If the transformation is bijective, it can also provide the motion trajectory of a robotic agent and therefore model the generation of actions in HRI. Within this chapter, we restrict the investigation of these transformations to model action observation in HHI. Each agent's individual behavior regarding the task progress is represented by a self-sustained phase oscillator with a constant natural frequency. Interaction is modeled through the coupling term, hence temporal coordination patterns as a result of the agents' interactive behavior are replicated by phase synchronized oscillators.

Remark 3.4 The agents' action tasks are not necessarily identical, as indicated in Figure 3.1, provided that transformations from the motion trajectories to phase representations exist.

Design of the Experimental Task

Our research questions regarding human movement synchronization place certain requirements on the design of an appropriate experimental task. The following points are considered as relevant to the investigation of synchronization:

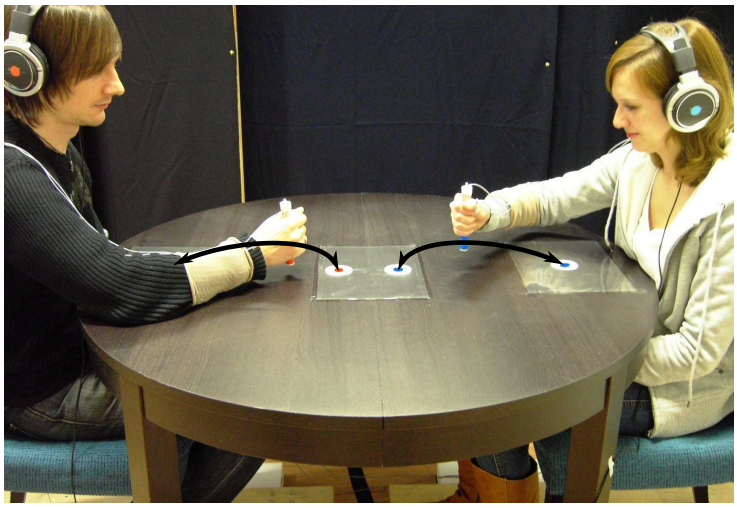

Fig. 3.2: Experimental task designed to study HHI behavior. Participants are performing goal-directed arm movements while sitting face to face.

- The task paradigm should integrate goal-directed as well as repetitive actions, which similarly appear as building blocks in real-life settings. To keep the task simple, a sequence consisting of a forward and a backward movement has to be performed repetitively, forming a closed trajectory, which we call the (movement) *cycle* in the following. Multiple cycles are to be completed in a continuous sequence, which allows synchronization to emerge among the agents. The forward as well as the backward movement (half-cycles) are point-to-point arm movements while carrying a tool in hand. This is where goal-directedness comes into play: The tool (a pen) has to be placed on two designated positions on a table alternately. Note that the agents perform identical tasks.

- The topology of workspaces is arranged without overlap of the movement trajectories. This enables the agents to perform in parallel without any interference or demand for collision avoidance, which could restrict movement synchronization. The workspace topology is known to strongly affect the temporal aspects of movement coordination [156]. Overlaps for example might lead to changes in the coordination behavior.

- During task execution, the agents' movements are affected by the type of sensory information that is available of the other agent's movements. Regarding visual information pick-up, it is known that focal and peripheral conditions of mutual movement observation mediate the stability of interpersonal coordination [139]. In order to provide full visual information, the agents are facing each other without any occlusions. Since they are always able to observe their opponents' movements as well as start and target positions, synchronization is made as easy as possible.

The experimental task involving the actions of two agents is illustrated in Figure 3.2.

Natural Dynamics of Human Interactive Behavior

The goal is to quantitatively model of synchronization behavior expected to emerge in the above task, by considering dyadic interaction as a coupled dynamical system. A general requirement for successful parameter identification is the perturbation of the system and the observation of the system response. This can be achieved either by an externally applied excitation, or by an initial perturbation of the system from its equilibrium. The latter provokes the natural response dynamics of the system. For instance, if a simple pendulum is pulled back from its equilibrium state and released in a different initial state, its natural frequency can be determined experimentally by measuring the frequency it swings at. Since any externally applied excitations (stimuli) such as enforcing frequencies presented e.g. via metronomes, or an imposed frequency detuning [153] could hinder natural HHI, the interaction of the partners is not actively controlled during our experiment, but rather observed only. Thus, the experiment can be classified as passive. It follows, that the parameters of the systems can not be changed, and only bivariate data will be available [126].

In order to investigate how movement synchronization is established over time and to foster parameter identification, we aim to observe the natural response of the human dyad by provoking different initial spatial relations between their hands. Therefore, the action start off among the dyad is artificially modulated by triggering it acoustically. Among all possible start off relations, three conditions are supposed to be capable of being differentiated in the experimental task.

3.2.2 Human-Human Experiment

Participants

In total 20 people (13 male) forming 10 dyads participated in the experiment. They were between 18 and 28 years old, at a mean age of 23.5 years. All were right handed, had normal or corrected-to-normal vision and were naïve as to the purpose of the experiment. For participation, they were paid 8 € per hour.

Experimental Setup

Participants were sitting face to face at a round table on which four circles were marked in two different colors, see Figure 3.3. Each color was assigned to one person who was equipped with a marking pen of equal type and size in the respective color. Participants had to hold the pens in their right hands forming a fist around them with the thumb pointing upwards. With this it was achieved that the pen was always in a orthogonal relation to the table surface. We encouraged participants to sit in an upright position and instructed them to put the left hand on their lap. To reduce tapping sound, and thus, the influence of the auditive modality on synchronization, pieces of felt were attached to the pen tips. Hand movements were captured with an infrared 3D-motion tracking system *(PTI VisualEyez II VZ4000)* at a sampling rate of 30 Hz for acoustical signal triggering and at a sampling rate of 200 Hz for data analysis. Further details on the system can be found in Appendix A.2.2. LED markers used for motion capturing were attached to the

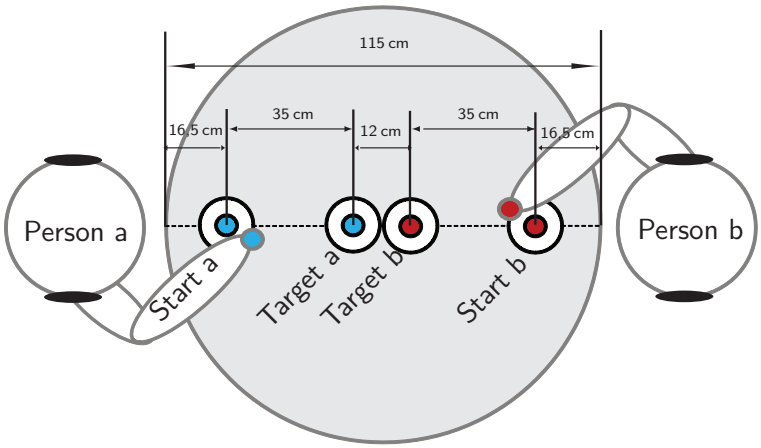

Fig. 3.3: Experimental setup with dimensions. Person a and person b sit in chairs opposite to each other. The task was to alternately tap on two assigned dots (start and target, diameter 8 mm) with a pen in hand. The dots were marked on a round table and each one was surrounded by a white area (diameter 60 mm).

top end of the pen and to the participants' basis thumb joint. Both participants had to wear a pair of stereo phones *(SONY MDR-XD200)* used to present the individual acoustic trigger signals.

Conditions

The following start-off conditions were acoustically triggered in the experiment:

- **ZC**: **Z**ero-**C**ycle difference.
  Both participants were triggered at the same time.

- **QC**: **Q**uarter-**C**ycle difference.
  The second participant was triggered when the first had passed one quarter of the first cycle, i.e. half the distance between start and target.

- **HC**: **H**alf-**C**ylce difference.
  The second participant was triggered when the first had passed half of the first cycle, i.e. reached the target point for the first time.

Procedure

The experiment started with capturing the individual calibration positions for each dyad. For this purpose, participants had to put their pen to their individual start and target point respectively. The written instruction included a description of the task, which was to alternately tap the individual start and target point with the pen tip. Furthermore, participants were asked to lift the pen between the points. Sliding the pen over the table was not allowed. No instructions were given regarding speed in order to provoke natural behavior. At the beginning of each trial participants were asked to rest in their respective start position and instructed to start executing the task as soon as they heard the acoustical

start signal (high-pitched tone) through their phones. Simultaneously with the start signal, motion capturing started. The stop signal (low-pitched tone) was presented automatically after both participants had performed at least ten cycles each. At the same time, motion capturing stopped and participants had to move their pen back to the start point. Six sets each consisting of six trials were performed which led to a total of 36 trials. Start-off conditions were kept constant within sets which led to a total of 12 trials per condition. In the conditions quarter-cycle and half-cycle, the delay of the start signal for the second person was calculated on-line from the movement data of the first person. Being first person was randomly assigned to person a or person b and counterbalanced in each set. The first trial in each set was excluded from analysis.

Measure of Synchronization

Synchronization between the agents can be detected when their phases are related to each other through the generalized phase difference (3.3) introduced in Section 3.2.1. Boundedness of the phase difference can be tested for different cycle frequencies of the coupled oscillatory system. For example, one agent performing one cycle while the other completing two cycles can be still referred to synchronization, which would be called synchronization of order 1:2. The participants in our experiment were performing at similar cycle frequencies $\dot{\theta}$, which is indicated by the standard deviation $\mathrm{SD}_{\dot{\theta}} = 0.12\,\mathrm{Hz}$ at the mean $\overline{\dot{\theta}} = 0.73\,\mathrm{Hz}$ over all trials. Thus, the analysis of synchronization is restricted to the order 1:1 by calculating the dyadic phase difference

$$\Phi(t) = \Phi_{1,1}(t) = \theta^{\mathrm{a}}(t) - \theta^{\mathrm{b}}(t). \tag{3.4}$$

The per-trial time series $\Phi(t)$ are defined to start at the movement onset of the delayed agent.

Remark 3.5 Since the investigated phase representations yield angular values defined on the circle $[0, 2\pi]$, the phase is unwrapped for the purpose of modeling, i.e. 2π-jumps are removed to obtain continuous $\Phi \in \mathbb{R}$.

Numerous approaches on measuring synchronization based on time series can be found in literature, see e.g. [84] for a comprehensive comparison. A common approach to quantify phase synchronization is the calculation of the synchronization index. Given the time series $\Phi(t)$ consisting of N directional observations $\Phi(t_j)$, directional statistics provides the synchronization index

$$\mathrm{SI} = \left| \frac{1}{N} \sum_{j=1}^{N} e^{i\Phi(t_j)} \right| = 1 - \mathrm{CV}, \tag{3.5}$$

where CV denotes the circular variance of an angular distribution. The synchronization index is also called mean phase coherence in literature. It denotes the length of the mean resultant vector of the phase difference samples $\Phi(t_j)$ transformed into unit vectors in the complex plane.

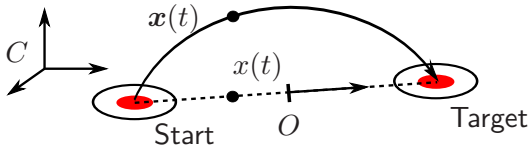

Fig. 3.4: Motion trajectory $\boldsymbol{x}(t) \in \mathbb{R}^3$ and projected trajectory $x(t) \in \mathbb{R}$ between the agent's start and target point. The origin O of the task space is set such, that $x(t)$ is zero-mean.

Remark 3.6 The SI lies in the interval [0,1]. Given a perfectly uniform distribution of phase differences, it would equal zero. In perfect synchronization it would equal one, which means that all samples of Φ point to the same direction.

Remark 3.7 The SI is typically biased due to non-uniformities in the individual phase distributions. If unbiased values spanning the whole range [0,1] are desired, the surrogate technique described in [84] allows for correction.

3.2.3 Phase Reconstruction Techniques

Assuming trajectories of limit cycle systems acquired in experiments, we present in the following two techniques, that provide estimates of phase variables from cyclic time series data. Later in this chapter, we are not only interested in steady-state synchronization, but also in the transient processes leading to phase synchronization. Therefore, those reconstruction techniques are such, that *non-stationary* features of the data can be reflected in *instantaneous* phase variables on a within-period scope.

Data Reduction

The experimental data gathered within this study consist of the agents' end effector positions $\boldsymbol{x} \in \mathbb{R}^3$ over time t, i.e. the motion trajectories $\boldsymbol{x}(t)$ expressed in a Cartesian frame C, see Figure 3.4. Data complexity is reduced to simplify the analysis, by considering only the information required for a minimal description of the task. The motion trajectory of each agent is projected into a one-dimensional subspace spanned by the vector difference of the respective target and starting point, as illustrated in Figure 3.4. This projection preserves the temporal relation of the agents' end effectors regarding the action task, thus it is proposed as the effective task space. The further analysis is conducted based on the scalar motion trajectory $x(t) \in \mathbb{R}$. The movement onset is defined as the instant of time when the difference between the position of the end effector x and its initial rest position exceeds 5 mm for the first time.

State-Space Technique

If the observed trajectory $x(t)$ is scalar and harmonic or at least quasi-harmonic, the two-dimensional state $\boldsymbol{\xi} = [\ x \quad \dot{x}\ ]^{\mathrm{T}}$ can be defined. It is sufficient to describe the state of a one-dimensional oscillatory system. By plotting $\boldsymbol{\xi}(t)$ in the embedding state space, the cyclic nature becomes obvious. For illustration purpose, the scalar trajectory of a human

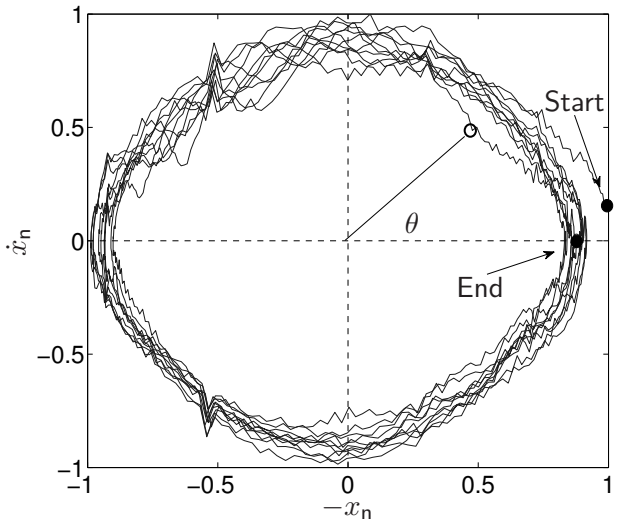

Fig. 3.5: State-space trajectory of quasi-harmonic human hand movements. Normalized velocity is plotted against the normalized position. The counter-clockwise evolving trajectories form approximately a closed curve of circular shape. The position x_n is reversed to obtain a phase θ increasing over time.

hand performing quasi-harmonic movements is depicted in Figure 3.5. Using the state-space technique, the phase of the underlying oscillatory system is given by the angle with respect to the abscissa in the state space. It reads

$$\theta(t) = \arctan\left(\frac{\dot{x}_\mathrm{n}(t)}{-x_\mathrm{n}(t)}\right), \tag{3.6}$$

with the normalized velocity and position,

$$\dot{x}_\mathrm{n}(t) = \frac{\dot{x}(t)}{|\dot{x}^*|} \quad \text{and} \quad x_\mathrm{n}(t) = \frac{x(t)}{|x^*|}. \tag{3.7}$$

The values $\dot{x}^*$ and x^* in (3.7) denote the observed extrema of the components of the state trajectory, which can be updated on-line after each half-cycle. State normalization ensures a phase characteristics that is widely independent of the actual physical constraints of the considered system, i.e. the peak amplitudes and velocities. In their benchmark on continuous phase computation using non-stationary, oscillatory test signals, Varlet and Richardson [179] emphasize the superior performance gained by half-cycle normalization.

For non-harmonic observables, the state-space trajectory differs from the simple circular shape. In such case, the only way to obtain a meaningful phase through this technique is band-pass filtering, which selects only a single frequency component or feature of the observable to be represented in the phase.

Remark 3.8 The state-space technique is well-suited for real-time analysis of quasi-harmonic, scalar observables. If the observations are noisy, low-pass filtering may be required due to differentiation, which introduces an additional phase lag in real-time application.

Spectral Technique

Comparisons of spectral signal analyses performed by (short-time) Fourier-, Hilbert- and wavelet-transform show equivalent results due to their formal equivalence, if their filter kernels are parameterized respectively [14]. Due to its relevance later in this thesis, we shortly review the analytic signal concept based on the Hilbert transform for computing the phase variable [142]. The Hilbert transform provides the instantaneous phase and amplitude of the signal[1] $x(t)$ via the construction of an analytic signal $\zeta(t) \in \mathbb{C}$. It is a complex function of time defined as

$$\zeta(t) = x(t) + j\tilde{x}(t) = A(t)e^{j\theta(t)}, \tag{3.8}$$

where $\tilde{x}(t)$ is the Hilbert transform of $x(t)$. It is given by

$$\tilde{x}(t) = \frac{1}{\pi}\text{P.V.}\int_{-\infty}^{\infty}\frac{x(\tau)}{t-\tau}d\tau, \tag{3.9}$$

where P.V. means that the integral is taken in the sense of the Cauchy principal value. The instantaneous amplitude $A(t) \in \mathbb{R}$ and phase $\theta(t) \in \mathbb{R}$ of the signal $x(t)$ are then defined by (3.8), with the phase given by

$$\theta(t) = \arg\left(\zeta(t)\right). \tag{3.10}$$

The analyzed trajectory $x(t)$ needs to represent a narrow band signal in order to obtain a meaningful phase by means of the Hilbert transform.

Remark 3.9 The spectral technique is nonlocal in time due to the infinite integral bounds in (3.9), thus, its real-time applicability is limited. Yet it is a well-suited tool for off-line analysis.

Remark 3.10 Both the state-space and the spectral technique require the observable x to be zero-mean, in order to yield phases that cover an angular range of π per half-period.

3.3 Analytical Results

In this section, results from the analysis of HHI behavior with importance towards a behavioral model of interpersonal movement coordination are presented. Starting with a purely descriptive data representation, we identify key patterns of movement synchronization, which are in consecutive steps further characterized both in terms of their steady-state and transient properties.

3.3.1 Synchronization Patterns

Stable relations between the movements of the dyads are established over the course of the trials [196]. The Lissajous plotting technique is adopted to intuitively visualize emerging

[1] The scalar trajectory $x(t)$ is treated as a signal.

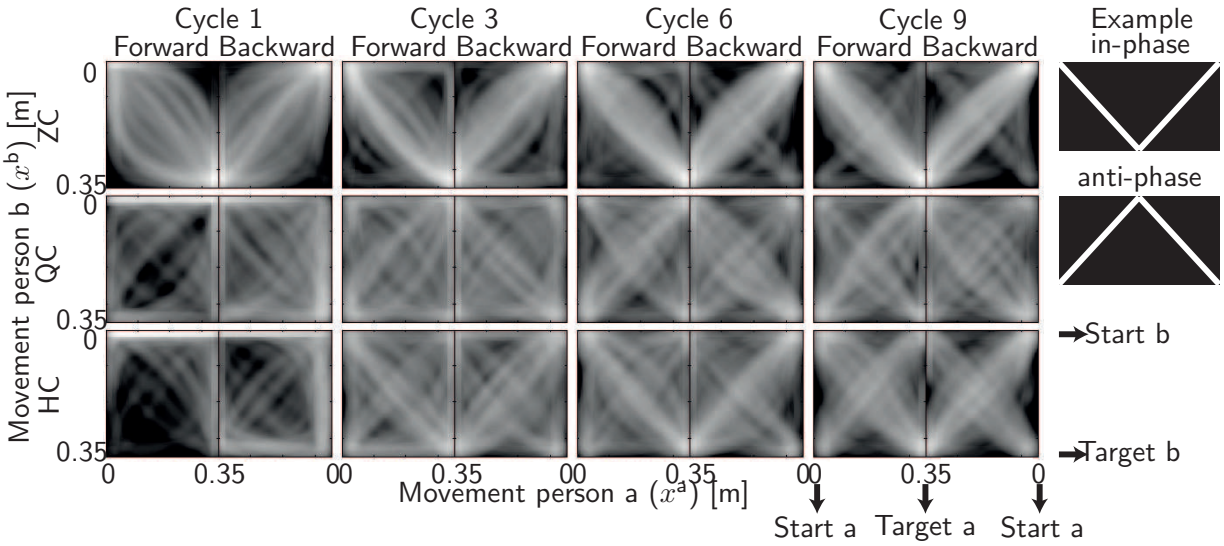

Fig. 3.6: How did synchrony evolve? Visualization of synchronization as Lissajous plots of the hand position of person b relative to that of person a, accumulated in a heat map. Data are plotted separately for the conditions zero-cycle (ZC), quarter-cycle (QC) and half-cycle (HC) as well as for the first, third, sixth and ninth cycle. The dyads tend to synchronize already early in the trial.

synchronization patterns. Position x^{b} of person b is represented as a function of position x^{a} of person a. In order to capture movement data of all trials, the frequency distribution is plotted as a heat map, in which brightness codes frequency. For each trial and cycle, the actual position of person b is determined as a function of person a's position. The resulting curves are sampled with an underlying grid of 100 × 100 bins. Forward and backwards movement are plotted separately, see Figure 3.6. In these plots, perfect 1:1 in-phase or anti-phase synchrony appear as straight diagonal lines, see Figure 3.6 right. When participants are not perfectly synchronized, data appear curved.

Remark 3.11 The in-phase and the anti-phase relation are particularly easy to identify in this graphical representation because they appear as straight lines. Other phase relations show gradually changing elliptic patterns.

Most importantly, the heat map visualizes that in-phase and anti-phase relationships are already established early in the trial. During the first cycle, data tend to be curved for all conditions. After that, movements are quickly adapted, which is depicted by the curves becoming straighter. Data of the zero-cycle condition shows that people are already almost perfectly adapted to each other after having performed the third cycle. Straight lines become prevalent indicating in-phase movements. In contrast, during the half-cycle condition both the in-phase and anti-phase relation are established roughly equally often until the ninth cycle. Roughly the same result is observed for the quarter-cycle condition, yet more curved lines appear during the quarter-cycle condition. Constant phase relations are established later there. This indicates that it is more difficult to establish a stable in-phase or anti-phase relation when starting off in an odd temporal relation.

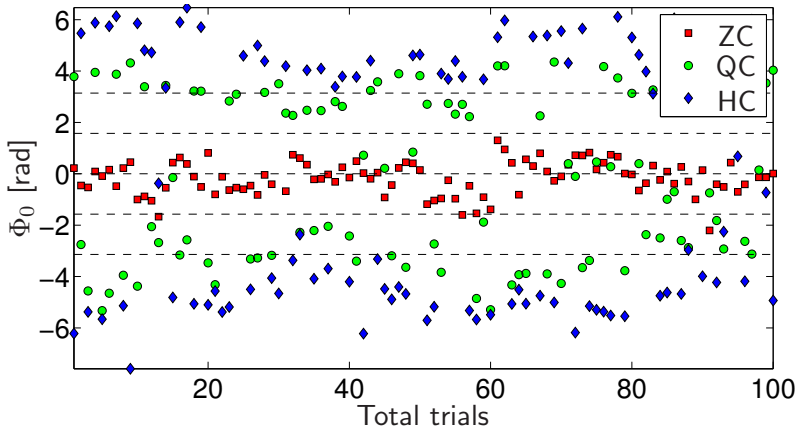

Fig. 3.7: Actual initial phase differences $\Phi_0 = \Phi(t = 0)$ over all trials for the conditions zero-cycle (ZC), quarter-cycle (QC) and half-cycle (HC), calculated with the spectral technique. Time $t = 0$ denotes the movement onset of the delayed person. Dashed lines indicate the phase relations triggered by the start off conditions.

3.3.2 Observing the Response to Initial Excitation

Considering the human interactive behavior as a system to be identified by system-theoretic methods bears differences compared to the identification of purely physical or technical systems. Two of them with importance to the experimental design are investigated in the following:

- Choosing reasonable observation lengths of human response behavior.
- Verifying effectiveness of the excitation induced by the presented stimulus.

Experimental Observation of Synchronization

In theory, a coupled oscillatory system is called synchronized, if its phase difference stays bounded for all times. However, in an HHI experiment, we are obliged to apply a weaker criterion to investigate synchronization due to a limited available observation length of human movements: A thorough trade-off between capturing a potential process of phase convergence and the influence of the participants' fatigue increasing over time has to be made. With the observation length of ten cycles chosen in the experiment, we are able to show that the transient process of synchronization is happening in the very first cycles of the task. The mutual temporal differences between the actions of both agents at key events, such as the time of target entry are significantly decreasing within the first three cycles only [196], which makes a length of ten cycles a reasonable choice.

Initial Phase Difference

In order to verify the efficacy of the excitation by the acoustic stimuli, the actually achieved initial phase differences are illustrated in Figure 3.7. The distribution shows clusters for the different start-off conditions, yet under quarter-cycle and half-cycle with an additional phase delay around π with respect to the phase relation which is intended to be triggered

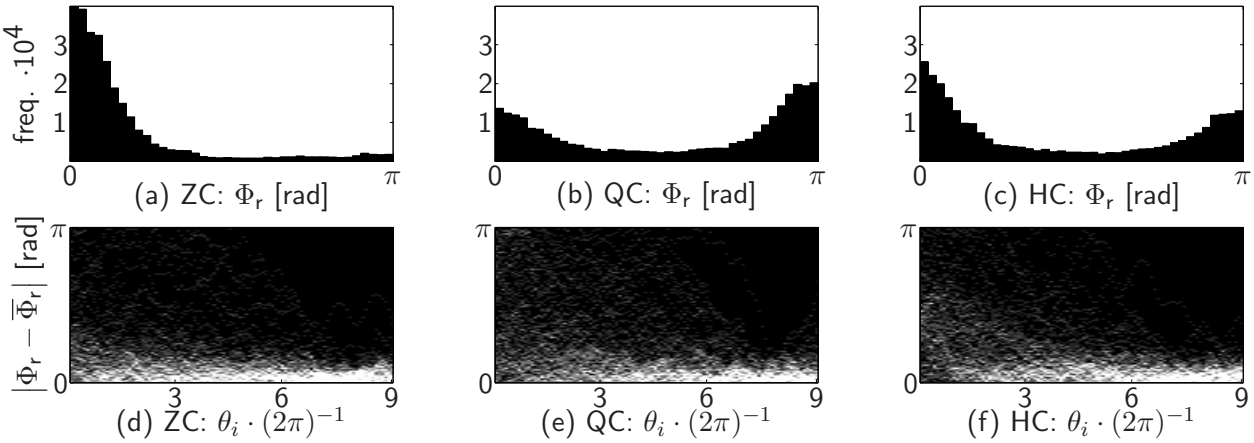

Fig. 3.8: Histograms of the relative phase difference Φ_r (a)-(c), and heat maps depicting the transients of Φ_r towards the respective attractor $\overline{\Phi}_r$ (ordinate) (d)-(f), accumulating all trials in the three conditions. Brightness codes frequency. The plot is indexed by the phase θ_i of the delayed person (abscissa). Phases are obtained from the spectral technique.

by the respective start off condition. These delays are mainly caused by the participants' reaction and dwell times when engaging in action. Due to the simultaneous start-off trigger, the actual initial phase difference is affected less by the delay in the zero-cycle condition. The symmetry of Φ_0 observed in Figure 3.7 is due to the balanced triggering of action start off. Being first is equally often assigned to each of the partners. In brief, the applied conditions are shown to effectively trigger a broad distribution of different initial phase relations, which is a prerequisite to perform reliable parameter estimation based on the response dynamics of the dyads.

Remark 3.12 In goal-directed tasks, a leadership among the dyad is defined by evaluating the sign of the phase difference $\Phi = \theta^{\mathrm{a}} - \theta^{\mathrm{b}}$: Positive values, i.e. person a's phase θ^{a} greater than person b's phase θ^{b} mean that person a is leading the task by preceding person b's action and vice versa.

3.3.3 Attractor Regimes

Histogram Analysis

In addition to the graphical representation of synchronization in the heat maps, the phase difference allows to further characterize the attractive domains of the synchronization process. Prevalent phase relations can be made visible by histogram representations of the phase difference time series, see Figure 3.8a-c. Since the attractor regime is sufficiently characterized by the relative phase relation within the dyad, we define the relative phase difference

$$\Phi_{\mathrm{r}}(t) = \begin{cases} |\Phi(t) \bmod 2\pi|\,, & \text{if } |\Phi(t) \bmod 2\pi| \leq \pi \\ 2\pi - |\Phi(t) \bmod 2\pi|\,, & \text{otherwise.} \end{cases}$$

The data samples of $\Phi_{\mathrm{r}}(t)$ are assigned to 40 equally spaced bins in $[0, \pi]$ and accumulated over all trials. Totally uncorrelated phases would cause approximately uniform distributions, whereas perfectly synchronized phases would result in sharp vertical lines. Distinct peaks at angular values around multiples of π are common to the histograms in the three conditions zero-cycle (ZC), quarter-cycle (QC) and half-cycle (HC), which suggest the attractors 0 and π. Those peaks would become even sharper if only the second half of each trial is considered, indicating nearly completed transient processes. The center values of such peaks can thus be treated as relevant features for the purpose of modeling. The width of the peaks is associated with the variance and the synchronization index (3.5) respectively.

With a closer look at the distributions, it can be stated that in ZC (Figure 3.8a), the participants' phase difference predominantly stays in a single regime around $\Phi_{\mathrm{r}} = 0$, which refers to the in-phase relation. Starting off in-phase means attaining the in-phase relation in nearly all of the trials. In QC (Figure 3.8b), two attractor regimes become visible, the in-phase attractor but also an attractor at $\Phi_{\mathrm{r}} = \pi$, which refers to the anti-phase relation. Starting off in quarter-cycle leads to both the in-phase and anti-phase relation, while it seems as if the latter was preferred. In HC (Figure 3.8c), the same attractors as in quarter-cycle appear. Starting off in HC leads idem to both the in-phase and anti-phase relation. Both in QC and HC, the actual initial phase differences are close to either of the preferred relations, cf. Figure 3.7, which explains the appearance of both attractors in the corresponding histograms.

Analysis of Transients

The histograms show the prevalent relative phase relations *over trials*, which are $\Phi_{\mathrm{r}} = 0, \pi$. Though two attractors can be clearly identified in Figure 3.8b-c, it can not be determined from the histograms, whether spontaneous switches between them occur *within trials*. Therefore, we investigate the transients of the relative phase difference $\left|\Phi_{\mathrm{r}}(t) - \overline{\Phi}_{\mathrm{r}}\right|$ over the cycles, where

$$\overline{\Phi}_{\mathrm{r}} = \frac{1}{N - \left\lfloor \frac{2N}{3} \right\rfloor + 1} \sum_{j=\left\lfloor \frac{2N}{3} \right\rfloor}^{N} \Phi_{\mathrm{r}}(t_j)$$

denotes the mean of each time series $\Phi_{\mathrm{r}}(t)$ taken over the last third of the total samples N of each trial. The resulting distributions depicted in Figure 3.8d-f are nicely aligned around zero between the sixth and the ninth cycle for most of the trials, which illustrates overall convergence to one of both attractors. The distributions appear scattered between zero and π up to the sixth cycle, again indicating convergence in the very first cycles of interaction. No preferred clusters around π are visible. Thus, we can conclude that besides the initial convergent process, within-trial switches between both attractors rarely occur during the observation length.

In short, both the Lissajous-like heat map presented in Section 3.3.1 and the above distribution of phase difference provide clear evidence of synchronization behavior in the goal-directed task. The process of synchronization is characterized by two attractor points of the relative phase difference, namely the in-phase and the anti-phase relation.

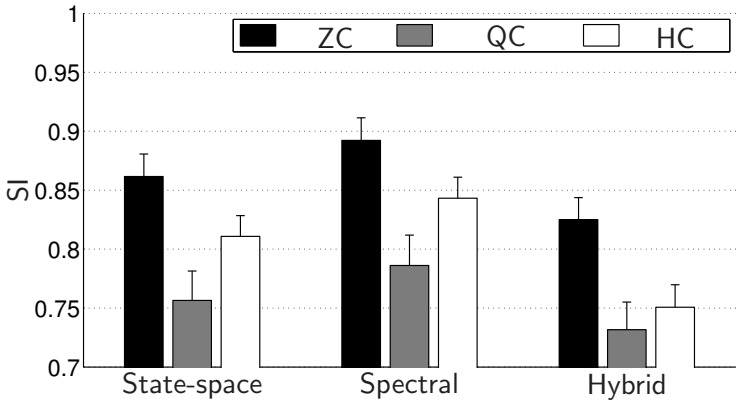

Fig. 3.9: Synchronization index SI for the conditions zero-cycle (ZC), quarter-cycle (QC) and half-cycle (HC), averaged over all trials. For comparison, the SI is calculated separately for the state-space, spectral and hybrid technique. The bars represent standard errors of the means.

3.3.4 Synchronization Index

The synchronization index SI given by (3.5) quantifies synchronization in a single number. Based on the definition that the collective remaining constant over time yields the highest degree of synchronization, the measure penalizes any variability of the collective including e.g. the transient process of getting synchronized. However, it has to be noted that the choice of the variables constituting the collective of the system affects this measure.

Comparison of Phase Estimation Techniques

The differing scores of the synchronization index SI presented in Figure 3.9 illustrate the influence of the phase estimation technique. Besides the state-space and the spectral technique reviewed in Section 3.2.3, results of the hybrid technique presented in [201] are reported as well. A one-way repeated measures ANOVA was performed to assess the difference between the SI obtained from the state-space, spectral and hybrid technique. As the sphericity criterion was not met, Greenhouse-Geisser correction was applied. SI differed quantitatively, $F(1.2, 34.9) = 66.78, p < .001$, which can be explained by a differing sensitivity of the technique to the apparent variabilities in the movement trajectories. Only the dominating frequency determines the phase of the spectral technique ($\overline{\mathrm{SI}} = 0.84$), which makes it rather insensitive to small, local movement variabilities. In contrast, such variabilities directly influence the instantaneous phase of both the state-space ($\overline{\mathrm{SI}} = 0.81$) and the hybrid technique ($\overline{\mathrm{SI}} = 0.77$). The inferior score of the hybrid technique suggests that the parameterization of the minimum jerk model chosen as the primitive representation [201] does not perfectly match the movement profiles observed in the experiment.

Relation to Attractor Strengths

In ZC, the highest index values are achieved on average. Thus, starting off in ZC enables the partners to reach highest quality of synchronization. Starting off in QC yields lowest values due to a rather high phase variability within the dyads, which is in agreement

with the distribution in Figure 3.8b. Medium index values are attained in HC. Though the resulting indexes show numerically similar trends within techniques, one-way repeated measures ANOVAs with the within-subject factor condition (ZC, QC, HC) performed for each technique did not reveal any significant differences between start off conditions, all $p > .05$. If we interpret the synchronization index as an indication of strength of the involved attractors, the attractor strengths of the in-phase and the anti-phase relation can not be distinguished in the present goal-directed task. In contrast, research work on interpersonal movement synchronization in purely rhythmic tasks provides evidence of differing attractor strengths. The anti-phase attractor is usually weaker than the in-phase attractor, or it even disappears completely [139, 150].

Remark 3.13 SI is calculated for whole trials including the transient process of synchronization. If the effects of transients is reduced by calculating the SI for the second half of the trials, qualitative results still show a similar trend.

3.4 Human-Human Synchronization Model

The dynamical systems approach is adopted in the following to describe movement synchronization. Emerging coordination patterns are represented by the attractors of a dynamical system. Thereby attractors denote the regions in the state-space to which the state trajectories of the system are attracted. In particular, we treat the observed phenomena of movement coordination in the goal-directed action task as a synchronization problem of two coupled oscillators forming a coupled dynamical system, which is in line with existing modeling approaches [53, 131, 152]. Therefore, we set up the appropriate model structure, which is then investigated with respect to its parameters, stability and predictive properties. Finally, we present the quantitative results obtained from gray-box parameter identification.

3.4.1 Model Structure

Coupled Phase Oscillators

First, we recall the general equations of motion of two limit cycle oscillators (3.2) that are mutually coupled. Under the assumption that the coupling functions are weak and the oscillatory dynamics are harmonic [87], the above equations can be reduced to a simpler set written in terms of the phase angles $\theta^{\mathrm{a/b}}$ of the oscillators as

$$\begin{aligned} \dot{\theta}^{\mathrm{a}} &= \omega^{\mathrm{a}} + C^{\mathrm{a}}(\theta^{\mathrm{b}} - \theta^{\mathrm{a}}) \\ \dot{\theta}^{\mathrm{b}} &= \omega^{\mathrm{b}} + C^{\mathrm{b}}(\theta^{\mathrm{a}} - \theta^{\mathrm{b}}), \end{aligned} \tag{3.11}$$

where $\omega^{\mathrm{a/b}} \in \mathbb{R}$ are the natural frequencies of the oscillators and $C^{\mathrm{a/b}} : \mathbb{R} \to \mathbb{R}$ the coupling functions depending on the phase difference between the oscillators.

Remark 3.14 In the modeling approach, the phases $\theta^{\mathrm{a/b}}(t)$ are assumed to be quasi-harmonic. Harmonicity of phases is either fulfilled due to the harmonic nature of the

movement trajectory, or it has to be ensured by appropriate phase transformations, e.g. the marker-based technique presented in Section 4.2.4.

Extending the Kuramoto Model

Several candidates for the coupling functions $C^{\mathrm{a/b}}$ in (3.11) are found in literature in the context of movement synchronization. One of them is the sinusoidal function proposed by Rand et al. [131], which yields the model equations

$$\dot{\theta}^{\mathrm{a}} = \omega^{\mathrm{a}} + K \sin(\theta^{\mathrm{b}} - \theta^{\mathrm{a}}) \tag{3.12}$$

$$\dot{\theta}^{\mathrm{b}} = \omega^{\mathrm{b}} + K \sin(\theta^{\mathrm{a}} - \theta^{\mathrm{b}}). \tag{3.13}$$

It is known as the classical Kuramoto model established by Kuramoto [87], where $K \in \mathbb{R}$ is the coupling gain between the oscillators. It is assumed to be isotropic for both oscillators. The model structure of coupled Kuramoto oscillators is adopted for the following reasons:

- Despite its simplicity, the observed main effects of synchronization are replicated: The natural frequencies refer to the agents' individual frequency levels as an individual behavior, whereas the additive non-linear coupling term allows weak synchronization between the agents to emerge.

- Emerging synchronization is explained as an effect of co-adaptation via isotropic bidirectional coupling. The directionality of the coupling characteristics would be hard to identify from short-time bivariate data recorded during natural HHI, since unsynchronized regimes have to be observed extensively [160].

- The goal-directedness of the task constrains the amplitudes of movements, thus only the quasi-harmonic phase variables need to be considered. The two-degrees-of-freedom model is expected to foster robust parameter identification from noisy experimental data.

The phase difference dynamics of the oscillator pair are obtained by subtracting (3.13) from (3.12). It can be compactly written as

$$\dot{\Phi} = \Delta\omega - 2K \sin \Phi, \tag{3.14}$$

with $\dot{\Phi} = \dot{\theta}^{\mathrm{a}} - \dot{\theta}^{\mathrm{b}}$ and the frequency detuning $\Delta\omega \in \mathbb{R}$, defined as

$$\Delta\omega = \omega^{\mathrm{a}} - \omega^{\mathrm{b}}. \tag{3.15}$$

The analytical results in Section 3.3 show that the phase relation between the interacting agents ends up predominantly either in in-phase ($\Phi = 0$) or in anti-phase ($\Phi = \pi$). Therefore, we extend the phase difference dynamics (3.14) by two additional equilibrium points per period of Φ, which yields the new differential equation of the phase difference

$$\dot{\Phi} = h(\Phi) = \Delta\omega - 2K \sin(2\Phi). \tag{3.16}$$

The corresponding model equations read

$$\dot{\theta}^{\mathrm{a}} = \omega^{\mathrm{a}} + K \sin\left[2\left(\theta^{\mathrm{b}} - \theta^{\mathrm{a}}\right)\right] \tag{3.17}$$

$$\dot{\theta}^{\mathrm{b}} = \omega^{\mathrm{b}} + K \sin\left[2\left(\theta^{\mathrm{a}} - \theta^{\mathrm{b}}\right)\right], \tag{3.18}$$

which is called the *extended Kuramoto model* in the following.

3.4.2 Stability Analysis

Next, the stability of the equilibrium points of the extended Kuramoto model is investigated.

Proposition 3.1 The extended Kuramoto model (3.17) and (3.18) has equilibrium points Φ_{e}, if and only if the parameter set $(\Delta\omega, K)$ satisfies the inequality

$$2\,|K| - |\Delta\omega| \geq 0. \tag{3.19}$$

Proof: To find the equilibrium points, we set $\dot{\Phi} = 0$ in (3.16), which yields

$$2K \sin\left(2\Phi_{\mathrm{e}}\right) = \Delta\omega. \tag{3.20}$$

Due to $\sin(\cdot) \in [-1, 1]$, solutions of (3.20) only exist, if (3.19) holds. □

Graphically represented, the equilibrium points Φ_{e} are given by the points of intersection of the curves $2K\sin(2\Phi)$ and $\Delta\omega$, see Figure 3.10.

In order to analyze the stability of the equilibrium points, we investigate whether perturbations grow or decay. Let $\eta = \Phi - \Phi_{\mathrm{e}}$ be a small perturbation away from Φ_{e}. First, we derive a differential equation for η given by

$$\dot{\eta} = \frac{\mathrm{d}}{\mathrm{d}t}(\Phi - \Phi_{\mathrm{e}}) = \dot{\Phi} = h(\Phi_{\mathrm{e}} + \eta).$$

Using Taylor's expansion and noting that $h(\Phi_{\mathrm{e}}) = 0$, one gets

$$\dot{\eta} = \eta h'(\Phi_{\mathrm{e}}) + O(\eta^2),$$

where $O(\eta^2)$ gathers quadratically small terms in η. The gradient

$$h'(\Phi_{\mathrm{e}}) = \frac{\mathrm{d}}{\mathrm{d}\Phi} h|_{\Phi=\Phi_{\mathrm{e}}} = -4K\cos(2\Phi_{\mathrm{e}}) \tag{3.21}$$

denotes the attractor strength of Φ_{e}. If $h'(\Phi_{\mathrm{e}}) \neq 0$, the approximation can be written as

$$\dot{\eta} = \eta h'(\Phi_{\mathrm{e}}). \tag{3.22}$$

It can be seen from (3.22) that the perturbation η grows exponentially, i.e. the equilibrium Φ_{e} is unstable, if $h'(\Phi_{\mathrm{e}}) > 0$. It decays, i.e. Φ_{e} is stable, if $h'(\Phi_{\mathrm{e}}) < 0$. The stability analysis can be visualized by investigating the dynamics of the vector field on the abscissa

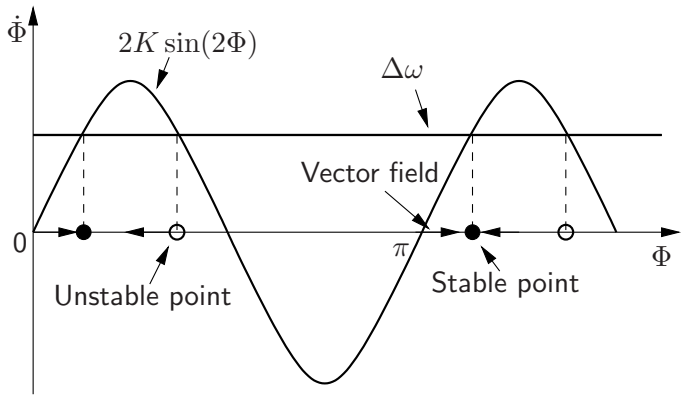

Fig. 3.10: Stability of the equilibrium points of the extended Kuramoto model. The phase difference between the two oscillators converges close to 0 (in-phase) or π (anti-phase) depending on the strength of coupling K and the frequency detuning $\Delta\omega$.

as shown in Figure 3.10. The solid and the open dots represent the stable and the unstable equilibrium points respectively. Two stable and two unstable equilibrium points exist per period of Φ.

Proposition 3.2 Besides the coupling gain K, the attractor strength (3.21) of the extended Kuramoto model is also function of the frequency detuning $\Delta\omega$. For $K > 0$, growing (decaying) of $\Delta\omega$ causes growing (decaying) of the stable equilibrium points Φ_e.

Proof: Solving (3.20) for the stable equilibrium point around $\Phi = 0$ yields

$$\Phi_\mathrm{e} = \frac{1}{2}\arcsin\frac{\Delta\omega}{2K},$$

with $\arcsin(\cdot)$ being strictly monotonic increasing in $[-1, 1]$. Due to periodicity, a similar relation can be derived for the stable equilibrium point around $\Phi = \pi$. □

Thus, the extended Kuramoto model explains an observed positive (negative) shift of the steady-state phase difference away from $0, \pi$ by a positive (negative) frequency detuning among the dyad.

Remark 3.15 The stable equilibrium points around $\Phi = 0, \pi$ have the same attractor strength and therefore equal stability properties, due to the 2π-periodicity of (3.21). The model structure is chosen, since there is no evidence for attractor switches or different attractor strengths in our goal-directed task.

Remark 3.16 The extended Kuramoto model can be modified to address different attractor strengths, yielding the phase difference dynamics

$$\dot{\Phi} = \Delta\omega - 2K\sin(2\Phi) - 2K_0\sin(\Phi)$$

with an additional sine term and coupling parameter $K_0 \in \mathbb{R}$. This is obviously the HKB model (3.1) extended to account for differing natural frequencies [39, 53].

Relation to the Natural Frequencies

The relation between the frequency detuning $\Delta\omega$ and the equilibrium frequency ω_e of the coupled oscillators in the extended Kuramoto model allows us to derive the natural frequencies $\omega^{\mathrm{a/b}}$, which describe the uncoupled oscillators. In equilibrium,

$$\dot{\Phi} = \dot{\theta}^\mathrm{a} - \dot{\theta}^\mathrm{b} = 0$$

holds, which is satisfied for the equilibrium frequency

$$\omega_\mathrm{e} = \dot{\theta}^\mathrm{a} = \dot{\theta}^\mathrm{b}. \tag{3.23}$$

This is the common frequency during synchronized regimes. It can be determined from experimental observation. Plugging (3.23) into the model equations (3.17), (3.18) and applying (3.15) yields

$$\omega^{\mathrm{a/b}} = \omega_\mathrm{e} \pm \frac{1}{2}\Delta\omega.$$

Thus, ω_e is the mean of ω^a and ω^b, which is a property of the Kuramoto model. In the context of behavior modeling, the natural frequencies indicate the agents' individually preferred movement cycle frequencies, which are assumed to be constant during interaction.

Remark 3.17 In the context of human motor behavior, however, the individual cycle frequencies predicted by the model have to be interpreted carefully. For instance, it is known that movement speeds differ when humans perform a motor task alone or jointly with others [180].

3.4.3 Identification and Results

Estimation of the Model Parameters

The model structure given by the non-linear dynamical equation (3.16) and the time series of the phase difference $\Phi(t)$ enables an estimation of the parameters $(\Delta\omega, K)$ for each trial. The estimation problem is solved with the iterative prediction-error method (PEM) [93], which minimizes an error objective function depending on the simulated model output and the time series data, as described in Section 2.2.3. A gray-box model which implements (3.16) is fed into the PEM-algorithm of *MATLAB System Identification Toolbox*. The initial state of the model is estimated jointly with the parameter set to achieve best fitting. Both the time-series data of the analytically derived phase difference and the simulated model output after the parameter estimation are illustrated for a representative trial in Figure 3.11. The dynamics of the trial investigated here are judged to be stable according to (3.19), hence the simulated phase difference converges to the attractor point close to π. Reasons for the oscillatory phase fluctuations visible in Figure 3.11 and present in most of the trials will be discussed in Section 3.5.

Remark 3.18 If the frequency detuning $\Delta\omega$ within the coupled system is known, which is e.g. the case for controllable eigenfrequencies of oscillatory mechanical systems, an alternative approach exists: The coupling strength K can then be identified via regression from

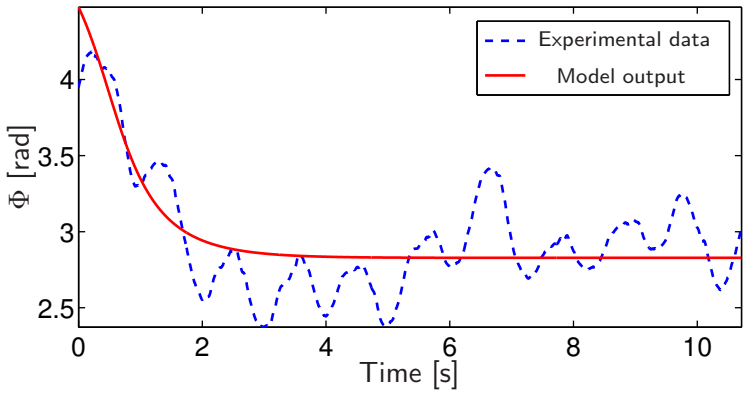

Fig. 3.11: Phase difference $\Phi(t)$ derived from experimental data via the spectral technique and simulated by means of the parameterized model. The parameters [rad·s^{-1}] are $\Delta\omega$=-0.49 and K=0.41 at an RMSE$_\Phi$=0.23.

Tab. 3.1: Means of estimated model parameters [rad·s^{-1}], mean RMSE$_\Phi$ assessing model fit and number of trials N_s with stable parameter sets. Means are taken over 294 valid trials, standard deviations are taken over dyads.

Phase technique	$\overline{\lvert K\rvert}$	SD$_{\lvert K\rvert}$	$\overline{\lvert K_s\rvert}$	$\overline{\Delta\omega}$	SD$_{\Delta\omega}$	$\overline{\text{RMSE}_\Phi}$	N_s
State-space	0.29	0.14	0.34	-0.08	0.19	0.41	218
Spectral	0.20	0.05	0.24	-0.06	0.14	0.26	223
Hybrid	0.29	0.11	0.33	-0.09	0.15	0.59	202

the phase difference Φ_e, which is observed during equilibrium $\dot{\Phi} = 0$ for different values of $\Delta\omega$, see the technique in [153].

Results of the Parameter Estimation

For comparison, the model parameters estimated for phase difference time series acquired with the state-space, spectral and hybrid technique are summarized in Table 3.1. The transformation of cyclic trajectories to phases is not unique, but based on certain assumptions as described in Section 3.2.3. The applied phase reconstruction technique affects the modeling results, consequently it is part of the modeling approach. More than two-thirds of the trials yield parameter sets with stable point attractors of the resulting dynamical system according to the stability criterion (3.19). Thus, it can be stated that the synchronization effects discovered in Section 3.3 are reproduced well by stable parameter sets in a majority of the trials. The influence of the unstable parameter sets on the overall coupling gain is rather small; if only the trials are considered, in which the partners synchronize according to (3.19), the coupling gain (denoted with $|K_s|$ in Table 3.1) is not much higher than $|K|$.

For statistical analysis, one-way repeated measures ANOVAs with the within-subject factor technique (spectral, hybrid, state-space) were performed. In order to compare the techniques, data was averaged over start off conditions. Greenhouse-Geisser correction was applied when the sphericity criterion was not met. In both cases a significant main effect between techniques is observed, $|K|$: $F(2,18) = 3.87$, $p < .05$, $|K_s|$: $F(2,18) =$

Tab. 3.2: Results of the trial-wise regression: R^2 represents the percentage of the variance explained by the model, N_v is the number of valid trials included into analysis for the respective condition, and $N_{p<.001}$ lists the number of significant model fits.

Phase technique	Condition	Median R^2	N_v	$N_{p<.001}$
State-space	Zero-cycle	0.313	98	98
	Quarter-cycle	0.994	97	97
	Half-cycle	0.996	99	99
Spectral	Zero-cycle	0.350	98	97
	Quarter-cycle	0.971	97	96
	Half-cycle	0.998	99	99
Hybrid	Zero-cycle	0.223	98	98
	Quarter-cycle	0.904	97	97
	Half-cycle	0.995	99	99

3.88, $p < .05$. Contrasts show that the spectral technique results in the smallest coupling gain on average compared to both the hybrid, $|K|$: $F(1,9) = 8.37$, $p < .05$, $|K_\mathrm{s}|$: $F(1,9) = 6.09$, $p < .05$, and the state-space technique $|K|$: $F(1,9) = 7.15$, $p < .05$, $|K_\mathrm{s}|$: $F(1,9) = 7.50$, $p < .05$, with the latter not being different from each other. This illustrates that the commonly detected synchronization effects are explained by a non-zero coupling term, though no instructions were given in the experiment, which would actively modulate the interaction.

A mean $\Delta\omega$ close to zero indicates a rather balanced frequency detuning over all dyads. Here, no significant differences between the techniques are found, $p > .6$. The considerably high SD $\Delta\omega$ leads to the conclusion that the frequency detuning predicted by the model is an individual parameter varying between dyads.

Evaluation of the Model Fit

For comparison of the root-mean-square error between model prediction and measurement (RMSE_Φ in Table 3.1) a one-way repeated measures ANOVA with the within-subject factor technique (spectral, hybrid, state-space) was performed. DoF were corrected with the Greenhouse-Geisser method. Highly significant differences between techniques are observed, $F(1.1, 9.7) = 28.37$, $p < .001$. Best model fit is achieved by the combination of the extended Kuramoto model and the spectral technique. It differs significantly from the RMSE_Φ obtained with the state-space technique, $F(1,9) = 167.47$, $p < .001$, and the hybrid technique, $F(1,9) = 38.53$, $p < .001$. Furthermore, RMSE_Φ is lower with the state-space than with the hybrid technique, $F(1,9) = 11.20$, $p < .01$. This is due to the filtering property of the Hilbert transform, as the frequency at the maximum of the power spectrum determines the instantaneous frequency and phase respectively. Both the state-space and hybrid technique are applied without filtering and thus, yield a higher phase variability than the spectral technique, which is not explained by the model.

Additionally, the goodness of fit achieved in combination with each of the three phase estimation techniques is assessed with the R-squared metric (R^2), which allows for an

estimation of how much variance of the data (in %) is explained by the respective model. The median values of the trial-wise R^2 are summarized in Table 3.2. In order to find out how often the variance of the data is explained above chance level, the significance of the per-trial model fit is tested by calculating the F-ratio. Nearly all of the valid trials yield significant fits, as reported in Table 3.2.

3.5 Discussion

Both the analytical results and the model identification provide evidence for and characterize the emerging synchronization of movements. Treating human dyadic interaction in a repetitive, goal-directed task as a synchronization problem with the phase difference of coupled oscillators as the collective seems to be a valid approach. Its implications are discussed in the following.

3.5.1 Interpretation of Results

In most of the trials, the participants fall into rhythmic patterns and synchronize as the effect of a spontaneously emerging, joint behavioral goal, although precision is required as individual goals for the partners. Special emphasis is put on the design of the task paradigm due to the potential dependency of results on the task context. The experimental setting is natural in the sense that it bears similarity to repetitive, goal-oriented action tasks. People are not instructed to synchronize, but only get an instruction required for the individual task performance, which allows natural interaction to emerge. Besides the start off condition, no control variables are introduced that could artificially modulate the flow of interaction. This should allow to interpret the results in the light of natural HHI.

As a result of the system identification, per-trial values of the parameter set $(\Delta\omega, K)$ are found. Within our modeling approach, the parameters are assumed to be time-invariant over the course of single experimental trials. The parameter sets averaged over trials can be treated as behavioral features of the dyads. However, accidental as well as deliberate parameter variations might be present due to both environmental influences and intrinsic changes of the human behavior.

The frequency detuning $\Delta\omega$ expresses shifts of the equilibrium points which attract the collective. It can serve as a measure of discrepancy regarding the agents' individually desired cycle frequency in the task. Furthermore, hypothetical natural frequencies of the agents can be determined. Their meaning might extend to the self-organization of leader and follower roles during movement coordination, which deserves, however, further investigation in the light of role behavior among humans.

The coupling gain K quantifies a dyad's weighing of two potentially competing goals: Being precise to fulfill the instructed goal versus being synchronized with the partner as an additional, voluntary goal. Non-zero mean values of K averaged over all trials indicate emerging interactive behavior of the partners which leads to the observed patterns of synchronization. The regression model employed by Schmidt et al. [153] to measure coupling strength and the extended Kuramoto model proposed in this chapter are locally identical due to the sinusoidal coupling, hence the resulting coupling from both task paradigms

can be put into relation. The overall mean[2] of $2\,|K|$ ($0.52\,\mathrm{rad}\cdot\mathrm{s}^{-1}$) in Table 3.1 is about one-third of the mean value ($1.70\,\mathrm{rad}\cdot\mathrm{s}^{-1}$) which is reported in [153] as the local model coupling strength of intentional interpersonal coordination. Since in their experiments, the participants were instructed to swing pendulums either in in-phase or anti-phase relation, a coupling strength stronger than in our spontaneous setting is plausible.

Residuals after Modeling

The extended Kuramoto model predicts only the dominant component of the collective dynamics via first-order non-linear dynamics. The median R^2 under condition ZC is remarkably low regardless of the technique. The measured phase difference remains constant and close to the attractor $\Phi = 0$ for most of the ZC trials, i.e. the dyad is initialized close to equilibrium. Therefore, the explanatory power of the extended Kuramoto model in ZC does not exceed much that of the pure mean value of the measured phase difference. Compared to the considerably high R^2 values obtained for the conditions QC and HC, this emphasizes the need for extensive observations of transient behavior in non-equilibrium regimes to gain meaningful model fits.

Spectral analysis of the residuals reveals oscillatory components at frequencies close to the participants' mean cycle frequency (0.73 Hz averaged over all trials), cf. Figure 3.11. This finding is in line with the observations made by [152] during the task of pendulum swinging. The oscillations can be explained by the following reasons. First and foremost, the observed phase fluctuations can be artifacts of the phase estimation. The instantaneous phase of measured oscillatory time series such as human movement trajectories can be uniquely determined only over cycles for a discrete marker event in the cycle, while the evolution within cycles strongly depends on the reconstruction technique. Neither the movement trajectories of the individuals are perfectly harmonic nor the phase estimation techniques achieve perfectly harmonic phases due to individual variabilities. Thus, the limit cycles appear in their state-space not perfectly circular but slightly distorted, see the example in 3.2.3. Even if we would assume equally distorted limit cycles for both partners, the phase difference $\Phi(t)$ would still oscillate with multiples of the cycle frequency, except for the case $\Phi(t) = 0$. In their note on coordination models, Fuchs and Kelso [39] show that these phase fluctuations can be reproduced by the original HKB model comprised by non-harmonic oscillators. Alternatively, this effect could be mitigated by linearizing phase estimation techniques.

Potentially, the model residuals contain additional relevant information. The coupling strength between the agents might not be constant over time but rather include a component depending on the individual phase. This assumption is backed by the workspace topology of the experimental task investigated here. Since simultaneous visual attention to one's own and the partner's movements is easier when getting close to the target area and the partner's workspace respectively, it might effect the coupling strength. The integrative role of the visual perception of relative phase is shown to affect the stability of coordination in [187].

[2] Values of K have to be doubled for comparison, since here, K refers to the single agent's unilateral coupling.

Influence of the Phase Estimation Technique

Different techniques on the calculation of instantaneous phases from experimental movement data are evaluated in this chapter. Their performance is assessed by

- the synchronization index SI, which penalizes the phase variability.
- the RMSE_Φ of the phase difference, which accounts for the residuals after model identification.

Comparison of the synchronization index and the RMSE-based model fit yield similar performance trends for the phase techniques. This similarity is explained by the following fact: The proposed model structure replicates the dominant process of phase convergence only, hence the model residuals directly reflect any additional variance of the collective. Both the RMSE_Φ and the SI are affected in the same way. Best performance results are achieved when the phases are generated by the spectral technique. Though it is a powerful tool when it comes to off-line analysis, the spectral technique is less suitable for on-line application. A short-time implementation of the Hilbert transform would be required, which comes at the cost of signal delay due to windowing. For movement tasks comprised by quasi-harmonic action sequences, where a two-dimensional state-space can be defined for embedding and the state variables can be constructed from measurement, the state-space technique is a good alternative. It can be also deployed on-line. The conceptual idea of the hybrid technique might be beneficially applied if the phase of more complex, non-harmonic primitive sequences is to be estimated on-line and models explicitly formulated in time exist.

3.5.2 Implications for the Design of Interactive Behavior

The composition of the individual (autonomous) and joint (collective) behavior defines the DoF of the presented behavioral model. Each is influenced by a single model parameter with an intuitive meaning:

- The autonomous oscillation renders an agent's individual behavior in that it ensures the urge and desired speed to proceed the action task. For the simple case of the harmonic phase oscillator, it is fully described by the natural frequency. Here, the phase represents the temporal distance to goal achievement, i.e. the completion of the period.
- The coupling function renders the agent's collective behavior, since it mediates the agent's urge to proceed depending on feedback from the partner's action. For the extended Kuramoto model, the characteristics and strength of this external forcing is fully defined by the sinusoidal coupling as a function of the difference between the own and the partner's phase.

Only few requirements have to be met in order to embed the behavioral model into the perception-action loop of robotic agents. In robotics, the phase oscillator is related to the notion of central pattern generators (CPGs) in its simplest form. CPGs are utilized to dictate the timing of continuous rhythmic motion, with or without environmental feedback.

Their application reaches back to bio-inspired modeling approaches of animal locomotion [18]. The phase evolution of the harmonic oscillator explicitly governs the timing of actions, i.e. in the unforced cases it represent the time variable. Thus, any kind of action generation scheme may be deployed provided that a formulation explicitly parameterized in time exists. An example with relevance to goal-directed HRI is the minimum jerk model [36], which replicates point-to-point movements of the human hand.

With regard to the informational coupling to the partner, the movement trajectory relevant to synchronization needs to be acquired, which is technically facilitated through visual tracking techniques. Perceptual processing delays should either be kept small or compensated to enable the desired temporal coordination. Similarly, the transformation of observed movements to the phase variable needs to be performed on-line. Since human movements are assumed to be non-stationary, the times of period completion are a-priori unknown. Therefore, phase estimation additionally requires predictions on the limit cycle. The state-space technique handles quasi-harmonic movements as observed in the movement task investigated above. However, joint action tasks such as the one investigated in Chapter 4 usually involve more complex limit cycle representations, which make the instantaneous phase estimation challenging. In this context, we will investigate an on-line version of the marker-based technique in Section 4.2.4.

3.6 Conclusion and Open Issues

The analytical perspective towards the design of interactive behavior is pursued, and a step-wise approach towards a behavioral model of human-human movement coordination is presented. Synchronization is discovered to be an essential principle of human movement coordination in the novel context of goal-directed action. Governed by a dynamical process, human dyads mostly fall into in-phase as well as anti-phase relations. The emerging relations are successfully replicated by the attractor dynamics of coupled phase oscillators inspired by the Kuramoto model, which is defined by the evolution of its phases. The proposed modeling concept fosters natural HHI and simultaneously facilitates the identification of the model parameters, which are the coupling strength and the frequency detuning among the dyad. Stable attractors resulting from the identified model match the movement relations observed in the experiment. The choice of the technique that transforms the movement trajectories into instantaneous phases is shown to significantly influence the model fit. Best fit is achieved by use of the spectral technique, which proves well-suited for the off-line analysis of simple repetitive actions. Due to the two-layered formulation of the coordination behavior in terms of the coupled phase dynamics and the movement-to-phase transformations, the concept facilitates the modeling of interactive behavior even if dyads are performing heterogeneous action tasks. By means of the identified model, interactive behavior of a robotic partner can be readily rendered on-line. Integrating the human behavioral model developed in this chapter, we will design and evaluate interactive behavior for joint action coordination of human-robot dyads in line with the synthetical perspective in Chapter 4.

Some interesting open issues remain concerning the endeavor of modeling human-human movement coordination. First and foremost, the directionality of coupling within the

dyads established through the visual modality could be assessed. However, this endeavor is challenging due to the noisy, short and bivariate time series data as obtained from the proposed experimental design. Actively controlling the coupling modality is suggested for the study design. Similarly, the potential dependency of the interpersonal coupling strength on the partners' visual foci or peripheral visual access respectively would be worth an investigation. In goal-directed settings such as the paradigm presented here, the determined coupling within dyads is supposed to reflect the individual weighing of the individually required goal fulfillment vs. the spontaneous desire to jointly synchronize. Particularly in the joint action context, the analysis of such kind of behavioral weighings poses further interesting challenges.

4 Synchronization Behavior for Action Coordination

Synchronization is a frequently observed phenomenon across different modalities and situations of interaction. In particular, the synchronization of movements is found to play an essential role in the interactive behavior of humans. Due to its ubiquity in human life, it is not surprising that evidence of interpersonal synchronization is provided in various laboratory tasks, that require jointly performed movements in shared workspaces, see e.g. [138, 139, 151, 178]. We showed in Chapter 3, that spontaneously emerging coordination patterns within human dyads also during goal-directed movement tasks are explained well by coupled dynamical processes of synchronization. This coordination behavior is even sustained, if an obstacle is placed unilaterally in the workspace such, that the movement trajectories become incongruent [198]. Studies targeting the social aspects of synchronization highlight that falling into synchrony with partners enhances perceptual sensitivity toward each other, fosters cooperative abilities [177] and leads to the attribution of more positive characteristics to the interaction partner [107]. These works give rise to the hypothesis, that bidirectional action coordination with synchronization as its key concept is a promising way to increase the social competence of robots when interacting with humans [100].

Inspired by the appealing prospect to enrich the interaction repertoire of robots, this chapter addresses the challenge of designing interactive behavior for artificial agents that engage in repetitive joint action tasks. These tasks involve actions performed by two or more individuals towards a shared goal in a common social setting, inducing action coordination in space and time [158]. Our goal is to develop enhanced interaction capabilities for robotic agents, which promote their social compatibility and support collision avoidance by increasing their predictability. Based on synchronization theory of coupled dynamical systems [126] and focusing on joint action coordination on a continuous time scale, we present a synchronization concept for repetitive, goal-directed movements composed by multiple primitives. In particular, limit cycle representations are found for the joint action task, that are segmented into sequences of primitives. Those can be mixed continuous and discrete, making the proposed concept applicable to a wide range of repetitive action tasks. Innovative is the synergetic integration of both the analytical and synthetical design perspective: Characteristics of human synchronization found in Chapter 3 are complemented by novel, enhanced synchronization modes within pairs of limit cycles, considering both continuous phases and discrete events from a unifying point of view. In line with the behavioral dynamics approach [149, 185], we design a dynamical process to synchronize the derived modes. Movement generation is addressed as well, in order to enable a robotic agent equipped with synchronization behavior to engage in repetitive joint action tasks. The presented experimental study employing a full-sized, anthropomorphic robot serves not only as proof of concept. It also defines a versatile testbed for the investigation of

human-robot action coordination in realistic settings.

This chapter is organized as follows: In Section 4.1 findings on human synchronization behavior, related approaches in robotics as well as applications of synchronization methods in human-computer and human-robot interaction are reviewed. Starting with a representation of the task and related definitions, we develop enhanced synchronization modes, the corresponding entrainment processes and the transformations between movements and phase in Section 4.2. Following the synthetical design perspective, in Section 4.3 synchronization behavior is implemented and a human-robot synchronization experiment is designed. The detailed assessment and evaluation of the implemented synchronization behavior is reported in Section 4.4. After the discussion of the results and insights in the context of human-robot joint action and from the design perspective in Section 4.5, we sum up and draw the conclusions in Section 4.6.

4.1 Background

Different aspects are related to the design of synchronization behavior from an interdisciplinary point of view. First, the background and results on continuous movement synchronization of human dyads presented in Chapter 3 are complemented by inspiring findings from research on human sensorimotor synchronization. Second, robotic applications implementing limit cycle systems are reviewed. Finally, we discuss works investigating human-machine movement synchronization in various application scenarios.

4.1.1 Human Sensorimotor Synchronization

The intended synchronization of human rhythmic movements with respect to purely discrete, periodic stimuli such as auditory metronome beats is often called sensorimotor synchronization (SMS). It is reproduced well by linear models of asynchrony correction based on variants of the Wing-Kristofferson model [188], see Repp [135], Repp and Su [137] for an exhaustive review. This class of simplified, linear models of phase and period correction assumes one sequential update per period, i.e. at the stimulus event. It is well-suited to explain perceptual and motor variabilities from an information-processing, cognitive point of view. Contrasting the aforementioned linear error correction with the dynamical system framework introduced in Section 3.1.2, it can be concluded that both modeling frameworks are not exclusively competing for the same phenomenon, but rather account for different synchronization processes present in different kinds of tasks [171]. When considering tasks and the available sensory feedback modalities that feature mixed discrete and continuous aspects, it is recently debated whether hybrid incarnations unifying both model classes may exist [136] or not [25], stating exclusivity of the modeled processes. Irrespective of the underlying process, it is found that the availability of discrete perceptual information such as distinguishable events during continuous movement provides anchoring points for time keeping with a stimulus and, thus, fosters human SMS [164]. Notably, in a recently investigated dyadic version of the finger tapping task, humans adjust their pacing on a fast time scale toward each other, thus improving coordination by mutually coupled SMS [79].

4.1.2 Limit Cycle Systems in Robotics

Models creating rhythmic movement based on self-sustained oscillators and thus, limit cycle systems are often called central pattern generators (CPGs) in robotics. The integration of sensory feedback is considered not necessary, yet it is often introduced to modulate CPG-based movements in response to the environment. In [127], the entrainment of robot drumming is modeled by a CPG based on a phase oscillator, which is connected to a non-linear dynamical system transforming the CPG signals into motion. While phase locking is achieved regarding the beats, linear interpolation is applied to obtain a continuous phase from the beat events. An extension of the CPG approach by reconfigurable dynamical systems is proposed in [24] to generate movements in multiple DoF. While switching is achieved between mixed discrete and rhythmic movements that are weakly constrained, the formulation seems to lack an intuitive specification of goal-directed tasks. In the same line of research, a unifying concept of encoding periodic movements based on dynamical systems which are capable of feedback modulation is presented in [41] and developed further in [125]. Adaptive frequency oscillators are proposed to on-line tune and extract the frequency and phase components of the trajectory. Results obtained from non-stationary trajectories, however, show a rather slow rate of convergence. Limit cycles used in CPGs offer robustness of motor behavior against perturbations, while also reducing the input dimensionality, i.e. few driving signals suffice to modulate the output behavior based on sensory feedback. An open issue is the missing methodology allowing a systematic, application-oriented design of CPGs. For a profound review of CPGs focusing on biological and robotic locomotion research, the reader is referred to [66]. An excellent review on design and classification of different limit cycle systems with a focus on robotic applications is provided in [15].

4.1.3 Human-Machine Movement Synchronization

Some works investigate the synchronization of rhythmic movements between humans and machines. Mutual entrainment is achieved by providing the human with visual or acoustic stimuli as real-time feedback to his movements. For example, a virtual walking assistant generating an acoustically-rendered pace is proposed to provide walking support to impaired persons [109]. Regular gait patterns are stimulated by a Kuramoto phase oscillator, while the natural frequency is modulated to enforce a target phase difference. The continuous phase dynamics is updated by discrete feedback obtained from the footstep events. Virtual partner interaction (VPI) is introduced by Kelso et al. [74] to systematically study human-machine coordination. In a proof-of-concept implementation, the coordination of finger movements between a human and a visually-rendered, virtual agent driven by the HKB model [53] is explored under different coupling conditions.

Few works address the mutual entrainment of rhythmic movements between human and robotic agents. Rope turning in cooperation with a human is investigated in [99] and later in [77] as an example of physically coupled, rhythmic entrainment. The robot manipulator is controlled to keep a certain phase relation between the sensed force and the turning frequency of the rope estimated by a classical phase-locked loop (PLL) [64]. Similarly, the idea of human-robot movement synchronization through a PLL is pursued in [174]. Wavelet transformation and Fourier series approximation extract and replicate rhythmic

movements of an a priori selected target frequency component. Demonstrated movements are imitated synchronously, yet the dynamics of synchronization are not considered explicitly. Both human-robot handshaking [72] and physical assistance for rhythmic knee movements [192] are realized by a model based on the Matsuoka neural oscillator [102]. This kind of synchronization-based control is proposed to foster purely rhythmic interaction with the human relying on torque feedback. Considering the same tasks, [147] implicitly achieve synchronization by employing an on-line polynomial design method of the attractor dynamics. This method originally proposed by Okada et al. [114] creates an attractor basin in the vicinity of a motion trajectory in state space, and thus allows to encode rhythmic movement trajectories.

All of the works above employ limit cycle systems to model interactive behavior. They are focused on fundamental research of human synchronization behavior and in the robotics domain, on the application of movement synchronization in experimental tasks that are mostly restricted to purely rhythmic trajectories. To the author's best knowledge, none of the existing works, except the author's previous [196, 201], analyze and model synchronization of goal-directed movement tasks with application to human-robot dyads.

4.2 Design of Synchronization Behavior

Applying synchronization theory of limit cycle systems and inspired by human behavioral principles, synchronization behavior is synthesized with application to repetitive joint action tasks. Descriptions of possible synchronization modes are derived, and a unified synchronization process is developed.

4.2.1 Representation of Repetitive Joint Action

This section provides the formal representations and definitions that are utilized in this chapter to characterize the joint action task as well as the behavioral goal of movement synchronization. Here, the notion of joint action originated from cognitive psychology [158] is extended to the interaction of robotic agents as well.

Definition 4.1 (Individual Task) Each agent's part of the joint action task is called the agent's individual task. It is represented by the state trajectory $\boldsymbol{\xi}(t)$, i.e. the evolution of the vector of relevant states $\boldsymbol{\xi} \in \mathbb{R}^n$ over time t.

Remark 4.1 The state vector can be composed by the configuration of the agent's limbs, his hand (effector) position, or any other coordinates that provide a minimal description of the movements associated with the individual task.

Remark 4.2 A certain set of states is considered suitable if the information conveyed through the chosen description allows to explain and model the synchronization behavior of the agents.

The proposed concept of movement synchronization exploits the repetitive aspect of the individual tasks. Therefore, the state trajectories are required to fulfill the conditions to be treated as cyclic representations.

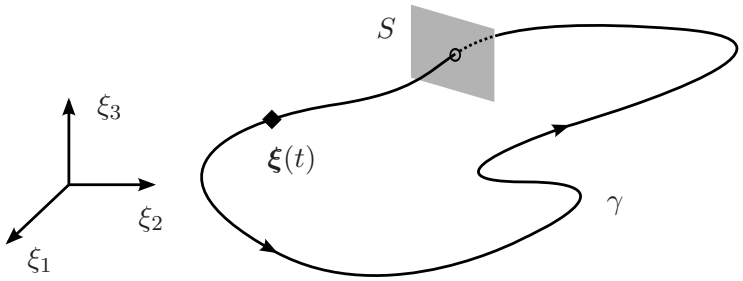

Fig. 4.1: Limit cycle γ of an exemplary cyclic state trajectory $\boldsymbol{\xi}(t)$ in its state space with $n = 3$. If γ is cyclic, yet not closed exactly, the period T is determined by the return time of $\boldsymbol{\xi}$ to the Poincaré secant surface S.

Continuous Representation – Limit Cycles

The state trajectory $\boldsymbol{\xi}(t)$ is assumed to be originated from self-sustained oscillations, i.e. it is *cyclic* and for any time t and certain finite time spans $T \in \mathbb{R}$ the condition

$$\boldsymbol{\xi}(t+T) = \boldsymbol{\xi}(t) \tag{4.1}$$

holds. The smallest $T > 0$ which fulfills (4.1) is denoted the *period*. It follows that the state space representation of $\boldsymbol{\xi}(t)$ is of circular shape, which is denoted the limit cycle $\gamma \subset \mathbb{R}^n$, see Figure 4.1. Due to interaction of the underlying oscillator with its environment, the period T may be time-varying. In this important case, γ is strictly speaking not periodic, but only recurrent or repetitive [61]. The (stable) limit cycle also represents an attractor of the dynamical system described by $\boldsymbol{\xi}$, since all trajectories initialized in the neighborhood of γ are attracted to it.

Remark 4.3 For trajectories subject to measurement noise or human variabilities, condition (4.1) is relaxed by examining the return times to the Poincaré secant surface [143], which allows for $\boldsymbol{\xi}(t+T) \approx \boldsymbol{\xi}(t)$.

Segmentation into Primitives

Definition 4.2 (Primitive and Segmentation Point) The limit cycle γ is composed by a number of $L \in \mathbb{N}$ segments $\mu_l \subseteq \gamma$ in an ordered sequence $l = 1, 2, \ldots, L$. Those segments are called primitives. Each primitive μ_l is delimited by two segmentation points, the start point $\boldsymbol{\xi}_{l-1} = \boldsymbol{\xi}(t_{l-1,i})$ and the end point $\boldsymbol{\xi}_l = \boldsymbol{\xi}(t_{l,i})$, see the example in Figure 4.2a. The positive index $i \in \mathbb{N}$ denotes the ith period.

The period is taken by $T_i = t_{L,i} - t_{0,i}$ in the following. It has to be noted that $\boldsymbol{\xi}_L \equiv \boldsymbol{\xi}_0$ and $t_{L,i} = t_{0,i+1}$ respectively, since $\boldsymbol{\xi}(t)$ is cyclic.

Definition 4.3 (Event) The instant of time $t_{l,i}$ for which $\boldsymbol{\xi}(t_{l,i}) = \boldsymbol{\xi}_l$ is called event, see Figure 4.2b.

Without loss of generality, we choose segmentation points featuring discriminable events, such as local extrema of the movement with vanishing velocity [84]. Segmentation points

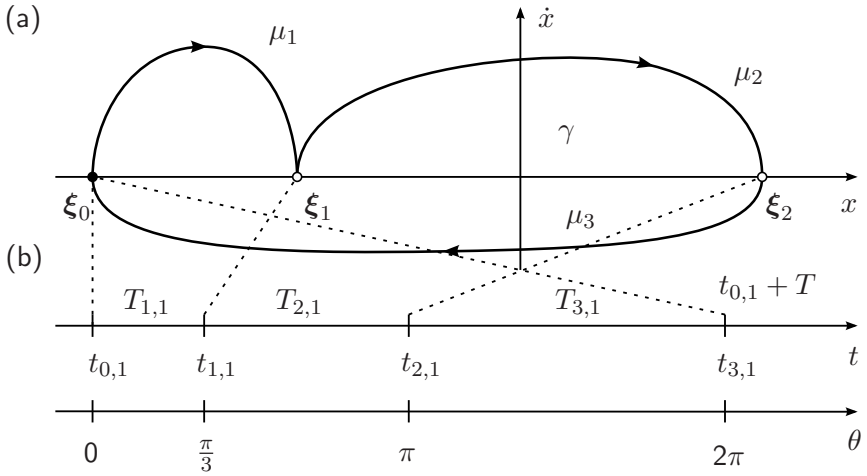

Fig. 4.2: (a) Exemplary limit cycle γ with the state $\boldsymbol{\xi} = [\, x \;\; \dot{x} \,]^{\mathsf{T}}$ and $L = 3$ primitives. The segmentation points $\boldsymbol{\xi}_i$ are given by the intersection of γ with the abscissa. (b) The corresponding events $t_{l,1}$, primitive durations $T_{l,1}$ and the uniformly growing phase θ depicted for period $i = 1$.

with zero or negligible velocity persisting for non-zero time intervals are considered as postures [61] and separate dwell primitives respectively. Those dwell primitives are also delimited by event pairs, denoting the times of movement stop and start. Discriminable events in cyclic trajectories are shown to support human mechanisms of temporal error correction [164], and thus affect human synchronization behavior.

Remark 4.4 The segmentation points $\boldsymbol{\xi}_l$ are assumed to be such, that any task-related constraints on the state are satisfied, i.e. goal points are hit and forbidden state regions are avoided.

The events $t_{l-1,i}$ and $t_{l,i}$ confine the primitive duration

$$T_{l,i} = t_{l,i} - t_{l-1,i}. \tag{4.2}$$

Definition 4.4 (Relative Primitive Duration) By relating the primitive duration $T_{l,i}$ and the period T_i, we further define the relative primitive duration

$$d_{l,i} = \frac{T_{l,i}}{T_i}. \tag{4.3}$$

It follows, that

$$\forall l : d_{l,i} \geq 0 \quad \text{and} \quad \sum_{l=1}^{L} d_{l,i} = 1. \tag{4.4}$$

When referring to the current period i, i.e. $t_{0,i} < t \leq t_{L,i}$, index i is omitted, and we simply write d_l. The L primitive durations d_l are gathered in the vector $\boldsymbol{d} = [\; d_1 \;\; \ldots \;\; d_L \;]^{\mathrm{T}}$.

Remark 4.5 The vector of relative primitive durations $\boldsymbol{d}$ thus provides the distribution according to which T_l is scaled under modulations of T.

Phase-Amplitudes Decomposition

Through coordinate transformation, a limit cycle γ with state $\boldsymbol{\xi} \in \mathbb{R}^n$ may be re-parameterized by the one-dimensional variable θ that is called the *phase* and describes the motion on γ, and the $(n-1)$-dimensional vector of *amplitudes* that describe motions transverse to γ. Phase and amplitudes are differentiated by their stability properties: The phase is neither stable nor unstable, whereas the amplitudes are stable coordinates. Consequently, after a perturbation of the state away from the limit cycle, we observe:

- The amplitudes relax back to the limit cycle.
- The phase remains neutrally, and thus, is easy to adjust.

The phase transformation is not unique. Different decompositions can be found for a certain limit cycle [40]. In this work, we assume the amplitudes to be constrained by the modeled action tasks. Consequently, only the phase is considered to be governed by synchronization.

Definition 4.5 (Phase) Among all possible transformations, we choose the phase obtained from the *harmonic phase oscillator*, which is one of the simplest oscillator models. Its unperturbed oscillations evolve at constant phase velocity $\dot{\theta} = \omega$, with positive $\omega \in \mathbb{R}^+$ denoting the natural frequency. Accordingly, its phase trajectory is defined

$$\theta(t) = \omega t + \theta_0, \tag{4.5}$$

which is growing uniformly in time with some initial phase θ_0. By setting

$$\omega = \frac{2\pi}{T}, \tag{4.6}$$

we further define the phase to be angular and 2π-periodic, evaluating

$$\theta(iT) = 2\pi i + \theta_0, \tag{4.7}$$

with index i counting periods.

Furthermore, the phase $\theta(t)$ needs to be uniquely related to a location of the state $\boldsymbol{\xi}(t)$ on γ. Therefore, the instant of time of the state hitting the secant surface as depicted in Figure 4.1 is denoted by the event $t_{0,i}$. We deliberately choose θ_0 such, that $\theta(t_{0,1}) = 0$ is anchored to the point $\boldsymbol{\xi}(t_{0,1}) = \boldsymbol{\xi}_0$ marking the event $t_{0,1}$. The phase of a *stationary* limit cycle with constant period T is then readily given by (4.5). The important case of *non-stationary* limit-cycles with a priori unknown period $T(t)$ is addressed by the instantaneous version of the marker-based technique presented later in this chapter.

Joint Behavioral Goal as Synchronization Problem

Agent a/b's individual task is represented by the limit cycle $\gamma^{\mathrm{a/b}}$ and assumed to be originated from self-sustained oscillations, which allows us to apply the theory of limit cycle oscillators. In order to describe the motion of the state on the limit cycle, the notion of phase is introduced and the harmonic phase is adopted.

Remark 4.6 The transformation into phase and amplitudes can be understood as a decomposition of the task into one DoF available for *voluntary* synchronization, i.e. the phase variable, and the remaining DoF *necessarily* complying with the task goals, i.e. the amplitude vector.

The joint behavioral goal is now treated as a synchronization problem by relating the phases $\theta^{\mathrm{a/b}}$ and the events $t^{\mathrm{a/b}}_{l^{\mathrm{a/b}},i^{\mathrm{a/b}}}$ of limit cycles pairs to each other in time. In addition to phase synchronization according to Definition 3.1, the quasi-simultaneous appearance of event pairs is considered, which is known as event synchronization [129].

Definition 4.6 (Event Synchronization) Let $t_{l,i}$ denote the time of the lth event in the ith period of γ. Then the event pair denoted by the tuple $(t^{\mathrm{a}}_{l^{\mathrm{a}}}, t^{\mathrm{b}}_{l^{\mathrm{b}}})$ shows event synchronization, if the events keep the temporal relation

$$\left|t^{\mathrm{a}}_{l^{\mathrm{a}},i^{\mathrm{a}}} - t^{\mathrm{b}}_{l^{\mathrm{b}},i^{\mathrm{a}}+m}\right| < \Delta t \quad \forall i^{\mathrm{a}}, \tag{4.8}$$

with some time span Δt and the period offset $m \in \mathbb{N}$.

Choosing $m = const.$ ensures to test for event synchronization of order 1:1. The choice of Δt is considered as problem dependent. To avoid ambiguities, a reasonable upper bound is given by

$$\Delta t \leq \frac{1}{2} \min_{i^{\mathrm{a}},i^{\mathrm{b}}} \left\{T^{\mathrm{a}}_{l^{\mathrm{a}},i^{\mathrm{a}}}, T^{\mathrm{a}}_{l^{\mathrm{a}}+1,i^{\mathrm{a}}}, T^{\mathrm{b}}_{l^{\mathrm{b}},i^{\mathrm{b}}}, T^{\mathrm{b}}_{l^{\mathrm{b}}+1,i^{\mathrm{b}}}\right\}, \tag{4.9}$$

which denotes half the minimum primitive duration or half the minimum inter-event distance respectively in the neighborhood of the considered pair $\left(t^{\mathrm{a}}_{l^{\mathrm{a}}}, t^{\mathrm{b}}_{l^{\mathrm{b}}}\right)$.

Remark 4.7 Definition 4.6 implies phase synchronization, since the time lag and, thus, the phase difference between the considered events is bounded. Event synchronization depending on the definition of relevant events provides a problem-specific characterization of the temporal organization of limit cycle pairs.

4.2.2 Synchronization Modes

After analyzing the common modes of the synchronization between quasi-harmonic trajectories, which are usually relevant for purely rhythmic movement tasks, we will broaden the repertoire of potential synchronization modes between limit cycles, that feature multiple primitives and events.

Modes between Harmonic Limit Cycles

Movement synchronization within human dyads is mainly investigated in task paradigms that require purely rhythmic movements such as finger tapping, and leg or pendulum swinging. These tasks are usually described by one-dimensional motion trajectories, resulting in the state $\boldsymbol{\xi} \in \mathbb{R}^2$ embedded in a position-velocity state space. Typically, each period of the trajectory is composed by two nearly equal and sinusoidal half-periods, allowing to characterize the oscillation as harmonic. Following Definition 4.2 and 4.3, the limit cycle γ of the state trajectory $\boldsymbol{\xi}(t)$ is segmented into $L = 2$ primitives $\mu_l \subset \gamma$, $l = 1, 2$, which are

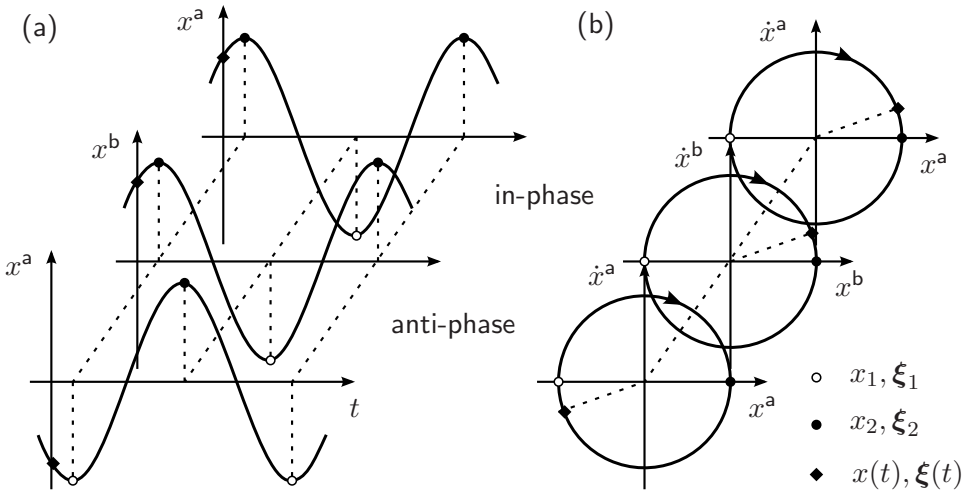

Fig. 4.3: Modes between harmonic oscillations: Phase synchronization resulting in in-phase or anti-phase relations comes about with event synchronization with respect to the segmentation points $\boldsymbol{\xi}_1^{\mathrm{a/b}}$ and $\boldsymbol{\xi}_2^{\mathrm{a/b}}$. (a) Motion trajectories $x^{\mathrm{a/b}}(t)$ illustrating the temporal relation. (b) Their limit cycle representations $\gamma^{\mathrm{a/b}}$ in a position-velocity state space, illustrating the phase difference.

symmetric due to their relative primitive durations being constant and equal with $d_l = \frac{1}{2}$, cf. Figure 4.3. For pairs of limit cycles $\gamma^{\mathrm{a/b}}$ originated from harmonic oscillations, the notions of the *in-phase* and the *anti-phase* relation usually characterize the common modes of synchronization. When we calculate the relative phase difference

$$\Phi_{\mathrm{r}}(t) = \Phi(t) \bmod 2\pi, \tag{4.10}$$

with $\Phi(t)$ from (3.4) and mod denoting the mathematical modulo division, the in-phase and the anti-phase mode map to $\Phi_{\mathrm{r}} = 0$ and $\Phi_{\mathrm{r}} = \pi$ respectively, cf. the angles in Figure 4.3b.

These modes are equivalently described by event synchronization: Evaluating the harmonic phase (4.5) at the event $t_{l,i}$ yields with (4.3)

$$\theta(t_{l,i}) = 2\pi \sum_{j=1}^{l} d_j + 2\pi(i-1). \tag{4.11}$$

For symmetric primitives with $d_1^{\mathrm{a/b}} = d_2^{\mathrm{a/b}} = \frac{1}{2}$, we obtain $\theta(t_{1,i}) \bmod 2\pi = \pi$ and $\theta(t_{2,i}) \bmod 2\pi = 0$. It follows that the relative phase difference (4.10) evaluates $\Phi_{\mathrm{r,e}} = 0$ and $\Phi_{\mathrm{r,e}} = \pi$, if the event pairs $(t^a_{1/2}, t^b_{1/2})$ and $(t^a_{1/2}, t^b_{2/1})$ appear synchronized. Summing up, quasi-harmonic cycles are considered to be composed by two symmetric primitives and events respectively. Their common synchronization modes are sufficiently described by the phase dynamics of coupled oscillator models [53, 131, 152, 201].

Modes between Multi-Primitive Limit Cycles

In repetitive joint action tasks, the limit cycles $\gamma^{\mathrm{a/b}}$ representing the agents' individual tasks can be composed by different sequences of multiple primitives, i.e. with the number

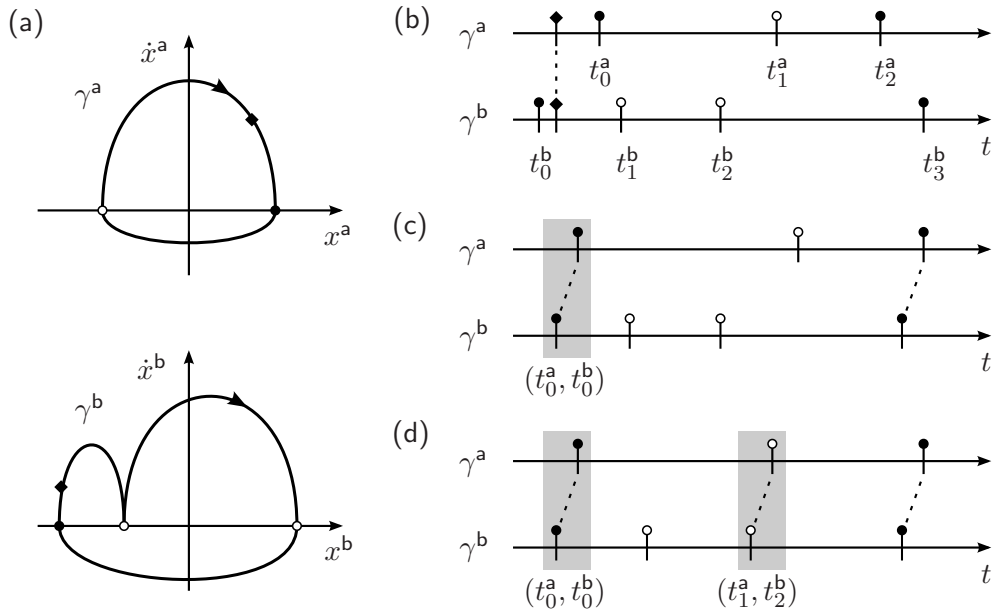

Fig. 4.4: (a) Exemplary limit cycles $\gamma^{\mathrm{a/b}}$ with $L^{\mathrm{a}} = 2$ and $L^{\mathrm{b}} = 3$ primitives in position-velocity state spaces. The evolution of the events in $\gamma^{\mathrm{a/b}}$, (b) without synchronization, (c) for synchronization of the events $(t_0^{\mathrm{a}}, t_0^{\mathrm{b}})$ as achieved by phase synchronization, (d) for additional synchronization of $(t_1^{\mathrm{a}}, t_2^{\mathrm{b}})$. The shaded areas indicate the time span Δt defining event synchronization.

of primitives $L^{\mathrm{a/b}} > 2$, the distributions of relative primitive durations $\boldsymbol{d}^{\mathrm{a}} \neq \boldsymbol{d}^{\mathrm{b}}$, or both. Here, the relevant modes of synchronization are assumed as the (simultaneous) synchronization of one or more event pairs $(t_{l^{\mathrm{a}}}^{\mathrm{a}}, t_{l^{\mathrm{b}}}^{\mathrm{b}})$, see the exemplary modes in Figure 4.4c-d.

By comparison of these modes it can be seen, that phase synchronization is not sufficient to describe the mode in Figure 4.4d. Phase synchronization models stable equilibrium points $\Phi_{\mathrm{r,e}}$ of the phase difference, which lead to $\Phi_{\mathrm{r}}(t) \to \Phi_{\mathrm{r,e}}$ and imply $T^{\mathrm{a}} - T^{\mathrm{b}} \to 0$ in the domains of attraction. This allows to synchronize single event pairs, like the one depicted in Figure 4.4c. If the within-cycle distributions of events differ, i.e. $\boldsymbol{d}^{\mathrm{a}} \neq \boldsymbol{d}^{\mathrm{b}}$ like in our example, the simultaneous synchronization of not more than one event pair is explained by pure phase dynamics. The events scale under changes of $T^{\mathrm{a/b}}$ with the distributions $\boldsymbol{d}^{\mathrm{a/b}}$, which are, however, left uncontrolled so far. Obviously, the simultaneous synchronization of *multiple* event pairs like the ones in Figure 4.4d requires an additional adjustment of $\boldsymbol{d}^{\mathrm{a/b}}$.

Remark 4.8 Only a task-dependent subset of events might be synchronized, e.g. only those that are perceived by the interaction partner or close to the partner's workspace.

4.2.3 Dynamical Entrainment Process

Synchronization behavior is modeled in line with the dynamical systems approach [185], which explains stable behavioral patterns by attractors of dynamical systems. First, we shortly review the phase dynamics derived in Chapter 3, that models the synchronization of human dyads performing quasi-harmonic limit cycles in a goal-directed movement task. The above analysis shows, that phase synchronization is able to account only for a limited

number of possible synchronization modes. Therefore, we design a unified synchronization process that features the simultaneous synchronization of multiple event pairs.

Phase Difference Dynamics

In accordance to the definition of phase synchronization, we recall the model structure (3.11) for a pair of cross-coupled phase oscillators. By subtraction, we obtain the phase difference dynamics

$$\dot{\Phi} = \Delta\omega + H(\Phi), \tag{4.12}$$

with $\dot{\Phi} = \dot{\theta}^{\mathrm{a}} - \dot{\theta}^{\mathrm{b}}$ and the frequency detuning $\Delta\omega = \omega^{\mathrm{a}} - \omega^{\mathrm{b}} \in \mathbb{R}$. The function $H : \mathbb{R} \to \mathbb{R}$ is the vector field of Φ forming the attractor landscape, which defines the preferred modes of phase synchronization.

Remark 4.9 Synchronization behavior is assumed to be voluntary and compliant with the task-related goals. We therefore require the coupling functions to be weak and 2π-periodic, i.e. equilibrium points Φ_e are equivalently described by equilibrium points $\Phi_{\mathrm{r,e}}$ of the relative phase difference (4.10) between the oscillators. Consequently, a large enough frequency detuning $\Delta\omega$ completely eliminates stable attractors, which is found to be in line with unintentional coordination behavior of humans [95].

Example 4.1 (The Extended Kuramoto Model Revisited) A realization that accounts for the observed process of human-human synchronization in goal-directed movement tasks is given by the extended Kuramoto model [201]. The natural frequencies model the individually preferred speed of task performance, whereas the sinusoidal coupling with the isotropic gain $K \in \mathbb{R}$ replicates the dyad's interactive behavior. The corresponding phase difference dynamics complying with the form of (4.12) reads

$$\dot{\Phi} = \Delta\omega - 2K \sin(2\Phi),$$

featuring two point attractors around $\Phi_{\mathrm{r,e},1} = 0$ and $\Phi_{\mathrm{r,e},2} = \pi$. The extended Kuramoto model implies equal attractor strengths for both the in-phase and the anti-phase attractor.

Synchronization of Single Event Pairs

In-phase and anti-phase synchronization between harmonic limit cycles is now generalized to synchronization modes of single event pairs in arbitrary combinations. Again, stable modes of synchronization are mapped to stable equilibrium points $\Phi_{\mathrm{r,e}}$ of the vector field H. The values of $\Phi_{\mathrm{r,e}}$, i.e. the locations in the attractor landscape, depend on the definition of the events $t_0^{\mathrm{a/b}}$ for which the initial phases (4.5) evaluate $\theta_0^{\mathrm{a/b}} = 0$. It makes sense to define them such, that the pair $(t_0^{\mathrm{a}}, t_0^{\mathrm{b}})$ denotes a synchronization mode, with the corresponding attractor $\Phi_{\mathrm{r,e}} = 0$. Using (4.11), the synchronization mode of any other event pair $(t_{l^{\mathrm{a}}}^{\mathrm{a}}, t_{l^{\mathrm{b}}}^{\mathrm{b}})$

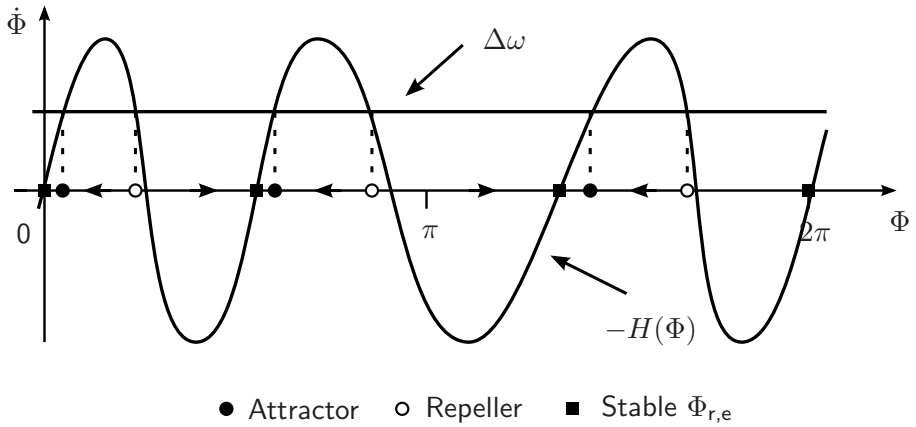

Fig. 4.5: R.h.s. terms of an exemplary phase difference dynamics (4.12) over $\Phi \in [0, 2\pi]$. The intersection points of the graphs of $\Delta\omega$ and $-H(\Phi)$ denote the equilibria with $\dot{\Phi} = 0$. The vector field is illustrated on the abscissa.

is then expressed by the equilibrium phase difference

$$\Phi_{\mathrm{e}} = \theta^{\mathrm{a}}(t^{\mathrm{a}}_{l^{\mathrm{a}}}) - \theta^{\mathrm{b}}(t^{\mathrm{b}}_{l^{\mathrm{b}}}) = 2\pi \left(\sum_{j=1}^{l^{\mathrm{a}}} d^{\mathrm{a}}_j - \sum_{j=1}^{l^{\mathrm{b}}} d^{\mathrm{b}}_j \right) . \tag{4.13}$$

For each event pair representing a synchronized mode, the vector field H of the phase difference dynamics (4.12) needs to feature a point attractor $\Phi_{\mathrm{r,e}}$, which is obtained from (4.13) with (4.10), see Figure 4.5 for an exemplary curve of H. The following points summarize the properties common to the design of the vector field H:

- The phase plot is of oscillating shape, modeling an alternating sequence of attractors and repellers.
- The gradient and extrema in the vicinity of an equilibrium point $\Phi_{\mathrm{r,e}}$ define its strength and region of attraction respectively [201], given a certain frequency detuning $\Delta\omega$.
- In order to obtain relative synchronization, we require $H(\Phi) = H(\Phi + 2\pi)$.
- In contrast to the extended Kuramoto model and similar coordination models, symmetry $H(-\Phi) = -H(\Phi)$ is generally not fulfilled.
- Positive (negative) values $\Delta\omega$ yield positive (negative) shifts of the attractor points.

Remark 4.10 The attractor landscape of the phase dynamics becomes time-varying, if the relative primitive durations $\boldsymbol{d}^{\mathrm{a/b}}$ are subject to adjustment, as proposed in the following.

Synchronization of Multiple Events Pairs

The dynamics of coupled phase oscillators (3.11) accounts for synchronization modes that can be achieved by mutual entrainment of both periods and phase difference within certain domains of attraction. However, the simultaneous synchronization of multiple event

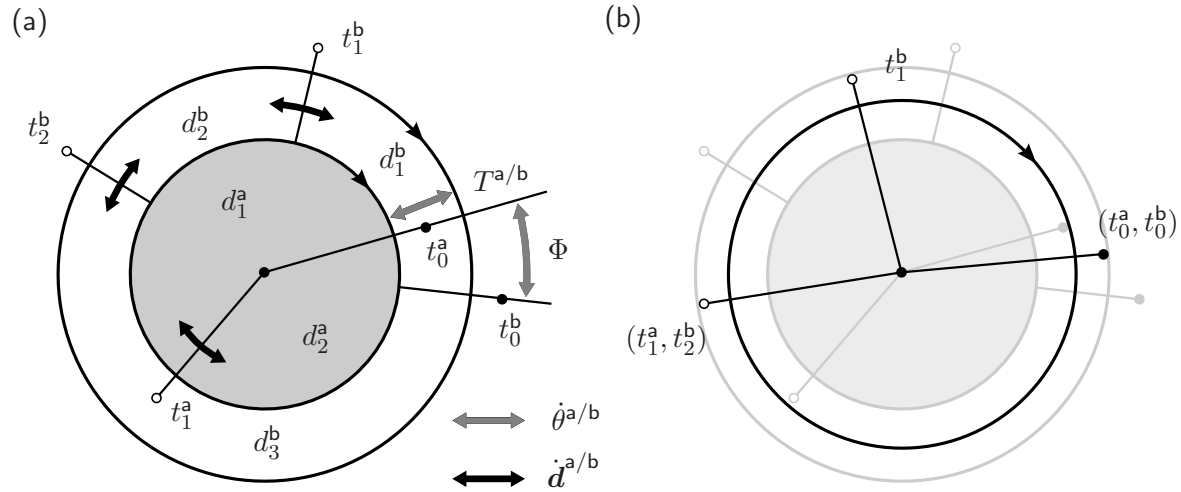

Fig. 4.6: Circular illustration of the synchronization problem between the exemplary limit cycles γ^{a} (inner circle) and γ^{b} (outer circle) introduced in Figure 4.4. (a) The DoF available for synchronization: The periods $T^{\mathsf{a/b}}$ and the phase difference Φ are both governed by the process (3.11). Additionally, the relative primitive durations $\boldsymbol{d}^{\mathsf{a/b}}$ are governed by the process (4.14). (b) Perfect synchronization of the event pairs $(t_0^{\mathsf{a}}, t_0^{\mathsf{b}})$ and $(t_1^{\mathsf{a}}, t_2^{\mathsf{b}})$, leading to coincident circles and events.

pairs remains generally unexplained, as shown previously. Therefore, the relative primitive durations $\boldsymbol{d}^{\mathrm{a/b}}$ are proposed as additional DoF, governed by the cross-coupled first-order dynamics of the form

$$\begin{aligned} \dot{\boldsymbol{d}}^{\mathrm{a}} &= \boldsymbol{D}^{\mathrm{a}}(\boldsymbol{d}^{\mathrm{a}}, \boldsymbol{d}^{\mathrm{b}}) \\ \dot{\boldsymbol{d}}^{\mathrm{b}} &= \boldsymbol{D}^{\mathrm{b}}(\boldsymbol{d}^{\mathrm{b}}, \boldsymbol{d}^{\mathrm{a}}), \end{aligned} \tag{4.14}$$

with the vector fields $\boldsymbol{D}^{\mathrm{a/b}} : \mathbb{R}^{L^{\mathrm{a}}} \times \mathbb{R}^{L^{\mathrm{b}}} \to \mathbb{R}^{L^{\mathrm{a/b}}}$ and $\boldsymbol{d}^{\mathrm{a/b}}$ subject to the condition (4.4). In Figure 4.6, the DoF of the overall synchronization process are illustrated for the exemplary mode in Figure 4.4d, which is defined for two event pairs.

Remark 4.11 Synchronization modes that would require to accommodate large differences between the components of $\boldsymbol{d}^{\mathrm{a/b}}$ or between combinations thereof might be infeasible, e.g. due to velocity constraints related to the agents' capabilities or their individual tasks.

Similar to the range of frequency detuning $\Delta\omega$ in (4.12) limiting stable phase synchronization, the process (4.14) is therefore assumed to be subject to locally bounded regions of attraction.

Remark 4.12 Normalization is preserved by adjusting the components of $\boldsymbol{d}^{\mathrm{a/b}}$ such that

$$\sum_{l=1}^{L^{\mathrm{a/b}}} \dot{d}_l^{\mathrm{a/b}} = 0, \tag{4.15}$$

which is the derivative of the normalization constraint in (4.4).

Example 4.2 (Entrainment of Relative Primitive Durations) In the following, we outline a possible realization of the process (4.14), that features the mode illustrated in Figure 4.6b. In this mode, the event pairs $(t_0^{\mathrm{a}}, t_0^{\mathrm{b}})$ and $(t_1^{\mathrm{a}}, t_2^{\mathrm{b}})$ appear synchronized simultaneously. The former is readily synchronized by the phase difference dynamics (4.12) employing the stable equilibrium point $\Phi_{\mathrm{r,e}} = 0$. In order to additionally synchronize the latter, we design the entrainment of $\boldsymbol{d}^{\mathrm{a}} = [\ d_1^{\mathrm{a}} \quad d_2^{\mathrm{a}}\ ]^{\mathrm{T}}$ to follow the dynamics

$$\dot{d}_1^{\mathrm{a}} = -\dot{d}_2^{\mathrm{a}} \tag{4.16}$$

$$\dot{d}_2^{\mathrm{a}} = K_d \sin \frac{\pi \left(d_{3,\mathrm{s}}^{\mathrm{b}} - d_2^{\mathrm{a}}\right)}{d_{2,\mathrm{u}}^{a} - d_{2,\mathrm{l}}^{a}}. \tag{4.17}$$

By (4.16), normalization is preserved. The positive gain $K_d \in \mathbb{R}^+$ in (4.17) enforces the solution $d_2^{\mathrm{a}} = d_{3,\mathrm{s}}^{\mathrm{b}}$ to be stable, saturated by

$$d_{3,\mathrm{s}}^{\mathrm{b}} = \begin{cases} d_{2,\mathrm{l}}^{a}, & \text{if } d_3^{\mathrm{b}} < d_{2,\mathrm{l}}^{a} \\ d_3^{\mathrm{b}}, & \text{if } d_{2,\mathrm{l}}^{a} \leq d_3^{\mathrm{b}} \leq d_{2,\mathrm{u}}^{a} \\ d_{2,\mathrm{u}}^{a}, & \text{otherwise.} \end{cases}$$

The positive thresholds $d_{2,\mathrm{l}}^{a}$ and $d_{2,\mathrm{u}}^{a}$ define the lower and upper bound on the entrainment of d_2^{a}. Assuming isotropic coupling between the agents, the entrainment of $\boldsymbol{d}^{\mathrm{b}}$ is designed analogously.

4.2.4 From Movement to Phase

The previously developed synchronization process governs the phase variables $\theta^{\mathrm{a/b}}(t)$ as well as the relative primitive durations $\boldsymbol{d}^{\mathrm{a/b}}(t)$. Since we target the integration of the synchronization behavior in the perception-action loop of robotic agents, the acquired movement trajectories need to be transformed on-line into these process variables. The problem considered first is to determine the partner's phase *instantaneously*, based on event predictions.

Marker-Based Technique

A novel, on-line version of the marker-based technique is proposed here. The marker technique is based on linear phase interpolation between a single marker event per period [143]. However, the desired phase variable is required to instantaneously reflect changes of the period here. Given a *prediction* of the event $\hat{t}_{0,i+1}(t) = \hat{t}_{L,i}(t)$ denoting the time of completion of the current period i, for time $t \in [t_{0,i}, \hat{t}_{0,i+1}(t))$ a phase estimate $\hat{\theta}(t)$ is proposed as the solution of

$$\hat{\omega}(t) = \dot{\hat{\theta}}(t) = \frac{2\pi i - \hat{\theta}(t)}{\hat{t}_{0,i+1}(t) - t}, \quad \text{with } \hat{\theta}(t_{0,i}) = 2\pi(i-1). \tag{4.18}$$

The instantaneous frequency or phase velocity (4.18) is given in the form of a linear differential equation with time-dependent coefficients.

Proposition 4.1 The phase obtained from (4.18) complies with Definition 4.5 prescribing the unperturbed phase evolution and 2π-periodicity.

Proof: In the unperturbed case, i.e. given a stationary limit cycle $t_{0,i+1} = const.$ and perfect prediction $\hat{t}_{0,i+1} = t_{0,i+1}$, the solution of (4.18) can be derived analytically. For the homogeneous part of (4.18) reading

$$\dot{\hat{\theta}}(t) + \frac{\hat{\theta}(t)}{\hat{t}_{0,i+1} - t} = 0$$

the general solution

$$\hat{\theta}(t) = C(t)(\hat{t}_{0,i+1} - t) \tag{4.19}$$

with parameter $C(t) \in \mathbb{R}$ is obtained. Applying the variation of parameters method, we derive

$$\dot{\hat{\theta}}(t) = \dot{C}(t)(\hat{t}_{0,i+1} - t) - C(t). \tag{4.20}$$

Plugging (4.19) and (4.20) into (4.18) yields

$$\dot{C}(t) = \frac{2\pi i}{(\hat{t}_{0,i+1} - t)^2}. \tag{4.21}$$

By integrating and inserting (4.21) in (4.19), one obtains

$$\hat{\theta}(t) = 2\pi i + C_0(\hat{t}_{0,i+1} - t) = 2\pi + C_0(\hat{t}_{0,i+1} - t) + \hat{\theta}(t_{0,i}), \tag{4.22}$$

with constant $C_0 \in \mathbb{R}$, which is for the initial condition $\hat{\theta}(t_{0,i})$ in (4.18) given by

$$C_0 = -\frac{2\pi}{\hat{t}_{0,i+1} - t_{0,i}}. \tag{4.23}$$

Finally, with (4.22) and (4.23) we can write

$$\hat{\theta}(t) = \frac{2\pi}{\hat{t}_{0,i+1} - t_{0,i}} (t - t_{0,i}) + \hat{\theta}(t_{0,i}),$$

which is obviously the harmonic angular phase. □

Time-varying predictions of the event $\hat{t}_{0,i+1}(t)$ are instantaneously reflected by the phase velocity (4.18), see the exemplary evolutions in Figure 4.7. Integration of (4.18) yields the estimated phase trajectory

$$\hat{\theta}(t) = \int_{t_{0,i}}^{t} \hat{\omega}(\tau)\mathrm{d}\tau + \hat{\theta}(t_{0,i}), \tag{4.24}$$

which is due to $\hat{\omega}(t) \geq 0$ monotonically increasing. For time $t \to \hat{t}_{0,i+1}(t)$, the solution of (4.18) converges $\hat{\theta} \to 2\pi i$.

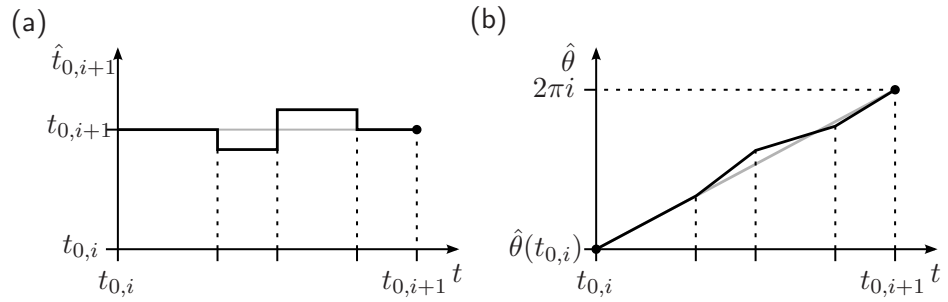

Fig. 4.7: (a) Exemplary evolution of the predicted event $\hat{t}_{0,i+1}$ over time t. (b) Corresponding evolution of the phase $\hat{\theta}$ obtained from (4.24). The slope of $\hat{\theta}$ instantaneously relates the left over phase $2\pi i - \hat{\theta} \geq 0$ in period i to the left over time span $\hat{t}_{0,i+1} - t > 0$. Black dots denote boundary conditions. Gray graphs depict perfect prediction and the corresponding harmonic phase respectively.

Remark 4.13 The marker-based technique is applicable on-line to any continuous or hybrid cyclic system, provided that a recurrent marker event can be distinguished and predicted. It is not restricted by the frequency components and the dimensionality of the analyzed observable.

Classification-Based Event Prediction

In the following, we present a method to obtain event predictions $\hat{t}_{l,i}$, $l = 1, 2, \ldots, L$ in the current period i, and thus via (4.2) and (4.3), also predictions of the relative primitive durations $\hat{\boldsymbol{d}}(t)$. To that extent, we assume the state trajectory $\boldsymbol{\xi}(t)$ to be fully observable up to time t. Further, the task-related segmentation points $\boldsymbol{\Xi} = \{\boldsymbol{\xi}_1, \ldots, \boldsymbol{\xi}_L\}$ are assumed to be known and constant. Then, the following two-step technique is proposed to obtain predictions from experimental measurements:

1. Reference limit cycles
$$\gamma^r : \boldsymbol{\xi}^r(t^r), \text{ with } t^r \in [t_0^r, t_L^r] \tag{4.25}$$
are acquired over single, complete periods. A family of limit cycles γ^r, $r = 1, 2, \ldots, R$ is built with the number of cycles $R \in \mathbb{N}$. These feature differing periods T^r covering the expected range of periods, see the example in Figure 4.8a.

2. The current state $\boldsymbol{\xi}$ is classified with respect to the family of reference limit cycles. First, the similarity to each γ^r is determined by the respective minimum of the distance metric
$$\Delta\xi^r = \min_{\boldsymbol{\xi}^r \in \gamma^r} \sqrt{(\boldsymbol{\xi}^r - \boldsymbol{\xi})^{\mathrm{T}} \boldsymbol{Q} (\boldsymbol{\xi}^r - \boldsymbol{\xi})}, \tag{4.26}$$
with $\boldsymbol{Q} \in \mathbb{R}^{n \times n}$ being a positive definite weighing matrix. Next, the closest cycle γ^{r^*} is selected by
$$r^* = \arg\min_r \Delta\xi^r. \tag{4.27}$$
If the state $\boldsymbol{\xi}$ is close to the segmentation points, the distances $\Delta\xi^r$ are nearly equal. In this case, undesired switchings of r^* are avoided by switching from previous $r^{*'}$ to

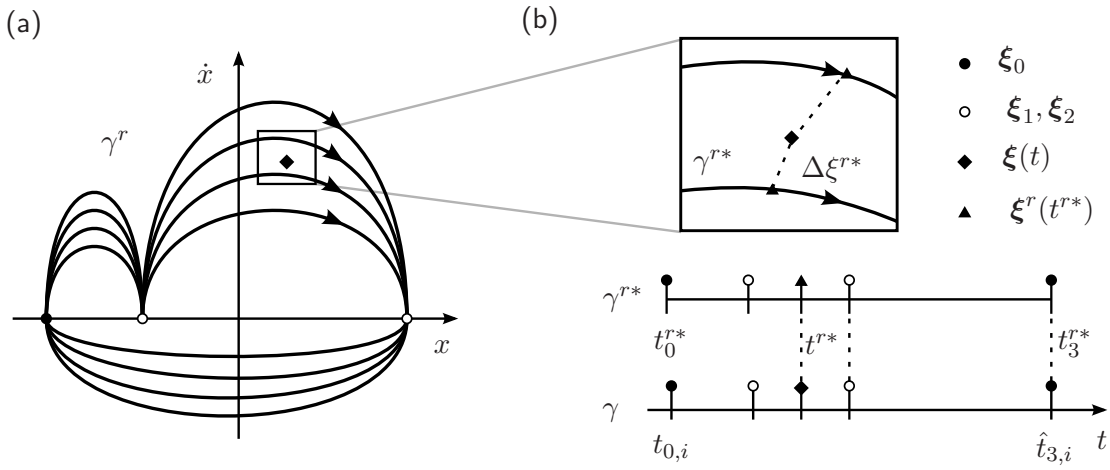

Fig. 4.8: (a) Family of $R = 4$ limit cycles γ^r with differing periods T^r. In the position-velocity state space, shapes differ due to $\dot{x}$ scaling with T^r. (b) Close-up illustrating distance-based classification *(top)*. Events are predicted based on the previously acquired evolution of events in γ^{r*} *(bottom)*.

current r^* only if a certain threshold

$$\Delta\xi_{\text{th}} < \Delta\xi^{r*'}(t) - \Delta\xi^{r*}(t)$$

is exceeded. Finally, predictions of any future event $t_{l,i}$ at time t are obtained from

$$\hat{t}_{l,i} = t + t_l^{r^*} - t^{r^*}, \text{ with } t_l^{r^*} > t^{r^*}. \tag{4.28}$$

The event $t_l^{r^*}$ denotes the event in γ^{r^*} corresponding to $t_{l,i}$, and t^{r^*} denotes the time at minimum distance $\Delta\xi^{r^*}$ in γ^{r^*}, see Figure 4.8b.

Remark 4.14 The quality of the event predictions depends on the number of reference limit cycles used for classification, and their distribution of periods, i.e. how fine-grained the covered portion of the state space is sampled.

4.2.5 From Phase to Movement

Robotic agents implementing the synchronization behavior require the transformation inverse to the previous one as well. By means of movement models, the process variables are transformed back to the cyclic movement trajectory representing the individual action task. After defining the required model properties, we develop a realization of this transformation.

General Movement Model

According to Definition 4.2, the trajectory is again composed by a given number of L primitives μ_l, $l = 1, \ldots, L$ connecting the segmentation points $\boldsymbol{\xi}_l$ with relative primitive durations d_l. Inverse to the phase-amplitude decomposition of the cyclic state trajectory,

we require the movement model to take the general form

$$\boldsymbol{\xi} = \boldsymbol{f}(\theta, \boldsymbol{d}, \boldsymbol{\Xi}). \tag{4.29}$$

The function $\boldsymbol{f} : \mathbb{R} \times \mathbb{R}^L \times \mathbb{R}^{Ln} \to \mathbb{R}^n$ denotes a mapping of the phase θ, the relative primitive durations $\boldsymbol{d} = [\ d_1 \ \ldots \ d_L\ ]^{\mathrm{T}}$, and the task-related set of segmentation points $\boldsymbol{\Xi} = \{\boldsymbol{\xi}_1, \ldots, \boldsymbol{\xi}_L\}$ onto the continuous state trajectory $\boldsymbol{\xi}$. In brief, an appropriate movement model needs to

- fulfill the condition (4.1) to be cyclic for finite periods T,
- facilitate temporal scaling implemented by θ and $\boldsymbol{d}$,
- facilitate spatial scaling depending on $\boldsymbol{\Xi}$.

Models complying with these properties are discussed in [41]. In the following, we reparameterize a model $\boldsymbol{\xi} = \boldsymbol{f}(t)$ explicitly depending on time t to comply with the form (4.29).

Remark 4.15 The process variables θ and $\boldsymbol{d}$ implement the DoF available for the *voluntary* behavior of movement synchronization. The movement model $\boldsymbol{f}$ has to *necessarily* comply with the task-related segmentation points $\boldsymbol{\Xi}$.

Utilizing the Minimum-Jerk Model

Human hand trajectories composed of point-to-point movements are known to be successfully reproduced by the minimum-jerk model formulated in a Cartesian frame [36]. It successfully renders movement trajectories of robots in goal-directed tasks, that resemble human hand movements [65]. With reference to the human-robot experiment described later on, we investigate this polynomial-type model here.

The state $\boldsymbol{\xi} = [\ \boldsymbol{x} \ \ \dot{\boldsymbol{x}}\ ]^{\mathrm{T}}$ is defined, with $\boldsymbol{x} \in \mathbb{R}^3$ and $\dot{\boldsymbol{x}} \in \mathbb{R}^3$ denoting the hand (effector) position and velocity in a Cartesian frame. The movement model (4.29) is then realized by a sequence of L point-to-point primitives

$$\mu_l : \boldsymbol{x} = \boldsymbol{f}_l(\chi_l) = (\boldsymbol{x}_l - \boldsymbol{x}_{l-1})\, g(\chi_l) + \boldsymbol{x}_{l-1}, \tag{4.30}$$

parameterized by $\chi_l \in [0, 1]$. The function $g : [0, 1] \to [0, 1]$ denotes the fifth-order polynomial

$$g(\chi_l) = 6\chi_l^5 - 15\chi_l^4 + 10\chi_l^3. \tag{4.31}$$

The start point $\boldsymbol{x}_{l-1}$ and the end point $\boldsymbol{x}_l$ of the primitive μ_l define the segmentation points $\boldsymbol{\xi}_{l-1}$ and $\boldsymbol{\xi}_l$, since (4.31) implies $\dot{\boldsymbol{x}}_{l-1} = \dot{\boldsymbol{x}}_l = 0$. For any choice $\chi_l \propto t$, (4.30) minimizes the jerk $\dddot{\boldsymbol{x}}$.

The parameter χ_l of the lth primitive (4.30) is substituted by the process variables θ and $\boldsymbol{d}$, i.e.

$$\chi_l = h_l(\theta, \boldsymbol{d}). \tag{4.32}$$

If (4.32) fulfills the condition

$$h_l(\theta, \boldsymbol{d}) = 1, \tag{4.33}$$

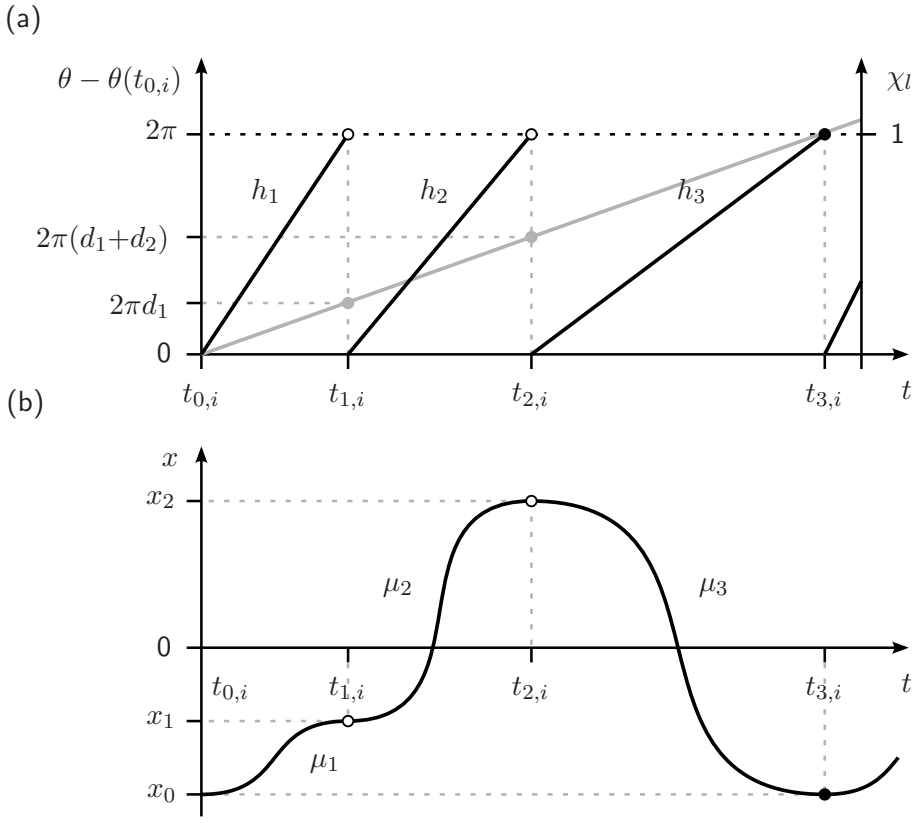

Fig. 4.9: Transformation of the process variables $\theta, \boldsymbol{d}$ into a limit cycle with $L = 3$ primitives μ_l, employing the minimum-jerk movement model. (a) Piecewise-continuous substitutions h_l illustrated for the unperturbed phase with $\dot{\theta} = const.$ (gray graph) and $\boldsymbol{d} = const.$ (b) Continuous, cyclic movement trajectory composed by polynomials f_l. For the corresponding limit cycle representation, cf. γ^{b} in Figure 4.4a.

the subsequent primitive is activated, i.e. the transition $\mu_l \mapsto \mu_{l+1}$ and $\mu_L \mapsto \mu_1$ respectively is triggered, see Figure 4.9a. The substitution h_l in the current period i is realized by

$$h_l(\theta, \boldsymbol{d}) = \frac{1}{2\pi d_l} s_l(\boldsymbol{d}) \left(\theta - \theta(t_{l-1,i})\right), \tag{4.34}$$

which is composed as follows. The phase value $\theta(t_{l-1,i})$ obtained from (4.11) is subtracted to account for the phase offset at the event of primitive entry $t_{l-1,i}$. The factor $\frac{1}{2\pi d_l}$ scales phase values $\theta \in [\theta(t_{l-1,i}), \theta(t_{l,i})]$ to values $\chi_l \in [0, 1]$. The positive, real-valued function

$$s_l(\boldsymbol{d}) = \frac{\sum_{j=l}^{L} d_j}{1 - \sum_{j=0}^{l-1} d'_j}, \text{ with } d'_0 := 0, \tag{4.35}$$

ensures, that the boundary condition $h_L(2\pi i, \boldsymbol{d}) = 1$ is fulfilled for any time-varying $\boldsymbol{d}$. With d'_j we denote the actual value that d_j assumed at past transition $\mu_j \mapsto \mu_{j+1}$.

Remark 4.16 If $\boldsymbol{d} = const.$ holds, $s_l(\boldsymbol{d}) = 1$ is satisfied, and the substitution (4.34) becomes piece-wise linear, i.e. $\chi_l \propto \theta$. If additionally $\dot{\theta} = const.$ holds, we obtain piecewise linear $\chi \propto t$. Thus, if the synchronization process is in steady state, the trajectory $\boldsymbol{\xi}(t)$

is composed by minimum-jerk movement primitives, cf. the example in Figure 4.9.

4.3 Human-Robot Movement Synchronization

The developed concept is applied to render synchronization behavior of a robotic agent that engages in a joint action task together with a human partner. The human-robot synchronization experiment fulfills two goals:

- It provides the proof of concept successfully illustrating the developed synchronization behavior by means of a robotic interaction partner.
- It serves to explore the potentials of the developed robotic behavior in joint action tasks with human interaction partners.

In the following, superscripts ^{a} and ^{b} denoting agent-associated variables are replaced by ^{H} and ^{R}, where variables associated with the human and the robot need to be distinguished.

4.3.1 The Joint Action Task

The design of the experimental task is inspired by the dot-tapping paradigm deployed in Chapter 3. The following points state the desired features:

- Both agents perform repetitive movements composed by sequences of *multiple primitives* with closed trajectories (cycles). Multiple cycles performed in a row allow to study synchronization behavior.
- Since we aim to investigate different modes of synchronization, the cycles needs to offer potentially relevant *synchronization events*.
- The task is *goal-directed*, i.e. the agents' effectors have to reach one or more goal points. In addition to these goals, the individual tasks mutually depend on each other such that a *joint action context* is established between the partners.
- *Overlapping workspaces* provoke close interaction and constrain synchronization, since collision avoidance is required in certain workspace regions.
- Mutual pick up of *visual information* about each others' actions is allowed to let interaction emerge.

Accordingly, the task paradigm depicted in Figure 4.10 is designed. Both the human and the robot perform cyclic sequences of multiple movement primitives with their right arm/manipulator, while sitting opposite to each other at a round table. The task is to carry barbell-shaped objects from pick points to place points, which are marked on the table. The objects have a height of 140 mm and a weight of 0.19 kg. They are equipped with an iron sheet and a plastic disc on top with reflective markers attached, allowing for magnetic grasping and marker-based tracking respectively. The participant wears a glove with an additional weight and markers attached. Total weight of the glove is 0.51 kg.

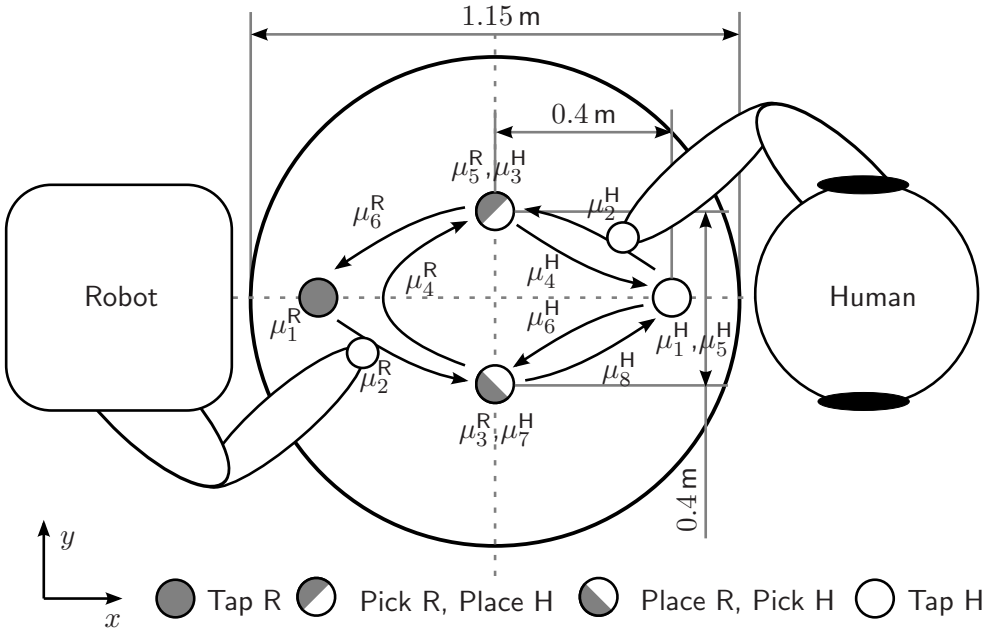

Fig. 4.10: The joint action task designed for the human-robot synchronization experiment. In a symmetric setup, both human and robot perform slightly different action tasks while facing each other. Odd-indexed primitives μ_l consider dwell times, even-indexed ones denote movements. Target points are marked by circles of 115 mm in diameter.

Its purpose is to naturally slow down the humans' movements to a velocity range that is technically feasible for the robotic agent. The agents' workspaces are arranged such, that two objects can be exchanged between the agents in a cyclic fashion. Within each pick-and-place movement, the table shall be touched at a tap point close to the agent. The robot only performs a tap when carrying an object, which shortens its path and makes the agents' movement cycles differ slightly.

4.3.2 Implementation

Design of the Behavioral Dynamics

Three synchronization modes are investigated in the above joint action task, see Figure 4.11. These modes allow to exchange the objects by sequential pick and place actions and thus, comply with the task-related goals. Note, that each of the segmentation points features two events, which are the entry and leave of the respective point. These frame the so-called dwell time, which is known to be part of human motor control in aiming tasks [2]. The above modes are represented by stable equilibrium relations the unified synchronization process needs to feature, see Table 4.1. Accordingly, the vector field H is designed, which defines the phase difference dynamics $\dot{\Phi} = \Delta\omega + H(\Phi)$, with $\Phi = \theta^{\mathrm{H}} - \theta^{\mathrm{R}}$. The unstable equilibrium points separating the regions of attraction are equally spaced between the stable equilibrium points, see Figure 4.12. By splitting the phase difference dynamics under the assumption of isotropic coupling, we obtain the cross-coupled phase

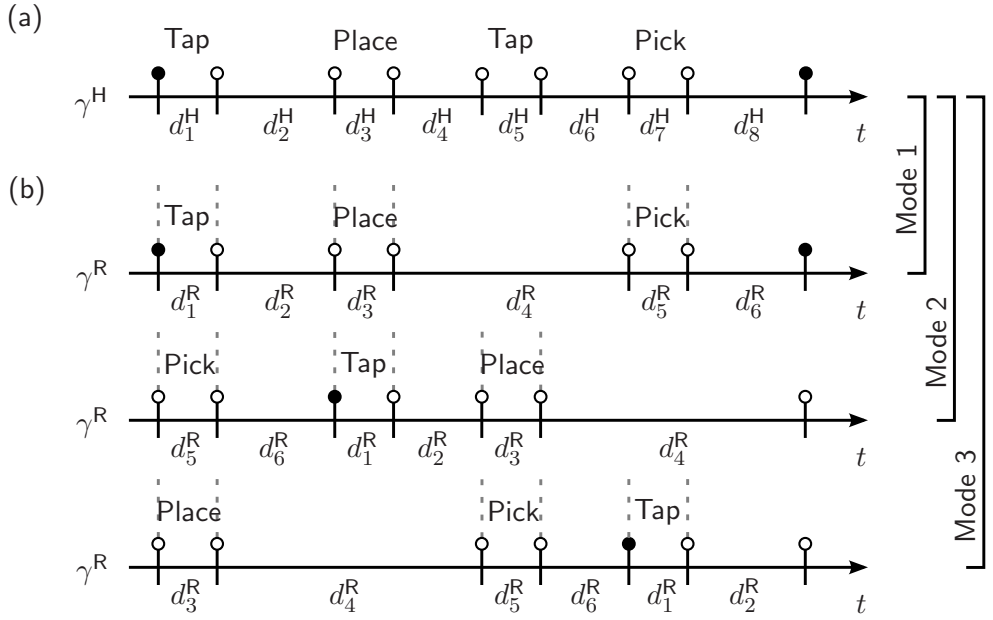

Fig. 4.11: (a) The evolution of events for the experimental task, with the relative durations d_l corresponding to the primitives μ_l in Figure 4.10. Again, odd-indexed durations are due to expected dwell times in the segmentation points. (b) The cycle γ^{R} synchronized to γ^{H} in three different modes, denoted mode 1-3. Vertical dashed lines indicate synchronized events. Intuitively speaking, the human precedes the robot in mode 2 and vice versa in mode 3.

entrainment process

$$\dot{\theta}^{\mathrm{H}} = \omega^{\mathrm{H}} + \frac{H(\theta^{\mathrm{H}} - \theta^{\mathrm{R}})}{2} \tag{4.36}$$

$$\dot{\theta}^{\mathrm{R}} = \omega^{\mathrm{R}} - \frac{H(\theta^{\mathrm{H}} - \theta^{\mathrm{R}})}{2}. \tag{4.37}$$

The processing delay Δt_{p} of the robot is compensated by adding the constant phase shift $\Delta\hat{\theta}^{\mathrm{H}} = \omega^{\mathrm{R}}\Delta t_{\mathrm{p}}$ to the human phase estimate $\hat{\theta}^{\mathrm{H}}$.

The entrainment process of the relative primitive durations is realized according to the

Tab. 4.1: Stable equilibrium relations of the implemented synchronization process.

Mode	Phase difference $\Phi_{\mathrm{r,e},m}$	Relative primitive durations $\boldsymbol{d}^{\mathrm{H/R}}$
$m = 1$	$\Phi_{\mathrm{r,e},1} = 0$	$d_1^{\mathrm{H}} = d_1^{\mathrm{R}}$, $d_2^{\mathrm{H}} = d_2^{\mathrm{R}}$, $d_3^{\mathrm{H}} = d_3^{\mathrm{R}}$, $d_7^{\mathrm{H}} = d_5^{\mathrm{R}}$, $d_8^{\mathrm{H}} = d_6^{\mathrm{R}}$
$m = 2$	$\Phi_{\mathrm{r,e},2} = 2\pi \sum_{j=5}^{6} d_j^{\mathrm{R}}$	$d_1^{\mathrm{H}} = d_5^{\mathrm{R}}$, $d_2^{\mathrm{H}} = d_6^{\mathrm{R}}$, $d_3^{\mathrm{H}} = d_1^{\mathrm{R}}$, $d_4^{\mathrm{H}} = d_2^{\mathrm{R}}$, $d_5^{\mathrm{H}} = d_3^{\mathrm{R}}$
$m = 3$	$\Phi_{\mathrm{r,e},3} = 2\pi \sum_{j=3}^{6} d_j^{\mathrm{R}}$	$d_1^{\mathrm{H}} = d_3^{\mathrm{R}}$, $d_5^{\mathrm{H}} = d_5^{\mathrm{R}}$, $d_6^{\mathrm{H}} = d_6^{\mathrm{R}}$, $d_7^{\mathrm{H}} = d_1^{\mathrm{R}}$, $d_8^{\mathrm{H}} = d_2^{\mathrm{R}}$

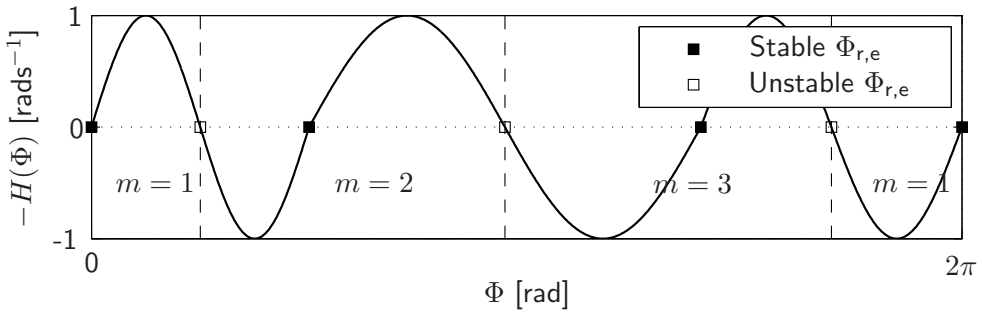

Fig. 4.12: The vector field function H designed by continuous concatenation of sine periods between the stable equilibrium points according to Table 4.1. Vertical dashed lines separate the regions of attraction for the case of equal frequencies $\Delta\omega = 0$ and define the active mode $m = 1, 2, 3$. The plot is parameterized by unit amplitude and $\boldsymbol{d}^{\mathrm{R}} = [0.05\ 0.25\ 0.05\ 0.4\ 0.05\ 0.2]^{\mathsf{T}}$.

example developed in Section 4.2.3. Within the regions of attraction defined by the lower bounds $\boldsymbol{d}_{\mathrm{l}}^{\mathrm{R}} = \frac{1}{2}\boldsymbol{d}_0^{\mathrm{R}}$ and the upper bounds $\boldsymbol{d}_{\mathrm{u}}^{\mathrm{R}} = \frac{3}{2}\boldsymbol{d}_0^{\mathrm{R}}$ around the initial values $\boldsymbol{d}_0^{\mathrm{R}}$ and depending on the active mode m, the equilibrium relations summarized in Table 4.1 are attracted.

Transformation between Movement and Phase

The instantaneous phase estimate $\hat{\theta}^{\mathrm{H}}(t)$ is determined according to Section 4.2.4. The state $\boldsymbol{\xi}^{\mathrm{H}} = [\ y^{\mathrm{H}}\ \ \dot{y}^{\mathrm{H}}]^{\mathrm{T}}$ is defined, with y^{H} and $\dot{y}^{\mathrm{H}}$ denoting the y-components of the tracked Cartesian position and velocity of the human hand. Velocity is obtained from numerical differentiation. For on-line segmentation, the threshold velocity $|\dot{y}^{\mathrm{H}}| = 0.03\,\mathrm{ms}^{-1}$ is used. Event prediction for phase estimation is performed based on $R = 21$ reference limit cycles that have been generated by the minimum-jerk movement model, see Figure 4.13. The weighing of position and velocity is defined by $\boldsymbol{Q} = \mathrm{diag}(1, 0.7)$. The metric difference threshold is set to $\Delta\xi_{\mathrm{th}} = 0.05$. The relative primitive durations are sampled at completion of each cycle i, i.e. $\boldsymbol{d}^{\mathrm{H}}(t_{8,i})$, through on-line segmentation of the human trajectory and averaged over the last three values.

The effector trajectory of the robot is realized by the minimum-jerk model described in Section 4.2.5, which yields the path depicted in Figure 4.14. The pick positions of the objects are visually tracked during interaction, whereas the place positions are calibrated in advance via markers.

Whenever the effector is close to either the human hand or to an empty pick/occupied place position, the phase velocity of the robot is modulated by

$$\dot{\theta}^{\mathrm{R}'} = c(\Delta x)\dot{\theta}^{\mathrm{R}}. \tag{4.38}$$

Depending on the Euclidean distance $\Delta x \in [0, \infty)$ between the effector position and the

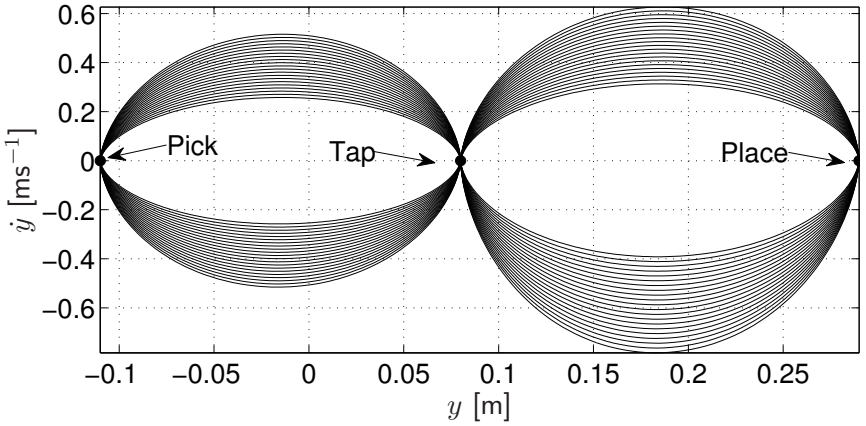

Fig. 4.13: Phase plot of the family of reference limit cycles with equally distributed phase velocities $\dot{\theta} \in [1, 2]$ rads^{-1}. Positions are expressed in the table-centered frame, which is aligned to the frame in Figure 4.10. The relative primitive durations are set $\boldsymbol{d}_0 = [0.05\ 0.2\ 0.05\ 0.16\ 0.05\ 0.22\ 0.05\ 0.22]^{\mathsf{T}}$. Those and the segmentation points denoted by filled dots are mean values, which resemble the observations made from pilot trials with a human experimenter.

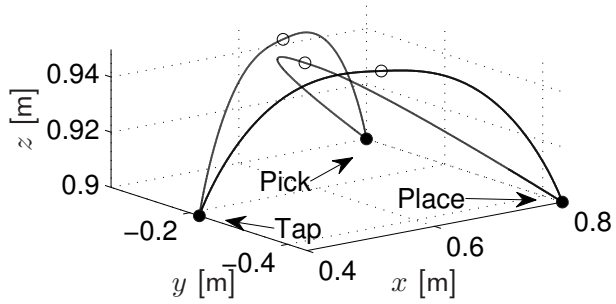

Fig. 4.14: Cyclic effector path of the robot obtained from the minimum-jerk model and expressed in robot coordinates. Filled dots denote segmentation points, open dots denote via points with relative elevation of 0.05 m above the xy-plane.

human hand or the occupied/empty goal points, the smooth blending function

$$c(\Delta x) = \begin{cases} 0, & \text{if } \Delta x < \Delta x_{\mathrm{l}}, \\ \frac{1}{2} - \frac{1}{2}\cos\left(\pi \frac{\Delta x - \Delta x_{\mathrm{l}}}{\Delta x_{\mathrm{u}} - \Delta x_{\mathrm{l}}}\right), & \text{if } \Delta x_{\mathrm{l}} \leq \Delta x < \Delta x_{\mathrm{u}}, \\ 1, & \text{otherwise} \end{cases}$$

is applied implementing a simple collision avoidance behavior. Within an upper distance bound $\Delta x_{\mathrm{u}} = 0.25\,\mathrm{m}$, the phase velocity $\dot{\theta}^{\mathrm{R}'}$ is gradually slowed down to zero, reached at a lower distance bound $\Delta x_{\mathrm{l}} = 0.15\,\mathrm{m}$.

Fig. 4.15: The experimental setup and scenario of a prototypical joint pick and place task *(left)*. Hand movements are made available to the robot in real time by tracking the glove the human interaction partner is wearing *(right)*.

4.3.3 Human-Robot Experiment

Participants

In total, 12 people (9 female) participated in this experiment. They were between 20 and 48 years old, at a mean age of 30.8 years. Prior to the experiment, they signed written informed consent. All were right handed, had normal or corrected-to-normal vision, and were naïve as to the purpose of the experiment. For participation, they were paid 8 € per hour.

Robot

A human-sized mobile robot equipped with a pair of seven DoF manipulators of anthropomorphic dimensions serves as the interaction partner in the experiment, see Figure 4.15. An admittance-type control scheme based on the wrench sensor in the wrist of the robot realizes basic compliant behavior of the manipulator when touching the environment, as described in Section 2.4.1. The effector of the right manipulator is equipped with an electromagnetic gripper which allows fast grasps and releases of ferromagnetic objects. Further details on the robot can be found in Appendix A.2.1. A marker-based motion capture system *(Qualisys)* is employed to visually track the Cartesian positions of the objects and the human hand, which are provided in real time at a sampling rate of 200 Hz. Further details on the system can be found in Appendix A.2.2. The Cartesian position of the robot effector is recorded as well. A marker-to-effector calibration routine enables robust vision-guided grasping of marked objects by minimizing the error between marker positions and the effector position the manipulator is controlled to. The algorithms implementing the estimation of the human phase, the synchronization processes and the trajectory generation are developed in *MATLAB/Simulink*. Utilizing *MATLAB Real-Time Workshop*, the corresponding routines are executed at a sampling rate of 1 kHz on the on-board PCs of the robot. The

overall processing delay between perception and action is approximately $\Delta t_\mathrm{p} = 30\,\mathrm{ms}$, which is the average time elapsing from marker movement until movement response of the robot.

Conditions

Two conditions manipulated the synchronization behavior of the robot:

- **NOS**: **No S**ynchronization.
  The robot performed at $\dot{\theta}^\mathrm{R} = \omega^\mathrm{R}$, with constant frequency $\omega^\mathrm{R} = 1.3\,\mathrm{rads}^{-1}$. Its relative primitive durations were set constant to $\boldsymbol{d}_0^\mathrm{R} = [0.05\ 0.2\ 0.05\ 0.45\ 0.05\ 0.2]^\mathrm{T}$.

- **PES**: **P**hase and **E**vent **S**ynchronization.
  The robot aimed to synchronize the three modes designed in Section 4.3.2, applying the parameters from NOS and the coupling gains $K = 0.3\,\mathrm{rads}^{-1}$ and $K_d = 0.02\,\mathrm{s}^{-1}$.

In both conditions, the effector trajectory of the robot was subject to the collision avoidance (4.38).

Procedure

The experimental procedure was as follows. The mobile platform of the robot was maneuvered to a target pose calibrated with respect to the table by means of markers, such that the goal points assigned to the robot were within the workspace of its right manipulator. Similarly, the participants were seated in a comfortable posture close to the table, cf. Figure 4.15. A written instruction handed to the participants provided the description of the human-robot joint action task. In particular, the participants were advised that for the task to be successfully fulfilled, joint action in cooperation with the robotic partner is required. In order to provoke natural interaction, they were instructed to perform at comfortable speed and to touch the marked positions precisely in a single movement. Direct hand-over and sliding the objects over the table was not allowed. The participants were neither informed about the synchronization behavior of the robot, nor were they advised to synchronize.

At the beginning of each trial, they were asked to rest with a objects in their hand in the respective tap position and instructed to start executing the task as soon as they heard an acoustical start signal (high-pitched tone) through their head phones. The stop signal (low-pitched tone) was presented after they had performed ten cycles. The start signal was timed such that the modes described in Figure 4.11 were provoked initially, i.e. for mode 1, both the participants and the robot were triggered simultaneously being in their tap points, for mode 2, the robot was triggered when the participants entered their place points, and for mode 3, the participants were triggered when the robot entered its place point. Six sets (two synchronization conditions $\times$ three start-off modes) each consisting of three trials were performed, which led to a total of 18 trials. These sets were carried out in a randomized sequence of two blocks, each with three sets under the same synchronization condition. The sets manipulating the start-off mode were presented in randomized order in each block.

4.3.4 Evaluation Criteria

The following measures are deployed to assess the synchronization behavior observed in the experiment.

Event Synchronization

The synchronization of events targeted by the behavioral dynamics of the robot is assessed based on the measured Cartesian position trajectories of the human hand $\boldsymbol{x}^{\mathrm{H}}(t)$ and the robot effector $\boldsymbol{x}^{\mathrm{R}}(t)$. Those are recorded simultaneously by the motion capture system, thus differing processing delays are eliminated. Trajectory segmentation and event extraction is performed identically to the implementation described in Section 4.3.2. According to Definition 4.6, we calculate for each synchronization mode m the temporal lags within all event pairs $(t^{\mathrm{H}}_{l^{\mathrm{H}}}, t^{\mathrm{R}}_{l^{\mathrm{R}}})$, where the indexes $l^{\mathrm{H/R}}$ are chosen corresponding to the events synchronized in mode m. For each mode m, the lag magnitudes are averaged per period i^{H}, i.e. over event pairs with $t^{\mathrm{H}}_{l,i^{\mathrm{H}}} \in [t^{\mathrm{H}}_{0,i^{\mathrm{H}}}, t^{\mathrm{H}}_{8,i^{\mathrm{H}}})$. Those averages provide continuous measures of asynchrony, which we denote $\mathrm{ASYN}_{m,i^{\mathrm{H}}}$. In each period i^{H}, the best fitting one out of the three modes is detected by selecting the smallest asynchrony. The per-trial average of the latter over all periods I^{H} reads

$$\mathrm{MASYN} = \frac{1}{I^{\mathrm{H}}} \sum_{i^{\mathrm{H}}=1}^{I^{\mathrm{H}}} \min_{m} \mathrm{ASYN}_{m,i^{\mathrm{H}}}, \tag{4.39}$$

which we call the mode-related asynchrony.

Remark 4.17 The mode-related asynchrony quantifies the mean time lag between multiple event pairs, measured in seconds. Only complete sets of event pairs corresponding to the defined modes are probed.

Mode Distribution and Mode Switches

At any time, one of three synchronization modes is considered to be *active*, and pursued by the robot in condition PES. According to the vector field design cf. Figure 4.12 and Table 4.1, we determine the active mode

$$m = \begin{cases} 1, & \text{if } \Phi_{\mathrm{r}} < \frac{\Phi_{\mathrm{r,e,1}}+\Phi_{\mathrm{r,e,2}}}{2} \vee \Phi_{\mathrm{r}} > \frac{\Phi_{\mathrm{r,e,3}}+2\pi}{2}, \\ 2, & \text{if } \Phi_{\mathrm{r}} \geq \frac{\Phi_{\mathrm{r,e,1}}+\Phi_{\mathrm{r,e,2}}}{2} \wedge \Phi_{\mathrm{r}} \leq \frac{\Phi_{\mathrm{r,e,2}}+\Phi_{\mathrm{r,e,3}}}{2}, \\ 3, & \text{otherwise.} \end{cases} \tag{4.40}$$

Given the evolution of the active mode $m(t)$, we analyze the relative distribution of modes $\frac{N_m}{N}$ as an indicator of the within-dyad preferred synchronization modes, where N_m is the number of samples in active mode m and N the total number of samples per trial. Furthermore, the temporal persistence of modes is measured by the number of mode switches, i.e. the number of samples $\{j \mid m(t_j) \neq m(t_{j+1})\}$ per trial.

Synchronization Index

Phase synchronization is again quantified by means of the synchronization index SI given by (3.5). However, the synchronization concept in this chapter introduces multiple modes, represented by differing equilibrium phase differences. Trials with one or more mode switches would heavily degrade the SI. Hence, we propose to calculate the synchronization index separately for epochs of the same *active mode*. The active mode is determined by (4.40). The resulting indexes SI_m are then combined per trial into the mode-related synchronization index

$$\mathrm{MSI} = \frac{1}{N} \sum_{m=1}^{3} N_m \mathrm{SI}_m, \tag{4.41}$$

weighted by the respective number of samples N_m in mode m.

Remark 4.18 The MSI lies in the interval [0, 1]. Given a perfectly uniform distribution of $\Phi(t)$, it would equal zero. It equals one only if the synchronization process is persistently in steady-state, which means that all samples of $\Phi(t)$ point to the same direction.

Entrainment Error of the Relative Primitive Durations

As shown in our synchronization concept, the entrainment across the relative primitive durations $\boldsymbol{d}^{\mathrm{H/R}}$ is essential to the synchronization of multiple event pairs. It is assessed by the root-mean-square error defined as the residual

$$\mathrm{RMSE}(d^{\mathrm{H}}_{l^{\mathrm{H}}} = d^{\mathrm{R}}_{l^{\mathrm{R}}}) = \sqrt{\frac{1}{N} \sum_{j=1}^{N} \left(d^{\mathrm{H}}_{l^{\mathrm{H}}}(t_j) - d^{\mathrm{R}}_{l^{\mathrm{R}}}(t_j) \right)^2}, \tag{4.42}$$

with the primitive indexes $l^{\mathrm{H/R}}$ chosen corresponding to the equilibrium relations summarized in Table 4.1. For each relation and epoch of the same active mode m given by (4.40), the entrainment errors are obtained from (4.42) and averaged over the five mode-dependent equilibrium relations afterwards, yielding the errors $\mathrm{RMSE}_{\boldsymbol{d},m}$. Analogously to the above definition of the mode-related synchronization index (4.41), those are then combined by the weighted average

$$\mathrm{RMSE}_{\boldsymbol{d}} = \frac{1}{N} \sum_{m=1}^{3} N_m \mathrm{RMSE}_{\boldsymbol{d},m}, \tag{4.43}$$

which assesses the overall entrainment error of $\boldsymbol{d}^{\mathrm{H/R}}$.

4.4 Experimental Results

The synchronization behavior is assessed through measures relying on *internal* variables of the robot. The observable degree of event synchronization between the movements is evaluated as *external* measure. Feedback gathered from a short questionnaire is reported as well. Note, that the results presented in the following are based on a group of nine participants unless stated otherwise. The remaining group of three participants performed

at movement speeds either far below or above the speed range the robot is capable of moving at, thus impeding movement synchronization in the experiment. Possible reasons are discussed in Section 4.5.

4.4.1 External Assessment of Synchronization

The following results allow to explain, how far the overall goal of our synchronization concept is reached objectively, i.e. if it fosters the entrainment of movements by synchronizing multiple event pairs. In addition, subjective feedback from the participants gives rise to discuss some perceived effects.

Subjective Reasoning

After having completed the experiment, participants were asked whether or not they had the feeling that the robot reacted to them. In case of a positive answer, they were asked to state if they found that perceived reactiveness pleasant (yes/no) and to give reasons for this answer. Eleven out of twelve participants recognized reactiveness of the robot in response to their movements during parts of the experiment. Ten out of eleven participants who answered positively stated that they liked the perceived reactiveness, giving reasons such as:

- It makes the robot appear lively.
- Having the control over task speed is pleasant.
- Adjustment towards similar speed is pleasant.
- It fosters smoother interaction.
- Negotiation among partners is beneficial.
- It is a nice feeling, but a bit uncanny as well.

The participant who disliked the reactive behavior of the robot described the interaction as flurry and unsteady.

Event Synchronization

The evaluation of the objective measure of event synchronization introduced in Section 4.3.4, the mode-related asynchrony MASYN, is depicted in Figure 4.16. A 2×3 repeated measures ANOVA with the within subject factors *condition* (NOS, PES) and *start-off mode* (1-3) reveals a clear decrease of asynchrony in each of the start-off modes, $F(1, 8) = 18.06$, $p = .003$, if the robot applies synchronization behavior, i.e. the condition PES. Irrespective of the synchronization condition, start-off mode 1 numerically results in lowest asynchrony values, whereas a slight trend towards an increased asynchrony is visible for mode 2 and 3. However, differences between start-off modes were not significant and no significant interaction effect was observed, both $p > .4$.

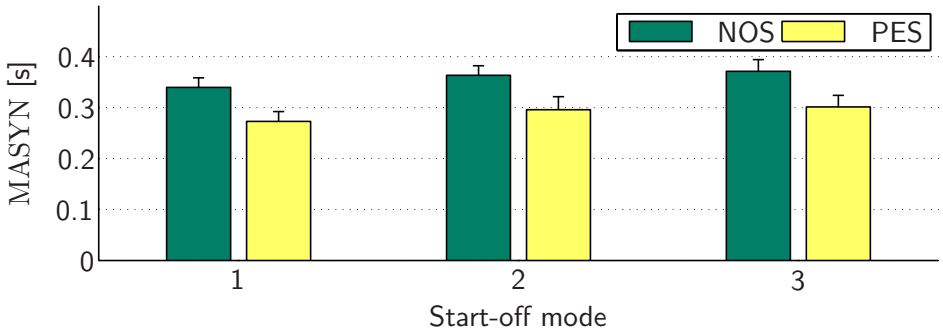

Fig. 4.16: The mode-related asynchrony MASYN averaged separately over all trials for the three start-off modes under the conditions NOS and PES. The bars represent standard errors of the means.

4.4.2 Internal Assessment of the Behavioral Dynamics

In the following, the behavioral dynamics are evaluated based on the internal representation, i.e. the internal variables of the robotic agent.

Entrainment of Phases and Relative Primitive Durations

To start, we explain the inner processes governing the synchronization behavior of the robot during an exemplary trial. The trajectories of relevant process variables are illustrated in Figure 4.17. After starting off in mode 3, cf. the initial phase difference in Figure 4.17b, the relation $d_2^{\mathrm{R}} = d_8^{\mathrm{H}}$ is entrained amongst others, see very left part in Figure 4.17a. Note that the attractor landscape generated by the vector field H is morphed depending on the entrained components of $\boldsymbol{d}^{\mathrm{R}}(t)$. Thereafter, the phase velocity of the robot $\dot{\theta}^{\mathrm{R}}$ is slowed down by the function $c(\Delta x)$ due to collision avoidance, Figure 4.17c. As the participant progresses fast, the robot is forced into mode 1. Through modulation of $\dot{\theta}^{\mathrm{R}}$ within the tuning range $[1, 1.6]\,\mathrm{rads}^{-1}$, which is defined by its natural frequency ω^{R} and coupling gain K, the robot attempts to sustain the mode being close to. It can be seen, that now the relation $d_2^{\mathrm{R}} = d_2^{\mathrm{H}}$ is pursued. After a while, the participant again increases speed, which leads the robot to finally switch to mode 2. Here, the relation $d_2^{\mathrm{R}} = d_4^{\mathrm{H}}$ becomes entrained.

Preferably Synchronized Modes

The relative amount of time spent in the synchronization modes and the relative amount of mode switches are illustrated in Figure 4.18. The former provides an intuition of how long, on average and with respect to the trial durations, each mode has been active within the robot behavior. It can be seen that under PES, the relative share of that mode increases, which the human-robot dyad has started with (upon trigger). To access the differences between NOS and PES with regard to the amount of time spent in triggered mode, planned comparisons were performed between conditions (NOS, PES) within the respective start-off mode. If participants were triggered to start off in mode 1, the relative amount spent in mode 1 is significantly higher under PES compared to NOS, $t(8) = -1.90$, $p = .047$. Since under NOS, the robot only observes but not actively pursues these modes, that increase

is due to robotic synchronization behavior in PES. Similar results were obtained for start-off mode 3, $t(8) = -2.57$, $p = .017$. However, the difference between relative mode share in PES and NOS during start-off mode 2 was only found to be numerical, $z = -.77$, $p > .2$. Mode 2 was also the dominant mode during NOS. Hence, no effect of the synchronization behavior is visible here. Overall this shows that when being triggered close to the attracted modes, the robot successfully sustains them. This is also reflected by the relative share of mode switches. Results of a 2×3 repeated measures ANOVA on condition and start-off mode show that the amount of mode switches decreased under PES in each of the start-off modes $F(1, 8) = 17.83$, $p = .003$. Neither a difference between start-off modes nor an interaction effect was observed, $p > .3$.

The preferred phase relations as a result of phase synchronization are reflected by histograms of the phase difference, see Figure 4.19 left, which is a representation complementary to the mode distributions above. Some preference towards certain phase relations can be recognized even under condition NOS, which is ascribed to human synchronization attempts due to the static behavior of the robot. Under PES, the distribution gets sharpened, forming three distinct peaks. When comparing that distribution in Figure 4.19 left with the distribution of actively attracted equilibrium points in Figure 4.19 right, their coincidence indicates successful phase entrainment through the robot behavior. Weight on the peak corresponding to mode 2 (i.e. $\Phi_{\mathrm{r,e},2}$) is strongest, followed by the peak at mode 1 (i.e. $\Phi_{\mathrm{r,e},1}$), which is in line with the distribution of modes in Figure 4.18. Note that the distributions of $\Phi_{\mathrm{r,e},2}$ and $\Phi_{\mathrm{r,e},3}$ are smeared due to their dependency on the relative primitive durations $\boldsymbol{d}^{\mathrm{R}}(t)$.

Quantitative Assessment of the Synchronization Process

The convergence and performance of the dynamical process of synchronization is measured by means of the process variables, which are the phases or the phase difference Φ respectively, and the relative primitive durations $\boldsymbol{d}^{\mathrm{H/R}}$. The results are illustrated in Figure 4.20. To access the differences between NOS and PES governed behavior, 2×3 repeated measures ANOVAs were performed with the within-subject factors condition and start-off mode. For MSI, the condition PES causes an increased entrainment compared to NOS, $F(1, 8) = 25.73$, $p = .001$, see Figure 4.20a. Between start-off modes no significant difference was observed, $p > .5$. Also, no significant interaction effect was detected. Similar results are obtained for the entrainment errors of durations, which are decreased by the entrainment process under PES, $F(1, 8) = 36.57$, $p < .001$, see Figure 4.20b. Lowest errors with respect to the attracted equilibrium relations are achieved in start-off mode 1 under PES, as shown by a significant interaction effect, $F(2, 16) = 5.29$, $p = .017$.

Instantaneous Phase Estimation

The characteristic evolution of the period and phase estimation obtained from the human movements are illustrated by means of the sample trajectories depicted in Figure 4.21. The events $t^{\mathrm{H}}_{8,i}$ result from on-line segmentation of the movement trajectory $y^{\mathrm{H}}(t)$, see Figure 4.21a. Those events denote the time of the human hand entering the tap point, and the completion times of the periods i. The instantaneous period $\hat{T}^{\mathrm{H}}(t)$ depicted in

Figure 4.21b is equivalent to the prediction $\hat{t}^{\mathrm{H}}_{8,i}(t)$, due to the definition of the instantaneous period $\hat{T}^{\mathrm{H}}(t) = \hat{t}^{\mathrm{H}}_{8,i}(t) - t^{\mathrm{H}}_{0,i}$. For comparison, the values T^{H}_i measured at period completion are shown as well. Note that due to the finite number of reference cycles used for event prediction, $\hat{T}^{\mathrm{H}}(t)$ is not continuous. More specifically, when the reference cycle selected by classification switches, corresponding event predictions switch as well. It can be seen that the on-line estimation of the human phase $\hat{\theta}^{\mathrm{H}}(t)$ successfully satisfies our demands: It reflects changes of $\hat{T}^{\mathrm{H}}(t)$ instantaneously and smoothly, while it still remains 2π-periodic with respect to the events $t^{\mathrm{H}}_{8,i}$ marking the period completions.

4.5 Discussion

The results and insights gained from the experiment described above are discussed with respect to the bipartite goal of the study, which is both the proof of concept and its exploration in human-robot joint action.

4.5.1 Implications on Human-Robot Joint Action

Both the objective improvement of event synchronization achieved in our exploratory study and the summary of subjective feedback underpin the endeavor to investigate synchronization behavior evident in HHI in the context of human-robot joint action. The behavioral dynamics pursues weak phase synchronization enforced by sinusoidal coupling of strength $K = 0.3\,\mathrm{rads}^{-1}$, which is close to the coupling strengths of uninstructed human-human movement synchronization identified in Chapter 3. Thus, the applied weak forcing is such that the participants could not only switch between synchronization modes, they also could have easily resisted or distorted synchronization within the constraints imposed by the hand-overs. In support of this, for a group of three participants we observed that, the degree of synchronization deteriorated under PES, which stands in contrast to the reported improvement of synchronization for the group of nine participants. Most participants appreciated the synchronization attempts of the robot. In short, their answers let us conclude that they had an enriched sense of interaction. However, the results presented in Section 4.4.1 also suggest some implications and pitfalls that need to be addressed carefully in the design of synchronization behavior:

- Subjectively pleasant, mutual entrainment of movements appears to be rather sensitive to parameterizations of the behavioral dynamics, first and foremost their attractors and their associated strengths. If those do not match the individual entrainment behavior of the human counterpart within certain ranges, inter-agent entrainment may fail and even worse, entrainment attempts of an artificial agent may be misinterpreted and lead to a degraded sensation of interaction compared to non-reactive behavior.

- The appearance of the robotic partner and, strongly connected, its capabilities anticipated by the participants, is expected to affect human interactive behavior [45]. Besides its manipulator kinematics having similarity to that of the human arm, the

design of the robotic agent used in the presented study is rather associated with functional and technical attributes, than with humanoid ones, see Figure 4.15. Moreover, we did not brief the participants on the capabilities they could expect from their robotic partner. One of the participants reported to perceive some uncanny-ness when facing the reactive behavior of the robot, which could likely be originated by the potential mismatch of rather crude appearance and sophisticated interaction capabilities. Both factors give rise to further investigations going beyond this work.

- Human interactive behavior may furthermore heavily depend on how the task context is conveyed and understood [17]. Human-robot experiments are usually conducted within controlled laboratory settings, which makes it hard to reliably create the desired context in the participants' minds, e.g. that of an everyday activity performed within familiar surroundings. While the implemented behavior is geared towards the abstract context of joint action, emphasis on the individual performance requirements and the cooperative aspect of the task is likely to vary between participants. For example, the instruction to precisely hit designated tap points might be assigned higher priority than an uninstructed and likely unconscious desire to reduce dwell times of the partner in favor of smooth and fluent interaction.

All of the above discussed points may affect uninstructed, i.e. emerging synchronization behavior in human-robot joint action. We hypothesize that among those points, reasons can be found for the hampered synchronization and behavioral mismatch we observed within the disregarded group of three participants.

4.5.2 Issues in the Design of Synchronization Behavior

Stability of the Cross-Coupled Entrainment Dynamics

One key idea of the synchronization concept is the design of synchronization modes by means of a dynamical synchronization process unifying both phase synchronization and the entrainment of relative primitive durations. It has to be emphasized that both processes are usually cross-coupled: The entrained components of $\boldsymbol{d}^{\mathrm{a/b}}$ depend on the attracted mode m, cf. Table 4.1 defining the modes implemented in the experiment. Changes of the relative primitive durations $\dot{\boldsymbol{d}}^{\mathrm{a/b}}$ due to mutual entrainment cause shifts of the equilibrium points $\dot{\Phi}_e^{\mathrm{a/b}}$ within the phase dynamics on the one hand. On the other hand, the attracted mode m is determined by the equilibrium point which is closest to the phase difference Φ. Depending on the designed modes and their attractor dynamics, the interaction of both processes might not be generally stable by itself, and therefore potentially result in oscillations between attracted modes. By defining reasonable bounds $\boldsymbol{d}_{\mathrm{l/h}}^{\mathrm{a/b}}$ and choosing the gain $K_d \ll K$, the entrainment process of durations is bound to certain attractor regions, and slow compared to the phase difference dynamics. Though we did not encounter that kind of instability in our experimental setting, the formal derivation of stability bounds remains an open issue.

Structure and Degrees of Freedom of the Behavioral Model

The presented design of synchronization behavior offers several interesting DoF which are not investigated in this chapter. The structure of the phase synchronization process is originated from the extended Kuramoto model proposed in Chapter 3 and variants of the HKB model [53] respectively, which evidently replicate human synchronization behavior. In contrast, the implemented entrainment structure of the relative primitive durations is considered prototypical, leaving room for further investigation and validation in the field of human-robot joint action. Similar to the phase dynamics of the HKB model, synchronization modes can be assigned differing weights through variable strengths of attraction. Another DoF is provided by the natural frequency. In line with oscillator theory, the natural frequencies of the harmonic oscillators govern the individual behavior, since they autonomously drive the agents' task progress at their individually desired speed. The domains of successfully negotiated entrainment between the agents is defined by the frequency difference.

Phase Estimation and Event Prediction

Since the definition of the instantaneous phase purely depends on recurrent events within the period, the movement trajectory can be of arbitrary shape, as long as predictions of those events are provided. Instead of the presented technique based on minimum distance classification in the state space, the application of machine learning techniques such as programming by demonstration [12] could be investigated alternatively, for the sake of a flexible encoding of observed movement sequences and event predictions.

4.6 Conclusion and Open Issues

A novel concept and design methodology is proposed to synthesize goal-directed synchronization behavior for robotic agents in repetitive joint action tasks. Those tasks are assumed to be performed by dyads of agents in a common interactive setting. We only require the tasks to be described by closed trajectories in state spaces, where the states capture the relevant movements. Based on oscillator theory, the closed state trajectories are interpreted as limit cycles, for which corresponding variables of the instantaneous phase are derived. Goal-directed repetitive movements are shown to contain much richer information concerning synchronization than purely their oscillating property. Through segmentation, we split complex movement trajectories into sequences of multiple primitives, which are separated by events, e.g. the occurrence of points with zero velocity. Beyond in-phase and anti-phase known from harmonic oscillations, enhanced synchronization modes within limit cycle pairs are synthesized. Their definition utilizes both continuous phases and discrete events as anchoring points for synchronization. The key idea of the synchronization concept is the design of interactive behavior synchronizing the synthesized modes by dynamical processes. In a unifying view, the entrainment of both phases and primitive durations is designed to happen simultaneously on a continuous time scale. Inverse to the phase estimation problem, action taking of the robotic agent governed by the synchronization behavior is addressed as well. In the prototypical scenario of a repetitive pick

and place task, we enable a full-sized, anthropomorphic robot driven by the developed synchronization behavior to cooperate with a human partner. Both objective synchronization measures and subjective feedback evidence effectiveness of the concept. Besides the proof of concept, the results gained from the exploratory study highlight the potential of the synchronization concept to enhance the social competence of robots interacting with humans.

The continuous attractor dynamics of the synchronization behavior facilitates the intuitive and systematic design of goal-directed movement coordination. Therefore, the synchronization concept is considered as a promising enhancement to the CPG approach in robotics. Applications ranging from intra- to inter-agent action coordination are worth looking at in this line of research. We expect the risk of mutual entrainment mismatch in HRI to diminish, if the behavioral rules of entrainment are derived from observations of HHI. Furthermore, humanoid robots as interaction partners should be employed in realistic joint action scenarios, in order to ultimately disentangle the effects of robotic motor coordination on human-robot joint action.

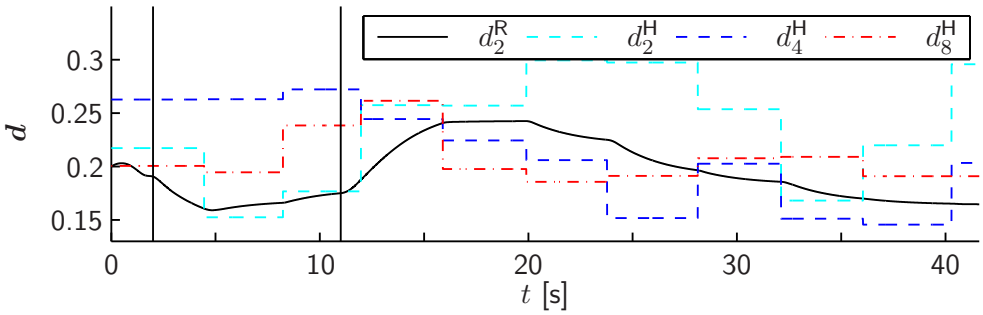

(a) The duration $d_2^R(t)$ of the robot entrained with one of the durations $d_{2,4,8}^H(t)$ of the human, depending on the active mode.

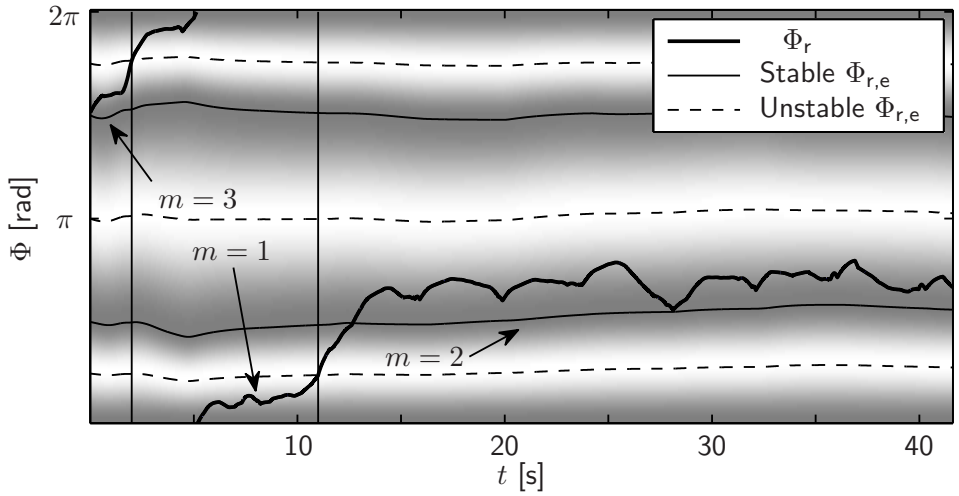

(b) The relative phase difference $\Phi_r(t)$, and the vector field H with its time-varying attractive regions (dark) and repulsive regions (bright) representing the modes $m = 1, 2, 3$.

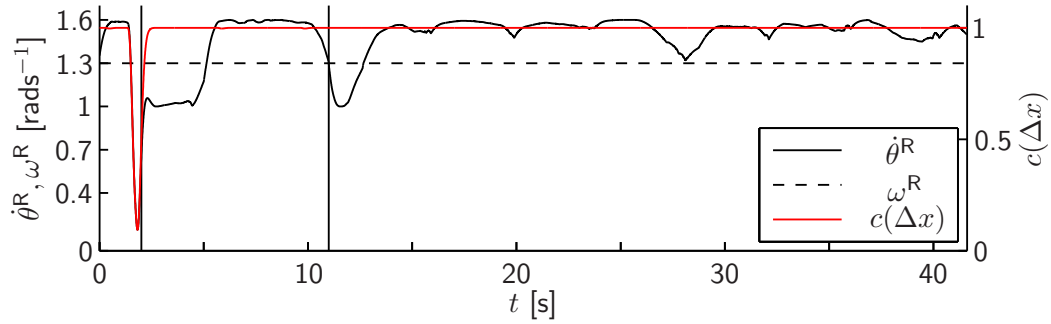

(c) The robot phase velocity $\dot{\theta}^R(t)$ and collision avoidance function $c(\Delta x)$.

Fig. 4.17: Evolution of selected process variables in a sample trial under condition PES and start-off mode 3. Vertical solid lines denote mode switches.

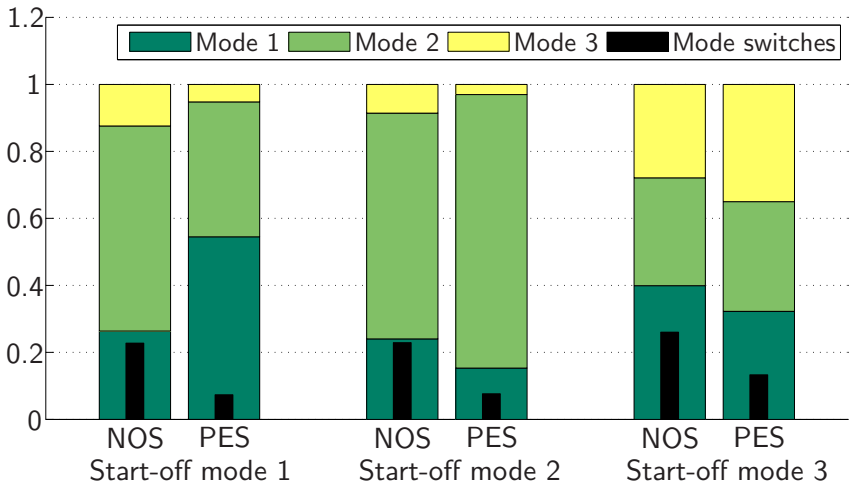

Fig. 4.18: Relative amount of time spent in each mode and relative amount of mode switches, both averaged separately over all trials for the three start-off modes under the conditions NOS and PES.

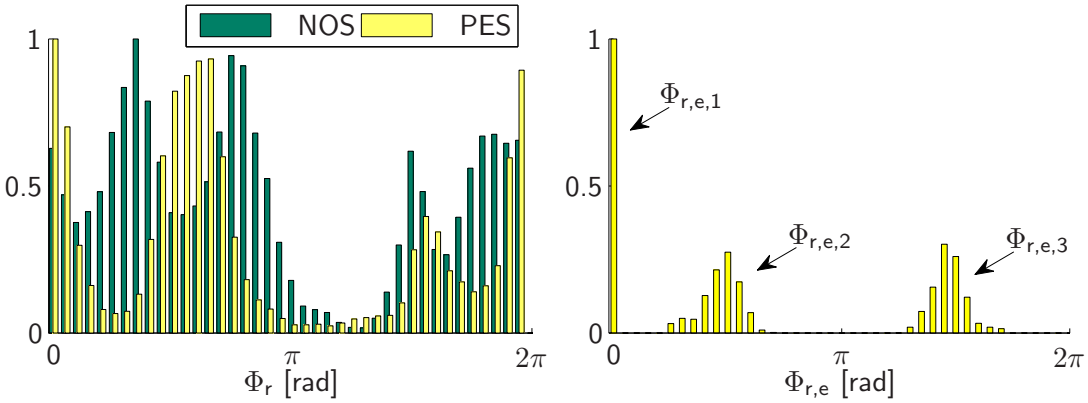

Fig. 4.19: Relative frequencies of occurrence of the relative phase difference Φ_r under the conditions NOS and PES *(left panel)*, and relative frequency of occurrence of the attracted equilibrium phase differences $\Phi_{r,e}$ under PES *(right panel)*.

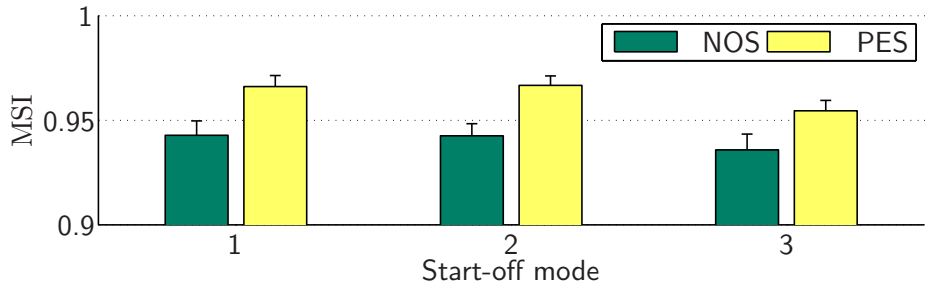

(a) The mode-related synchronization index MSI.

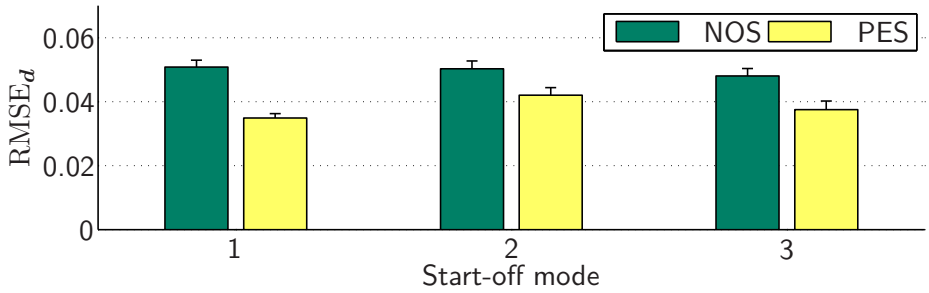

(b) The root-mean-square error of durations entrainment RMSE$_d$.

Fig. 4.20: Entrainment measures averaged separately over all trials for the three start-off modes under the conditions NOS and PES. The bars represent standard errors of the mean.

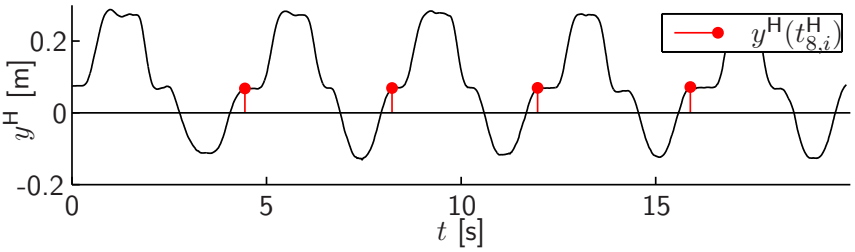

(a) The y-component of the human hand position, and the events $t^{\mathsf{H}}_{8,i}$.

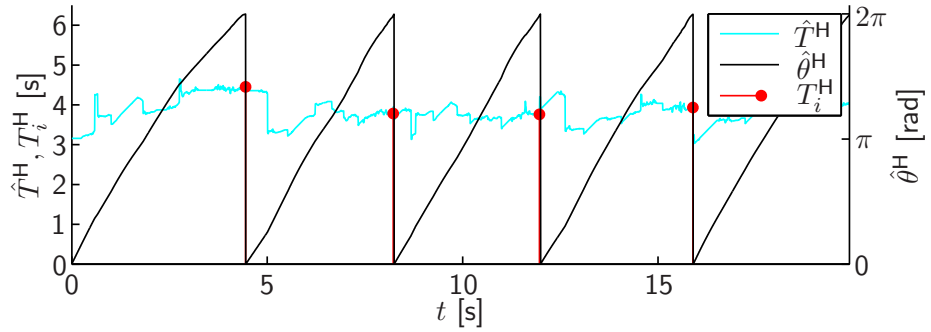

(b) The estimated instantaneous period $\hat{T}^{\mathsf{H}}(t)$, the measured period T^{H}_i, and the estimated phase $\hat{\theta}^{\mathsf{H}}(t)$ taken modulo 2π.

Fig. 4.21: The evolution of the instantaneous phase estimation for the first half of the sample trial.

5 Role Behavior for Physical Cooperation

The transport of a heavy and bulky object is a popular example that highlights the need for cooperative manipulation performed by two or more partners, in order to share the physical load and achieve commonly desired goal configurations of the object. Employing robots as assistants or partners in various kinds of haptic joint action tasks is an appealing prospect to disburden and safe human workforce. The twofold feature of haptic interaction during physical cooperation is particularly challenging. Physical coupling allows human partners to bidirectionally negotiate and accomplish the joint action task through the same modality. Additionally, the strong implicit nature of the haptic communication channel requires sophisticated interpretive capabilities to understand the partners' behavior on a fast time scale. One key point to be negotiated is the necessary effort to accomplish cooperative physical tasks. Observable effects of human negotiation in such tasks are emerging strategies in terms of temporally consistent haptic interaction patterns, found by Reed et al. [134] and called *specialization*. These patterns refer to a self-organized distribution of the agents' individual contributions. Forming patterns of interaction seems to ease mutual understanding of the partners, as improved task performance has been observed repeatedly in cooperative settings [34, 133].

As soon as autonomous physical assistants are able to produce their own goal-directed behavior, the question of interactive role allocation arises similarly. Motion planning techniques can be used to calculate the necessary force contribution of the robot towards the task goals. However, the assignment and possible re-allocation of roles can evolve dynamically during task execution, and therefore cannot be precomputed. This results in the challenge of synthesizing interactive behavior, that takes the human habit to establish and dynamically change roles into account, and renders an intuitive interaction to the human partner. A deep understanding of the physical meaning of roles in human-robot cooperative manipulation is believed to be indispensable to develop human-centered role behavior for physical assistant robots. Through system-theoretic modeling of the cooperative manipulation problem, we explicitly investigate input redundancies arising from the geometrical properties of non-point mass objects, which is novel in the context of pHRI. The cooperative task is decomposed into *redundant* and *non-redundant* DoF. Meaningful effort sharing policies in the redundant DoF are derived, that allow to render static role behavior of robotic partners. On top of those, a set of strategies for dynamic role allocation based on human haptic feedback is developed in a synthetical design perspective. The extensive experimental evaluation of prototypical role allocation schemes in a realistic and immersive full-scale scenario allows to gain unique insights on interactive role behavior, that go beyond state-of-the-art VR studies. While quantitative task performance is improved significantly by continuously changing roles, a constant role allocation achieves best subjective ratings.

This chapter is organized as follows: In Section 5.1 we provide an overview on the

research history towards physical robot assistance and recent advances on incorporating human behaviors and role allocations. Similarities and differences with respect to the field of haptic shared control are discussed as well. The system-theoretic modeling concept is introduced in Section 5.2, along with the decomposition approach leading to efficient effort sharing policies within cooperating dyads. In Section 5.3 the interaction control scheme is developed, which embeds the effort sharing strategy. Rendered static role behavior is both analytically and experimentally characterized. After a discussion of distinct adjustment criteria and policies, we synthesize two dynamic role allocation schemes in Section 5.4. The experimental study and evaluation of dynamic role behavior with a real robotic partner is presented in Section 5.5. Finally, in Section 5.6, we draw the conclusion on role behavior design from a synthetical perspective, and highlight some discovered points for future research.

5.1 Background

Related existing approaches towards physical robotic helpers are often restricted to smooth and intuitive, yet reactive behavior of robots in physical interaction with humans rather than situation-dependent active task contribution. Starting from the last decade, advances in human behavior research and modeling facilitates the design of actively contributing partners capable of pHRI tasks. While some works investigate leader-follower schemes to render interactive robot behavior, to date, only little research is devoted to the topic of dynamic role allocation between human and robotic partners. Therefore, we review approaches from the related field of haptic shared control as well.

5.1.1 Physical Robotic Assistance

Starting Out with Purely Reactive Behavior

The synthesis of robotic assistants for cooperative load sharing tasks reaches back to the early 1990's when [81] deploy an object-centered impedance control scheme similar to [154] for a set of robots cooperating with a number of humans. Successful robot implementations named *MR Helper* [82] and the distributed variant *DR Helpers* [59] encourage research groups to work on synthesis methods for cooperative human-robot object manipulation strategies. An overview of the achievements of Hirata and Kosuge in this field is given in [80]. The application of cooperative load transport is also targeted by Gillespie et al. [42] using the rather different *cobot* approach. While robotic helpers actively render a virtual object impedance behavior with features such as collision avoidance, cobots cannot move on their own—they are inherently passive. However, motion induced by a human operator is projected along virtual curvatures by arranging counter-acting forces in the cobots. This approach focuses on desired paths or workspace constraints rather than desired virtual dynamic object behavior. Similarly, the concept of *virtual fixtures* introduced by Rosenberg [141] defines overlays such as virtual rulers guiding the operator's effector motion in telepresence setups. An approach combining desired virtual constraints and desired virtual object dynamics is proposed in [165]. In their work, a robotic partner renders a virtual nonholonomic constraint—namely a virtual wheel—that prohibits sideway

slipping motion and thus simplifies operation similar to a wheelbarrow. This simplification however, inhibits maneuvering of bulky objects in narrow passages. Representing a dynamic pHRI task, cooperative rope turning is investigated by [77, 98]. Based on rhythm entrainment and controlled energy transfer, stable rope turning with a human partner is realized. Yet, even in the more recent work [77], the human is still in charge of the swing-up phase, until a stable rope turning motion is achieved by the robot. All of these approaches consider robotic partners that follow and react to user operation, which limits their capabilities to gravity compensation or collision avoidance when maneuvering heavy or bulky loads.

Exploring and Incorporating Human Interactive Behavior

A deep understanding of human interactive behavior is considered essential to render natural interaction strategies for physical cooperation between humans and robots. Several approaches target efficient physical interaction by rendering human-oriented feedback behavior of reactive robots. The group of Ikeura investigates the feedback behavior of a following manipulator during cooperative object transport. Human impedance characteristics are found to be superior in terms of subjective scores [67] and enable natural movement profiles [68]. Going further, Tsumugiwa et al. [172] show an improved performance in a cooperative calligrahic task, when the feedback control of the robot is adapted on-line with respect to the estimated human feedback behavior. In a similar setting, the derivative of the human force feedback is interpreted as an indicator of the human intention, and the damping parameter of the robot controller is adapted accordingly [28]. In order to overcome the limitations of purely reactive assistance behavior, active task contribution of a robot partner needs to respect human intentions. A significant body of work is dedicated to fundamental modeling of human behavior in cooperative haptic tasks, or to transfer findings from HHI to cooperative robotic partners. The popular concept of jerk minimization in human arm movements found by Flash and Hogan [36] for point-to-point movements is transferred to cooperative manipulation in [97] and later also in [20]. It enables a robotic partner to not just react to the human operator input, but also to predict human intentions in terms of the movement goal and duration, and to assist accordingly. Corteville et al. [20] emphasize the resulting bell-shaped velocity profile as well as an adjustable degree of assistance to be vital to natural cooperation. In a human-human cooperative object transfer task, Miossec and Kheddar [108] later discover a variant of the minimum-jerk model to fit best the observed movement profiles. Reed and colleagues observe temporally consistent behavior patterns during human-human physical cooperation [133, 134]. The authors call this phenomenon specialization. In a Turing test, they successfully transfer their results to a human-robot setup such that participants can not distinguish between the robotic partner and an actual human partner, yet the human specialization effect can not be reproduced [132]. Their findings on evolving specialization are further investigated in [48]. Humans are shown to prefer a certain dominance difference among collaborating partners in contrast to equally shared control. In this context, (physical) dominance refers to the actual achievement of influence or control over another and therefore reflects the individual share of the overall contribution to task success. In particular, effort distributions appear to be partly person-specific and partly interaction-dependent, and thus,

time-varying. Human following behavior in response to a leading robotic manipulator is investigated in a cooperative vertical lifting task in [118]. Behavioral hallmarks, such as different, modality-related frequency domains of human response are discovered, with the goal of synthesizing human-like interaction controllers. Similar to the object-lifting approach in [82] and based on observed criteria of human response behavior, corresponding robot follower controllers are synthesized guided by human preferences [119].

Leader-Follower and Role Allocation Schemes

A controller blending scheme that allows the allocation of leader and follower roles by independent blending variables is proposed by Evrard and Kheddar [31]. While homotopy blending of two extreme controllers for each agent is a very generic approach accounting for a variety of interaction behaviors, the functional modeling how to adjust the blending parameter remains an open issue. Based on the movement model of [108], the controller blending scheme is capable of reproducing the phenomenon of specialization in simulation, as well as smooth self-collision avoidance of a humanoid robot [32]. Recent thoughts from this group on the leader-follower assignment problem are found in [76]. In particular, it is indicated that blending of stable leader and follower controllers will not necessarily result in a stable overall behavior. An overall system architecture implemented on a small scale humanoid robot that comprises a confidence-based role adaptation using homotopy blending is presented in [169]. The blending variable is drawn from state estimation of a human motion model, which is interpreted as confidence. An emerging interest in smart physical robotic assistants for human workers in industrial settings is visible since a few years. Basic physical assistance for the well defined task of precise positioning of windshields during car manufacturing processes is developed in [189]. Their framework proposes a strict geometrical separation of the DoF and weighs the assisting force contribution to the task according to defined haptic cues. The theory of risk-sensitive optimal feedback control is applied to the haptic assistance problem by Medina et al. [104]. Employing a probabilistic model of the human task-related behavior, the authors are able to render a meaningful, confidence-based role allocation behavior, based on the predicted variabilities of both human movements and force contributions. Moreover, different characteristics (attitudes) of the role allocation are representable within the risk-sensitivity framework, i.e. human force variabilities interpreted as unexpected behavior are handled in a more or less dominant way. Later, the authors modify their approach to reflect both current and predicted variabilities of the human contribution [105] through on-line noise estimation. By interpreting the current force variabilities as the current level of human disagreement, an enhanced interaction performance in a cooperative object transport task through a virtual maze is achieved. The choice of the risk-sensitivity parameter is considered as attitude design problem in [144]. A functional dependency of the parameter composed by two factors is proposed, integrating both an adaptation to diverging noise levels and environmental constraints. The role assignment problem arising in human-robot joint action is thoroughly reviewed by Jarrassé et al. [70], considering both psychological studies of HHI and related works in pHRI.

5.1.2 Relation to Haptic Shared Control

The research field of haptic shared control is mostly directed towards assistance and haptic guidance of humans in controlling machines, e.g. vehicular control [46], but also in virtual environment tasks [113, 116] and in tele-operation scenarios [121]. The control input of the virtual assistant is usually rendered as an additive force superposed to the human control input. Smooth changes of the degree of assistance allow to implement continuously changing levels of automation. Applications and design guidelines for systems incorporating haptic shared control are comprehensively discussed in [1]. Shared control of an admittance-controlled mobility aid for elderly people is proposed in [191]. Homotopy blending between the force inputs of the human and the virtual assistant smoothly shifts the control authority of the vehicle, depending on the on-line evaluation of a multi-criterion performance index. Blending between a number of finite control states (user dominant, equal control and blending) in a dynamic virtual task is proposed in the haptic negotiation framework of Oguz et al. [113]. During the cooperative solving of a haptic board game, their system realizes dynamic role exchange by granting control to the virtual partner or the operator regarding human intentions through an adjustment of both partners' coupling stiffnesses. The human operator is assumed to display the intention of gaining control by applying large forces to the system compared to known force profiles. Later, Kucukyilmaz et al. [86] show that this dynamic role exchange scheme improves task efficiency significantly compared to an equal control guidance scheme, and that it constitutes a personal and subjectively pleasing interaction model. Notably, this framework is targeted to human-computer interaction (HCI) scenarios, since both the coupling of the virtual assistant and the human operator are adjusted. Recently, dynamically changing levels of haptic assistance that depend on single or multi-criterion measures of performance are postulated by Passenberg et al. [123]. The authors propose a rigorous assistance taxonomy regarding the reference of performance measures, which may be internal or external, and the adaptation characteristics of the assistance policy, which may be constant, continuous or discretely switching. In a haptic shared-control scenario, different implementations of the performance reference and the assistance policy are compared regarding their overall performance and perceived workload. Results from the study render adaptive assistance policies combined with multi-criterion performance measures to be beneficial. Despite many inspiring affinities between related works in the field of haptic shared control and the role allocation problem for physical cooperation, some important differences emerge from the interaction of the physically coupled entities, i.e. the human, the robotic partner and the cooperatively manipulated object:

- In virtual environment and tele-operation scenarios, shared control approaches may rely on the possibility to adjust the coupling between the human operator and the jointly manipulated object. In contrast, during physical robotic assistance, the potentially varying coupling and control input of the human partner cannot be controlled, but only observed or inferred.

- Haptic shared control schemes usually assume collocation of the partners' control inputs, i.e. the operator and the virtual assistant are directly coupled, both acting on one control interface. In contrast, cooperative object manipulation in pHRI usually

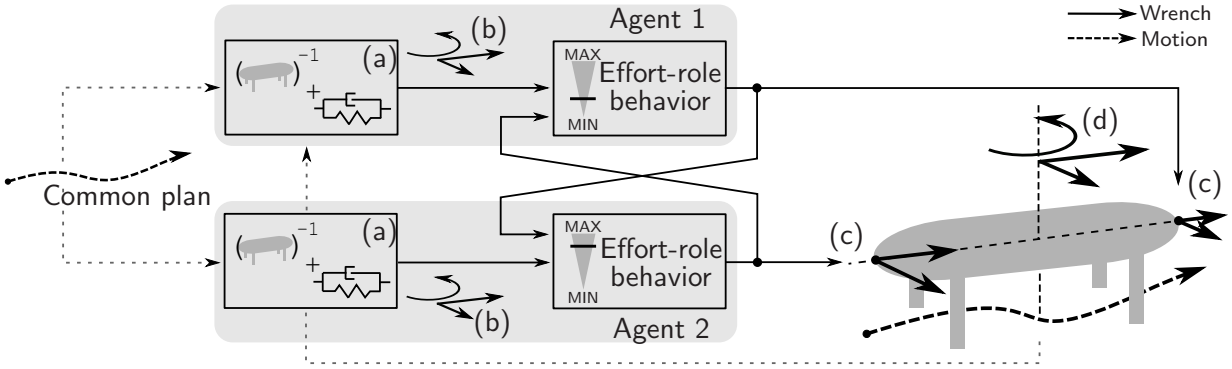

Fig. 5.1: Conceptual overview: Two agents cooperatively manipulates a common object according to a shared plan. Both agents employ an inverse object model and impedance control loop (a) generating desired object-centered wrenches (b). The effort-role behavior determines the control inputs applied at the agents' grasp points (c), which compose the object-centered wrench (d) required for configuration tracking of the object. Later, a scheme to allocate the agents' roles based on mutual feedback of the control inputs will be developed.

involves a time-varying coupling between the partners, mediated by the physical properties of the object, i.e. its geometry and dynamics.

5.2 Physical Effort Sharing in Cooperative Manipulation

The cooperative task of jointly manipulating a rigid bulky object by human-robot teams is addressed in the following. In contrast to state-of-the-art approaches restricted to the cooperative manipulation of virtual point-mass objects or one common interaction point respectively, we explicitly consider spatially distributed grasp points of the partners. The effort sharing concept is developed based on the task representation in an object-centered point of view.

5.2.1 Problem Formulation and Concept

Definition of the Effort Sharing Problem

The envisaged scenario facilitates the *cooperation* between a human and an assistive robot. Cooperation is defined according to [115, 120] as the willing participation of all agents towards a common goal along a shared plan. In line with this, we focus on manipulation tasks which require physical cooperation between the partners through close coupling with an object, see Figure 5.1. When two or more agents cooperate by jointly manipulating a common object, the problem of sharing the physical effort of the task arises. The physical coupling imposed by the geometrical and dynamical properties of the task has to be addressed and exploited such that each agent's effort in terms of input wrenches allow for a smooth and efficient cooperation. We confine the effort sharing problem to the following conditions:

- One human *cooperates* with one robot or alternatively, a system of robots with centralized communication towards achieving a common known goal, e.g. reaching certain object configuration(s) when jointly manipulating an object.
- Constraints of the environment are such that the task is achievable, i.e. a feasible path to the goal exists.
- All participants *tightly grasp* a single *rigid* object with commonly known shape and dynamics.
- Object dynamics are holonomic, i.e. the manipulated system does not have any velocity-dependent constraints. Concretely, such a system can be accelerated in arbitrary direction of the configuration space.
- The grasp points are such that the task is *controllable* and its control inputs are *redundant*. Therefore, we require at least the same number of non-redundant control inputs as corresponding configuration variables [19, 195].
- The partners interact with each other only through the haptic channel provided by the physical coupling. Other forms of communication, e.g. speech or gestures, are beyond the scope of this work. We believe that the interaction via the haptic modality needs to be understood profoundly, before other modalities are added.

System-Theoretic Modeling Concept

Dynamic modeling is performed to capture the physical and geometrical properties of the manipulation task under environmental constraints. Specifically, we model the dynamics of the manipulated object including the agents' contact points, see Figure 5.1. Adopting an object-centered point of view, the agents' contributions to the task are defined by spatially distributed control inputs, i.e. the forces that affect the object motion towards the goal.

Research on human cooperation strategies suggest an object-centered formulation of the desired path. Human dyads are found to achieve better tracking performance in a cooperative task, when they have common visual access to the central part of the manipulated object [146]. Thus, the desired motion of the manipulated object is intuitively represented by an object-centered trajectory, which is considered to result from an a priori negotiation between the agents. In this work, we assume shared goals in terms of known intermediate configurations of the manipulated object. Trajectories for the cooperating dyad can be precomputed by the robot through planning techniques as proposed in [78], following human-inspired optimality criteria such as the least-action principle [89], or through probabilistic encoding and reproduction of human demonstrations [90, 199]. Recently, even fusion strategies of both learning and planning are investigated regarding their synergetic potentials in the context of trajectory generation in cooperative pHRI [88].

Impedance control loops closed on motion feedback are employed by each agent and ensure compliant tracking of the desired object trajectory. The human motor control system is known to accomplish haptic tasks by a combination of impedance control and inverse dynamics of the task, see e.g. [38]. As the object model is assumed to be commonly known, each agent is able to apply an inverse dynamics model of the object, in order to

compute the required feedforward wrench on the object for motion tracking. The automatic parameter identification of unknown rigid body dynamics is a sophisticated problem, which is frequently addressed in the literature since [6]. Depending on the non-linearities involved, even state-of-the-art methods require structural knowledge of the contributing friction phenomena. Here, we assume the properties of the cooperative manipulation problem to be known to the robot, in terms of geometry, grasp points and relevant dynamics.

This is where the demand for an *effort sharing strategy* comes into play: Redundancies of the control inputs, which are usually present if two or more agents are manipulating a single object [195], span a subspace of the control inputs, which can be deliberately distributed between the agents without affecting the motion of the object.

Definition 5.1 (Effort Sharing Policy and Role) Effort sharing describes the distribution of voluntary, redundant force inputs among the agents. The agents can be assigned a certain input behavior in terms of an *effort sharing policy*. The behavioral pattern due to a certain effort sharing policy is referred to as the *role* that the agent takes on in the redundant task space.

The identification of meaningful effort sharing policies is addressed in the following sections. Synthesized effort-role behavior is embedded in the interaction control scheme of the robotic agent, and mediates its force contribution to the task. While a feedforward assignment of roles in a centralized manner works well for robotic agents, such an assignment is inappropriate for humans. Investigation of human cooperative behavior in dyadic tracking tasks provides evidence for role distributions, which are partly person-specific and partly interaction-dependent [48]. If we assume persistent validity of the agents' shared plan, which holds true for a static environment, the applied input of a *single* human agent can be estimated based on the object dynamics and fed back to allocate the role of the robot on-line. Assuming a technical manipulation system which allows to acquire measurements of the human input forces, also *multiple* human agents may contribute to the task. However, the concept developed in this work, as well as the conducted experimental studies adhere to the role allocation problem within a human-robot dyad.

5.2.2 Task Representation

The synthesis of role behavior relies on an object-related formulation of the cooperative manipulation problem. Note, that the presented aspects of multi-contact rigid-body kinematics and dynamics are based on the models commonly known from grasp analysis [128]. Those are employed usually to coordinate a number of (micro-) manipulators, which form the fingers of a robotic hand, in order to achieve stable grasps of the considered object. In the following, the manipulators are replaced by cooperative, individual agents, that form a mixed human-robot team. By splitting the agent-object system at the grasp points, we focus on the object part, and the agents' inputs at these points.

The general problem of joint object transfer in free space involves the contribution of N agents, that are assumed to tightly grasp a rigid object of arbitrary shape, as shown in Figure 5.2. A body frame C is rigidly attached to the object and the inertial frame is denoted by I. Besides a collision-free trajectory in compliance with the environment,

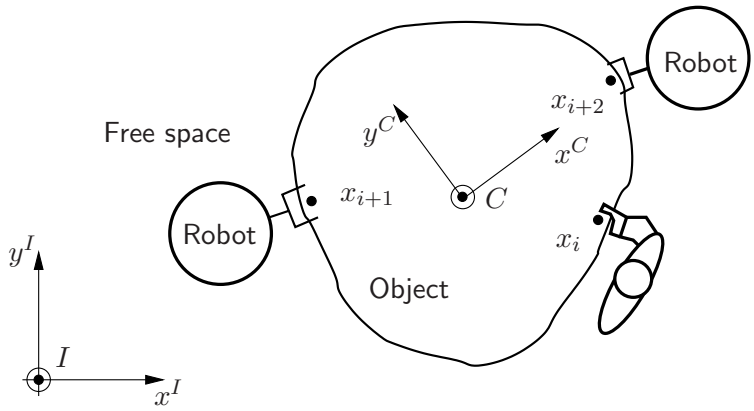

Fig. 5.2: Cooperative manipulation of a rigid object by multiple agents acting at different grasp points.

the dynamical and geometrical model of the manipulated object—the physical coupling between the agents—is crucial to the system-theoretic analysis of the task.

We assume that the rigid-body dynamics of the object are described by

$$\boldsymbol{M}_c\ddot{\boldsymbol{x}}_c + \boldsymbol{f}_c(\boldsymbol{x}_c, \dot{\boldsymbol{x}}_c) = \boldsymbol{u}_c, \tag{5.1}$$

where $\boldsymbol{x}_c \in \mathbb{R}^{n_c}$ is the configuration of the object, that describes the position and orientation of C with respect to I. For the special case of planar systems, $n_c = 3$ holds. The positive-definite matrix $\boldsymbol{M}_c \in \mathbb{R}^{n_c \times n_c}$ denotes the object inertia. The vector $\boldsymbol{f}_c \in \mathbb{R}^{n_c}$ is the sum of environmental forces such as friction and gravitation. The vector $\boldsymbol{u}_c \in \mathbb{R}^{n_c}$ denotes the *external wrench* acting on the object and expressed in I. It is composed by forces and torques, that are exerted by the agents.

Agent i contributes to the manipulation task via input wrench $\boldsymbol{u}_i \in \mathbb{R}^{n_c}$ applied at the grasp point $\boldsymbol{x}_i \in \mathbb{R}^3$ on the object, $i = 1, \ldots, N$. In order to formally represent the type of grasp and to consider only the efficient input wrench components of the agents, we introduce the *applied wrench* $\tilde{\boldsymbol{u}}_i \in \mathbb{R}^{\tilde{n}_i}$, with $\tilde{n}_i \leq n_c$. It is given by

$$\tilde{\boldsymbol{u}}_i = {}^I\boldsymbol{T}_C \boldsymbol{B}_i {}^C\boldsymbol{T}_I \, \boldsymbol{u}_i, \tag{5.2}$$

where ${}^C\boldsymbol{T}_I$ and ${}^I\boldsymbol{T}_C$ denotes the rotational transformation from frame I to frame C and vice versa. Matrix $\boldsymbol{B}_i$ is a $\tilde{n}_i \times n_c$ selection matrix referred to the body frame C, with elements $b_{k,l} \in \{0, 1\}$ determining which independent torque and force components agent i can effectively transmit at the grasp point. Note that $\boldsymbol{B}_i$ is also known as the wrench basis in grasp analysis [111], which models the type of contact between finger and object. The external wrench on the object is then composed by wrench superposition

$$\boldsymbol{u}_c = \sum_{i=1}^{N} \boldsymbol{G}_i \tilde{\boldsymbol{u}}_i, \tag{5.3}$$

where matrix $\boldsymbol{G}_i \in \mathbb{R}^{n_c \times \tilde{n}_i}$ denotes the partial grasp matrix [128]. It is given by the Jacobian of the kinematic constraint $\boldsymbol{\phi}_i(\boldsymbol{x}_c) : \mathbb{R}^{n_c} \to \mathbb{R}^3$, which describes the position of

the grasp point $\boldsymbol{x}_i$ with respect to the object frame. Thus, the kinematics comprising position $\boldsymbol{x}_i$ and velocity $\dot{\boldsymbol{x}}_i$ of the grasp point of agent i read

$$\boldsymbol{x}_i = \boldsymbol{\phi}_i(\boldsymbol{x}_c) \tag{5.4}$$
$$\dot{\boldsymbol{x}}_i = \boldsymbol{G}_i^{\mathrm{T}} \dot{\boldsymbol{x}}_c. \tag{5.5}$$

By substituting (5.3) into (5.1), we obtain the object model

$$\boldsymbol{M}_c \ddot{\boldsymbol{x}}_c + \boldsymbol{f}_c(\boldsymbol{x}_c, \dot{\boldsymbol{x}}_c) = \boldsymbol{G}\tilde{\boldsymbol{u}}, \tag{5.6}$$

with the complete grasp matrix $\boldsymbol{G} \in \mathbb{R}^{n_c \times \tilde{n}}$ composed by the stacked matrix

$$\boldsymbol{G} = \begin{bmatrix} \boldsymbol{G}_1 & \dots & \boldsymbol{G}_N \end{bmatrix}, \tag{5.7}$$

and the applied wrench $\tilde{\boldsymbol{u}} \in \mathbb{R}^{\tilde{n}}$ given by the stacked vector

$$\tilde{\boldsymbol{u}} = \begin{bmatrix} \tilde{\boldsymbol{u}}_1^{\mathrm{T}} & \dots & \tilde{\boldsymbol{u}}_N^{\mathrm{T}} \end{bmatrix}^{\mathrm{T}}.$$

The total number of effective control inputs is denoted by $\tilde{n} = \sum_1^N \tilde{n}_i$. The dynamics and kinematics of the cooperatively manipulated object serve as the basis for the effort sharing problem and the synthesis of role behavior.

5.2.3 Input Wrench Decomposition

In this section, an effort sharing strategy is developed based on the *redundant* DoF, that naturally arise from actuation redundancy. First, we recall the object model (5.6) with the complete grasp matrix $\boldsymbol{G}$ and the stacked applied wrench $\tilde{\boldsymbol{u}}$ gathering all efficient input components of all partners.

Remark 5.1 In general, only parts of the applied wrenches cause object motion and hence constitute the external wrench. The remaining component of the applied wrench is called *internal wrench* and causes squeeze (stretch) forces on the object.

Following the system-theoretic modeling concept above, a desired external wrench $\hat{\boldsymbol{u}}_c \in \mathbb{R}^{n_c}$ is calculated from the inverse object dynamics (5.1), which is to be imposed on the object to track a shared plan given as a desired trajectory of the object configuration $\boldsymbol{x}_{c,\mathrm{d}}(t)$. Consequently, we aim to solve the decomposition of a desired $\hat{\boldsymbol{u}}_c$ into each agent's applied wrench $\tilde{\boldsymbol{u}}_i$. This decomposition may be written as

$$\tilde{\boldsymbol{u}} = \boldsymbol{A}\hat{\boldsymbol{u}}_c, \tag{5.8}$$

where $\boldsymbol{A} \in \mathbb{R}^{\tilde{n} \times n_c}$ denotes the decomposition matrix. Using (5.8), the dynamical object model depending on the desired external wrench reads

$$\boldsymbol{M}_c \ddot{\boldsymbol{x}}_c + \boldsymbol{f}_c(\dot{\boldsymbol{x}}_c) = \boldsymbol{G}\boldsymbol{A}\hat{\boldsymbol{u}}_c.$$

In order to achieve tracking of the desired trajectory through feedforward control of the inverse dynamics, matrix $\boldsymbol{A}$ has to be chosen to sustain $\boldsymbol{u}_c = \hat{\boldsymbol{u}}_c$, i.e. $\boldsymbol{A}$ has to be an inverse

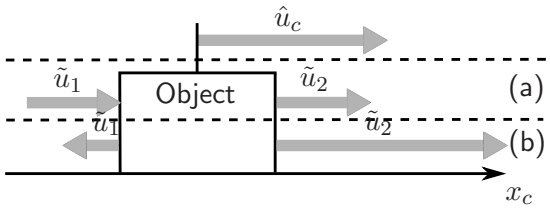

Fig. 5.3: Illustration of the input decomposition in a one-dimensional redundant task. (a) Minimum-norm solution for $\tilde{\boldsymbol{u}} = [\tilde{u}_1 \;\; \tilde{u}_2]^\mathsf{T}$. (b) Possible, but inefficient solution causing an internal wrench.

of $\boldsymbol{G}$, fulfilling

$$\boldsymbol{G}\boldsymbol{A} = \boldsymbol{I}, \tag{5.9}$$

with $\boldsymbol{I}$ being the $n_c \times n_c$ identity matrix. Note that $\dim(\boldsymbol{u_c})$ is equal to the dimension of the configuration space n_c, since the task is required to be controllable and holonomic. In our setting, we further assume that the number of actual inputs is larger than the required number of inputs for task completion,

$$\tilde{n} > n_c.$$

Example 5.1 (Minimal Redundant Task) A minimal example of such actuation redundancy is the movement of an object in one-dimensional space by two agents, each applying an input wrench u_i. The task is redundant, as one agent's input would be sufficient for controlling the object. Arbitrary compositions of both agent's input forces are possible to realize a certain $\hat{u}_c$, see Figure 5.3.

Therefore, the choice of $\boldsymbol{A}$ in (5.9) is not unique. A particularly interesting solution for the effort-sharing matrix $\boldsymbol{A}$ is the generalized Moore-Penrose pseudoinverse $\boldsymbol{G}^+$ of the complete grasp matrix $\boldsymbol{G}$, which yields the minimum-norm solution for the Euclidean norm $\|\tilde{\boldsymbol{u}}\|$, see [27]. Since we are solving for wrenches, there is particular physical meaning of the minimum-norm solution: The applied wrench obtained with $\boldsymbol{G}^+$ represents an *efficient* decomposition, because the external wrench is composed by a minimum magnitude of the applied wrench components, cf. Figure 5.3a. Hence, the applied wrench has no components which could cause ineffective internal wrenches.

Additionally, the nullspace or kernel of $\boldsymbol{G}$ defined as

$$\mathrm{Ker}(\boldsymbol{G}) = \{\tilde{\boldsymbol{u}} | \boldsymbol{G}\tilde{\boldsymbol{u}} = \boldsymbol{0}\}$$

provides a solution space for $\tilde{\boldsymbol{u}}$. Note that in a physical meaning, the null-space component causes no motion of the object, as it does not affect the external wrench. When we replace $\boldsymbol{A}$ by $\boldsymbol{G}^+$ in (5.8), the family of all solutions for $\tilde{\boldsymbol{u}}$ is given by

$$\tilde{\boldsymbol{u}} = \boldsymbol{G}^+\hat{\boldsymbol{u}}_c + \sum_{j=1}^{\mathrm{nullity}(\boldsymbol{G})} \lambda_j \mathrm{Ker}_j(\boldsymbol{G}), \tag{5.10}$$

with the kernel vector $\mathrm{Ker}_j(\boldsymbol{G}) \in \mathbb{R}^{\tilde{n}}$ and the corresponding parameter $\lambda_j \in \mathbb{R}$. Depending on the choice of λ_j, the solution $\tilde{\boldsymbol{u}}$ potentially produces internal wrenches, as depicted

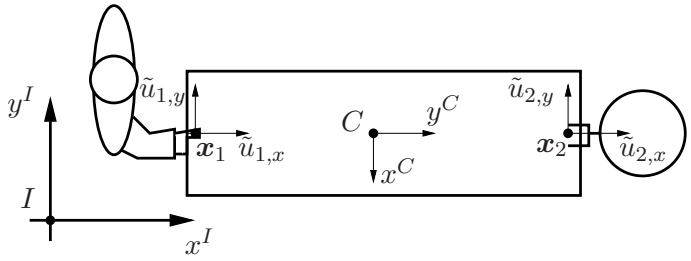

Fig. 5.4: Illustrative scenario of planar cooperative manipulation: One human *(left)* and one robot *(right)* jointly move a bulky object in the x-y-plane.

in Figure 5.3b. In fact, the solution (5.10) provides an effort sharing strategy by input wrench decomposition: In *redundant* DoF where effort sharing between the agents can take place and which are affected by λ_j, and in *non-redundant* DoF where each agent's input is uniquely defined by a necessary contribution. In the following, we show how λ_j can be used to parameterize the effort sharing strategy between the agents in a single redundant direction.

5.2.4 Effort Sharing Policies

In this section, we show how the agents can be assigned meaningful policies regarding their effort behavior in a single redundant DoF. With reference to the experiments described later and for intuitiveness of analysis, we consider from this section on a planar cooperative manipulation task involving two agents for the design of effort sharing policies. The presented strategy may be conducted in multiple redundant DoF without loss of generality.

Analysis of the Planar Dyadic Task

An exemplary planar dyadic task satisfying the conditions from Section 5.2.1 is shown in Figure 5.4. The joint transport of a large table on ball casters, or the joint movement of any other heavy object by sliding it on a surface can be such a task. Both, the human ($i = 1$) and the robotic agent ($i = 2$) could provide input wrenches $\boldsymbol{u}_i$ of dimension $n_c = 3$, with the configuration

$$\boldsymbol{x}_c = \begin{bmatrix} x_{c,\phi} & x_{c,x} & x_{c,y} \end{bmatrix}^{\mathrm{T}},$$

which generally include torques. However, a common property of bulky objects regarding their handling is the lack of sensitivity of the object dynamics to certain torque components, i.e. these torques cannot be applied effectively at the grasp points, see also [189]. This can be explained within our illustrative scenario. Assume a beam-like bulky object with a long geometrical axis, which is manipulated by two partners using a single-handed grasp on the respective end of the object, similar to the one depicted in Figure 5.4. In order to induce a desired rotational motion around the z^C-axis, from experience the reader might agree that it is rather cumbersome to apply the required torque component through the wrist. It is much easier to apply an appropriate force component through the whole arm, which induces turning by translational motion of the grasp point.

Since our analysis focuses on the primary effects of the redundant DoF for effort sharing,

the wrench basis

$$\boldsymbol{B}_{1,2} = \begin{bmatrix} 0 & 1 & 0 \\ 0 & 0 & 1 \end{bmatrix}$$

is chosen in our illustrative scenario. Putting it into (5.2) reduces the input wrench to the effectively applied wrench

$$\tilde{\boldsymbol{u}} = \begin{bmatrix} u_{1,x} & u_{1,y} & u_{2,x} & u_{2,y} \end{bmatrix}^{\mathrm{T}}. \tag{5.11}$$

The kinematic constraints (5.4) of the system can be written as

$$\boldsymbol{x}_i = \begin{bmatrix} x_{c,x} & x_{c,y} \end{bmatrix}^{\mathrm{T}} - \boldsymbol{R}\boldsymbol{r}_{ic}^{C},$$

with

$$\boldsymbol{R} = \begin{bmatrix} \cos\phi & -\sin\phi \\ \sin\phi & \cos\phi \end{bmatrix}$$

denoting the rotation of object frame C with respect to the inertial frame I by angle ϕ, and

$$\boldsymbol{r}_{ic}^{C} = \begin{bmatrix} r_{ic,x} & r_{ic,y} \end{bmatrix}^{\mathrm{T}}$$

being the vector from the grasp point of agent i to the origin of C. Note, that $\boldsymbol{r}_{ic}^{C} = const.$ throughout the task due to the rigid grasps. According to (5.5), the 4×3 transpose of the grasp matrix

$$\boldsymbol{G}^{\mathrm{T}} = \begin{bmatrix} \sin\phi\, r_{1c,x} + \cos\phi\, r_{1c,y} & 1 & 0 \\ -\cos\phi\, r_{1c,x} + \sin\phi\, r_{1c,y} & 0 & 1 \\ \sin\phi\, r_{2c,x} + \cos\phi\, r_{2c,y} & 1 & 0 \\ -\cos\phi\, r_{2c,x} + \sin\phi\, r_{2c,y} & 0 & 1 \end{bmatrix} \tag{5.12}$$

can be derived. Since we can calculate

$$\forall\phi: \quad n_c = \mathrm{rank}(\boldsymbol{G}) = 3$$

for different grasp constraints $\boldsymbol{r}_{1,c} \neq \boldsymbol{r}_{2,c} \neq \boldsymbol{0}$, our planar system is redundant regarding the applied wrench (5.11), since $\tilde{n} = 4$.

Thus, parts of the task effort in terms of applied wrenches can be shared arbitrarily among the contributing agents within the redundant DoF, without influence on the external wrench of the object. In the following, we introduce *effort sharing policies* which are described by a certain choice of the parameter λ in (5.10) and characterize meaningful shares.

Remark 5.2 From (5.12), we can derive straightforwardly the optimal selection of grasp points with respect to the manipulability of the system. Here, the manipulability measure $w : \mathbb{R}^2 \times \mathbb{R}^2 \to \mathbb{R}^+$ of the system is considered, which is defined as

$$w = \sqrt{\det\left(\boldsymbol{G}\boldsymbol{G}^{\mathrm{T}}\right)}. \tag{5.13}$$

After straightforward calculation of (5.13) using (5.12), one finds

$$w = \sqrt{2}\|\boldsymbol{r}_{1,c} - \boldsymbol{r}_{2,c}\|.$$

Maximizing the value of w minimizes the applied wrenches at the grasp points for a given external wrench $\boldsymbol{u}_c$ by maximizing the eigenvalues in (5.3). This leads to the intuitive result that the partners should grasp the object with maximum distance. Note that this optimization is only valid for bounded $\boldsymbol{r}_{i,c}$ and does not explicitly weigh angular vs. translational motion.

Identification of Meaningful and Efficient Policies

In a first step, we will investigate static sharing policies yielding constant role behaviors, while in Section 5.4.2 our notion of roles will be extended to encompass a dynamic allocation within dyads. In the given planar example, the only redundant DoF is intuitively represented by the y^C-axis of the object frame C, cf. Figure 5.4. Hence, components of the external input wrench along this axis can be arbitrarily shared among the two agents. Let us recall now the decomposition (5.10) leading to the agents' applied wrench $\tilde{\boldsymbol{u}}$. The nullspace $\mathrm{Ker}(\boldsymbol{G})$ is spanned by the family

$$\begin{aligned} \mathrm{Ker}(\boldsymbol{G}) &= \mathrm{diag}\,(\boldsymbol{R}, \boldsymbol{R})\ \mathrm{Ker}(\boldsymbol{G})^C, \text{ with} \\ \mathrm{Ker}(\boldsymbol{G})^C &= \begin{bmatrix} 0 & 1 & 0 & -1 \end{bmatrix}^{\mathrm{T}}, \end{aligned} \tag{5.14}$$

allowing one DoF for the design of different effort sharing policies through the choice of the scalar parameter λ in (5.10). Three extreme policies of particular physical meaning are discussed below:

- *Balanced-effort policy:* By choosing the policy

$$\pi_{\mathrm{bal}} : \lambda = 0, \tag{5.15}$$

  the min-norm solution for $\tilde{\boldsymbol{u}}$ is obtained. The effort in terms of magnitude of the applied wrench is equally shared among the agents, see Figure 5.5a.

- *Maximum-robot-effort policy:* If we want to have the robot to take over all of the sharable effort, then the applied human force in the y^C-direction would be zero, i.e. $\tilde{u}^C_{1,y} = 0$. Hence, λ is chosen such that the human does not contribute any *voluntary* effort to the task, which yields the policy

$$\pi_{\mathrm{max}} : \lambda = -\begin{bmatrix} 0 & 1 & 0 & 0 \end{bmatrix} \tilde{\boldsymbol{u}}^C_{\mathrm{bal}}, \tag{5.16}$$

  with the min-norm applied wrench

$$\tilde{\boldsymbol{u}}^C_{\mathrm{bal}} = \mathrm{diag}\,(\boldsymbol{R}, \boldsymbol{R})^{\mathrm{T}}\, \boldsymbol{G}^{+} \hat{\boldsymbol{u}}_c. \tag{5.17}$$

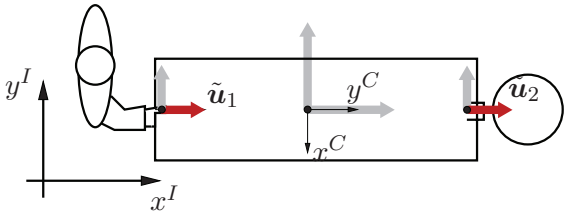

(a) Equal share of the voluntary effort.

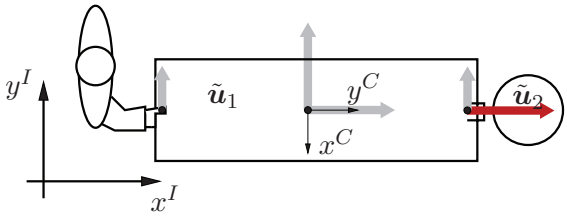

(b) The robot takes all the voluntary effort.

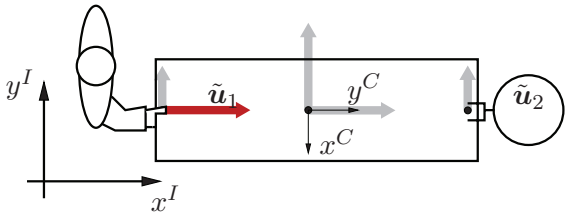

(c) The human takes all the voluntary effort.

Fig. 5.5: Given exemplary external wrench realized by three different effort sharing policies.

The required human effort in terms of the Euclidean norm

$$\|\tilde{\boldsymbol{u}}_1^C\| = \sqrt{(\tilde{u}_{1,x}^C)^2 + (\tilde{u}_{1,y}^C)^2}$$

is minimized now, since $\tilde{u}_{1,x}^C$ refers to the necessary input contribution, see Figure 5.5b. Intuitively spoken, the human has to apply wrenches only in those DoF, which simply *can not* be accomplished by the robot alone, i.e. rotation, and motion in x^C-direction in our example.

- *Minimum-robot-effort policy:* Dual to policy $\pi_{\max}$, the human has to take over all of the sharable effort, if we satisfy $\tilde{u}_{2,y}^C = 0$ through the policy

$$\pi_{\min} : \lambda = \begin{bmatrix} 0 & 1 & 0 & 0 \end{bmatrix} \tilde{\boldsymbol{u}}_{\text{bal}}^C, \tag{5.18}$$

where $\tilde{\boldsymbol{u}}_{\text{bal}}^C$ is again given by (5.17). This policy results in a minimum-effort robot assistance, i.e. in each DoF, the human has to apply wrench components to accomplish the task, see Figure 5.5c.

When we introduce the family of effort sharing policies

$$\pi : \lambda = -\alpha \begin{bmatrix} 0 & 1 & 0 & 0 \end{bmatrix} \tilde{\boldsymbol{u}}_{\text{bal}}^C, \tag{5.19}$$

with policy parameter $\alpha \in \mathbb{R}$, obviously the policies π_{bal}, $\pi_{\max}$ and $\pi_{\min}$ are parameterized by setting $\alpha = 0$, $\alpha = 1$ and $\alpha = -1$ respectively. The following section shows, how $\hat{\boldsymbol{u}}_c$ is obtained, utilizing a motion-generation and interaction control scheme.

Remark 5.3 Policies (5.19) with $\alpha \in [-1, 1]$ and the kernel family parameterized by (5.14) are efficient, since no counter-acting internal wrench on the object is generated. In Figure 5.5b-c the extreme, yet still efficient cases for $|\alpha| = 1$ are depicted, which are obtained intuitively from Figure 5.5a by shifting the voluntary effort. Setting $|\alpha| > 1$ generates counter-acting wrenches, cf. Figure 5.3b.

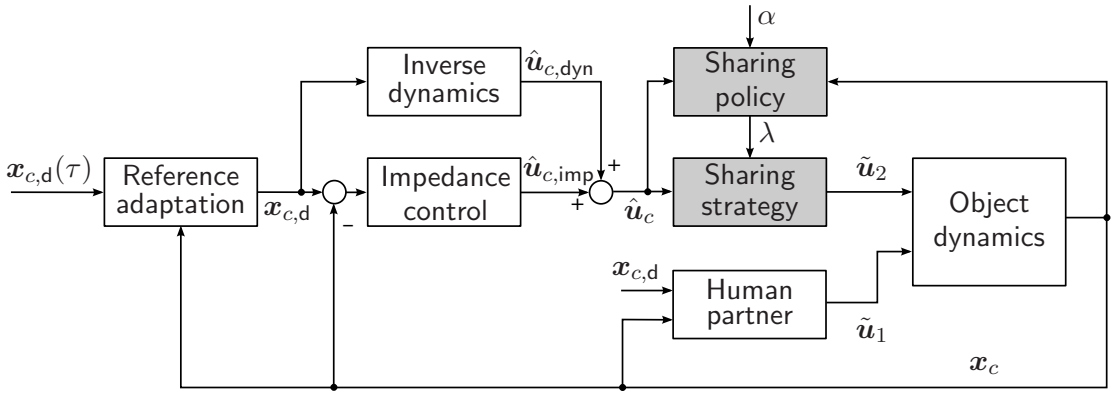

Fig. 5.6: The interaction control scheme deployed to investigate static role behavior. The human partner is supposed to track the common desired trajectory $\boldsymbol{x}_{c,\mathrm{d}}$.

5.3 Static Role Behavior

So far, the effort sharing strategy realizes efficient decompositions based on the wrenches acting on the jointly manipulated object. However, for an artificial partner applying the proposed strategy, an interaction control scheme is required, which enforces its active contribution towards the commonly shared plan. In the following, we introduce an interaction control scheme for robotic assistants that can be real or virtual. The static role behavior rendered to the human partner is both systematically analyzed by separating DoF and experimentally evaluated in a small VR user study.

5.3.1 Interaction Control Scheme

The flow chart of the proposed scheme is depicted in Figure 5.6, with its building blocks explained below.

Generating the Reference Configuration

As outlined in Section 5.2.1, we assume a reference trajectory of the object configuration $\boldsymbol{x}_{c,\mathrm{d}}(\tau)$ to be produced by an appropriate planning or learning technique, with parameter τ denoting the time. Further, $\boldsymbol{x}_{c,\mathrm{d}}(\tau)$ is required to be twice continuously differentiable, such that continuous velocity and acceleration trajectories,

$$\dot{\boldsymbol{x}}_{c,\mathrm{d}}(\tau) = \frac{\mathrm{d}}{\mathrm{d}\tau}\boldsymbol{x}_{c,\mathrm{d}}(\tau) \quad \text{and} \quad \ddot{\boldsymbol{x}}_{c,\mathrm{d}}(\tau) = \frac{\mathrm{d}^2}{\mathrm{d}\tau^2}\boldsymbol{x}_{c,\mathrm{d}}(\tau)$$

exist as well. This can be achieved by trajectory refinement methods, e.g. cubic spline interpolation.

Remark 5.4 From a synthetical design perspective, the velocity and acceleration profiles $\dot{\boldsymbol{x}}_{c,\mathrm{d}}(\tau)$ and $\ddot{\boldsymbol{x}}_{c,\mathrm{d}}(\tau)$ can also describe kinetic limitations of the robotic agent with respect to the task and the environment, considering both technical feasibility and safety. Kinodynamic motion planning techniques can be alternatively used to produce trajectories with bounds on velocities and accelerations [26].

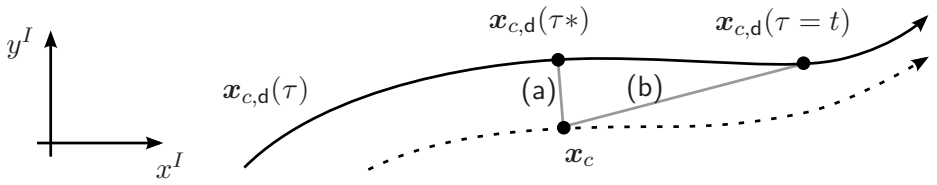

Fig. 5.7: Exemplary reference trajectory $\boldsymbol{x}_{c,\mathrm{d}}(\tau)$ and actual configuration $\boldsymbol{x}_c$, with (a) the desired configuration $\boldsymbol{x}_{c,\mathrm{d}}(\tau^*)$ obtained from reference adaptation, and (b) possible desired configuration $\boldsymbol{x}_{c,\mathrm{d}}(\tau = t)$ resulting from replay over time t.

If the preplanned trajectory $\boldsymbol{x}_{c,\mathrm{d}}(\tau)$ would be strictly replayed over time t, i.e. setting $\tau = t$, the input wrench generated from the object-centered motion tracking described below would grow with increasing difference $\boldsymbol{x}_{c,\mathrm{d}}(\tau) - \boldsymbol{x}_c$, see Figure 5.7b. Since we expect the human partner to induce certain deviations from the preplanned trajectory $\boldsymbol{x}_{c,\mathrm{d}}(\tau)$, a reference adaptation scheme similar to [91] is proposed here. In each actual object configuration $\boldsymbol{x}_c(t)$, the closest reference configuration $\boldsymbol{x}_{c,\mathrm{d}}(\tau^*(t))$ is chosen by

$$\tau^*(t) = \arg\min_{\tau} \|\boldsymbol{x}_{c,\mathrm{d}}(\tau) - \boldsymbol{x}_c(t)\|_{\boldsymbol{Q}}, \tag{5.20}$$

as illustrated in Figure 5.7a. The positive definite matrix $\boldsymbol{Q} \in \mathbb{R}^{3\times3}$ weighs the components of $\boldsymbol{x}_c$, e.g. rotations vs. translations. In this work, we put the focus on translational distance to path, by setting $\boldsymbol{Q} = \mathrm{diag}\,(0, 1, 1)$. The velocity and acceleration reference is then chosen by the corresponding $\dot{\boldsymbol{x}}_{c,\mathrm{d}}(\tau^*(t))$ and $\ddot{\boldsymbol{x}}_{c,\mathrm{d}}(\tau^*(t))$.

Object-Centered Motion Tracking

The robotic agent needs the capability to impose the desired object configuration $\boldsymbol{x}_{c,\mathrm{d}}$ as a result of the common plan. Tracking behavior is synthesized in an object-centered representation by means of the external wrench

$$\hat{\boldsymbol{u}}_c = \hat{\boldsymbol{u}}_{c,\mathrm{dyn}} + \hat{\boldsymbol{u}}_{c,\mathrm{imp}} \tag{5.21}$$

to be applied on the object. The wrench component $\hat{\boldsymbol{u}}_{c,\mathrm{dyn}}$ compensates in a feedforward branch for the dynamics of the robot-object system, with

$$\hat{\boldsymbol{u}}_{c,\mathrm{dyn}} = \hat{\boldsymbol{M}}(\boldsymbol{x}_c, \dot{\boldsymbol{x}}_{c,\mathrm{d}})\ddot{\boldsymbol{x}}_{c,\mathrm{d}} + \hat{\boldsymbol{f}}(\boldsymbol{x}_c, \dot{\boldsymbol{x}}_{c,\mathrm{d}}). \tag{5.22}$$

The mass matrix $\hat{\boldsymbol{M}}(\boldsymbol{x}_c, \dot{\boldsymbol{x}}_{c,d}) \in \mathbb{R}^{3\times3}$ and the friction term $\hat{\boldsymbol{f}}(\boldsymbol{x}_c, \dot{\boldsymbol{x}}_{c,d}) \in \mathbb{R}^3$ lump together the mass $\boldsymbol{M}_c$ and friction $\boldsymbol{f}_c$ of the object dynamics (5.1) and, in case of a physical robot, its admittance apparent at the end effector.

Example 5.2 (Lumped Robot-Object Dynamics) An admittance control law (2.16) with mass $\boldsymbol{M}_r \in \mathbb{R}^{2\times2}$ and damping $\boldsymbol{D}_r \in \mathbb{R}^{2\times2}$ rendered at the grasp point $\boldsymbol{x}_2 \in \mathbb{R}^2$ and expressed in the inertial frame I is considered. Recalling the kinematic constraint of the robot (5.5),

$$\dot{\boldsymbol{x}}_2 = \boldsymbol{G}_2^{\mathrm{T}} \dot{\boldsymbol{x}}_c,$$

we obtain through derivation

$$\ddot{\boldsymbol{x}}_2 = \boldsymbol{G}_2^{\mathrm{T}} \ddot{\boldsymbol{x}}_c + \dot{\boldsymbol{G}}_2^{\mathrm{T}} \dot{\boldsymbol{x}}_c. \tag{5.23}$$

Using (5.3) and (5.23), the inertial wrench component of (5.22) is then superposed by

$$\hat{\boldsymbol{M}}(\boldsymbol{x}_c, \dot{\boldsymbol{x}}_{c,\mathrm{d}}) \ddot{\boldsymbol{x}}_{c,\mathrm{d}} = \boldsymbol{M}_c \ddot{\boldsymbol{x}}_{c,\mathrm{d}} + \boldsymbol{G}_2 \boldsymbol{M}_r \left(\boldsymbol{G}_2^{\mathrm{T}} \ddot{\boldsymbol{x}}_{c,\mathrm{d}} + \dot{\boldsymbol{G}}_2^{\mathrm{T}} \dot{\boldsymbol{x}}_{c,\mathrm{d}} \right).$$

Similarly, via (5.3) and (5.5) the friction term of (5.22) is calculated by

$$\hat{\boldsymbol{f}}(\boldsymbol{x}_c, \dot{\boldsymbol{x}}_{c,\mathrm{d}}) = \boldsymbol{f}_c(\boldsymbol{x}_c, \dot{\boldsymbol{x}}_{c,\mathrm{d}}) + \boldsymbol{G}_2 \boldsymbol{D}_r \boldsymbol{G}_2^{\mathrm{T}} \dot{\boldsymbol{x}}_{c,\mathrm{d}}.$$

Remark 5.5 Apart from the feedback configuration $\boldsymbol{x}_c$, the inverse dynamics (5.22) rely on feedforward variables ($\dot{\boldsymbol{x}}_{c,\mathrm{d}}$, $\ddot{\boldsymbol{x}}_{c,\mathrm{d}}$). Using their corresponding feedback variables would result in total cancellation of the robot-object dynamics, which is obviously unrealizable.

An object-centered impedance-type control law acting on the tracking error of the configuration $\boldsymbol{x}_c$ generates the feedback component of the external wrench

$$\hat{\boldsymbol{u}}_{c,\mathrm{imp}} = \boldsymbol{K}_p(\boldsymbol{x}_{c,\mathrm{d}} - \boldsymbol{x}_c) + \boldsymbol{K}_d(\dot{\boldsymbol{x}}_{c,\mathrm{d}} - \dot{\boldsymbol{x}}_c). \tag{5.24}$$

The stiffness gain $\boldsymbol{K}_p \in \mathbb{R}^{3\times3}$ and the damping gain $\boldsymbol{K}_d \in \mathbb{R}^{3\times3}$ render a compliant behavior guaranteeing smooth rising of counteracting wrenches, if the object configuration deviates from the expected.

Embedding the Effort Sharing Strategy

The external wrench (5.21) guaranteeing object-centered motion tracking feeds the effort sharing strategy. The applied wrench of the robot $\tilde{\boldsymbol{u}}_2$ is calculated as the solution (5.10) to the effort sharing problem, based on the configuration-dependent parameter λ. Using (5.17), the static role is then defined by the effort sharing policy (5.19), i.e. the voluntary contribution of the robot for a certain choice of the policy parameter α. Note, that the scheme from Figure 5.6 assumes a robotic agent capable to ideally apply the wrench $\tilde{\boldsymbol{u}}_2$. For physical agents, the dynamics of force control need to be considered as well, which will be addressed later.

Remark 5.6 The effort sharing strategy can be regarded as a selective filter acting on the external wrench $\hat{\boldsymbol{u}}_c$, depending on the imposed role.

Remark 5.7 The role of the human is assumed complementary and allocated in a feedforward, centralized manner. Hence, the actual applied wrench of the human $\tilde{\boldsymbol{u}}_1$ does not necessarily agree. We will experimentally investigate the effects of static role behavior on cooperative pHRI.

5.3.2 Analysis of the Interactive Behavior

A better understanding of the overall interactive behavior rendered by the previously introduced interaction control scheme is sought through an analysis of the robot-object

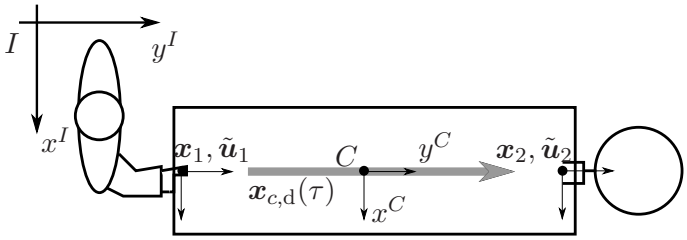

Fig. 5.8: Case study within the planar dyadic scenario, considering the task of purely translational object transfer in the redundant direction y^C. Any deviations in path direction $\Delta x_{c,y}$ vanish due to reference adaptation.

dynamics apparent at the grasp point of the human partner $\boldsymbol{x}_1$. For the sake of simplicity, we focus on the relevant case of moving the object along its redundant direction y^C, i.e. the reference $\dot{\boldsymbol{x}}_{c,\mathrm{d}}(\tau)$ is such that

$$\dot{\boldsymbol{x}}_{c,\mathrm{d}}(\tau) = \mathrm{diag}\,(1, \boldsymbol{R}) \begin{bmatrix} \dot{x}^C_{c,\phi,\mathrm{d}}(\tau) & 0 & \dot{x}^C_{c,y,\mathrm{d}}(\tau) \end{bmatrix}^{\mathrm{T}} \quad \forall \tau.$$

Furthermore, we assume pure translation, i.e. $\dot{x}_{c,\phi,\mathrm{d}} = 0$. Without loss of generality, we align the inertial frame I and the object frame C by setting $x_{c,\phi}(t=0) = 0$, see Figure 5.8. Then, the min-norm solution (5.17) reads

$$\tilde{\boldsymbol{u}}_{\mathrm{bal}} = \begin{bmatrix} \tilde{u}_{1,x} & \frac{1}{2}\hat{u}_{c,y} & \tilde{u}_{2,x} & \frac{1}{2}\hat{u}_{c,y} \end{bmatrix}^{\mathrm{T}}$$

Using the kernel vector (5.14) and the effort sharing policy (5.19), the min-norm solution $\tilde{\boldsymbol{u}}_{\mathrm{bal}}$ is modified by the effort sharing strategy (5.10). First, we are interested in the applied wrench of the robot,

$$\tilde{\boldsymbol{u}}_2 = \begin{bmatrix} \tilde{u}_{2,x} & \frac{1}{2}\hat{u}_{c,y} \end{bmatrix}^{\mathrm{T}} - \frac{1}{2}\alpha \hat{u}_{c,y} \begin{bmatrix} 0 & -1 \end{bmatrix}^{\mathrm{T}}. \tag{5.25}$$

In (5.25) the selective nature of the wrench decomposition becomes obvious. While the *necessary* component $\tilde{u}_{2,x}$ remains unaffected, the *voluntary* component is scaled by the policy parameter,

$$\tilde{u}_{2,y} = \frac{1}{2}\,(1+\alpha)\,\hat{u}_{c,y}. \tag{5.26}$$

In the following, we qualitatively analyze the dynamics of the coupled robot-object system in response to deviations defined as

$$\Delta \boldsymbol{x}_c = \boldsymbol{x}_{c,\mathrm{d}}(\tau^*) - \boldsymbol{x}_c, \quad \text{and} \quad \Delta \dot{\boldsymbol{x}}_c = \dot{\boldsymbol{x}}_{c,\mathrm{d}}(\tau^*) - \dot{\boldsymbol{x}}_c. \tag{5.27}$$

This analysis is conducted separately in the *redundant* and *non-redundant* DoF. Notably, the separation is based on the assumption that the object dynamics (5.1) and the grasp matrix (5.12) are such, that cross-coupling between the DoF of the object configuration $\boldsymbol{x}_c$ is negligible, as e.g. in the symmetric scenario from Figure 5.8. For illustration purpose, we describe the static role behavior obtained from the extreme policies $\pi_{\min}$ and $\pi_{\max}$.

Role-Dependent Behavior in the Redundant DoF

First, we investigate the dynamic behavior in the redundant DoF. The y^C-component of the object model (5.6) reads

$$\tilde{u}_{1,y} + \tilde{u}_{2,y} = m_{c,y}\ddot{x}_{c,y} + f_{c,y}(x_{c,y}, \dot{x}_{c,y}). \tag{5.28}$$

Applying (5.21), (5.22) and (5.24) to (5.28) yields for the human applied wrench

$$\tilde{u}_{1,y} = m_{c,y}\ddot{x}_{c,y} + f_{c,y}(x_{c,y}, \dot{x}_{c,y}) - \frac{1}{2}(1+\alpha)\left(\hat{m}_y\ddot{x}_{c,y,\mathrm{d}} + \hat{f}_y(x_{c,y}, \dot{x}_{c,y,\mathrm{d}}) + k_{d,y}\Delta\dot{x}_{c,y}\right) \tag{5.29}$$

Note that the stiffness term $K_{p,y}\Delta x_{c,y}$ is vanished in (5.29) due to the reference adaptation, which ensures $\Delta x_{c,y} = 0$ in path direction. The following insights on the static role behavior in the redundant DoF are gained from (5.29):

- For the *minimum-effort policy* $\pi_{\min}$, i.e. $\alpha = -1$, the human purely faces the object dynamics (5.28) without assistance ($\tilde{u}_{2,y} = 0$), and in case of a physical robot, the lumped robot-object dynamics.

- For the *maximum-effort policy* $\pi_{\max}$, i.e. $\alpha = 1$, the robot fully compensates the object dynamics without human contribution ($\tilde{u}_{1,y} = 0$), if we assume a perfect object model $m_{c,y} = \hat{m}_y$ and $f_{c,y} = \hat{f}_y$, and absence of disturbances. In this case, deviations $\Delta\dot{x}_{c,y} \neq 0$ from the reference $\dot{\boldsymbol{x}}_{c,\mathrm{d}}(\tau^*)$ relate to the human applied wrench through

  $$\tilde{u}_{1,y} = -m_{c,y}\Delta\ddot{x}_{c,y} - \Delta f_{c,y} - k_{d,y}\Delta\dot{x}_{c,y}.$$

  The wrench components $m_{c,y}\Delta\ddot{x}_{c,y}$ and $\Delta f_{c,y}$ refer to the over- or undercompensated portions of the object mass and friction due to the deviation $\Delta\dot{x}_{c,y}$. The remaining impedance term $k_{d,y}\Delta\dot{x}_{c,y}$ causes a viscous, corrective behavior towards the desired velocity rendered to the human partner.

Remark 5.8 The analysis above investigates the static relation $\frac{\Delta\boldsymbol{x}_c}{\tilde{\boldsymbol{u}}_1}$, i.e. how *quasi-static* deviations $\Delta\boldsymbol{x}_c$, $\Delta\dot{\boldsymbol{x}}_c$ relate to the human applied wrench $\tilde{\boldsymbol{u}}_1$. Due to the feedforward compensation (5.22), the apparent impedance $\frac{\delta\boldsymbol{x}_c}{\delta\tilde{\boldsymbol{u}}_1}$, which is the response $\delta\boldsymbol{x}_c$ to dynamic changes $\delta\tilde{\boldsymbol{u}}_1$, is governed by the superposition of both the (robot-)object dynamics and the object-related impedance imposed by the robot.

Role-Invariant Behavior in the Non-Redundant DoF

Deviations of the object $\Delta x_{c,\phi}$ and $\Delta x_{c,x}$ refer to the non-redundant DoF of the task. Here, a non-zero component $\tilde{u}_{1,x}$ of the human applied wrench usually induces a mixture of both deviations, due to the coupling by the grasp matrix in (5.6). Note, that those deviations are not accommodated by the reference adaptation (5.20), see Figure 5.9. Thus, the dynamic behavior in the non-redundant DoF is governed by the (robot-)object dynamics and the object-centered impedance, which are invariant with respect to the effort sharing policy, cf. the x-component of (5.25).

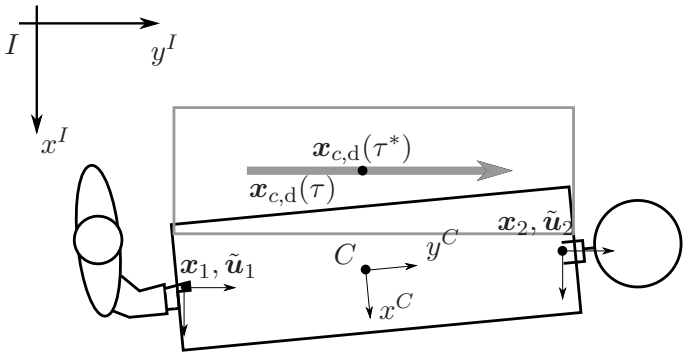

Fig. 5.9: Case study from Figure 5.8 for deviations in the non-redundant DoF $\Delta x_{c,\phi}$ and $\Delta x_{c,x}$ from the desired configuration $\boldsymbol{x}_{c,\mathrm{d}}(\tau^*)$ (gray silhouette). The deviations remain for cooperative compensation by object-centered impedance control.

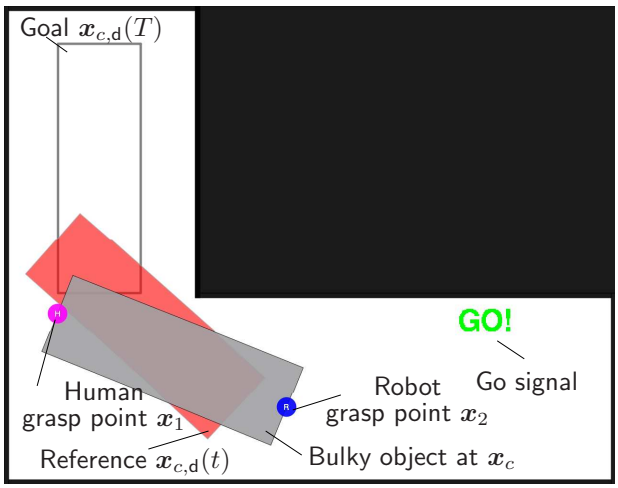

Fig. 5.10: Screen shot of the virtual environment used for the planar transport task.

Remark 5.9 The case study illustrates the *anisotropic impedance* characteristics resulting from the reference adaptation: In path direction $\Delta x_{c,y}$, the object-related impedance enforced by the robot reduces to the velocity-dependent wrench enforced by the gain $K_{d,y}$. It renders a bounded urge of the robot towards the goal. In the remaining directions, a configuration-dependent wrench with gains $K_{p,x}$ and $K_{p,\phi}$ is enforced as well. It compensates for deviations perpendicular to the path.

5.3.3 Experimental Evaluation

For experimental evaluation of the decomposition approach on effort sharing with human partners, we consider a prototypical object transport task and adopt the planar scenario from Section 5.2.4. This experiment aims to show an interdependency between different effort sharing policies of a virtual robot partner and the jointly achieved task performance. The participants were asked to move a virtual bulky object jointly with a virtual robot partner through an L-shaped corridor, see the screen display in Figure 5.10. The task was to cooperatively track the configuration reference trajectory shown in red as good as possible. The goal configuration was displayed as transparent silhouette.

Remark 5.10 In the virtual scenario, the term *bulky* refers to the relative dimensions of the object with respect to the environment, rather than its absolute expansion.

Conditions

Three conditions manipulated the effort sharing policy of the virtual robotic partner:

- **MIN**: Minimum robot effort.
  Applying the policy parameter $\alpha = -1$, the robot only contributes to the steering motion but leaves the entire effort in the sharing direction (y^C) to the human.

- **BAL**: Balanced effort.
  The balanced-effort strategy achieved by $\alpha = 0$ results in a robot behavior contributing to steering as well as half of the required effort in the sharing direction.

- **MAX**: Maximum robot effort.
  By setting $\alpha = 1$, the robot fulfills the tracking motion in the direction of sharing completely alone. The human force input is only required for steering.

Participants, Setup and Procedure

Ten unpaid, male participants took part in this experiment. They were between 24 and 33 years old, at a mean age of 27.7 years. All were right handed and had normal or corrected-to-normal vision.

Through the VR-System described in Appendix A.1, the participants were able to apply forces to the object at the given human grasp point on the opposite side of the grasp point of the virtual partner. Visual-haptic rendering of the virtual environment was performed as explained in Appendix B. The virtual object was assigned the mass $\boldsymbol{M}_c = \mathrm{diag}\left(0.042\,\mathrm{kgm}^2, 20\,\mathrm{kg}, 20\,\mathrm{kg}\right)$, and the dimensions of 0.15 m by 0.05 m. Its motion was damped by isotropic, viscous friction $\boldsymbol{D}_c = 120\,\mathrm{Nsm}^{-1} \cdot \boldsymbol{I}_4$, acting at the grasp points $\boldsymbol{x}_{1,2}$. The virtual robot applied the interaction control scheme from Section 5.3.1 to shape its force input to the object. Since we aim to isolate the effects of the effort role behavior, a pre-planned, fixed configuration trajectory was assumed. The reference trajectory $\boldsymbol{x}_{c,d}(\tau)$, with $\dot{\boldsymbol{x}}_{c,d}(\tau)$, $\ddot{\boldsymbol{x}}_{c,d}(\tau)$ was generated from supporting points and then interpolated using cubic splines. The desired configuration $\boldsymbol{x}_{c,d}$ was chosen by the reference adaptation, depending on the current configuration. The object-centered impedance was set to $\boldsymbol{K}_p = \mathrm{diag}\left(1.0\,\mathrm{Nmrad}^{-1}, 100.0\,\mathrm{Nm}^{-1}, 100.0\,\mathrm{Nm}^{-1}\right)$ and to $\boldsymbol{K}_d = \left(0.6\,\mathrm{Nmsrad}^{-1}, 50.0\,\mathrm{Nsm}^{-1}, 50.0\,\mathrm{Nsm}^{-1}\right)$, respectively.

For each of the three conditions, a sequence of five trials was performed. The sequences were randomized for each participant. Participants were informed about the behavior they could expect from the virtual partner before each sequence. Each trial took $T = 13\,\mathrm{s}$, regardless of the final object configuration. A five-second break allowed the participants to settle between each trial. The first trial of each sequence was discarded from further evaluation.

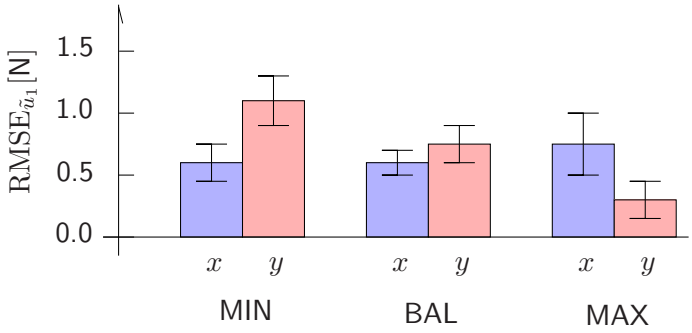

Fig. 5.11: Mean and standard deviation of the root-mean-square error of the wrenches applied by the human partner. Components x, y are expressed in the object frame C.

Results and Discussion

The root-mean-square errors (RMSE) of the applied wrench and the configuration are analyzed, with the resulting values reported in Figure 5.11 and Figure 5.12 respectively. Visible trends are discussed in the following. The wrench RMSE is calculated separately for the wrench components by

$$\mathrm{RMSE}_{\tilde{u}_1} = \sqrt{\frac{1}{T}\int_0^T \left(\tilde{u}_1(t) - \tilde{u}_{1,\mathrm{m}}(t)\right)^2 \mathrm{d}t}.$$

It is strongly affected by the effort sharing policy of the robot. Erroneous (unnecessary) human wrench inputs in the redundant direction of effort sharing y^C decrease by more than 50% for the maximum-robot-effort condition in relation to the minimum-robot-effort condition. However, wrenches in the perpendicular direction x^C seem widely unaffected by the applied sharing policy. Similarly, the configuration RMSE is calculated per component by

$$\mathrm{RMSE}_{x_c} = \sqrt{\frac{1}{T}\int_0^T \left(x_{c,\mathrm{d}}(t) - x_c(t)\right)^2 \mathrm{d}t}$$

It is visibly affected by the effort sharing policy. The tracking performance in y^C-direction improves with increasing robot effort. A reciprocal effect can be observed in angular tracking performance, i.e. in ϕ-direction which deteriorates simultaneously. A potential explanation is the increasing difficulty of mental task modeling, as the robot compensates a major share of the object dynamics. No clear conclusion can be drawn for the x^C-direction perpendicular to the direction of effort sharing.

In summary, the following insights are gained from the experimental results:

- In the direction of redundancy-based effort sharing, cooperation quality improves with an increasing degree of robot assistance.
- Tracking performance in the perpendicular i.e. non-redundant motion direction remains widely unaffected by the rendered effort sharing strategy.
- The resulting trends of this experiment support a generalization of fundamental

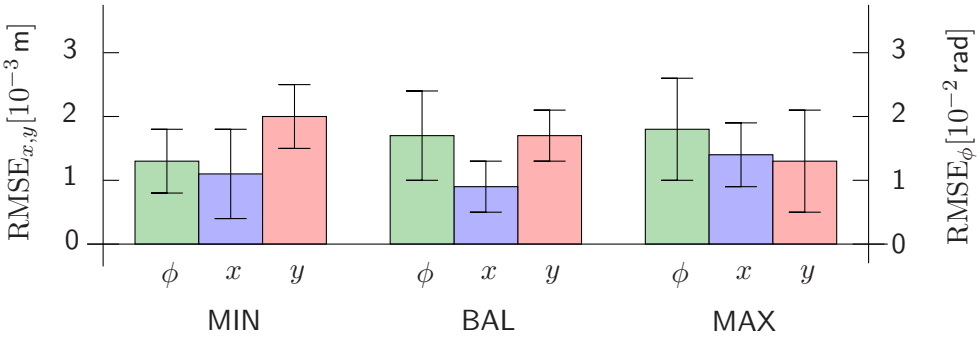

Fig. 5.12: Mean and standard deviation of the root-mean-square error of the configuration. Components x, y are expressed in the object frame C.

findings on human-robot haptic cooperation in point-mass manipulation [108, 134] to non-point-mass manipulation.

5.4 Design of Dynamic Role Behavior

Before we synthesize dynamic role allocations on top of the derived effort sharing strategy, we distinguish and review important features of existing role allocation strategies applied in cooperative scenarios in the domains haptic HCI, haptic shared control of mechanisms, and pHRI. The interaction control scheme known from above is enhanced to conceptually illustrate how admittance-controlled, physical robots are integrated and how feedback from a single human partner is acquired for dynamic role allocation. Dynamic role behaviors resulting from the presented concept are implemented and experimentally evaluated.

5.4.1 Role Allocation Strategies

The goal of a role allocation strategy is to achieve a common task or the related physical effort respectively, by potentially time-varying and asymmetric contributions of the partners. Heterogeneous capabilities of the partners may even lead to synergetic, complementary contributions to cooperatively accomplish the task. In the following, we structure existing role allocation strategies that have been investigated for application in robotic or virtual assistants along three main building blocks. Those are identified as the set of *adjustment criteria*, the *role allocation scheme*, and the embedding *interaction control scheme*. Notably, the latter two may form an atomic unit that governs the interactive role behavior.

Synopsis of Adjustment Criteria

In the context of robotic role allocation in pHRI tasks, a variety of adjustment criteria is deployed. By their temporal scope, we distinguish:

- *Off-line versions* provide performance ratings on a between-trial scope, i.e. measures from one or more executions (trials) of the same task are acquired and evaluated

afterwards. In general, those criteria are suited equally well for evaluation and comparison of robotic implementations in pHRI experiments.

- *On-line versions* yield performance ratings on a within-trial scope, taken from instantaneous measurements. Averaging over finite time windows or integrating instantaneous measurements over the course of the trial, possibly with forgetting factors, comprises multiple measurement samples in the criterion.

Implemented adjustment criteria found in literature focus on sensory information extracted through the haptic modality, as it is considered fundamental to the role allocation problem and intuitively accessible through the physical coupling. In the context of goal-directed pHRI tasks, spatio-temporal criteria are applied frequently, such as:

- *Completion time* of the task. The velocity of the object measuring the task progress towards the goal may be taken as the differential, on-line version [123].

- *Spatial deviations from a reference path* or trajectory of the common object or interaction point [191]. Those are applicable only in pursuit tracking tasks, where a preferred or optimal common reference can be defined.

- *Spatial distance to obstacles* to be avoided in the environment [144, 191] as well as *distance to self-collision* as an exemplary individual constraint of the robotic agent [32]. If admissible for the task, also the number of collisions with obstacles or the time being in contact with forbidden regions is used [123].

- *Movement variability* of the partner as the predicted covariance [104] or the *observation likelihood* [169] of the motion state drawn from a probabilistic model of the partner's task-related behavior. The task model is built by several—initially under passive assistance, to allow for observation—cooperative executions of the same task [90, 199].

The close coupling in pHRI gives rise to criteria that assess the physical effort spent by the partners:

- *Norm of the applied wrench* of the partner, averaged over execution time [122]. Any kind of interaction force at the grasp point is interpreted as effort, no matter of its direction, or whether it is actively induced through muscular contraction or purely resulting from passive limb dynamics.

Negotiation processes between the partners due to individual deviations from the common plan and disagreement due to differing intentions are assessed by:

- *Norm of the internal wrench* on the object or interaction point, averaged over execution time [122]. Internal wrenches, no matter of the sign, are waisted effort with respect to task efficiency, since they do not cause motion but only internal stress. Yet, the internal wrenches, which are also called interactive forces [48], are purposeful for the communication between the partners through haptics.

- *Deviations from a reference wrench* [113]. Going below or beyond certain thresholds on previously acquired wrench profiles is interpreted as the partner's intent to shift the control authority.

- *Expected variabilities* of the partner's contribution, given by the predicted variance of the partner's wrench input. The latter is obtained from a probabilistic task model [104]. The *current variabilities* given by the windowed sample covariance of the measured wrench input are employed to additionally represent an instantaneous level of disagreement [105].

Some works investigate the interaction and merging of multiple adjustment criteria for the purpose of role allocation. Weighted superpositions of multiple measures into a single, scalar-valued performance index are applied in [122, 123, 191]. In the modified, linear-quadratic control approach of [104, 105], weighing of input and movement variabilities is defined by the parameters of the cost functional.

Remark 5.11 Weighing of multiple criteria usually implies a trade-off and remains subject to design, as their individual importance may depend on the characteristics of the task, the environmental situation and also the partner. Normalized formulations of the criteria may facilitate a more intuitive design of the weighing.

Role Allocation Schemes with Explicit Policy Parameters

Similar to the effort sharing policies derived above, roles are frequently characterized by means of a bounded scalar variable, which we commonly denote by the policy parameter α in the following. Note, that in literature, the terms blending variable, assistance level or policy parameter are often used synonymously. Such parameterization allows to treat role allocation and interaction control as divisible problems. The actual role or assistance behavior of the artificial agent is then subject to interaction control, which renders the task-dependent wrench contribution.

Some of the aforementioned adjustment criteria may be instantaneously and explicitly mapped to corresponding values of the policy parameter, usually after normalization [169]. Smooth trigonometric blending to model the functional dependency on single criteria and non-linear adaptation laws depending on a multi-criterion performance index are found in [32, 191]. Role blending based on a finite state machine with state transitions triggered by threshold conditions on the adjustment criterion is proposed by [113], and hysteresis-based blending is applied in [123].

Constant assistance levels may be derived, which are optimal with respect to some single or multi-criterion performance index. Evaluations of the performance index for one or several executions of the cooperative task under systematic variation of the assistance level allow to model static functional relationships between the former and the latter, e.g. through polynomial fitting [122].

Passenberg et al. [123] also propose continuously changing assistance levels as a result of linear adjustment laws, for which performance error measures are defined and minimized. This kind of role allocation can be understood as a tracking control problem of an on-line performance index with respect to a certain reference performance.

Remark 5.12 The policy parameter is usually embedded in the control scheme as proportional scaling factor, that directly modulates the control input. Therefore, blending techniques such as low-pass filtering are applied frequently to obtain a continuous-valued policy parameter and smooth control inputs [113, 123]. Suitable choices for blending times lie above or in the order of human motor response times [86], to give human partners the opportunity to successfully accommodate to the changing role behavior.

Embedding Schemes for Interaction Control and Assistance

All of the schemes reviewed below assume the grasp points of the cooperating dyad to be coincident with the object configuration. Therefore, the cooperative manipulation problem reduces to a single interaction point $\boldsymbol{x}_1 = \boldsymbol{x}_2 = \boldsymbol{x}_c$. Furthermore, all of both agents' input components provide full actuation redundancy, i.e. the independent control inputs fulfill $\tilde{n}_1 = \tilde{n}_2 = n_c$. A popular example task applied in such setting is the cooperative manipulation of point-mass objects. For the sake of clarity, we continue the notation used in this chapter.

The controller blending scheme proposed by Evrard and Kheddar [31] renders variable role behavior that allows role allocation by an independent blending variable $\alpha_i \in [0, 1]$ per agent $i = 1, 2$. The mathematical notion of homotopy between a pair of functions is exploited to render a blend of control inputs

$$\tilde{\boldsymbol{u}}_i = \alpha_i \, \mathcal{L} + (1 - \alpha_i) \, \mathcal{F}, \tag{5.30}$$

with $\mathcal{L}$ and $\mathcal{F}$ being template controllers for the extreme cases of a leader and a follower respectively. The leader and follower are implemented for instance by two distinct impedance controllers similar to (5.24), e.g. a low or zero-stiffness follower controller with vanishing wrench input and a stiff leader controller enforcing the desired object motion. The gradual blend of two extreme controllers for each agent may render a variety of interaction behaviors.

Though being rather tailored to computer-assisted tele-operation than cooperative pHRI scenarios, variable assistance levels provided by guiding virtual fixtures are equivalent the role allocation problem of a virtual partner. In [122, 123] for example, guidance behavior towards a predefined, error-free path $\boldsymbol{x}_{c,\mathrm{d}}(\tau)$ is rendered by the composition of a passive virtual fixture in path direction, and by an active virtual fixture perpendicular to the path direction. With the deviation $\Delta\boldsymbol{x}_c$ and $\Delta\dot{\boldsymbol{x}}_c$ from (5.27) generated by a reference adaptation scheme (5.20), the applied wrench of such an assistance reads

$$\tilde{\boldsymbol{u}}_2 = \alpha_{\parallel} \, c_{\mathrm{f}} \left(\operatorname{sgn} \left(\Delta\dot{\boldsymbol{x}}_c \right) \right) \, \tilde{\boldsymbol{u}}_{1,\mathrm{m}\parallel} + \alpha_{\perp} \boldsymbol{K}_{p,\perp} \Delta\boldsymbol{x}_c. \tag{5.31}$$

The passive virtual fixture is obtained from up or down scaling of the measured applied wrench of the human $\tilde{\boldsymbol{u}}_{1,\mathrm{m}\parallel}$ in path direction by the function $c_{\mathrm{f}} : \mathbb{R} \to \mathbb{R}$, depending on the direction of motion $\operatorname{sgn}(\Delta\dot{\boldsymbol{x}}_c)$. Spring-like compensation of deviations $\Delta\boldsymbol{x}_c$ with stiffness $\boldsymbol{K}_{p,\perp} \in \mathbb{R}^{n_c \times n_c}$ is provided by the active virtual fixture perpendicular to the path. The role allocation problem in multiple redundant DoF is decomposed into a single DoF in path direction, which is governed by the assistance level $\alpha_{\parallel}$ and the remaining,

perpendicular DoF, which are governed by $\alpha_\perp$, with both $\alpha_\parallel, \alpha_\perp \in [0, 1]$.

Remark 5.13 The role allocations, each generating a time-varying assistance level or policy parameter, may be designed based on different adjustment criteria and separately in DoF. Yet, strict decompositions neglect potentially remaining interdependencies of the adjustment criteria between DoF.

Remark 5.14 The passive virtual fixture in (5.31) renders the role behavior of a *supportive follower*. Variable parts of the human applied wrench $\tilde{\boldsymbol{u}}_{1,\mathrm{m}\parallel}$ are replicated by the assistance, resulting in an effort contribution mirrored to that of the human. Such an assistance scheme does not feature a *proactive*, autonomous urge towards the common goal. The active virtual fixture in (5.31) acting in perpendicular DoF renders a compensating behavior equivalent to the one analyzed in Section 5.3.2.

Implicit Role Allocation by Optimal Feedback Control

In a control-theoretic approach, both the role distribution (even the role allocation) and interaction control are an inextricable and implicit result of control design, i.e. the approach does not rely on an explicit policy parameter. Rigorous, cost-based formulation of interactive behaviors and role distributions is proposed by Jarrassé et al. [69]. Through cost function templates considering task error and effort terms of both contributors, the authors are able to simulate a variety of dyadic interactive behaviors by different parameterizations of linear-quadratic controllers. Dynamic role allocation by optimal control techniques is investigated in [104, 105, 144]. A linear state feedback control law renders the control input to the linear task dynamics, which is the input wrench of a virtual assistant,

$$\tilde{\boldsymbol{u}}_2 = -\boldsymbol{K}\left(\boldsymbol{\xi}_c - \boldsymbol{\xi}_{c,\mathrm{d}}\right). \tag{5.32}$$

By defining the state $\boldsymbol{\xi}_c = [\ \boldsymbol{x}_c \quad \dot{\boldsymbol{x}}_c\ ]^{\mathrm{T}}$ composed by the position and velocity of the grasp point of the assistant, (5.32) resembles an impedance-type tracking of the desired state $\boldsymbol{\xi}_{c,\mathrm{d}} \in \mathbb{R}^{2n_c}$ with feedback matrix $\boldsymbol{K}(t) \in \mathbb{R}^{n_c \times 2n_c}$. Variable stiffness and damping gains result from choosing $\boldsymbol{K}(t)$ as the solution of the risk-sensitive optimal feedback control problem, where the assistance policy is represented by a cost function depending on the process noise.

Remark 5.15 Depending on the parameterization of the cost function, the gain values in $\boldsymbol{K}(t)$ dynamically rise or fall as a function of the variabilities of both the human input and movements, resembling e.g. a risk-seeking or risk-averse role allocation behavior (attitude) of the assistant. The systematic, cost-minimizing formulation renders this approach theoretically appealing.

In the following, we synthesize both a continuous and a discrete role allocation scheme based on explicit, dynamical formulations of the policy parameter $\alpha(t)$. Specifically, the instantaneous agreement of the human partner, defined by interactive forces, is employed as an on-line adjustment criterion for role allocation.

5.4.2 Synthesis of Role Allocations

The effort sharing policies (5.19) derived in Section 5.2.4 with constant policy parameter α imply a *static* role behavior in terms of the effort sharing ratio among the dyad in the redundant direction. They furthermore result from a feedforward calculation of the agents' applied wrenches, which can not be imposed to human partners. In contrast, the *dynamic* role allocation strategies developed in the following vary the policy parameter α over time during task execution. Here, wrench feedback from the human partner is considered in a single adjustment criterion.

Remark 5.16 The role and the corresponding allocation strategy refers to a single redundant DoF of the task. As outlined above, the partners may apply different role allocation schemes in each of multiple redundant DoF.

Remark 5.17 The resulting robot behavior in terms of its autonomous urge towards the task goal is influenced by the velocity profile $\dot{\boldsymbol{x}}_c(\tau)$ of the configuration trajectory planned by the robot.

Constant Role Allocation as Baseline

The baseline strategy with respect to the experimental evaluation that will follow in Section 5.5, is defined by a role allocation remaining constant over the course of the task. Any arbitrary choice of a constant parameter α directly affects the urge of the robot to accomplish the task. Given a certain reference velocity profile, the choice of $\alpha = 0$ results in an equal, feedforward composition of the external wrench in the redundant DoF. This case is particularly appealing due to its symmetry: A human partner applying the same wrench as the robot in the redundant DoF moves the object according to the reference velocity profile of the robot. In contrast, a human partner who applies the same wrench in the opposite direction cancels the applied wrench of the robot.

Remark 5.18 Similar to the choice of the velocity profile $\dot{\boldsymbol{x}}_c(\tau)$, the value of the policy parameter α defining a constant role allocation may be chosen depending on performance evaluations from previous task executions.

Weighted Proactive Role Allocation

Dynamic role behavior is realized by a weighted proactive role allocation strategy. We propose a continuous, first order integrator that governs the policy parameter according to

$$\alpha(t) = \alpha_0 + \int_{t_0}^{t} \dot{\alpha}(\tau)\mathrm{d}\tau, \tag{5.33}$$

with the initial policy value α_0. Boundedness, i.e. $\alpha \in [-1, 1]$, is ensured by an anti-windup saturation to allocate only efficient policies. The rate of change of the policy $\dot{\alpha}(t)$

is designed to switch between the cases

$$\dot{\alpha}(t) = \begin{cases} -\tau_{\mathrm{w}-} \left| \hat{u}_{1,y}^{C}(t) \right|, & \text{if } \xi(t) = 0 \\ \tau_{\mathrm{w}+}\, u_{y,\mathrm{th}}^{C}, & \text{if } \xi(t) = 1 \wedge \left| \hat{u}_{1,y}^{C}(t) \right| < u_{y,\mathrm{th}}^{C} \\ \tau_{\mathrm{w}+} \left| \hat{u}_{1,y}^{C}(t) \right|, & \text{otherwise.} \end{cases} \tag{5.34}$$

The meaning of the feedback variables and parameters in (5.34) and their effects are explained as follows:

- Different alternatives to construct an indicator of human agreement exist, as discussed in the previous section. In this work, we define agreement straightforwardly by means of human wrench feedback. The binary variable $\xi(t) \in \{0, 1\}$ represents the human instantaneous (dis-)agreement. With the component $\hat{u}_{1,y}^{C}(t)$ denoting the estimate of the wrench currently applied by the human in the redundant direction, we define the agreement variable

$$\xi(t) = \begin{cases} 0, & \text{if } \operatorname{sgn}\left(\tilde{u}_{1,y}^{C}(t)\right) \neq \operatorname{sgn}\left(\hat{u}_{1,y}^{C}(t)\right) \wedge \left| \hat{u}_{1,y}^{C}(t) \right| > u_{y,\mathrm{agr}}^{C} \\ 1, & \text{otherwise.} \end{cases} \tag{5.35}$$

  Thus, (dis-)agreement is determined by comparing the directions of the wrench $\tilde{u}_{1,y}^{C}(t)$ resulting from feedforward calculation and the actually applied wrench $\hat{u}_{1,y}^{C}(t)$.

- The positive threshold $u_{y,\mathrm{agr}}^{C} \in \mathbb{R}^{+}$ captures human wrench inputs close to zero. Those are treated as neutral or silent agreement, i.e. the contribution of the robot rises *proactively* and gradually. This behavior is designed under the assumption, that the partner would clearly indicate his/her disagreement through non-zero wrenches. Setting the initial value $\alpha_0 = -1$ in (5.33) produces initially a minimum-robot-effort behavior.

- The positive constants $\tau_{\mathrm{w}-} \in \mathbb{R}^{+}$ and $\tau_{\mathrm{w}+} \in \mathbb{R}^{+}$ define the fundamental decay and rise times of the policy parameter α. When designing assistive behavior, a faster reaction to disagreement ($\xi = 0$) than to agreement ($\xi = 1$) is considered to be a reasonable option, i.e. $\tau_{\mathrm{w}-} > \tau_{\mathrm{w}+} > 0$. This choice lets the role behavior rapidly fall back to minimum effort, if the human signals discomfort by applying a counteracting wrench.

- The factor $\left| \hat{u}_{1,y}^{C}(t) \right|$ performs a dynamic *weighing*, which yields a role behavior with a progressively changing policy depending on the magnitude of the partner's contribution. High wrench magnitudes are interpreted to emphasize (dis-)agreement, and thus, speed up the role allocation dynamics accordingly. The positive threshold $u_{y,\mathrm{th}}^{C} \in \mathbb{R}^{+}$ defines a lower bound on the weighing factor, that still lets the robot contribution rise in case of small partner wrenches.

The qualitative behavior of the weighted proactive role allocation with $\alpha_0 = -1$ is illustrated by means of a simulation example depicted in Figure 5.13a.

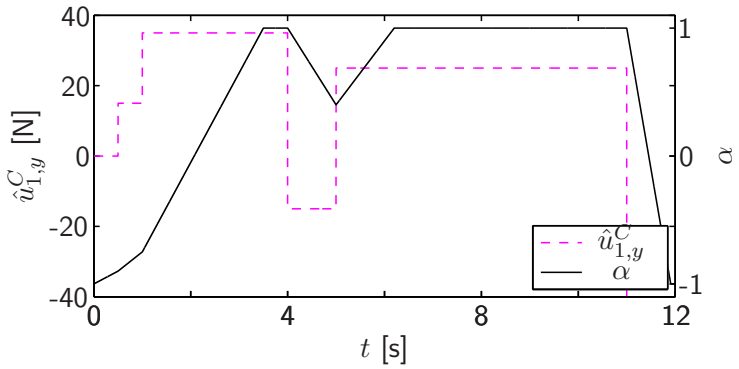

(a) Weighted proactive role allocation.

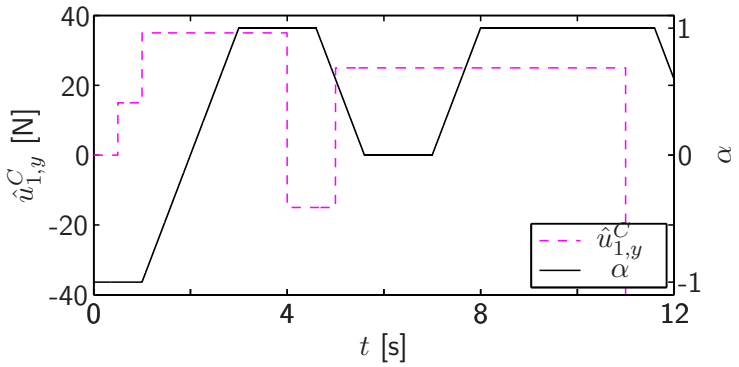

(b) Discrete proactive role allocation.

Fig. 5.13: Evolutions of the policy parameter $\alpha(t)$ simulated for an artificial profile of the human wrench component $\hat{u}^C_{1,y}(t)$. In the example, the robot expects a wrench component $\tilde{u}^C_{1,y} > 0$ from the human, hence $\hat{u}^C_{1,y} \geq 0$ denotes agreement and lets α gradually rise.

Remark 5.19 In the dyadic case, the robotic agent may compute an estimate of its partner's applied wrench, since the object dynamics (5.1) and kinematics (5.4), (5.5) are known to the robot. In Section 5.4.3, we will outline appropriate estimation approaches.

Remark 5.20 The agreement threshold $u^C_{y,\mathrm{agr}}$ in (5.35) also accounts for an inevitable noise level of the estimation or measurement process of $\hat{u}^C_{1,y}(t)$, which might not be interpretable as deliberate agreement indicator.

Discrete Proactive Role Allocation

In order to investigate whether a dynamic role allocation rendering a small number of distinct policies is more understandable for the human partner than continuous policy blending, we develop a discretized version of the continuous role allocation introduced before. Therefore, the discrete policy parameter $\alpha_{\mathrm{dis}}(t_i)$ is introduced, which takes values from the finite set $\alpha_{\mathrm{dis}} \in \{\alpha_i, \ldots, \alpha_n\}$ at discrete time steps t_i.

With respect to the effort sharing policies derived in Section 5.2.4, we choose $n = 3$ values, representing the meaningful policies $\pi_{\mathrm{min}}, \pi_{\mathrm{bal}}$ and π_{max}. In this case, a suitable,

discrete update law is given by

$$\alpha_{\mathrm{dis}}(t_{i+1}) = \begin{cases} \alpha_{\mathrm{dis}}(t_i) - 1, & \text{if } \alpha_{\mathrm{dis}}(t_i) \geq 0 \wedge \Delta\alpha(t_i) < -\Delta\alpha_{\mathrm{th}} \\ \alpha_{\mathrm{dis}}(t_i) + 1, & \text{if } \alpha_{\mathrm{dis}}(t_i) \leq 0 \wedge \Delta\alpha(t_i) > \Delta\alpha_{\mathrm{th}} \\ \alpha_{\mathrm{dis}}(t_i), & \text{otherwise.} \end{cases} \tag{5.36}$$

Equation (5.36) increments or decrements α_{dis} depending on a continuous, internal policy difference $\Delta\alpha$, which is obtained from integration of

$$\Delta\dot{\alpha}_{\mathrm{i}}(t) = \begin{cases} \tau_{\mathrm{d}+}, & \text{if } \xi(t) = 1 \\ -\tau_{\mathrm{d}-}, & \text{otherwise.} \end{cases} \tag{5.37}$$

The positive constants $\tau_{\mathrm{d}+} \in \mathbb{R}^+$ and $\tau_{\mathrm{d}-} \in \mathbb{R}^+$ denote the rise and decay times of $\Delta\alpha(t)$ depending on the agreement indicator $\xi(t)$ from (5.35). In contrast to (5.34), dynamic weighing is not considered here, in order to keep the role allocation dynamics as simple as possible. Note that depending on (5.36), we reset the internal policy difference

$$\Delta\alpha(t_{i+1}) = 0, \quad \text{if } \alpha_{\mathrm{dis}}(t_{i+1}) \neq \alpha_{\mathrm{dis}}(t_i). \tag{5.38}$$

The symmetric dead zone $-\Delta\alpha_{\mathrm{th}} \leq \Delta\alpha(t_i) \leq \Delta\alpha_{\mathrm{th}}$ defined by (5.36) in combination with (5.38) renders a hysteresis-like behavior, that avoids chattering of α_{dis}.

Role allocations with perfectly discrete switching behavior would directly result in jumps of the applied wrench, as locally $\tilde{u}^C_{2,y} \propto \alpha$ holds. In turn, those jumps would not only lead to a jerky motion, but also challenge the adaptation dynamics of the partner. Therefore, a smooth, linear transition between the three discrete roles is proposed, by obtaining the continuous parameter $\alpha(t)$ from the solution of the differential equation

$$\dot{\alpha} = \tau_{\mathrm{b}} \operatorname{sgn}\left(\alpha_{\mathrm{dis}}(t_i) - \alpha\right),$$

with positive $\tau_{\mathrm{b}} \in \mathbb{R}^+$ denoting the blending time constant. The qualitative behavior of the discrete role allocation scheme with $\alpha_{\mathrm{dis}}(t_0) = \alpha(0) = -1$ is illustrated by means of the simulation depicted in Figure 5.13b.

5.4.3 Interaction Control Scheme

In the following, we enhance and detail the interaction control scheme developed in Section 5.3.1. Admittance-type control of the robot manipulator is considered in the flow chart depicted in Figure 5.14. Utilizing the pre-planned configuration trajectory $\boldsymbol{x}_{c,\mathrm{d}}(\tau)$, the reference adaptation described in Section 5.3.1 selects the appropriate $\boldsymbol{x}_{c,\mathrm{d}}$ based on the actual object configuration $\boldsymbol{x}_c$. By means of the desired $\dot{\boldsymbol{x}}_{c,\mathrm{d}}(\tau^*), \ddot{\boldsymbol{x}}_{c,\mathrm{d}}(\tau^*)$, the inverse dynamics comprising the object model as well as the robot admittance generates a feedforward component of the external wrench $\hat{\boldsymbol{u}}_{c,\mathrm{dyn}}$. The feedback component $\hat{\boldsymbol{u}}_{c,\mathrm{imp}}$ as output of the impedance control law ensures tracking of $\boldsymbol{x}_{c,\mathrm{d}}(\tau^*)$ under model uncertainties and unexpected human behavior. The effort-role behavior (*left gray box*) consists of three modules, which are the role allocation scheme, the sharing policy and the sharing strategy.

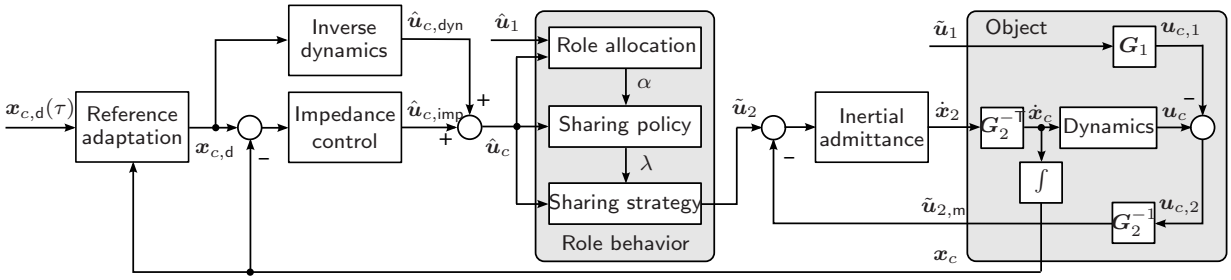

Fig. 5.14: Overall interaction control scheme embedding the dynamic effort-role behavior.

Depending on the role allocation scheme (constant, weighted proactive or discrete proactive), the input behavior of the robot $\tilde{\boldsymbol{u}}_2$ is rendered based on the external wrench $\hat{\boldsymbol{u}}_c$ and the estimate of the human applied wrench $\hat{\boldsymbol{u}}_1$. The applied wrench $\tilde{\boldsymbol{u}}_2$ is realized by the inertial, admittance-type force control described in Section 2.4, imposing motion on the object at the grasp point $\boldsymbol{x}_2$. The inertial formulation allows to make use of the extended workspace of a mobile robot composed by a manipulator-base system.

Remark 5.21 For a rigid grasp on the object and $\tilde{n}_2 < n_2$, the ineffective components of the complete input wrench $\boldsymbol{u}_2$ of the robot are controlled to zero, e.g. the torque $\boldsymbol{u}_{2,\phi} = 0$.

Estimating the Partner Variables

The robotic agent may compute an estimate of the applied wrench $\hat{\boldsymbol{u}}_1$ of a single human partner. We assume that the kinesthetic feedback available through its end effector due to the rigid grasp at $\boldsymbol{x}_2$ is sufficiently accurate, i.e. measurements $\boldsymbol{x}_2, \dot{\boldsymbol{x}}_2$, and $\ddot{\boldsymbol{x}}_2$ of the grasp configuration are obtained. Then, the object motion $\boldsymbol{x}_c, \dot{\boldsymbol{x}}_c$, and $\ddot{\boldsymbol{x}}_c$ can be inferred by the partial grasp matrix of the robot $\boldsymbol{G}_2^{\mathrm{T}}$, which is invertible for a rigid grasp. In the dyadic case, the external wrench is superposed by the partners' wrench components according to (5.3),

$$\boldsymbol{u}_c = \boldsymbol{u}_{c,1} + \boldsymbol{u}_{c,2}, \tag{5.39}$$

see also the object model (*right gray box*) in Figure 5.14. Thus, we obtain the estimated applied wrench

$$\hat{\boldsymbol{u}}_1 = \boldsymbol{G}_1^{-1} \left(\boldsymbol{u}_c - \boldsymbol{G}_2 \tilde{\boldsymbol{u}}_{2,\mathrm{m}} \right), \tag{5.40}$$

where the external wrench $\boldsymbol{u}_c$ is calculated using the inverse dynamics (5.1), $\tilde{\boldsymbol{u}}_{2,\mathrm{m}}$ is the measured applied wrench of the robot and $\boldsymbol{G}_1$ is the partial grasp matrix of the human.

Remark 5.22 Due to the superposition (5.39), only a single agent's unknown input can be determined uniquely by (5.40). Furthermore, certain non-linearities, such as static friction prevent invertibility of the object dynamics and therefore the partner's input estimation.

5.5 Evaluation of Dynamic Role Behavior

In a unique large-scale setup, a human-robot interaction study is designed, which requires the cooperative manipulation of a real bulky and heavy object. The participants were asked to maneuver a table jointly with a human-sized mobile robot through the cluttered

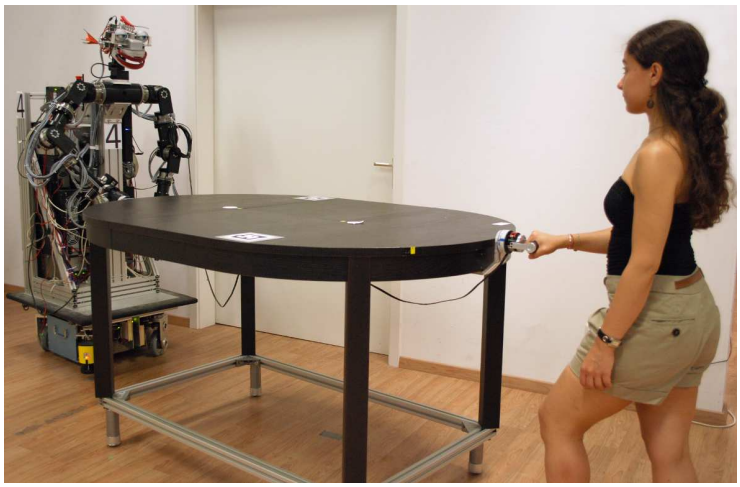

Fig. 5.15: Prototypical scenario of cooperative object manipulation and experimental setup: A human-robot dyad jointly transporting a bulky table.

lab area, see Figure 5.15. With the realization and experimental evaluation of this joint action task, we pursue two main goals:

- The proof of concept by means of a physical assistance robot that employs the developed effort sharing strategy as well as role allocation schemes.
- Valuable observations of the effects of role behavior on the collaborative experience of the human partner and the joint task performance in a realistic and immersive interaction scenario. Specifically, we are interested in answering the questions: Do dynamic role allocation schemes improve task performance quantitatively compared to a static one? How is the interactive behavior resulting from such schemes perceived by the human partner?

5.5.1 Human-Robot Experiment

Participants

In total, 18 participants (6 female), aged between 19 and 44, took part in the study. Prior to the experiment, they signed written informed consent. All participants were right handed and used solely their right hands for cooperative manipulation. For participation, they were paid 8 € per hour.

Experimental Setup

A wooden table was cooperatively manipulated by the participant and a human-sized mobile robot, see Figure 5.15. The table was mounted on an aluminum frame standing on ball-caster feet, which provided low-friction and holonomic maneuverability of the table. A handle and a flange were rigidly attached to the table at facing sides forming the grasp points of the human and the robot, see Figure 5.16. The flange was a solid wooden plate that provided a slippage-free and zero-backlash grasp for the two-finger gripper of the robot.

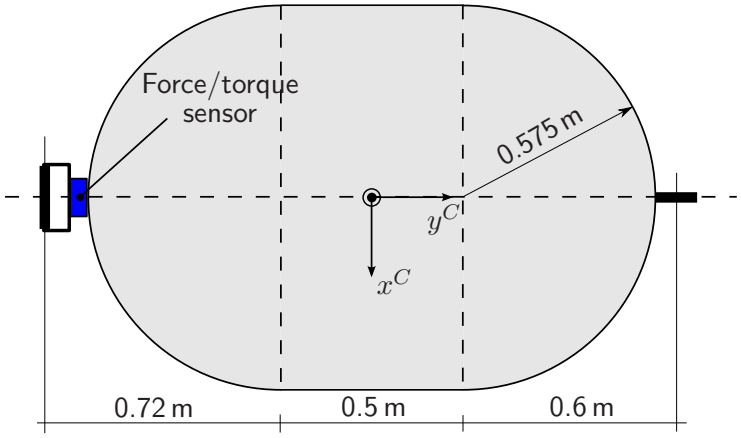

Fig. 5.16: Cooperatively manipulated table equipped with a handle and wrench sensor for the human *(left side)* and a grasp flange for the robot *(right side)*. The grasp points were at a height of 0.92 m over ground.

An off-line estimation of the object dynamics used in (5.22) revealed the parameters of the table mass matrix

$$\boldsymbol{M}_c = \mathrm{diag}(13.5\,\mathrm{kgm}^2, 44\,\mathrm{kg}, 44\,\mathrm{kg}).$$

The table friction $\boldsymbol{f}_c$ was considered as a Coulomb-type friction of 14 N in total, acting equally distributed at the table feet.

The human-sized mobile robot described in Appendix A.2.1 and the enhanced interaction control scheme developed in Section 5.4.3 were employed. The inertial admittance of the robot (2.16) and the object-centered impedance (5.24) were parameterized as follows regarding the task-relevant DoF:

$$\begin{aligned}
\boldsymbol{M}_r &= \mathrm{diag}(0.4\,\mathrm{kgm}^2, 20\,\mathrm{kg}, 20\,\mathrm{kg}),\\
\boldsymbol{D}_r &= \mathrm{diag}(10\,\mathrm{Nmsrad}^{-1}, 100\,\mathrm{Nsm}^{-1}, 100\,\mathrm{Nsm}^{-1}),\\
\boldsymbol{K}_p &= \mathrm{diag}(200\,\mathrm{Nrad}^{-1}, 200\,\mathrm{Nm}^{-1}, 200\,\mathrm{Nm}^{-1}),\\
\boldsymbol{K}_d &= \mathrm{diag}(50\,\mathrm{Nmsrad}^{-1}, 50\,\mathrm{Nsm}^{-1}, 50\,\mathrm{Nsm}^{-1}).
\end{aligned}$$

The reference trajectory of the table configuration $\boldsymbol{x}_{c,\mathrm{d}}(\tau)$ was taught once before the experiments through human demonstration. Recording of the required motion data was performed by the mobile robot, utilizing the sensor readings from its manipulator kinematics and base odometry. The experimenter was enabled to haptically guide the table-robot system in arbitrary direction, since the robot rendered a smooth following behavior through inertial admittance control with respect to its rigid grasp point. Second order low-pass filtering with 0.4 Hz cut-off frequency guaranteed smooth derivatives $\dot{\boldsymbol{x}}_{c,\mathrm{d}}(\tau)$ and $\ddot{\boldsymbol{x}}_{c,\mathrm{d}}(\tau)$.

Conditions

Three conditions manipulated the role behavior of the robot according to the role allocation schemes synthesized in Section 5.4.2:

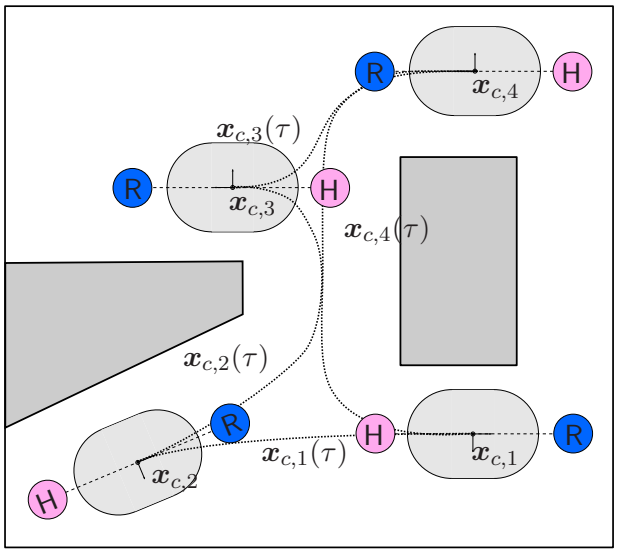

Fig. 5.17: Bird's eye view of the lab area used in the experiment with four designated parking configurations of the table $\boldsymbol{x}_{c,i}$. The outer box represents the boundaries of the environment spanning a square of approximately $8\,\mathrm{m} \times 8\,\mathrm{m}$. Gray regions are occupied by obstacles. The dotted curves represent the paths $\boldsymbol{x}_{c,i}(\tau)$ connecting the parking configurations.

- **CRA**: **C**onstant **R**ole **A**llocation.
  The robot contributed to the task without changing its role. It rendered static role behavior by means of the balanced-effort policy $\pi_{\mathrm{bal}}\,(\alpha = 0)$ at all times.

- **WPRA**: **W**eighted **P**roactive **R**ole **A**llocation.
  As long as the wrench applied by the human was in the expected direction, or the human was inactive, the robot increased its policy parameter $\alpha(t)$ gradually with time. Otherwise, it decreased $\alpha(t)$. In the experiment, we used the time constants $\tau_{\mathrm{w}+} = 0.02\,(\mathrm{Ns})^{-1}$ and $\tau_{\mathrm{w}-} = 0.04\,(\mathrm{Ns})^{-1}$. The wrench thresholds were $u^C_{y,\mathrm{th}} = 10\,\mathrm{N}$ and $u^C_{y,\mathrm{agr}} = 1\,\mathrm{N}$.

- **DPRA**: **D**iscrete **P**roactive **R**ole **A**llocation.
  Similar to WPRA, the robot changed its role by increasing or decreasing $\alpha(t)$ gradually. Three discrete roles were rendered by the policies $\pi_{\mathrm{min}}, \pi_{\mathrm{bal}}$ and π_{max}. During the experiment, we used the time constants $\tau_{\mathrm{d}+} = 0.2\,\mathrm{s}^{-1}$ and $\tau_{\mathrm{d}-} = 2\,\mathrm{s}^{-1}$, as well as the blending time constant $\tau_{\mathrm{b}} = 2\,\mathrm{s}^{-1}$. The policy difference threshold was set to $\Delta\alpha_{\mathrm{th}} = 0.6$.

Procedure

A trial consisted of moving the table jointly with the robot to three designated parking configurations $\boldsymbol{x}_{c,i}, i \in \{2, 3, 4\}$, and then coming back to the initial configuration $\boldsymbol{x}_{c,1}$, as shown in Figure 5.17. The overall reference completion time summing the durations of the four demonstrated trajectory segments was 52 s, with translational peak velocities ranging within $0.7 - 1.0\,\mathrm{ms}^{-1}$. The trial and data collection started with an acoustical signal

presented to the participant. Detailed instructions about the task and the conditions were given before the experiment. The participants were allowed to apply pushing and pulling forces using only their right hands by holding the handle of the table. Lifting the table off the ground and talking during the experiment were prohibited. The positions of the human and the robot in each of the parking configurations were clearly marked on the floor of the area. These marks were also shown to the participants before the experiment. The free space available for maneuvering the table between the parking configurations was constrained by obstacles in such a way, that ambiguities and alternatives for possible common paths were avoided.

The conditions (CRA, WPRA, and DPRA) were presented to the participants in permuted order using a balanced Latin Square design to avoid learning effects. Under each condition, the participants performed three trials. After each trial, a small break was given to initialize the table and robot pose. After performing these three trials successfully, the participants were given a questionnaire to comment on their experience. Afterwards, they were presented a new condition.

5.5.2 Evaluation Criteria

Both quantitative and subjective measures deployed for the evaluation are introduced in the following. The data collected in the first 300 ms and in the final leg of segment $\boldsymbol{x}_{c,4}$ (see Figure 5.17) is discarded. Force and movement data are low-pass filtered using a first-order filter with 15 Hz cut-off frequency.

Task performance

The completion time CT of each trial is taken as a measure of task performance.

Physical Effort

The per-trial means of the wrench magnitudes applied by the partners, denoted by $\overline{|\tilde{u}_{i,y}^{C}|}$, as well as their conducted mechanical work are considered as indicators of the physical effort made by them. The individual effort is captured by the accumulated work during the trial

$$\mathrm{AW}_i = \int_0^{\mathrm{CT}} \left| \tilde{\boldsymbol{u}}_{i,\mathrm{m}}(t)^{\mathrm{T}} \dot{\boldsymbol{x}}_i(t) \right| \mathrm{d}t,$$

where $\tilde{\boldsymbol{u}}_{i,\mathrm{m}}$ denotes the measured wrench exerted by agent i, and $\dot{\boldsymbol{x}}_i$ the velocity of the corresponding grasp point. The accumulated work done on the table by the partners during a trial considers the accumulated energy transfer on the table, i.e. how efficiently the table could be moved to the parking configurations. It is calculated by

$$\mathrm{AW}_{\mathrm{table}} = \int_0^{\mathrm{CT}} \left| \boldsymbol{u}_c(t)^{\mathrm{T}} \dot{\boldsymbol{x}}_c(t) \right| \mathrm{d}t,$$

where the motion-causing external wrench $\boldsymbol{u}_c(t)$ is obtained by evaluating (5.3) for the measured wrenches $\tilde{\boldsymbol{u}}_{i,\mathrm{m}}(t)$. Note that the absolute energy flow is accumulated, since the human partner is assumed not to recoup by absorbing energy, i.e. through breaking actions.

Amount of Disagreement

In the cooperative task, disagreement is assumed to occur when the partners pull or push the table in opposite directions along the y^C-axis. Instead of contributing to object motion, part of the forces in this axis are wasted for compressing or tensioning the table. These forces are called interactive forces and according to [48] defined as

$$u_I = \begin{cases} \tilde{u}^C_{1,y}, & \text{if } \operatorname{sgn}(\tilde{u}^C_{1,y}) \neq \operatorname{sgn}(\tilde{u}^C_{2,y}) \\ & \wedge\, |\tilde{u}^C_{1,y}| \leq |\tilde{u}^C_{2,y}| \\ -\tilde{u}^C_{2,y}, & \text{if } \operatorname{sgn}(\tilde{u}^C_{1,y}) \neq \operatorname{sgn}(\tilde{u}^C_{2,y}) \\ & \wedge\, |\tilde{u}^C_{1,y}| > |\tilde{u}^C_{2,y}| \\ 0, & \text{otherwise.} \end{cases} \tag{5.41}$$

The quality of cooperation is assessed by weighing the interactive forces as the effect of disagreement with the time spent in disagreement. Since we are not interested whether the agents disagree by pushing or pulling against each other (which is indicated by the sign of u_I), we propose the amount of disagreement

$$\mathrm{AD} = \int_0^{\mathrm{CT}} |u_I(t)|\,\mathrm{d}t,$$

as measure of cooperation quality. It is calculated based on the magnitude of the interactive forces (5.41).

Subjective Reasoning

After each condition, the participants were asked to fill in a questionnaire. It consisted of the set of six questions taken from the NASA task load index (NASA-TLX) [56], as well as 14 questions developed in [7, 85]. The participants answered on a seven-point Likert scale. Some of the latter questions were rephrased and asked again within the questionnaire in arbitrary order, hence the average responses to the rephrased questions is used for the evaluation. The NASA-TLX evaluates the degree to which each of six factors contribute to the perceived workload of the task. Those factors are *mental*, *physical* and *temporal demand*, as well as *performance*, *effort* and *frustration level*. The remaining questions were asked in the following categories: The extent to which the participants had a sense of *collaboration* with the robot during the task (two questions). The level of *interaction* the participants experienced during the task (two questions). The level of *comfort* and *pleasure* (each one question). The participants' perceived degree of *control* on the movement of the table (two questions). The *predictability* of the robotic movements during the task (two questions). The level of *trust* in their robotic partner controlling the table (two questions). *Human-likeness*, i.e. the extent to which the robotic actions resembled those of a human being acting in a similar real-life scenario (two questions). The formulations are found in Appendix C.

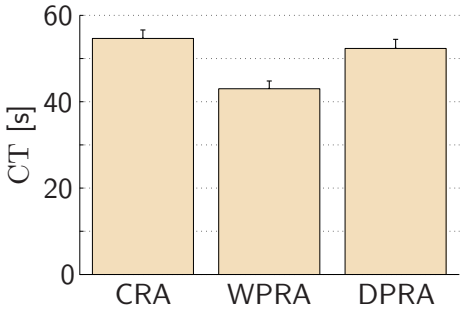

Fig. 5.18: Average task completion times. The bars represent standard errors of the means.

5.5.3 Experimental Results

The results of the experiment with respect to the quantitative and subjective measures defined above are presented. Statistically significant differences between the conditions are investigated using one way repeated measures ANOVAs. Multiple comparisons are performed via post-hoc t-tests with Bonferroni correction. Mauchly's test is conducted to check if the assumption of sphericity is violated. If so, DoF are corrected using Huynh-Feldt estimates of sphericity.

Task Performance

The mean completion times as measure of task performance are shown in Figure 5.18. The ANOVA results reveal a statistically significant effect of the condition on completion time ($p < 0.001$). Specifically, the participants completed the task significantly faster under WPRA compared to the other conditions. The completion time is numerically smaller under DPRA than under CRA, yet this difference is not significant.

Physical Effort

The ANOVA results reveal that the condition has a significant effect on the mean applied wrenches of both the human and the robot ($p < 0.001$), see also Figure 5.19a. The mean wrench applied by the human under WPRA is significantly smaller than it is under the other conditions ($p < 0.001$), and it is significantly higher under DPRA ($p < 0.001$). On the other hand, the mean wrench applied by the robot is significantly higher under WPRA and DPRA than it is under CRA ($p < 0.001$).

The results of the work done individually by the partners are in parallel to those observed for the mean wrenches applied by the agents, see Figure 5.19b. ANOVA results suggest a significant effect of the condition on the individual work done by the agents and the work done on the table ($p < 0.001$). The participants put the least work under WPRA ($p < 0.001$), and the most under DPRA ($p < 0.001$). Furthermore, the total work done on the table under WPRA is smaller than that under CRA ($p < 0.05$) and DPRA ($p < 0.001$). It is the largest under DPRA ($p < 0.001$). The robot conducts significantly more work under WPRA and DPRA than it does under CRA ($p < 0.001$). Even though we observe the highest robot work in DPRA, the difference between the WPRA and DPRA conditions is not significant.

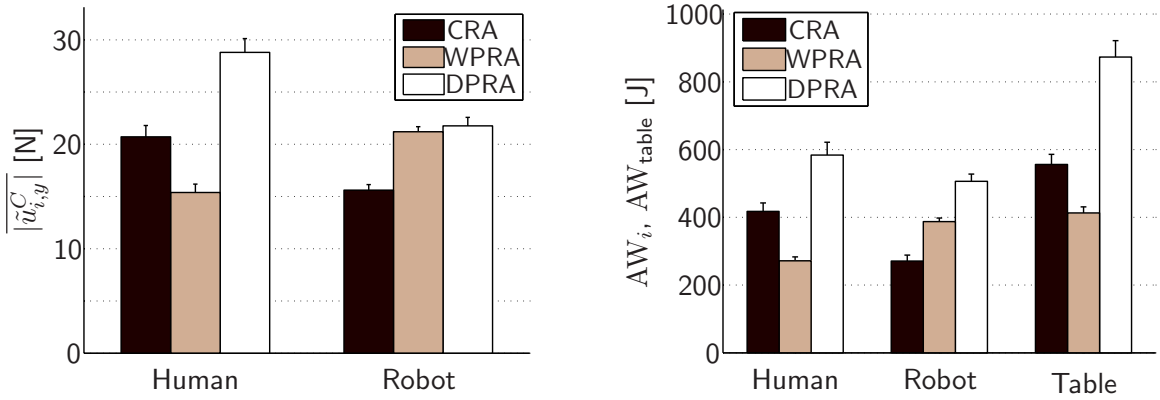

(a) Mean wrenches applied by the partners. **(b)** Work done individually and on the table.

Fig. 5.19: The averaged measures of physical effort under each condition. The bars represent standard errors of the means.

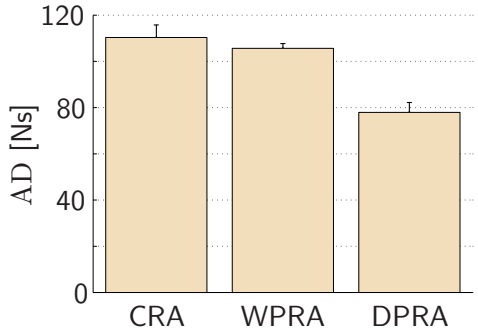

Fig. 5.20: The amount of disagreement averaged over all trials under each condition. The bars represent standard errors of the means.

Amount of Disagreement

The amount of disagreement accumulated under each condition is illustrated in Figure 5.20. The ANOVA results indicate a significant effect of the condition on the amount of disagreement ($p < 0.05$). Multiple comparisons imply that the amount of disagreement is similar under CRA and WPRA, whereas it is lower under DPRA than under CRA ($p < 0.001$) and WPRA ($p < 0.001$). Note that only the signs of the applied wrenches are considered to decide whether there is a disagreement between the partners. Also, interactive forces $< 1\,\mathrm{N}$ are not treated as disagreement.

Role Allocation

The policy parameter $\alpha(t)$ is investigated to gain a better understanding of the dynamic role allocation behavior. In Figure 5.21, the evolution of the role allocation behavior under WPRA and DPRA is illustrated by means of selected sample trials. Upon examining these plots, we observe that even though the human wrench profile bears some similarity under WPRA and DPRA, the robotic role behavior is drastically different. In particular, frequent transitions of the discrete role under DPRA become obvious, in contrast to the continuous

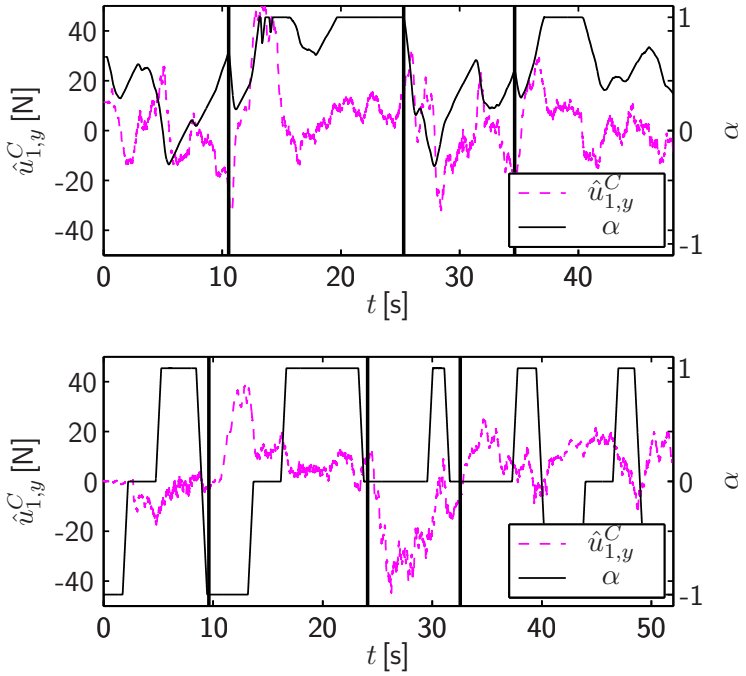

Fig. 5.21: Sample trials under the condition WPRA *(top panel)* and DPRA *(bottom panel)*: Evolution of the policy parameter $\alpha(t)$ depending on the human wrench component $\hat{u}^C_{1,y}(t)$. Vertical bold lines separate the four task segments.

blending under WPRA. Phases of disagreement in vicinity of the parking configurations let the robot role under DPRA repeatedly fall back to the balanced and minimum-effort policy respectively.

The predominant roles the robot actually takes on during dynamic role allocation are assessed by the frequency distributions of the policy parameter α, see Figure 5.22. It is observed that the robot acts towards maximum effort under WPRA, which is due to long periods of agreement with the human partner. Under DPRA, we see an almost uniform distribution between the three discrete roles, with an emphasis on the minimum and balanced effort sharing policy. Non-zero intermediate values are explained by the smooth transition behavior between these three states.

Subjective Reasoning

The participants' responses to the questionnaire are gathered in Figure 5.23, with the key results summarized as follows:

- The participants judged the task as physically and mentally less demanding under WPRA. The physical demand under DPRA was significantly higher than it was under WPRA ($p < 0.005$) and CRA ($p < 0.05$).

- The participants felt significantly less comfortable under DPRA than they felt under CRA ($p < 0.01$) and WPRA ($p < 0.005$).

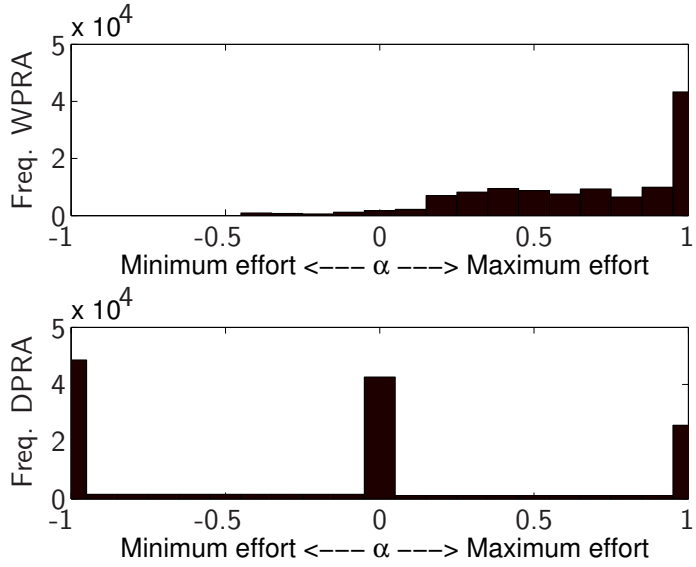

Fig. 5.22: Frequency distribution of the policy parameter α over all trials under the condition WPRA *(top panel)* and DPRA *(bottom panel)*.

- The participants believed that their control over the task under DPRA was significantly more than that under WPRA ($p < 0.05$).
- Under DPRA, the predictability of the robot was significantly lower than it was under CRA ($p < 0.05$).

5.5.4 Discussion

The subjective evaluation considered along with the quantitative results provides insight about the joint task performance as well as the participants' perception of different role allocation schemes. Those are discussed and structured by contrasting the static role behavior introduced as baseline condition, and the implementations of dynamic role allocation behavior. Furthermore, we differentiate the effects specific to the continuous and discrete implementation.

Static vs. Dynamic Role Behavior

The quantitative measures show a clear benefit of the dynamic role behavior rendered under the condition WPRA compared to the static role behavior under CRA. While the human contribution of physical effort and the task completion time is significantly lowered, the robot proactively contributes more effort under WPRA. This is also recognized from the policy distribution, which is shifted towards the region of maximum-robot effort due to pronounced phases of human agreement. Simultaneously, the work done on the table is smallest under WPRA, which is an indicator of the overall efficiency of the dyad in terms of energy exchange with the object.

In agreement with the physical effort measures, also the perceived physical and mental demand appears lowered under WPRA. Regarding most of the remaining aspects of inter-

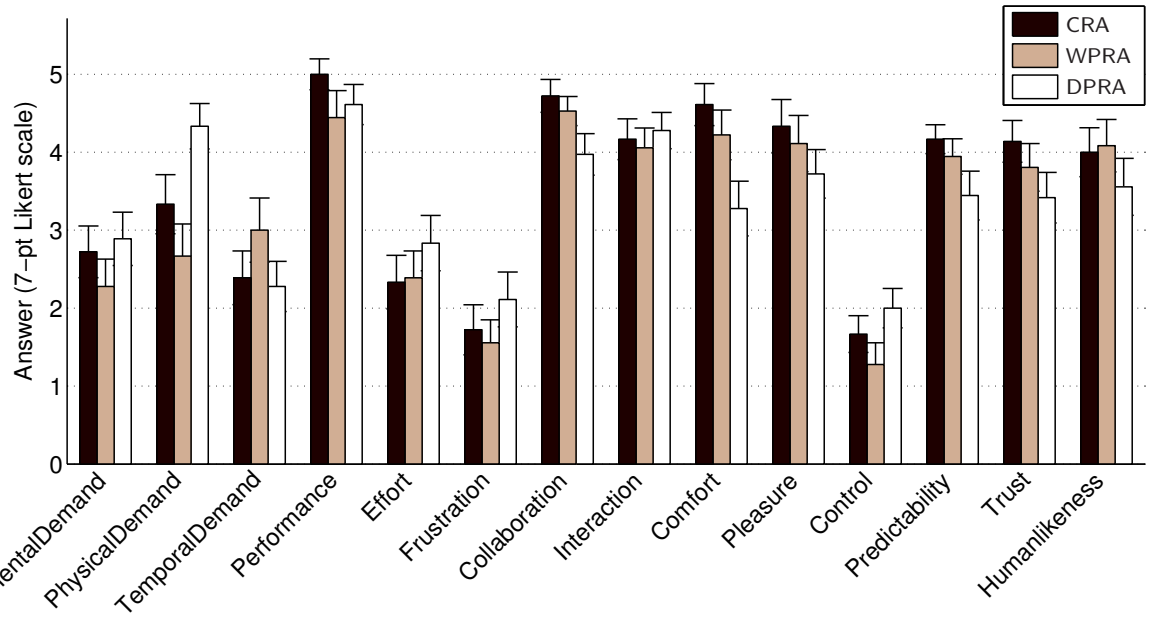

Fig. 5.23: Means of the subjective measures in each condition. The bars represent standard errors of the means.

action, however, both implementations of dynamic role behavior achieve numerically lower subjective ratings than the baseline CRA. This obvious gap between clear quantitative improvements and deteriorated subjective ratings indicates room for further research on human-oriented allocation dynamics, in order to increase subjective acceptance of dynamic role allocation schemes.

Continuous Blending vs. Discrete Switching of Roles

The high effort policies that the robot could predominantly employ under WPRA result in the lowest task completion times. Similarly, the continuous scheme WPRA outperforms the discretized version DPRA in terms of the physical effort required from the participants. However, the efficient task performance under WPRA could have made the participants think that the task required them to be faster, explaining the high temporal demand. The low physical effort spent by the participants under WPRA compared to that of the robot may correlate with the low-rated levels of control and interaction. Hence, the participants failed to perceive the interactive nature of the task. However, due to the smooth behavior under WPRA, the participants had a better sense of predictability of the robotic actions than under DPRA.

During trials performed under DPRA, intermittent accelerations and decelerations of the table could be observed, cf. Figure 5.21. This behavior explains the large values obtained for the physical effort of both partners, and also the exceedingly large work done on the table. In addition, the completion times being significantly higher than under WPRA renders the discrete implementation DPRA inefficient. Yet, the low level of disagreement under DPRA might lead to the conclusion that the discrete roles of the robot are observable to the human. When considering disagreement-causing force oscillations as indication of

negotiation processes [133], the participants acted at least in a determinate way in terms of their applied forces. In agreement with the quantitative results, the subjective measures indicate a high perceived workload under DPRA. The low-rated levels of predictability and trust, with similar trends for collaboration, comfort and pleasure, may be the effects of abrupt role transitions and difficulties in inferring the role transitions of the robot in advance. As a result of missing predictability, the participants may be driven to being more dominant in guiding the table, which eventually increases their perceived control level. Thus, the high physical effort spent by the participants under DPRA may correlate with the high-rated level of control (with a similar trend for the interaction level).

Implications for Cooperative pHRI Tasks

The aforementioned points draw a clear distinction between the implemented schemes of dynamic role allocation regarding the domains of pHRI. The discretized version DPRA invokes distinct and observable role transitions. Such a scheme may be a beneficial alternative for interactive training applications. In training, it is necessary for the learner to recognize the role of the trainer (i.e. the robot), so that he/she can consciously adapt to it. When the trainer's role is not perceived, the learner typically tends to obey the guiding system and does not learn the dynamics of the task [37]. Under the continuous version WPRA, the human would tend to go along under the supervision of the robot most of the time, seldom take initiative and hence, fail to gain training experience, cf. the policy distribution in Figure 5.22.

In many other applications, users would probably prefer comfort over having a strong sense of control and interaction. For instance, when working with an assisting robot in a cooperative manipulation task, users would prefer to finish the task in the fastest and the least demanding way. In such a setting, proactive behavior enforced by a continuous scheme is expected to be the better alternative, as it evidently increases task performance and simultaneously lowers human effort.

5.6 Conclusion and Open Issues

Guided by system-theoretic modeling of the cooperative manipulation problem, a novel strategy for physical effort sharing among human-robot teams is developed. The input redundancies arising from multiple, spatially distributed grasp points on the common object are exploited, and parameterized policies of particular meaning are identified. The interaction control scheme proposed for embedding of the effort sharing strategy proves suitable for pHRI, as the participants in our VR experiment could successfully accommodate to the resulting static role behavior rendered by the virtual assistant. Although only little research has been devoted to the role allocation problem in pHRI, a valuable synopsis of relevant adjustment criteria, policies and interaction control schemes is provided. For evaluating the utility of dynamic role behavior in a realistic scenario, two role allocation schemes are synthesized and prototyped. The effort role of a real robotic assistant is allocated either in a continuous or discrete fashion along the redundant DoF of the task. Results of the large-scale experimental study show quantitative improvements of the task

performance achieved by the continuous role allocation based on human force feedback. Yet, the subjective ratings of the participants suggest the constant role allocation to be preferred.

A number of interesting open issues arise from this work and remain for future research. The user study on dynamic role behavior shows a clear gap between quantitative performance improvement and increased workload perceived by the participants. This trade-off encourages an iteration of the design process from the analytical perspective: The role allocation of human dyads may be analyzed in similar scenarios, in order to design the adjustment dynamics accordingly. The role allocations synthesized in this chapter focus on a single instantaneous agreement criterion, which is derived from force feedback in a single redundant DoF. Further adjustment criteria, as the ones discussed in Section 5.4.1, need to be integrated into dynamic role allocation schemes. Also, role allocations and possible interdependencies in multiple redundant DoF are worth to be investigated. Differentiating the specific influence and meaning of the impedance parameters, i.e. the role-dependent stiffness and damping imposed by the agents, might be key to a comprehensive understanding and modeling of human-robot interactive role behavior. The acquisition of human partner variables in an on-line and autonomous fashion poses further challenges. For instance, the emerging field of human-wearable haptic devices highlights promising directions to locally, but reliably acquire auxiliary kinesthetic feedback from human interaction partners.

6 Conclusions and Future Directions

In this dissertation, an interdisciplinary design methodology on the interactive motor behavior of artificial agents is proposed, that enables close joint action of humans and robots. Despite the inspiring multitude of real world applications, research in this domain is still in its infancy. The main reasons are the specific challenges arising from motor interaction with human partners in shared workspaces: Seamless interaction requires actions and reactions to be negotiated on short time scales based on mutual sensory feedback. Erroneous, unexpected or even slightly delayed motor actions may inevitably break the natural flow of joint actions or make the task fail completely. For their successful integration in the human society, the interactive motor capabilities of robot companions must be designed to be socially compatible and comparable to that of their human interaction partners. Applicable models of human interactive behavior, and also the conceptual guidelines to develop them, are rarely found in the existing literature. In a so far unique approach, this work combines knowledge from human behavioral science, experimental psychology, system theory and robotics into a holistic design concept. In this chapter, we draw the conclusions from the analysis and the synthesis of interactive motor behaviors conducted by means of the design methodology. The potential implications on related research fields are discussed as well. Finally, a number of promising directions for future research are given, that follow directly from the considerations in this work.

6.1 Concluding Remarks

Human-oriented design is the core of the methodology characterized in Chapter 2. The fundamental building blocks of interactive motor behavior are extracted from the main mechanisms of human joint action. Since the human motor system is known to follow the common coding principle of perception and action, human behavioral models allow not only to predict the partner's actions, but also to make actions predictable to the partner by employing them in behavior rendering. Therefore, HHI experimental studies and modeling as well as identification techniques are co-designed in the analytical perspective as the first methodological step. So-derived quantitative models and known behavioral and system theoretic principles are then integrated to develop interactive motor behavior in the synthetical perspective as the second methodological step. Prototyping and evaluation of the synthesized behavior in HRI experiments complete the design process. Due to the diversity of human motor behaviors and possible interaction scenarios, the design problem is confined to two relevant classes of dyadic joint action within this thesis. Those are characterized by visual coordination and visual-haptic cooperation respectively.

The coordination of movements is a frequently encountered basic feature of human interactive behavior, both intrapersonal and interpersonal. The principle of movement synchronization is found to be the main enabler of purely rhythmic action coordination.

With the aim to exploit this human behavioral feature later in human-robot joint action, the spontaneous visual coordination of goal-directed actions is evidenced and quantified in Chapter 3. In a new experimental paradigm of rhythmic HHI, spontaneously emerging synchronization of goal-directed arm movements within human dyads is investigated. The innovative modeling and identification concept captures the natural dynamics of the inter-human synchronization behavior in response to an initially applied excitation. Hence, no additional manipulations are required, that could bias natural HHI. The observed behavioral dynamics and coordination patterns are successfully modeled by the synchronization dynamics of a pair of cross-coupled phase oscillators. Two meaningful parameters make the identified behavioral model appealing due to its simplicity as well as its applicability: The frequency detuning or the natural frequencies of the autonomous oscillator dynamics render the individual urge to proceed the action task, whereas the coupling strength mediates the interactive motor behavior in response to the partner.

This quantified mechanism of human movement coordination lays the foundations for the development of synchronization behavior addressed in Chapter 4. Applying the synthetical design perspective, the goal is to equip robotic agents with an intuitive and socially compatible capability that enables visual coordination in joint action with human partners. In a novel design concept, a wide range of repetitive joint action tasks is made accessible to synchronization theory through generic limit cycle representations. Discrete events, e.g. that of passing zero-velocity points in state space, are known to serve as anchoring points for human movement synchronization. Based on this behavioral principle, we develop a variety of enhanced synchronization modes between pairs of heterogeneous limit cycles. Those coordination patterns are entrained by a unified dynamical process that allows to synchronize both events and phases simultaneously on a continuous time scale. The interactive motor behavior driven by the synchronization concept is successfully evaluated in a realistic HRI experiment. Objective and subjective measures evidence the efficacy of the concept towards the goal of intuitive and pleasant joint action with robotic partners.

During physical cooperation, humans are known to apply efficient strategies to negotiate the effort arising from e.g. jointly manipulated heavy and bulky loads. The interaction partners dynamically form self-organized and temporally consistent haptic patterns. This phenomenon called specialization leads to the assignment of situation-specific roles to the partners. Inspired by the human principle of specialization, interactive motor behavior for visual-haptic cooperation of human-robot dyads is synthesized in Chapter 5. Starting point is a system-theoretic modeling concept of the cooperative manipulation problem. The geometrical properties resulting from spatially distributed grasp points of the partners are utilized to develop an effort sharing strategy based on the redundant components of the contributions. Meaningful static role behaviors are identified, embedded in an object-related interaction control scheme and successfully evaluated in a VR experimental scenario. After discussing first attempts towards role blending, both a continuous and a discrete variant of dynamical role allocation based on feedback of the human contribution are synthesized. By means of a human-sized robotic assistant, the interactive role behavior is evaluated in a realistic joint action task, that requires full-body kinesthetic HRI. Results evidence a significant increase of the task performance achieved by the robot rendering dynamic role behavior, while the subjective feedback encourages further efforts on improving

the acceptance of dynamically changing roles.

In the following, we highlight some implications on the involved research fields derived from the contributions made by this thesis.

Implications on Related Research Fields

The *experimental paradigms and designs* presented in this thesis provide valuable guidelines for the further investigation of interactive motor behaviors in HHI and HRI: Variants of the goal-directed movement task designed in Section 3.2 allow to study the fundamental aspects of inter-agent motor coordination in a confined setting. The combination of rhythmic and goal-directed arm movements in a dyadic setting is so far unique. The circular pick and place task introduced in Section 4.3 provokes realistic motor actions, that involve reaching, grasping and handing over of objects under coordination constraints. It enables to study the spatio-temporal aspects of joint action coordination resembling that of real world tasks. Similarly, the pHRI community is encouraged to complement interaction studies in VR and small-scale scenarios by immersive full-scale scenarios. The experimental paradigm of cooperative table pushing employed in Section 5.5 allows an evaluation of prototypical robotic assistants under realistic conditions regarding the physical properties of bulky objects and environmental manipulation constraints.

Physical cooperation in joint action tasks is conceptually realized by an object-centered formulation of the cooperative manipulation problem and human-centered strategies for dynamic role allocation. Together with the experimental paradigm, the proposed *interaction control scheme embedding the effort sharing strategy* provides a seminal basis and formal testbed to synthesize and evaluate multi-criteria and multi-dimensional role allocation schemes.

The synchronization concept based on the unified entrainment process of both continuous phase variables and discrete events provides a valuable contributions to the robotics community. As an *alternative to classical central pattern generators (CPG)*, it enables to intuitively and flexibly specify coordinative motor behavior of artificial agents in response to environmental feedback. Through the phase and event representations, motor coordination is effectively decoupled from the agent-specific realization of the perception-action system.

The developed model of human movement coordination may stimulate research and modeling efforts in the neighboring research field of *human social behavior*. In particular, the degree of cross coupling quantified by the human behavioral model may be explored in its role as an indicator of the partners' situation-specific weighing between self-centered autonomous and partner-centered coordinative behavior.

6.2 Outlook

The design process guided by the proposed methodology is successfully run through in two innovative scenarios of joint action, leading to advanced models of interactive motor behavior. The promising first achievements of this work, but also the emerged open issues motivate future research towards seamless HRI in joint action tasks. Some of the most

interesting points are composed in the following.

The focus of this work is on the executive level of interaction, i.e. how motor actions are dynamically and bidirectionally adjusted on short time scales to achieve tight coordination. Yet, the designed behavioral models feature goal-directedness, i.e. they are adjustable in the spatial domain and compatible with changing task goals. Now that the executive level of interaction is better understood, the *integration of negotiation processes on the decisive level* is believed an important next step towards seamless interaction. Albeit goal negotiation may be subject to longer time scales in many situations, the cross-effects between both interaction levels are worth to be explored.

Joint attention is suggested as elementary concept of natural joint action. Further exploitation of the visual modality by detecting the direction of the partner's gaze enables the robot to uncover, which spacial aspects or goals of the task are currently paid attention by the human. The *integration of gaze tracking* into future behavior designs as an auxiliary attention indicator and action predictor is supposed to foster an even tighter shaping of motor coordination to the partner's demands and capabilities.

Human-human movement coordination is modeled on a dyadic scope in this work. For parameter identification, the coupling dynamics within the dyads is assumed isotropic. Asymmetries, and thus, the coupling strength on an individual scope, could be derived from the available time series data of the individuals. Promising approaches to scrutinize the *directionality of the coupling dynamics* in pairs of bivariate time series data include methods assessing the direction of information flow and mutual predictability based on information theory, and the mutual dependencies of the reconstructed individual phase dynamics. Such approaches will allow a more differentiated view of the individual effort put into motor adaptation. For example, the coordination effort spent by the human during joint action with an interactive robotic partner could be assessed.

The insights obtained from both the design of role behavior and synchronization behavior suggest, that HRI can be improved further by a design iteration in the analytical perspective. The concept of movement synchronization opens up the entirely new field of joint action coordination, in which interactive motor behavior is explored. Although the behavioral model previously identified in the goal-directed HHI paradigm is integrated into the design, the synthesized entrainment dynamics are considered only a first, prototypical realization of such advanced coordination capabilities. Even better matchings of the human-robot coordination characteristics are expected from a model-directed investigation of the *entrainment behavior of human-human dyads* in the deployed joint action task. Dynamic role behavior is synthesized based on system theory and known behavioral principles. Its evaluation in HRI reveals an emerging gap between improved quantitative and deteriorated subjective measures. The task paradigm of cooperative table pushing allows to observe the *role allocation behavior of human-human dyads* in similar study designs. Besides motion and force, additional behavioral variables, such as the foci of attention, may be analyzed to gain a more complete picture on their function in the partners' role allocation. Time series analysis and system identification are expected to reveal a deeper understanding of the human role behavior and the fundamental time constants of role blending.

A Experimental Setups

A.1 VR-System for Visual-Haptic Rendering

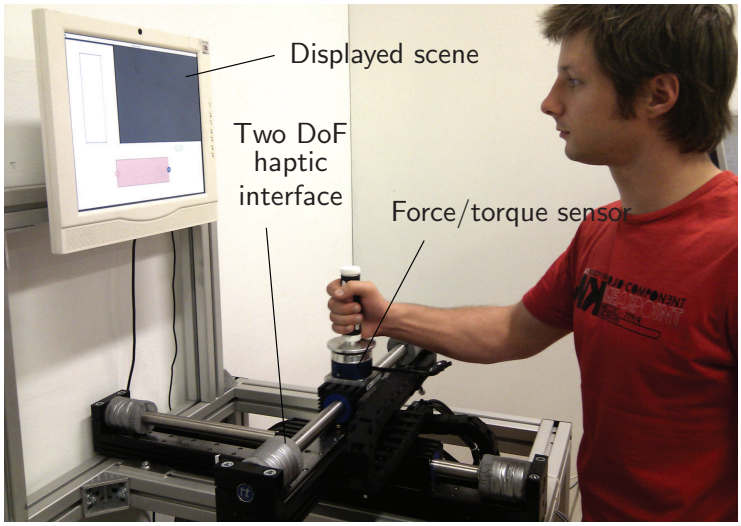

Fig. A.1: The two DoF VR system used in the experiment described in Section 5.3.3.

The experimental setup of the two DoF haptic interface consists of two linear actuators mounted on top of a solid rack to allow for comfortable operation while standing in front of the device, see Figure A.1. A *Thrusttube module 2504 (Copley Controls)* is orthogonally mounted on top of a *Thrusttube module 2510*. The actuators are equipped with optical position encoders with a resolution of 1 μm. Using *Xenus XTL (Copley Controls)* servo drivers, the actuators are current controlled. The human force input applied at the rubber-coated handle is measured using a six DoF wrench sensor *67M25A3-I40-DH (JR3)*. The handle is free-spinning, thus rendering zero torques in the vertical axis. For visual feedback from the virtually rendered scene, a 17 inch TFT-LCD monitor is mounted at eye level of the operator. The haptic interface is connected to a personal computer equipped with a *Sensoray 626* DAQ card. The entire control scheme is implemented in *MATLAB/Simulink* and, using the *MATLAB Real-Time Workshop*, executed on the *Gentoo Linux* operating system with the *Real-Time Application Interface (RTAI)* [168]. The control algorithm runs at a frequency of 1 kHz. For rejection of device non-linearities such as friction, the haptic interface is high-gain position controlled. Visual rendering of the 2D scene is done using the software libraries provided by the *QT UI development framework (Digia)*.

A.2 Environment for Full-Scale Interaction

A.2.1 Six DoF Mobile Manipulator

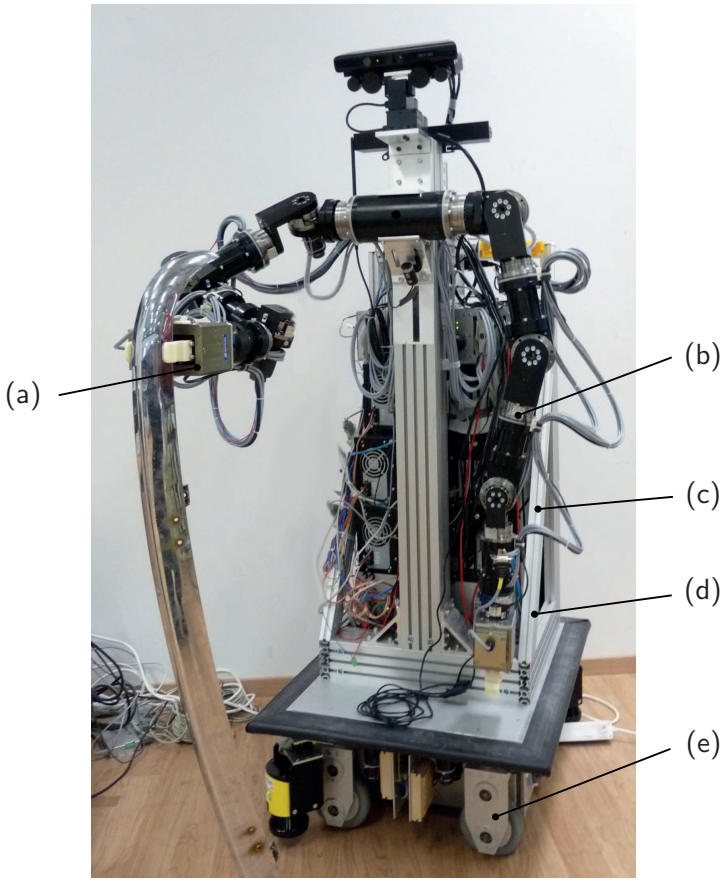

Fig. A.2: The human-sized mobile robot used in the experiments described in Section 4.3 and Section 5.5.

The mobile robot depicted in Figure A.2 stands on a four-wheeled omni-directional mobile platform (e) which offers roughly human-like maneuverability and smooth motion [54]. Two identical anthropomorphic seven DoF manipulators (b) are front-mounted on the top of the main chassis and provide a human-like work space [162, 163]. In the experiments, only the right arm is used. Mounted onto a six DoF wrench sensor *67M25A3-I40-DH (JR3)*, the manipulator is equipped with either a two-finger parallel gripper *PG70 (Schunk)* (a) for tight object grasps, or an electromagnetic gripper for fast grasps and releases of ferromagnetic objects. Lithium-ion polymer batteries (d) power the system for long periods without recharging. For computational power, the robot carries three industrial-type personal computers (c). The manipulator control scheme and the algorithms for interaction control are implemented in *MATLAB/Simulink* and executed under *Ubuntu Linux* with the *PREEMPT_RT* real-time kernel patch [167] using the *MATLAB Real-Time Workshop*. The control algorithms run at a frequency of 1 kHz. Control of the mobile platform and a synchronized data management is realized utilizing the *KogmoRTDB* real-time database [44] available at [43]. A detailed description of the software architecture of the robot can be

found in [5]. During the experiments, all data collection is done by the mobile robot. For the experiment described in Section 5.5, a second, identical wrench sensor mounted at the human grasp point of the table is connected to one of the robot PCs. The table configuration as well as the grasp points are tracked using the kinematics model of both the mobile manipulator and the rigidly grasped object, transformed by the odometry readings of the mobile base. Through a wireless network connection, the experimenter is able to submit on-line commands to the robot as required by the experimental procedures.

A.2.2 Motion Capture Systems

Active-Marker Based Tracking

For the experiment described in Section 3.2, a single camera bar of the system *VisualEyez II VZ4000 (PTI PhoeniX Technologies)* is used. The camera bar is mounted overhead at a height of approximately 3 m above the work space to be tracked, with the cameras facing downwards normally and centered around the workspace. Due to single bar operation, factory calibration of the system guarantees an accuracy < 0.5 mm without custom calibration. The objects to be tracked are equipped with active markers, which are infrared LEDs of high-power and wide-angle type. During motion capture, these LEDs are triggered to flash by a wireless target control module, which allows to uniquely identify the three-dimensional position of the objects. The proprietary software package *VZSoft* for controlling the system and gathering motion capture data runs on a *Microsoft Windows*-based personal computer. The real-time interface of the system provides data at a frequency of 30 Hz for on-line processing through a network connection. In addition, data are stored simultaneously at a frequency of 200 Hz for off-line analysis.

Passive-Marker Based Tracking

The experiment described in Section 4.3 is conducted utilizing a motion capture system consisting of eleven networked cameras, one *Oqus 3+* and ten *Oqus 4 (Qualisys)*. The cameras are mounted at ceiling height approximately 3 m over the work space to be tracked. They are distributed on a square-shaped frame of approximately 10 m $\times$ 10 m centered around the work space and aligned to maximize both overlapping of the camera fields of view and the volume available for tracking. Prior to the experiment, the system is calibrated within the required work space by means of a manual calibration routine, which yields an accuracy < 3 mm. Passive markers are attached to the objects to be tracked. Ball-shaped, reflective markers of 12 mm and 20 mm in diameter are used, which are illuminated by the infrared spots of the cameras. For unique object identification, a minimum set of four markers is rigidly attached to each object, forming a unique geometrical configuration. The software suite *Qualisys Track Manager (QTM)* for interaction with the motion capture system runs on a *Microsoft Windows*-based personal computer. It provides capture data of the three-dimensional object coordinates at a frequency of 200 Hz through the real-time interface for on-line processing. Capture data are made available to the robot at low latency through a network connection. Low-pass filtering is applied to the data using a 25-point moving average FIR filter at a sampling rate of 1 kHz.

B Haptic Rendering of VR Scenes

B.1 Haptic Interfaces

A haptic interface or haptic display is a mechanical device, typically a robotic manipulator, that is capable of conveying haptic cues to a human operator [3]. Though haptic displays addressing the tactile part exist as well, we only consider the kinesthetic part of the haptic modality and a single interaction point. Pen-shaped or bar-shaped handles, or gloves attached to the haptic device are utilized frequently to provide the interaction point for the hand of the human operator. The control method applied to a haptic interface in order to simulate and display a haptic environment to the human is called haptic rendering. Based on the preferred rendering scheme, we distinguish two types of haptic interfaces:

- *Impedance-type devices* measure the motion of the interaction point and display the forces generated from an impedance-type virtual environment. Inner force control loops may be employed. Such devices are typically lightweight and highly back-drivable. They advantageously render low mass dynamics, yet their workspaces and force output capabilities are mostly rather limited.

- *Admittance-type devices* measure the forces at the interaction point in addition to the device motion and display the motion generated from an admittance-type virtual environment. Typically, the mechanical structure of those devices is solid, heavy and hardly back-drivable. Inner position or velocity control loops shape the device dynamics. While such devices may have large workspaces and force capabilities, the minimum displayable mass is bounded due to stability reasons.

In this work, the focus is on the latter class, since those devices are well-suited to render the interaction with heavy objects as desired for the investigation of physical effort sharing presented in Section 5.3.3. An overview on popular haptic devices and their designs is found in [57, 101].

B.2 Haptic Rendering with Admittance-Type Devices

A variety of control schemes for haptic rendering is found in literature, see [175] for a detailed classification and discussion of existing approaches. Here, we consider the control of an admittance-type device for haptic rendering, such as the one in Appendix A.1. The control scheme is illustrated in Figure B.1. The inner position control loop cancels the usually nonlinear dynamics of the admittance-type haptic device. In this scheme, a stiff PD-controller generates the control input $\boldsymbol{u}_\mathrm{p}$ to the motors, which may be supported by a feedforward compensation of the measured human wrench $\boldsymbol{u}_{1,\mathrm{m}}$ and computed-torque terms. Since the position feedback is usually available with high resolutions and with low

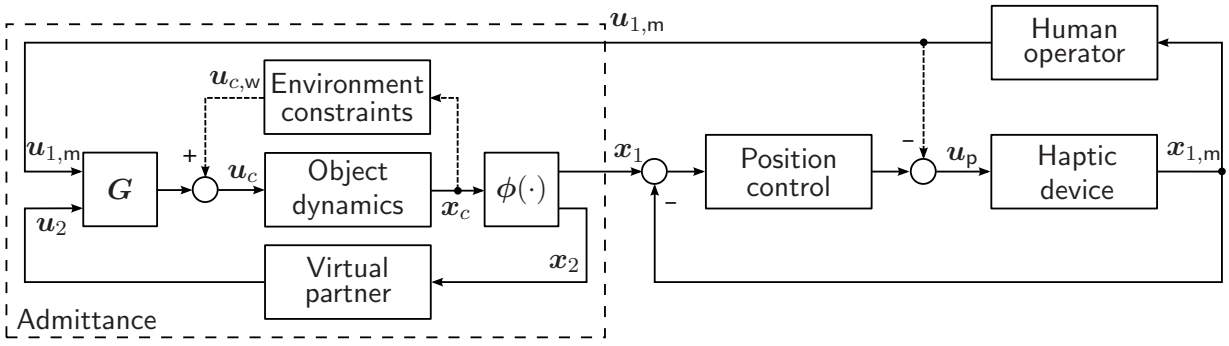

Fig. B.1: Haptic rendering of a virtual environment by an admittance-type control scheme. In addition to the object dynamics, the integration of an artificial partner and environmental constraints is illustrated as well.

measurement noise, high-gain control can be applied. As a result, we obtain $\boldsymbol{x}_1 \approx \boldsymbol{x}_{1,\mathrm{m}}$, where $\boldsymbol{x}_1$ is the commanded and $\boldsymbol{x}_{1,\mathrm{m}}$ the actual, measured position of the interaction point.

The human operator reacts to the motion of the interaction point $\boldsymbol{x}_{1,\mathrm{m}}$ by generating the wrench $\boldsymbol{u}_{1,\mathrm{m}}$, which is measured by the haptic device. Thus, the human behavior is represented by an impedance causality in this scheme. Through the exchange of the wrench $\boldsymbol{u}_{1,\mathrm{m}}$ and the motion $\boldsymbol{x}_1$, the admittance-type environment is coupled to the human operator, as indicated by the dashed box in Figure B.1.

The simplest implementation of the admittance-type virtual environment is the linear dynamics of the elementary mass-spring-damper system (2.13). With reference to the cooperative manipulation problem addressed in Chapter 5, the virtual environment shall be enhanced to render the cooperative object transfer by the human operator and a virtual partner through a constrained environment, cf. Figure B.1. The object dynamics follow an admittance causality, implementing the object mass and friction according to (5.1). The geometric relation of the grasp points on the object is represented by the grasp constraints $\boldsymbol{\phi}$ and the grasp matrix $\boldsymbol{G}$, cf. (5.5) and (5.7). Notably, the grasp point $\boldsymbol{x}_1$ becomes the haptic interaction point. Applying the wrench $\boldsymbol{u}_2$ at the virtual grasp point $\boldsymbol{x}_2$, the virtual partner is impedance-type, e.g. it performs compliant tracking of some object-related motion trajectory. In this work, we apply haptic rendering to investigate the interactive behavior between a virtual and a human partner in different implementations. Additionally, active environmental constraints due to contact with e.g. rigid or deformable obstacles, or surrounding walls may contribute impedance-type rejecting wrenches $\boldsymbol{u}_{c,\mathrm{w}}$ to the object dynamics.

Remark B.1 The simulation of impact situations between the interaction point and a stiff environment is challenging both with respect to stability and kinesthetic immersion. In fact, virtual walls provide a popular benchmark scenario for haptic interfaces [145]. Basic implementations consider spring-damper systems to render a finite stiffness based on the penetration depth.

If the complexity of the virtual environment is moderate, its dynamics and geometric constraints may be analytically derived and explicitly modeled within the control loop as

outlined above. Alternatively, software tools for real-time simulation of multi-body physics are utilized [194], such as the *SimMechanics* toolbox of *MATLAB/Simulink*, in order to efficiently specify more complex virtual environments.

B.3 Visual Rendering of Virtual Environments

Realistic rendering of virtual environments requires visual feedback to the human operator in congruence with the haptic feedback. To this end, monitors or head-mounted displays are employed frequently as graphic displays. Due to computational complexity, the visual rendering scheme is usually implemented to run independently from the physical simulation at update rates around 30 Hz. Therefore, the spatial information of moving bodies such as the object configuration $\boldsymbol{x}_c$ is updated based on feedback from the haptic rendering scheme. Object silhouettes and workspace boundaries that are composed by simple geometric primitives and displayed in a two-dimensional scene provide visual guidance to the human operator when performing planar tasks, e.g. pursuit tracking [33, 195] or constrained, goal-directed tasks [89, 105]. Three-dimensional scene rendering is employed to achieve sufficient feedback and high degrees of immersion in more complex virtual environments [7, 31, 194]. The implementation of such scences is eased by various graphics toolkits available for common programming languages.

C Questionnaire

The questionnaire administered in the human-robot experiment for the evaluation of dynamic role behavior in Section 5.5 is included below. According to the categories described in Section 5.5.2, the following statements were rated by the participants:

C.1 Task Load

- *Mental demand:*
  - The task required a large amount of mental and perceptual activity (e.g. thinking, deciding, calculating, remembering, looking, searching, etc.).
- *Physical demand:*
  - The task required a large amount of physical activity (e.g. pulling, pushing, turning, controlling, activating, etc.).
- *Temporal demand:*
  - I felt time pressure due to the rate or pace at which the task occurred.
- *Performance:*
  - I was successful in accomplishing the goals of the task set by the experimenter (or myself).
- *Effort:*
  - I had to work hard (mentally and physically) to accomplish the task.
- *Frustration:*
  - I felt irritated / stressed / annoyed during the task.

C.2 Task Experience

- *Collaboration:*
  - During the task, the robot and I acted towards a common goal.
  - The robot was trying to help me.
- *Interaction:*
  - My communication with the robot was interactive.
  - The robot responded to my actions.

- *Comfort:*
  - I felt comfortable in moving the table with the robot.
- *Pleasure:*
  - The way I interacted with the robot made the task enjoyable.
- *Degree of Control:*
  - The robot did not have control on the movement of the table, but it was only following my actions.
  - I observed and passively obeyed the robot's actions during the task.
- *Predictability:*
  - I could easily understand what the robot's plan was during the task.
  - The robot was good at predicting what I will do.
- *Trust:*
  - I believed that the robot would perform safely and correctly in moving the table.
  - I could trust the robot with moving the table during the task.
- *Human-likeness:*
  - The actions that the robot performed resembled those a human would do on a similar real-life scenario.
  - I felt that the robot behaved like a human being while moving the table with me.

Bibliography

[1] D. Abbink, M. Mulder, and E. Boer. Haptic shared control: smoothly shifting control authority? *Cogn., Technol. & Work*, 14(1):19–28, 2012.

[2] J. J. Adam and F. G. Paas. Dwell time in reciprocal aiming tasks. *Hum. Mov. Sci.*, 15(1):1–24, 1996.

[3] R. J. Adams and B. Hannaford. Stable haptic interaction with virtual environments. *IEEE Trans. Robot. Autom.*, 15(3):465–474, 1999.

[4] A. Albu-Schäffer, S. Haddadin, C. Ott, A. Stemmer, T. Wimböck, and G. Hirzinger. The DLR lightweight robot: design and control concepts for robots in human environments. *Ind. Rob.*, 34(5):376–385, 2007.

[5] D. Althoff, O. Kourakos, M. Lawitzky, A. Mörtl, M. Rambow, F. Rohrmüller, D. Brscic, D. Wollherr, S. Hirche, and M. Buss. An Architecture for Real-time Control in Multi-robot Systems. In *Cognitive Systems Monographs*, pages 43–52. Springer, 2009.

[6] C. Atkeson, C. An, and J. Hollerbach. Estimation of Inertial Parameters of Manipulator Loads and Links. *Int. J. Rob. Res.*, 5(3):101–119, 1986.

[7] C. Basdogan, C.-H. Ho, M. Srinivasan, and M. Slater. An Experimental Study on the Role of Touch in Shared Virtual Environments. *ACM Trans. Comput.-Hum. Interact.*, 7(4):443–460, 2000.

[8] P. Beek, R. Schmidt, A. Morris, M. Sim, and M. Turvey. Linear and nonlinear stiffness and friction in biological rhythmic movements. *Biol. Cybern.*, 73(6):499–507, 1995.

[9] P. J. Beek, C. E. Peper, and D. F. Stegeman. Dynamical models of movement coordination. *Hum. Mov. Sci.*, 14:573–608, 1995.

[10] P. J. Beek, C. E. Peper, and A. Daffertshofer. Modeling Rhythmic Interlimb Coordination: Beyond the Haken-Kelso-Bunz Model. *Brain Cogn.*, 48(1):149–165, 2002.

[11] M. Beetz, F. Stulp, B. Radig, J. Bandouch, N. Blodow, M. Dolha, A. Fedrizzi, D. Jain, U. Klank, I. Kresse, et al. The assistive kitchen–a demonstration scenario for cognitive technical systems. In *Proc. IEEE Ro-Man*, pages 1–8, 2008.

[12] A. Billard, S. Calinon, R. Dillmann, and S. Schaal. Robot Programming by Demonstration. In B. Siciliano and O. Khatib, editors, *Handbook of Robotics*, pages 1371–1394. Springer, 2008.

[13] C. Breazeal. Social interactions in HRI: the robot view. *IEEE Trans. Syst. Man Cybern. C Appl. Rev.*, 34(2):181–186, 2004.

[14] A. Bruns. Fourier-, Hilbert- and wavelet-based signal analysis: are they really different approaches? *J. Neurosci. Methods*, 137(2):321–332, 2004.

[15] J. Buchli, L. Righetti, and A. Ijspeert. Engineering entrainment and adaptation in limit cycle systems. *Biol. Cybern.*, 95(6):645–664, 2006.

[16] E. Burdet, R. Osu, D. W. Franklin, T. E. Milner, and M. Kawato. The central nervous system stabilizes unstable dynamics by learning optimal impedance. *Nat.*, 414(6862):446–449, 2001.

[17] T. Chaminade. A Social Cognitive Neuroscience Stance on Human-Robot Interactions. In *Int. Conf. SKILLS 2011*, volume 1, page 00014, 2011.

[18] A. H. Cohen, P. J. Holmes, and R. H. Rand. The nature of the coupling between segmental oscillators of the lamprey spinal generator for locomotion: A mathematical model. *J. Math. Biol.*, 13(3):345–369, 1982.

[19] E. S. Conkur and R. Buckingham. Clarifying the definition of redundancy as used in robotics. *Robotica*, 15(5):583–586, 1997.

[20] B. Corteville, E. Aertbelien, H. Bruyninckx, J. D. Schutter, and H. V. Brussel. Human-inspired Robot Assistant for Fast Point-to-point Movements. In *Proc. IEEE ICRA*, pages 3639–3644, 2007.

[21] K. Dautenhahn. Socially intelligent robots: dimensions of human–robot interaction. *Philos. Trans. R. Soc. Lond. B Biol. Sci.*, 362(1480):679–704, 2007.

[22] A. de Rugy, R. Salesse, O. Oullier, and J.-J. Temprado. A neuro-mechanical model for interpersonal coordination. *Biol. Cybern.*, 94(6):427–443, 2006.

[23] A. De Santis, B. Siciliano, A. De Luca, and A. Bicchi. An atlas of physical human–robot interaction. *Mechanism and Machine Theory*, 43:253–270, 2008.

[24] S. Degallier, C. Santos, L. Righetti, and A. Ijspeert. Movement generation using dynamical systems : a humanoid robot performing a drumming task. In *Proc. IEEE-RAS Humanoid Robots*, pages 512–517, 2006.

[25] D. Delignières and K. Torre. Event-Based and Emergent Timing: Dichotomy or Continuum? A Reply to Repp and Steinman (2010). *J. Mot. Behav.*, 43(4):311–318, 2011.

[26] B. Donald, P. Xavier, J. Canny, and J. Reif. Kinodynamic Motion Planning. *J. Assoc. Comput. Mach.*, 40(5):1048–1066, 1993.

[27] K. Doty, C. Melchiorri, and C. Bonivento. A Theory of Generalized Inverses Applied to Robotics. *Int. J. Robot. Res.*, 12:1–19, 1993.

[28] V. Duchaine and C. M. Gosselin. General model of human-robot cooperation using a novel velocity based variable impedance control. In *Proc. IEEE EuroHaptics*, pages 446–451, 2007.

[29] A. Edsinger and C. C. Kemp. Human-robot interaction for cooperative manipulation: Handing objects to one another. In *Proc. IEEE Ro-Man*, pages 1167–1172, 2007.

[30] T. Eisenhammer, A. Hübler, N. Packard, and J. A. S. Kelso. Modeling experimental time series with ordinary differential equations. *Biol. Cybern.*, 65(2):107–112, 1991.

[31] P. Evrard and A. Kheddar. Homotopy Switching Model for Dyad Haptic Interaction in Physical Collaborative Tasks. In *Proc. EHS EuroHaptics*, pages 45–50, 2009.

[32] P. Evrard and A. Kheddar. Homotopy-based controller for physical human-robot interaction. In *Proc. IEEE Ro-Man*, pages 1–6, 2009.

[33] D. Feth, R. Groten, A. Peer, and M. Buss. Control-theoretic model of haptic human-human interaction in a pursuit tracking task. In *Proc. IEEE Ro-Man*, pages 1106–1111, 2009.

[34] D. Feth, R. Groten, A. Peer, S. Hirche, and M. Buss. Performance Related Energy Exchange in Haptic Human-Human Interaction in a Shared Virtual Object Manipulation Task. In *Proc. EHS EuroHaptics*, pages 338–343, 2009.

[35] P. M. Fitts. The information capacity of the human motor system in controlling the amplitude of movement. *J. Exp. Psychol.*, 47(6):381–391, 1954.

[36] T. Flash and N. Hogan. The coordination of arm movements: An experimentally confirmed mathematical model. *Neurosci.*, 5:1688–1703, 1985.

[37] B. Forsyth and K. Maclean. Predictive haptic guidance: intelligent user assistance for the control of dynamic tasks. *IEEE Trans. Vis. Comp. Graph.*, 12(1):103–113, 2006.

[38] D. Franklin, R. Osu, E. Burdet, M. Kawato, and T. Milner. Adaptation to Stable and Unstable Dynamics Achieved By Combined Impedance Control and Inverse Dynamics Model. *J. Neurophys.*, 90(5):3270–3282, 2003.

[39] A. Fuchs and J. A. S. Kelso. A theoretical note on models of interlimb coordination. *J. Exp. Psychol. Hum. Percept. Perf.*, 20(5):1088–1097, 1994.

[40] A. Fuchs, V. Jirsa, H. Haken, and J. A. S. Kelso. Extending the HKB model of coordinated movement to oscillators with different eigenfrequencies. *Biol. Cybern.*, 74(1):21–30, 1995.

[41] A. Gams, A. Ijspeert, S. Schaal, and J. Lenarčič. On-line learning and modulation of periodic movements with nonlinear dynamical systems. *Auton. Robots*, 27(1):3–23, 2009.

[42] R. Gillespie, J. Colgate, and M. Peshkin. A General Framework for Cobot Control. *IEEE Trans. Robot. Automat.*, 17(4):391–401, 2001.

[43] M. Goebl. KogMo-RTDB - Real-time Database for Cognitive Automobiles, 2012. URL `http://www.kogmo-rtdb.de`.

[44] M. Goebl and G. Färber. A Real-Time-capable Hard- and Software Architecture for Joint Image and Knowledge Processing in Cognitive Automobiles. In *Proc. IEEE IV*, pages 734–740, 2007.

[45] J. Goetz, S. Kiesler, and A. Powers. Matching robot appearance and behavior to tasks to improve human-robot cooperation. In *Proc. IEEE Ro-Man*, pages 55–60, 2003.

[46] P. G. Griffiths and R. B. Gillespie. Sharing control between humans and automation using haptic interface: primary and secondary task performance benefits. *Hum. Factors*, 47(3):574–590, 2005.

[47] R. Groten. *Haptic human-robot collaboration: How to learn from human dyads*. PhD thesis, Technische Universität München, 2011.

[48] R. Groten, D. Feth, H. Goshy, A. Peer, D. Kenny, and M. Buss. Experimental Analysis of Dominance in Haptic Collaboration. In *Proc. IEEE Ro-Man*, pages 723–729, 2009.

[49] R. Groten, D. Feth, A. Peer, and M. Buss. Shared Decision Making in a Collaborative Task with Reciprocal Haptic Feedback - an Efficiency-Analysis. In *Proc. IEEE ICRA*, 2010.

[50] R. Groten, D. Feth, A. Peer, and M. Buss. Psychological experiments in haptic collaboration research. In A. Peer and C. D. Giachritsis, editors, *Immersive Multimodal Interactive Presence*, Springer Series on Touch and Haptic Systems, pages 65–90. Springer London, 2012.

[51] S. Haddadin, A. Albu-Schaffer, A. De Luca, and G. Hirzinger. Collision detection and reaction: A contribution to safe physical human-robot interaction. In *Proc. IEEE/RSJ IROS*, pages 3356–3363, 2008.

[52] H. Haken. *Synergetics: an introduction : nonequilibrium phase transitions and self-organization in physics, chemistry and biology*. Springer series in synergetics. Springer-Verlag, 1978.

[53] H. Haken, J. A. S. Kelso, and H. Bunz. A theoretical model of phase transitions in human hand movements. *Biol. Cybern.*, 51(5):347–356, 1985.

[54] U. Hanebeck, N. Saldic, and G. Schmidt. A Modular Wheel System for Mobile Robot Applications. In *Proc. IEEE/RSJ IROS*, pages 17–22, 1999.

[55] M. Hans, B. Graf, and R. Schraft. Robotic home assistant care-o-bot: Past-present-future. In *Proc. IEEE Ro-Man*, pages 380–385, 2002.

[56] S. G. Hart and L. E. Stavenland. Development of NASA-TLX (Task Load Index): Results of empirical and theoretical research. In P. A. Hancock and N. Meshkati, editors, *Human Mental Workload*, chapter 7, pages 139–183. Elsevier, 1988.

[57] V. Hayward, O. R. Astley, M. Cruz-Hernandez, D. Grant, and G. Robles-De-La-Torre. Haptic interfaces and devices. *Sens. Rev.*, 24(1):16–29, 2004.

[58] M. Hillman. 2 Rehabilitation Robotics from Past to Present – A Historical Perspective. In Z. Bien and D. Stefanov, editors, *Advances in Rehabilitation Robotics*, volume 306 of *Lecture Notes in Control and Information Science*, pages 25–44. Springer Berlin Heidelberg, 2004.

[59] Y. Hirata and K. Kosuge. Distributed Robot Helpers Handling a Single Object in Cooperation with Human. In *Proc. IEEE ICRA*, pages 458–463, 2000.

[60] N. Hogan. Impedance control: An approach to manipulation. I–Theory. II–Implementation. III–Applications. *ASME Trans. J. Dyn. Syst. Meas. Control B*, 107:1–24, 1985.

[61] N. Hogan and D. Sternad. On rhythmic and discrete movements: reflections, definitions and implications for motor control. *Exp. Brain Res.*, 181(1):13–30, 2007.

[62] J. Hölldampf, A. Peer, and M. Buss. Synthesis of an interactive haptic dancing partner. In *Proc. IEEE Ro-Man*, pages 527–532, 2010.

[63] M. J. Hove and J. L. Risen. It's all in the timing: Interpersonal synchrony increases affiliation. *Soc. Cogn.*, 27(6):949–960, 2009.

[64] G.-C. Hsieh and J. C. Hung. Phase-locked loop techniques. A survey. *IEEE Trans. Ind. Electron.*, 43(6):609–615, 1996.

[65] M. Huber, H. Radrich, C. Wendt, M. Rickert, A. Knoll, T. Brandt, and S. Glasauer. Evaluation of a novel biologically inspired trajectory generator in human-robot interaction. In *Proc. IEEE Ro-Man*, pages 639–644, 2009.

[66] A. J. Ijspeert. 2008 special issue: Central pattern generators for locomotion control in animals and robots: A review. *Neural Netw.*, 21(4):642–653, 2008.

[67] R. Ikeura, H. Monden, and H. Inooka. Cooperative motion control of a robot and a human. In *Proc. IEEE Ro-Man*, pages 112 –117, 1994.

[68] R. Ikeura, T. Moriguchi, and K. Mizutani. Optimal variable impedance control for a robot and its application to lifting an object with a human. In *Proc. IEEE Ro-Man*, pages 500 – 505, 2002.

[69] N. Jarrassé, T. Charalambous, and E. Burdet. A framework to describe, analyze and generate interactive motor behaviors. *PloS ONE*, 7(11):e49945, 2012.

[70] N. Jarrassé, V. Sanguineti, and E. Burdet. Slaves no longer: review on role assignment for human-robot joint motor action. *Adapt. Behav.*, 2013.

[71] V. K. Jirsa and J. A. S. Kelso. The excitator as a minimal model for the coordination dynamics of discrete and rhythmic movement generation. *J. Mot. Behav.*, 37(1):35–51, 2005.

[72] T. Kasuga and M. Hashimoto. Human-robot handshaking using neural oscillators. In *Proc. IEEE ICRA*, pages 3802–3807, 2005.

[73] B. A. Kay, J. A. S. Kelso, E. L. Saltzman, and G. Schöner. Space-time behavior of single and bimanual rhythmical movements: data and limit cycle model. *J. Exp. Psychol. Hum. Percept. Perform.*, 12(2):178–192, 1987.

[74] J. A. S. Kelso, G. C. de Guzman, C. Reveley, and E. Tognoli. Virtual Partner Interaction (VPI): Exploring Novel Behaviors via Coordination Dynamics. *PLoS ONE*, 4(6):e5749, 2009.

[75] O. Khatib. Mobile manipulation: The robotic assistant. *Rob. Auton. Syst.*, 26(2): 175–183, 1999.

[76] A. Kheddar. Human-robot haptic joint actions Is an equal control-sharing approach possible? In *Proc. IEEE HSI*, pages 268–273, 2011.

[77] C. H. Kim, K. Yonekura, H. Tsujino, and S. Sugano. Physical Control of the Rotation Center of an Unsupported Object-Rope Turning by a Humanoid Robot-. In *Proc. IEEE-RAS Humanoid Robots*, pages 148–153, 2009.

[78] A. Kirsch, T. Kruse, E. Sisbot, R. Alami, M. Lawitzky, D. Brščić, S. Hirche, P. Basili, and S. Glasauer. Plan-Based Control of Joint Human-Robot Activities. *Künstl. Intell.*, 24(3):223–231, 2010.

[79] I. Konvalinka, P. Vuust, A. Roepstorff, and C. D. Frith. Follow you, follow me: Continuous mutual prediction and adaptation in joint tapping. *Q. J. Exp. Psychol.*, 63(11):2220–2230, 2010.

[80] K. Kosuge and Y. Hirata. Human-Robot Interaction. In *Proc. IEEE ROBIO*, pages 8–11, 2004.

[81] K. Kosuge, H. Yoshida, and T. Fukuda. Dynamic control for robot-human collaboration. In *Proc. IEEE Ro-Man*, pages 398–401, 1993.

[82] K. Kosuge, M. Sato, and N. Kazamura. Mobile robot helper. In *Proc. IEEE ICRA*, pages 583–588, 2000.

[83] H. Krebs, J. Palazzolo, L. Dipietro, M. Ferraro, J. Krol, K. Rannekleiv, B. Volpe, and N. Hogan. Rehabilitation Robotics: Performance-Based Progressive Robot-Assisted Therapy. *Auton. Robots*, 15(1):7–20, 2003.

[84] T. Kreuz, F. Mormann, R. G. Andrzejak, A. Kraskov, K. Lehnertz, and P. Grassberger. Measuring synchronization in coupled model systems: A comparison of different approaches. *Phys. D: Nonlinear Phenom.*, 225(1):29–42, 2007.

[85] A. Kucukyilmaz, M. Sezgin, and C. Basdogan. Conveying Intentions through Haptics in Human-Computer Collaboration. In *Proc. IEEE WHC*, pages 421–426, June 2011.

[86] A. Kucukyilmaz, T. Sezgin, and C. Basdogan. Intention Recognition for Dynamic Role Exchange in Haptic Collaboration. *IEEE Trans. Haptics*, 6(1):58–68, 2013.

[87] Y. Kuramoto. *Chemical Oscillations, Waves and Turbulence*. Springer, Heidelb., 1984.

[88] M. Lawitzky, J. R. Medina, D. Lee, and S. Hirche. Feedback motion planning and learning from demonstration in physical robotic assistance: differences and synergies. In *Proc. IEEE/RSJ IROS*, pages 3646–3652, 2012.

[89] M. Lawitzky, M. Kimmel, P. Ritzer, and S. Hirche. Trajectory generation under the least action principle for physical human-robot cooperation. In *Proc. IEEE ICRA*, pages 4285–4290, 2013.

[90] D. Lee and C. Ott. Incremental kinesthetic teaching of motion primitives using the motion refinement tube. *Auton. Robot.*, pages 1–17, 2011.

[91] S. Lee, S.-Y. Yi, J.-O. Park, and C.-W. Lee. Reference adaptive impedance control and its application to obstacle avoidance trajectory planning. In *Proc. IEEE/RSJ IROS*, pages 1158–1162, 1997.

[92] S. Lee, K. Lee, S. Lee, J. Kim, and C. Han. Human-robot cooperation control for installing heavy construction materials. *Auton. Robots*, 22(3):305–319, 2007.

[93] L. Ljung. *System identification: Theory for the user*. Prentice Hall, Upper Saddle River, 1999.

[94] L. Ljung and T. Glad. *Modeling of Dynamic Systems*. PTR Prentice Hall, 1994.

[95] S. M. Lopresti-Goodman, M. J. Richardson, P. L. Silva, and R. C. Schmidt. Period basin of entrainment for unintentional visual coordination. *J. Mot. Behav.*, 40(1): 3–10, 2008.

[96] J. Lumsden, L. K. Miles, M. J. Richardson, C. A. Smith, and C. N. Macrae. Who syncs? Social motives and interpersonal coordination. *J. Exp. Soc. Psychol.*, 48(3): 746–751, 2012.

[97] Y. Maeda, T. Hara, and T. Arai. Human-Robot Cooperative Manipulation with Motion Estimation. In *Proc. IEEE/RSJ IROS*, pages 2240–2245, 2001.

[98] Y. Maeda, A. Takahashi, T. Hara, and T. Arai. Human-robot cooperation with mechanical interaction based on rhythm entrainment-realization of cooperative rope turning. In *Proc. IEEE ICRA*, pages 3477–3482, 2001.

[99] Y. Maeda, A. Takahashi, T. Hara, and T. Arai. Human-robot Cooperative Rope Turning–an example of mechanical coordination through rythm entrainment. *Adv. Robotics*, 17(1):67–78, 2003.

[100] L. Marin, J. Issartel, and T. Chaminade. Interpersonal motor coordination: From human-human to human-robot interactions. *Interact. Stud.*, 10(3):479–504, 2009.

[101] J. Martin and J. Savall. Mechanisms for haptic torque feedback. In *Proc. IEEE Eurohaptics*, pages 611–614, 2005.

[102] K. Matsuoka. Sustained oscillations generated by mutually inhibiting neurons with adaptation. *Biol. Cybern.*, 52(6):367–376, 1985.

[103] D. T. McRuer and H. R. Jex. A review of quasi-linear pilot models. *IEEE Trans. Hum. Factors Electron.*, HFE-8(3):231–249, 1967.

[104] J. R. Medina, D. Lee, and S. Hirche. Risk-sensitive optimal feedback control for haptic assistance. In *IEEE ICRA*, pages 1025–1031, 2012.

[105] J. R. Medina, T. Lorenz, D. Lee, and S. Hirche. Disagreement-aware physical assistance through risk-sensitive optimal feedback control. In *Proc. IEEE/RSJ IROS*, pages 3639–3645, 2012.

[106] M. P. Michalowski, S. Sabanovic, and H. Kozima. A dancing robot for rhythmic social interaction. In *Proc. ACM/IEEE HRI*, pages 89–96, 2007.

[107] L. K. Miles, L. K. Nind, and C. N. Macrae. The rhythm of rapport: Interpersonal synchrony and social perception. *J. Exp. Soc. Psychol.*, 45(3):585–589, 2009.

[108] S. Miossec and A. Kheddar. Human motion in cooperative tasks: Moving object case study. In *Proc. IEEE ROBIO*, pages 1509–1514, 2008.

[109] Y. Miyake. Interpersonal synchronization of body motion and the walk-mate walking support robot. *IEEE Trans. Rob.*, 25(3):638–644, 2009.

[110] R. R. Murphy. Human-robot interaction in rescue robotics. *IEEE Trans. Syst. Man Cybern. C Appl. Rev.*, 34(2):138–153, 2004.

[111] R. Murray, Z. Li, and S. Sastry. *A mathematical introduction to robotic manipulation*, chapter Multifingered Hand Kinematics. CRC Press, 1994.

[112] N. Nitzsche, U. Hanebeck, and G. Schmidt. Design Issues of Mobile Haptic Interfaces. *J. Robot. Syst.*, 20(9):549–556, 2003.

[113] O. Oguz, A. Kucukyilmaz, T. Sezgin, and C. Basdogan. Haptic Negotiation and Role Exchange for Collaboration in Virtual Environments. In *Proc. IEEE Haptics*, pages 371–378, 2010.

[114] M. Okada, K. Tatani, and Y. Nakamura. Polynomial design of the nonlinear dynamics for the brain-like information processing of whole body motion. In *Proc. IEEE ICRA*, pages 1410–1415, 2002.

[115] R. Olfati-Saber, A. Fax, and R. Murray. Consensus and Cooperation in Networked Multi-Agent Systems. *Proc. IEEE*, 95:215–233, 2007.

[116] M. K. O'Malley, A. Gupta, M. Gen, and Y. Li. Shared control in haptic systems for performance enhancement and training. *Trans. ASME J. Dyn. Syst. Meas. Control*, 128(1):75, 2006.

[117] O. Oullier, G. C. De Guzman, K. J. Jantzen, J. Lagarde, and J. A. S. Kelso. Social coordination dynamics: Measuring human bonding. *Soc. neurosci.*, 3(2):178–192, 2008.

[118] C. Parker and E. Croft. Experimental investigation of human-robot cooperative carrying. In *Proc. IEEE/RSJ IROS*, pages 3361–3366, 2011.

[119] C. A. Parker and E. A. Croft. Design & Personalization of a Cooperative Carrying Robot Controller. In *Proc. IEEE ICRA*, pages 3916–3921, 2012.

[120] L. Parker. Distributed Intelligence: Overview of the Field and its Application in Multi-Robot Systems. *J. Phys. Agents*, 2:5–14, 2008.

[121] C. Passenberg, A. Peer, and M. Buss. A survey of environment-, operator-, and task-adapted controllers for teleoperation systems. *Mechatronics*, 20(7):787–801, 2010.

[122] C. Passenberg, R. Groten, A. Peer, and M. Buss. Towards real-time haptic assistance adaptation optimizing task performance and human effort. In *Proc. IEEE WHC*, pages 155 –160, 2011.

[123] C. Passenberg, A. Glaser, and A. Peer. Exploring the Design Space of Haptic Assistants: the Assistance Policy Module. *IEEE Trans. Haptics*, 6(4):440–452, 2013.

[124] R. A. Peterson. *Constructing effective questionnaires*. Sage, 2000.

[125] T. Petrič, A. Gams, A. J. Ijspeert, and L. Žlajpah. On-line frequency adaptation and movement imitation for rhythmic robotic tasks. *Int. J. Rob. Res.*, 30(14):1775–1788, 2011.

[126] A. Pikovsky, M. Rosenblum, and J. Kurths. *Synchronization - A universal concept in nonlinear sciences*. Cambridge University Press, Cambridge, 2001.

[127] D. Pongas, A. Billard, and S. Schaal. Rapid synchronization and accurate phase-locking of rhythmic motor primitives. In *Proc. IEEE/RSJ IROS*, pages 2911–2916, 2005.

[128] D. Prattichizzo and J. Trinkle. Grasping. In B. Siciliano and O. Khatib, editors, *Springer Handbook of Robotics*. Springer, Berlin, Heidelberg, 2008.

[129] R. Quian Quiroga, T. Kreuz, and P. Grassberger. Event synchronization: A simple and fast method to measure synchronicity and time delay patterns. *Phys. Rev. E*, 66(4):041904, 2002.

[130] M. Rahman, R. Ikeura, and K. Mizutani. Cooperation characteristics of two humans in moving an object. *Mach. Intell. Robot. Control*, 4(2):43–48, 2002.

[131] R. H. Rand, A. H. Cohen, and P. J. Holmes. *Neural Control of Rythmic Movement in Vertebrates*, chapter Systems of Coupled Oscillators as Models of Central Pattern Generators. Wiley, New York, 1988.

[132] K. Reed and M. Peshkin. Physical Collaboration of Human-Human and Human-Robot Teams. *IEEE Trans. Haptics*, 1(2):108–120, 2008.

[133] K. Reed, M. Peshkin, M. Hartmann, E. Colgate, and J. Patton. Kinesthetic Interaction. In *Proc. IEEE ICORR*, pages 569–574, 2005.

[134] K. Reed, M. Peshkin, M. Hartmann, J. Patton, P. Vishton, and M. Grabowecky. Haptic cooperation between people, and between people and machines. In *Proc. IEEE/RSJ IROS*, pages 2109–2114, 2006.

[135] B. H. Repp. Sensorimotor synchronization: A review of the tapping literature. *Psychon. Bull. Rev.*, 12(6):969–992, 2005.

[136] B. H. Repp and S. R. Steinman. Simultaneous Event-Based and Emergent Timing: Synchronization, Continuation, and Phase Correction. *J. Mot. Behav.*, 42(2):111–126, 2010.

[137] B. H. Repp and Y.-H. Su. Sensorimotor synchronization: A review of recent research (2006-2012). *Psychon. Bull. Rev.*, 20(3):403–452, 2013.

[138] M. J. Richardson, K. L. Marsh, and R. C. Schmidt. Effects of visual and verbal interaction on unintentional interpersonal coordination. *J. Exp. Psychol. Hum. Percept. Perform.*, 31(1):62–79, 2005.

[139] M. J. Richardson, K. L. Marsh, R. W. Isenhower, J. R. L. Goodman, and R. C. Schmidt. Rocking together: Dynamics of intentional and unintentional interpersonal coordination. *Hum. Mov. Sci.*, 26(6):867–891, 2007.

[140] B. Robins, E. Ferrari, and K. Dautenhahn. Developing scenarios for robot assisted play. In *Proc. IEEE Ro-Man*, pages 180–186, 2008.

[141] L. Rosenberg. Virtual fixtures: Perceptual tools for telerobotic manipulation. In *Proc. IEEE VR*, pages 76 –82, 1993.

[142] M. Rosenblum and J. Kurths. *Nonlinear Analysis of Physiological Data*, chapter Analysing Synchronization Phenomena from Bivariate Data by Means of the Hilbert Transform, pages 91–99. Springer, Heidelb., 2007.

[143] M. Rosenblum, A. Pikovsky, J. Kurths, C. Schäfer, and P. Tass. Chapter 9 Phase synchronization: From theory to data analysis. In F. Moss and S. Gielen, editors, *Neuro-Informatics and Neural Modelling*, volume 4 of *Handbook of Biological Physics*, pages 279 – 321. North-Holland, 2001.

[144] M. Saida, J. R. Medina, and S. Hirche. Adaptive attitude design with risk-sensitive optimal feedback control in physical human-robot interaction. In *Proc. IEEE Ro-Man*, pages 955–961, 2012.

[145] K. Salisbury, F. Conti, and F. Barbagli. Haptic rendering: introductory concepts. *IEEE Comput. Graph. Appl.*, 24(2):24–32, 2004.

[146] A. Salleh, R. Ikeura, S. Hayakawa, and H. Sawai. Cooperative Object Transfer: Effect of Observing Different Part of the Object on the Cooperative Task Smoothness. *J. Biomech. Sci. Eng.*, 6(4):343–360, 2011.

[147] T. Sato, M. Hashimoto, and M. Tsukahara. Synchronization based control using online design of dynamics and its application to human-robot interaction. In *Proc. IEEE ROBIO*, pages 652–657, 2007.

[148] R. Schmidt and M. T. Turvey. Phase-entrainment dynamics of visually coupled rhythmic movements. *Biol. Cybern.*, 70(4):369–376, 1994.

[149] R. Schmidt, P. Fitzpatrick, R. Caron, and J. Mergeche. Understanding social motor coordination. *Hum. Mov. Sci.*, 30(5):834–845, 2011.

[150] R. C. Schmidt and B. O'Brien. Evaluating the Dynamics of Unintended Interpersonal Coordination. *Ecol. Psychol.*, 9(3):189–206, 1997.

[151] R. C. Schmidt, C. Carello, and M. T. Turvey. Phase transitions and critical fluctuations in the visual coordination of rhythmic movements between people. *J. Exp. Psychol. Hum. Percept. Perform.*, 16(2):227–247, 1990.

[152] R. C. Schmidt, B. K. Shaw, and M. T. Turvey. Coupling Dynamics in Interlimb Coordination. *J. Exp. Psychol. Hum. Percept. Perform.*, 19(2):397–415, 1993.

[153] R. C. Schmidt, M. Bienvenu, P. A. Fitzpatrick, and P. G. Amazeen. A comparison of intra- and interpersonal interlimb coordination: coordination breakdowns and coupling strength. *J. Exp. Psychol. Hum. Percept. Perform.*, 24(3):884–900, 1998.

[154] S. Schneider and R. Cannon. Object Impedance Control for Cooperative Manipulation: Theory and Experimental Results. *IEEE Trans. Robot. Automat.*, 8(3): 383–394, 1992.

[155] G. Schöner and J. A. Kelso. Dynamic pattern generation in behavioral and neural systems. *Sci.*, 239(4847):1513–1520, 1988.

[156] A. Schubö, C. Vesper, M. Wiesbeck, and S. Stork. *HCI and Usability for Medicine and Health Care, Lecture Notes in Computer Science*, volume 4799, chapter Movement C, pages 143–154. Springer Berlin / Heidelberg, 2007.

[157] N. Sebanz and G. Knoblich. Prediction in joint action: what, when, and where. *Top. Cogn. Sci.*, 1(2):353–367, 2009.

[158] N. Sebanz, H. Bekkering, and G. Knoblich. Joint action: bodies and minds moving together. *Trends Cogn. Sci.*, 10(2):70–76, 2006.

[159] B. Sellner, F. W. Heger, L. M. Hiatt, R. Simmons, and S. Singh. Coordinated multiagent teams and sliding autonomy for large-scale assembly. *Proc. IEEE*, 94(7): 1425–1444, 2006.

[160] D. A. Smirnov and R. G. Andrzejak. Detection of weak directional coupling: Phase-dynamics approach versus state-space approach. *Phys. Rev. E*, 71(3):36207, 2005.

[161] G. Sofianidis, V. Hatzitaki, G. Grouios, L. Johannsen, and A. Wing. Somatosensory driven interpersonal synchrony during rhythmic sway. *Hum. Mov. Sci.*, 31(3):553 – 566, 2012.

[162] B. Stanczyk. *Developement and Control of an Anthropomorphic Telerobotic System.* PhD thesis, Technische Universität München, 2006.

[163] B. Stanczyk and M. Buss. Development of a Telerobotic System for Exploration of Hazardous Environments. In *Proc. IEEE/RSJ IROS*, pages 2532–2537, 2004.

[164] B. E. Studenka and H. N. Zelaznik. Synchronization in repetitive smooth movement requires perceptible events. *Acta Psychol.*, 136(3):432 – 441, 2011.

[165] T. Takubo, H. Arai, Y. Hayashibara, and K. Tanie. Human-Robot Cooperative Manipulation Using a Virtual Nonholonomic Constraint. *Int. J. Robot. Res.*, 21: 541–553, 2002.

[166] J. Tan, N. Xi, and Y. Wang. Integrated task planning and control for mobile manipulators. *Int. J. Rob. Res.*, 22(5):337–354, 2003.

[167] The Preempt RT community. Real-Time Linux Wiki, 2013. URL `http://rt.wiki.kernel.org`.

[168] The RTAI Team. RTAI - the RealTime Application Interface for Linux, 2013. URL `www.rtai.org`.

[169] A. Thobbi, Y. Gu, and W. Sheng. Using Human Motion Estimation for Human-Robot Cooperative Manipulation. In *Proc. IEEE/RSJ IROS*, pages 2873–2878, 2011.

[170] E. Todorov. Optimality principles in sensorimotor control. *Nat. neurosci.*, 7(9): 907–915, 2004.

[171] K. Torre and R. Balasubramaniam. Two different processes for sensorimotor synchronization in continuous and discontinuous rhythmic movements. *Exp. Brain Res.*, 199(2):157–166, 2009.

[172] T. Tsumugiwa, T. Yokogawa, and K. Hara. Variable Impedance Control Based on Estimation of Human Arm Stiffness for Human-Robot Cooperative Calligraphic Task. In *Proc. IEEE ICRA*, pages 644–650, 2002.

[173] M. T. Turvey, L. D. Rosenblum, R. C. Schmidt, and P. N. Kugler. Fluctuations and Phase Symmetry in Coordinated Rhythmic Movements. *J. Exp. Psychol. Hum. Percept. Perform.*, 12(4):564–583, 1986.

[174] T. Ubukata, S. Kotosaka, and H. Ohtaki. Trajectory Generation for Adaptive Motion by Phase Feedback - Synchronization of Multicycle Human Movement. *J. Robotics and Mechatronics*, 21(3):342–352, 2009.

[175] M. Ueberle and M. Buss. Control of kinesthetic haptic interfaces. In *Proc. IEEE/RSJ IROS, Workshop on Touch and Haptics*, 2004.

[176] U. Unterhinninghofen, T. Schauß, and M. Buss. Control of a Mobile Haptic Interface. In *Proc. IEEE ICRA*, pages 2085–2090, 2008.

[177] P. Valdesolo, J. Ouyang, and D. DeSteno. The rhythm of joint action: Synchrony promotes cooperative ability. *J. Exp. Soc. Psychol.*, 46(4):693–695, 2010.

[178] N. R. van Ulzen, C. J. C. Lamoth, A. Daffertshofer, G. R. Semin, and P. J. Beek. Characteristics of instructed and uninstructed interpersonal coordination while walking side-by-side. *Neurosci. Lett.*, 432(2):88–93, 2008.

[179] M. Varlet and M. J. Richardson. Computation of continuous relative phase and modulation of frequency of human movement. *J. Biomech.*, 44(6):1200–4, 2011.

[180] C. Vesper, A. Soutschek, and A. Schubö. Motion coordination affects movement parameters in a joint pick-and-place task. *Q. J. Exp. Psychol.*, 62(12):2418–2432, 2009.

[181] C. Vesper, S. Butterfill, G. Knoblich, and N. Sebanz. A minimal architecture for joint action. *Neural Netw.*, 23(8):998–1003, 2010.

[182] J. Wainer, D. J. Feil-Seifer, D. A. Shell, and M. J. Mataric. Embodiment and human-robot interaction: A task-based perspective. In *Proc. IEEE Ro-Man*, pages 872–877, 2007.

[183] Z. Wang, J. Yuan, and M. Buss. Modelling of human haptic skill: A framework and preliminary results. In *Proc. IFAC*, pages 14761–14766, 2008.

[184] Z. Wang, A. Peer, and M. Buss. An HMM approach to realistic haptic human-robot interaction. In *Proc. IEEE EuroHaptics*, pages 374–379, 2009.

[185] W. H. Warren. The Dynamics of Perception and Action. *Psychol. Rev.*, 113(2): 358–389, 2006.

[186] A. Weiss, R. Bernhaupt, M. Tscheligi, D. Wollherr, K. Kuhnlenz, and M. Buss. A methodological variation for acceptance evaluation of human-robot interaction in public places. In *Proc. IEEE Ro-Man*, pages 713–718, 2008.

[187] A. D. Wilson, D. R. Collins, and G. P. Bingham. Perceptual coupling in rhythmic movement coordination: stable perception leads to stable action. *Exp. Brain Res.*, 164(4):517–528, 2005.

[188] A. M. Wing and A. Kristofferson. Response delays and the timing of discrete motor responses. *Percept. Psychophys.*, 14(1):5–12, 1973.

[189] T. Wojtara, M. Uchihara, H. Murayama, S. Shimoda, S. Sakai, H. Fujimoto, and H. Kimura. Human-robot collaboration in precise positioning of a three-dimensional object. *Automatica*, 45(2):333–342, 2009.

[190] H. A. Yanco and J. L. Drury. A taxonomy for human-robot interaction. In *Proc. AAAI Fall Symposium on Human-Robot Interaction*, pages 111–119, 2002.

[191] H. Yu, M. Spenko, and S. Dubowsky. An Adaptive Shared Control System for an Intelligent Mobility Aid for the Elderly. *Auton. Robots*, 15(1):53–66, 2003.

[192] X. Zhang and M. Hashimoto. SBC for motion assist using neural oscillator. In *Proc. IEEE ICRA*, pages 659–664, 2009.

[193] A. Z. Zivotofsky and J. M. Hausdorff. The sensory feedback mechanisms enabling couples to walk synchronously: An initial investigation. *J. NeuroEng. Rehabil.*, 4(1): 28, 2007.

Own Related Publications

[194] P. Donner, A. Mörtl, S. Hirche, and M. Buss. Human-Robot Cooperative Object Swinging. In *Proc. IEEE ICRA*, pages 4328–4334, 2013.

[195] M. Lawitzky, A. Mörtl, and S. Hirche. Load Sharing in Human-Robot Cooperative Manipulation. In *Proc. IEEE Ro-Man*, pages 185–191, 2010.

[196] T. Lorenz, A. Mörtl, B. Vlaskamp, A. Schubö, and S. Hirche. Synchronization in a goal-directed task: human movement coordination with each other and robotic partners. In *Proc. IEEE Ro-Man*, pages 198–203, 2011.

[197] T. Lorenz, A. Mörtl, and S. Hirche. Movement synchronization fails during non-adaptive human-robot interaction. In *Proc. ACM/IEEE HRI*, pages 189–190, 2013.

[198] T. Lorenz, B. N. S. Vlaskamp, A.-M. Kasparbauer, A. Mörtl, and S. Hirche. Dyadic movement synchronization while performing incongruent trajectories requires mutual adaptation. *Front. Hum. Neurosci.*, 8(461), 2014.

[199] J. Medina, M. Lawitzky, A. Mörtl, D. Lee, and S. Hirche. An Experience-Driven Robotic Assistant Acquiring Human Knowledge to Improve Haptic Cooperation. In *Proc. IEEE/RSJ IROS*, pages 2416–2422, 2011.

[200] A. Mörtl, M. Lawitzky, A. Kucukyilmaz, M. Sezgin, C. Basdogan, and S. Hirche. The Role of Roles: Physical Cooperation between Humans and Robots. *Int. J. Rob. Res.*, 31(13):1656–1674, 2012.

[201] A. Mörtl, T. Lorenz, B. Vlaskamp, A. Gusrialdi, A. Schubö, and S. Hirche. Modeling inter-human movement coordination: synchronization governs joint task dynamics. *Biol. Cybern.*, 106(4):241–259, 2012.

[202] A. Mörtl, T. Lorenz, and S. Hirche. Rhythm Patterns Interaction – Synchronization Behavior for Human-Robot Joint Action. *PLOS ONE*, 9(4):e95195, 2014.